

Clemson University

TigerPrints

All Dissertations

Dissertations

8-2018

First Principles-Based Microkinetic Modeling of Ethanol from Syngas on Bimetallic Co-Pd Catalysts

Anuradha Gundamaraju

Clemson University, agundamaraju@gmail.com

Follow this and additional works at: https://tigerprints.clemson.edu/all_dissertations

 Part of the [Chemical Engineering Commons](#)

Recommended Citation

Gundamaraju, Anuradha, "First Principles-Based Microkinetic Modeling of Ethanol from Syngas on Bimetallic Co-Pd Catalysts" (2018). *All Dissertations*. 2967.

https://tigerprints.clemson.edu/all_dissertations/2967

This Dissertation is brought to you for free and open access by the Dissertations at TigerPrints. It has been accepted for inclusion in All Dissertations by an authorized administrator of TigerPrints. For more information, please contact kokeefe@clemson.edu.

FIRST PRINCIPLES-BASED MICROKINETIC MODELING OF ETHANOL FROM SYNGAS
ON BIMETALLIC Co-Pd CATALYSTS

A Dissertation
Presented to
the Graduate School of
Clemson University

In Partial Fulfillment
of the Requirements for the Degree
Doctor of Philosophy
Chemical Engineering

by
Anuradha Gundamaraju
August 2018

Accepted by:
Dr. David A. Bruce, Committee Chair
Dr. Rachel B. Getman
Dr. Joseph K. Scott
Dr. Steven J. Stuart

ABSTRACT

In the future, the availability of reliable alternative fuels will be crucial for any country to become energy independent. One such alternative is ethanol as it can be used both as a fuel and as a fuel additive. Most of the ethanol produced in the world today is derived from biomass. The biomass feedstocks and fermentation broths used in ethanol production both contain high amounts of water and therefore, the energy efficiency of the process is lessened by product separation processes (azeotropic separation of water and ethanol) that are non-trivial and highly inefficient (due to the evaporation of water). An alternative route to produce ethanol, which negates the need for costly distillation processes, is via the catalytic conversion of syngas (CO and H₂) generated from biomass.

Syngas is a mixture of carbon monoxide and hydrogen, which results from the reforming of natural gas, as well as the gasification of coal, biomass, and solid wastes. In theory, syngas can be readily converted to ethanol using chemical catalysts, but to-date no high efficiency, low-cost catalyst has been found.

In this work, sub-nanometer size, bimetallic cobalt-palladium particles are found to be active and selective catalysts for the desired reaction as the particles contain two metals having different CO dissociation capabilities. The reaction mechanism considered for this study includes forty-six reversible reactions, including Fischer-Tropsch reactions. We used Density Functional Theory (DFT) coupled with nudged elastic band methods to determine the activation barrier heights and enthalpy change with reactions for the full

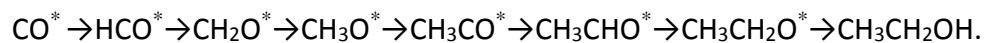
reaction pathway needed for ethanol production from syngas. To lessen the computational burden, linear Bronsted-Evans–Polanyi (BEP) relations, for association and dissociation reactions, are developed.

A microkinetic model is built using the reaction information derived from combined DFT and BEP studies, which is used to examine if there is a synergistic effect between Co and Pd favoring the production of ethanol. Coverage dependent sticking coefficients are used to examine the effects of surface coverage on reactivity. It also incorporates diffusion of intermediate species between the sites.

One of the first and important steps in the syngas to ethanol conversion process is carbon monoxide (CO) adsorption on the metal catalyst. Therefore, computational models were developed to help understand CO adsorption energetics as well as surface coverage effects on a Co_7Pd_6 catalyst. From these initial studies, we determined the adsorption energies of CO on both cobalt and palladium as a function of CO surface coverage (where the number of CO species on the catalyst surface was varied from 1 to 6). Further, we calculated the infrared spectra for adsorbed CO species and key bond lengths (metal–carbonyl carbon and adsorbed CO bond lengths) using DFT. Results from the DFT simulations compared favorably with experimental values.

Separate microkinetic models results on Co, CoPd and Pd sites indicate that ethanol formation happens only on CoPd bimetallic sites indicating the synergetic effect of Co and Pd to make ethanol from syngas. A batch reactor is modeled and 24 ordinary

differential equations are solved simultaneously to obtain time evolution of products and intermediates. The pathway for ethanol production is identified as:



Further, the microkinetic model was modified to include diffusion reactions. Ratio of number of sites of cobalt, cobalt-palladium and palladium is altered to study Co_xPd_y catalysts of different cobalt and palladium ratios.

DEDICATION

I would like to dedicate this dissertation to my husband Ravi Eluripati for his constant encouragement, love, and support throughout my Ph.D. program. I would also like to dedicate my work to my parents (Venkat Rao and Swarnalatha Gundamaraju) for putting me through the best education possible to make my Ph.D. doctorate dream possible and to my loving and caring daughter Laasya who completed our family.

ACKNOWLEDGEMENTS

There are so many people without whom this dissertation would not have been possible.

First-of-all, I would like to express my most sincere gratitude to my advisor Dr. David A. Bruce for his constant encouragement and guidance throughout the program. Every meeting I had with Dr. Bruce has been a great learning experience and enjoyable with his subtle sense of humor while explaining complex processes. I am truly grateful for his personal commitment to get me through the program and his unwavering support during the tough phases throughout the program. This work would have never been possible without his support.

I would like to thank my committee members Dr. Getman, Dr. Scott and Dr. Stuart for readily agreeing to be my committee members. Their support to help me graduate from Clemson University is very much appreciated.

I am very thankful to all wonderful professors and staff in the Chemical Engineering department. My special thanks to Dr. Hirt and Dr. Husson for their administrative support during the most stressful times. Thanks to Terry, Joy, Diana and Bill for treating me like family and making my stay at Clemson most enjoyable & memorable.

I would like to say a heartfelt thank you to my fellow doctorates and good friends Dr. Ming and Dr. Felipe, whose support and advice helped me greatly.

Thanks to Clemson University resources, IT helpline and Palmetto cluster support center for their helpful facilities & continuous support.

Lastly, I would like to gratefully acknowledge the support of the following family members and very close friends who have made my life easy with their unconditional love and support. Their constant words of encouragement have kept me going without losing track of my goals - Raja Rao Eluripati, Sreedevi Eluripati, Krishna and Sravanti Gundamaraju, Kiran and Prashanti Gundamaraju, Kalyan and Swathi Gundamaraju, Rajeev and Aruna Eluripati, Chaitanya and Harsha Uppaluri, Hemanth and Harshith Gundamaraju, and A.G.Saritha Gangaputra.

TABLE OF CONTENTS

	Page
ABSTRACT	ii
DEDICATION	v
ACKNOWLEDGEMENTS	vi
LIST OF TABLES	x
LIST OF FIGURES	xii
1. CHAPTER ONE INTRODUCTION AND LITERATURE REVIEW	1
Introduction.....	1
Sources of Syngas	2
Other uses of ethanol.....	3
Ethanol from syngas	4
Primary syngas to ethanol catalysts examined to-date	5
Dissertation objectives	18
References.....	22
2. INTRODUCTION TO DENSITY FUNCTIONAL THEORY	32
Introduction.....	32
Density functional theory (Nobel prize 1998)	35
Hohenberg-Kohn's theorems	36
Kohn-Sham's equations:.....	37
Basis sets	39
Exchange correlation Functionals:	43
Commercial DFT software's.....	45
3. Study of CO adsorption and coverage effects on Co ₇ Pd ₆ 13 atom bimetallic catalyst cluster..	50
Introduction.....	50
Experimental	52
Results and Discussion	54
Conclusions.....	72
4. DFT and Microkinetic modeling study of Syngas to ethanol conversion on Isolated Sites of a BIMETALLIC Co ₇ Pd ₆ NANOCUSTER.....	83
Introduction.....	83

Table of Contents (Continued)	Page
Experimental	87
Results and discussion.....	98
Conclusions.....	124
5. Ethanol synthesis from syngas: Combined microkinetic model on Co_xPd_y cluster, study OF DIFFUSION effects on product distribution.....	136
Introduction.....	136
Experimental	139
Results and discussion.....	153
Conclusions.....	175
6. Composition effects of Cobalt – palladium bimetallic catalyts for ethanol synthesis from syngas (Co+H₂).....	185
Introduction.....	185
Experimental	189
Results and Discussion	191
Conclusions.....	199
7. Conclusions and recommendations	203
Conclusions.....	203
Recommendations.....	207
Key assumptions in this dissertation	211
APPENDICES.....	217
APPENDIX A	217
APPENDIX B	231
APPENDIX C	249
APPENDIX D	272
V I T A.....	302

LIST OF TABLES

Table	Page
TABLE 3. 1. CO binding on Co ₇ Pd ₆ cluster.....	60
TABLE 3. 2. Comparison of CO binding energies calculated from Jaguar and VASP	62
TABLE 3. 3. Comparison of experimental and computational values for vibrational frequency ..	72
Table 4. 1. List of intermediate species and gas phase reactants and products.....	89
Table 4. 2. Adsorption energies and preferred adsorption site of key intermediates on cobalt, CoPd and palladium surfaces	99
Table 4. 3. Activation energies on palladium surface compared to literature values	101
Table 4. 4. Activation energies on cobalt surface compared to literature value	103
Table 4. 5. Activation energies and equilibrium constants of CO hydrogenation reactions.....	106
Table 4. 6. Activation energies and equilibrium constants of CH _x O dissociation reactions.....	107
Table 4. 7. Activation energies and equilibrium constants of CO hydrogenation reactions.....	107
Table 4. 8. Product distributions observed for syngas conversion using the present microkinetic model and experiments using supported metal catalysts.	121
Table 4. 9. Activation energies of key CO insertion and hydrogenation reactions.....	123
Table 5. 1. List of intermediate species and gas phase reactants and products.....	148
Table 5. 2. Product distribution from separate Microkinetic models	158
Table 5. 3. Activation energies for key diffusion reactions D1 to D22 corrected by a factor of 0.7	164

List of Tables (Continued)

Table	Page
Table 5. 4. Microkinetic model results with and without diffusion reactions compared to experimental results on CoPd catalyst.....	165
Table 6. 1. Cluster composition effects, a comparison of activation energies of key syngas to ethanol reactions on Co ₇ Pd ₆ and Co ₉ Pd ₄ catalysts.....	193
Table 6. 2. Activation energy trends for different types of reaction on Co rich surface and Co ₇ Pd ₆ surface.....	194
Table 6. 3. CO coverage effects, a comparison of activation energies of key syngas to ethanol reactions on a pristine Co ₇ Pd ₆ cluster and a Co ₇ Pd ₆ (CO) ₆ cluster having Pd sites saturated with CO.....	196
Table 6. 4. Activation energy trends for different types of reaction on Co ₇ Pd ₆ surface at high and low coverage	198

LIST OF FIGURES

Figure	Page
Figure 2. 1. Gaussian functions approximated by slater type orbitals (STOs) ⁸	40
Figure 2. 2. STO-3G wave function used to represent the 1S orbital of Hydrogen atom. We can see that STO-3G cannot represent the cusp at $r=0$. ⁸	41
Figure 2. 3. Widely used 6-31G ⁺⁺ basis set ⁸	42
Figure 3. 1. Transition metals grouped as catalysts for carbon chain elongation (Red color) and alcohol formation reactions (Blue color).....	55
Figure 3. 2. 13 atom metal cluster containing 7 cobalt atoms and 6 palladium atoms. Cobalt and palladium are segregated.....	56
Figure 3. 3. Thirty-eight atom (Co ₆ Pd ₃₂) cluster with cobalt atoms as core and palladium atoms in shell.	56
Figure 3. 4. Energy of Co ₇ Pd ₆ cluster at different spin states.....	57
Figure 3. 5. Two fold electronic interactions between palladium atoms in the cluster and CO molecule (Blyholder model).	58
Figure 3. 6. CO binding energies on atop and bridge when center Pd atom is involved in binding vs. when center Pd atom is not involved.	63
Figure 3. 7. Average adsorption energy for a CO molecule as a function of CO surface coverage on palladium sites of the Co ₇ Pd ₆ cluster using DFT methods with B3LYP functionals.....	64
Figure 3. 8. Average adsorption energy for a CO molecule as a function of CO surface coverage on palladium sites of the Co ₇ Pd ₆ cluster using DFT methods with MO6 functionals.....	65
Figure 3. 9 HOMO shift from Pd side to Cobalt side when 4 atoms are bonded in bridge configuration.	66

List of Figures (Continued)

Figure	Page
Figure 3. 10. Average CO adsorption energy change with the number of CO molecules adsorbed to Pd sites of the cluster using DFT methods employing B3LYP or M06 functionals.....	67
Figure 3. 11. Metal carbonyl bond lengths changing with number of CO on surface of Pd on Co_7Pd_6 cluster.....	68
Figure 3. 12. Carbon-oxygen bond lengths changing with number of CO on surface of Pd	69
Figure 3. 13. Variations in carbon-oxygen bond lengths as a function of CO surface coverage on the cobalt sites of a Co_7Pd_6 cluster.....	70
Figure 3. 14. Variations in cobalt-carbonyl carbon bond lengths as a function of CO surface coverage on the cobalt sites of a Co_7Pd_6 cluster.....	70
Figure 3. 15. Calculated shift in IR absorption frequency for CO vibrations as a function of Co surface coverage for CO molecules adsorbed on Pd bridge sites of the cluster.....	72
Figure 4. 1. Three-fold catalytic surface sites on the optimized Co_7Pd_6 catalyst: Co_3 , Pd_3 and mixed sites CoPd_2 and Co_2Pd sites. Cobalt and Palladium are represented in pink and blue, respectively.	87
Figure 4. 2. BEP relationships for association and dissociation reactions obtained from DFT calculations on the Co_7Pd_6 catalyst ²⁸	91
Figure 4. 3. Reaction mechanism for the conversion of syngas to ethanol and related products. Surface intermediates are represented by *. CO insertion reactions are shown with red arrows, hydroxylation reactions by black arrows, hydrogenation reactions by blue arrows, and Fischer-Tropsch type reactions by green arrows.....	93
Figure 4. 4. Sticking coefficient as a function of coverage on cobalt surface.....	109

List of Figures (Continued)

Figure	Page
Figure 4. 5. Sticking coefficient as a function of coverage on palladium surface.....	109
Figure 4. 6. Sticking coefficient as a function of coverage on cobalt-palladium surface	110
Figure 4. 7. Rate constants for important reactions for methane and methanol formation on palladium surface. CH_2O^* and CH_3O^* formation is favored compared to CH_x formation. CH_2O^* and CH_3O^* then undergo hydrogenation to form methanol.....	112
Figure 4. 8. Rate constants for important reactions for methane and methanol formation on Cobalt surface. CH_x^* formation is favored, concentration of CH_x^* is higher and favored product is methane.	113
Figure 4. 9. Rate constants for important reactions for methane and methanol formation on cobalt-palladium surface. Both CH_xO^* formation CH_x^* and is favored, concentration of CH_x^* is higher.....	114
Figure 4. 10. Rate constants for reversible reactions leading to ethanol formation at CoPd interface.	116
Figure 4. 11. Time evolution of products on palladium rich surfaces	119
Figure 4. 12. Time evolution of products on cobalt rich surface.....	120
Figure 4. 13. Time evolution of products on cobalt-palladium interface.....	120
Figure 5. 1. Thirteen atom metal cluster of seven cobalt atoms and six palladium atoms.....	139
Figure 5. 2. BEP relationships for association and dissociation reaction types obtained from DFT calculations for the Co_7Pd_6 catalyst. Transition state energies are related to final product reaction energies for gas phase reactants combining with vacant site(s) to form adsorbed products. ³⁹	143

List of Figures (Continued)

Figure	Page
Figure 5. 3. Sticking coefficient as a function of coverage on cobalt surface.....	154
Figure 5. 4. Sticking coefficient as a function of coverage on palladium surface.....	155
Figure 5. 5 Sticking coefficient as a function of coverage on cobalt-palladium surface	155
Figure 5. 6. Reaction mechanism of syngas to ethanol conversion. Although ethanol is desired product other products methanol, methane, ethane, ethylene and acetaldehyde are formed as byproducts. Intermediates on surface of the catalyst are represented by *. Color of the arrows indicate the type of reaction. CO insertion reactions are shown with red arrows, hydroxylation reaction by black arrows, hydrogenation reactions by blue arrows, and CH ₂ insertion reactions are represented in green.....	157
Figure 5. 7. Ternary diagrams for product selectivity with and without diffusion reactions included in the model. Product selectivity in (mol%) a) methane without diffusion, b) methane with diffusion, c) ethane without diffusion, d) ethane with diffusion Axis x, y and z represent concentrations of metal sites Pd, CoPd, Co sites respectively	170
Figure 5. 8. Ternary diagrams for product selectivity with and without diffusion reactions included in the model. Product selectivity in (mol%) a) methanol with diffusion, b) methanol without diffusion, c) ethanol without diffusion, and d) ethanol with diffusion. Axis x, y and z represent concentrations of metal sites Pd, CoPd, Co sites respectively. Note that the scale for a and d is different	171

List of Figures (Continued)

Figure	Page
Figure 6. 1. Key reactions identified for the synthesis of ethanol from syngas and structures of the geometry optimized Co_7Pd_6 and Co_9Pd_4 clusters.	187
Figure 6. 2. Co_7Pd_6 cluster with CO ligands bound to each Pd surface site.	190

CHAPTER ONE

INTRODUCTION AND LITERATURE REVIEW

Introduction

With the world's population increasing, the average standard of living improving, and globalization of trade becoming commonplace, it is to be expected that the world's energy demands will continue to increase. To meet this ever-growing demand there is a need to develop new technologies for generating and storing energy.¹

The US Energy Information Administration's recent International Energy Outlook 2016 projects that world energy consumption will grow by 48% between 2012 and 2040. Although research into renewable fuels and the production of energy from renewable sources is growing, more than three-fourths of the world's energy is still dependent on fossil fuels.²

With a growing population and increases in mobility for much of this population, the demand for liquid transportation fuels is also increasing. Renewable energy technologies that are fast growing are solar energy, wind energy, geothermal energy and biofuels. Out of these, only biofuels addresses the ever-increasing demand for liquid fuels. Today most of the transportation energy needs are met by nonrenewable sources like fossil fuel derived gasoline and diesel. There are growing environmental concerns associated with the use of fossil fuels, and the reserves of these fuels are limited, and data suggests that if consumption continues at its present rate then supplies will be

greatly diminished within a century. One of the promising renewable alternatives to meet the demand for liquid fuel is ethanol. Ethanol can be used as a fuel or as an additive to fossil derived gasoline fuels. Additionally, ethanol can be used for the production of hydrogen using fuel cells.^{3,4}

Currently, ethanol is primarily being produced via fermentation of biomass resources such as sugar cane, corn steep liquor, and select lignocellulosic feed stocks. In spite of being an attractive process, ethanol from fermented biomass has its challenges. For example, the transportation of biomass to the production site can be expensive, and separation of the azeotropic water-ethanol mixtures resulting from bioprocessing are costly and energy intensive. Additionally, the biomass fermentation process used to synthesize ethanol is limited to only a few select components of the biological feed stocks, namely the sugar based components, and the lignin components in the biomass cannot be converted by current technologies.⁵⁻⁷

An alternative route to produce ethanol is from syngas. Syngas is a mixture of carbon-monoxide and hydrogen that is routinely derived from fossil or renewable sources of methane. This mixture of CO and H₂ can be catalytically converted to ethanol, but current technologies are too costly to be used for large-scale production.^{3,8-10}

Sources of Syngas

Syngas has been known to be an important reactant in Fischer-Tropsch processes to produce higher hydrocarbons like diesel and kerosene. Syngas can be produced via the

gasification of coal, biomass and petroleum.^{3,11,12} Additionally, the increased findings of shale gas reserves in recent years have meant there is greater need to develop technologies for the conversion and use of methane, which is the main component of shale gas. Methane can be converted to syngas by steam reforming, auto thermal reforming or dry reforming of methane. In addition to these sources, syngas can be recovered from the exit stream of many industrial processes, such as the production of steel from iron ore.¹³

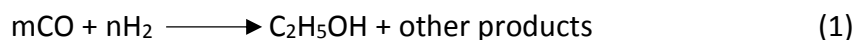
In the present study, we are interested in the production of ethanol from syngas via non-aqueous based chemical reaction processes employing heterogeneous catalysts.¹⁴ The hydrogenated products generated from a reactor of this type would require less energy to separate, making it more cost effective to isolate a clean ethanol product that could meet fuel grade standards.

Other uses of ethanol

Apart from using ethanol as an alternative fuel, it can also be used as a fuel additive to reduce pollution. Ethanol is a good additive for improving the octane value and burning efficiency of gasoline. It can also be used as a solvent in many industrial processes; for example, it is used in the pharma industry for the production of medicines and drugs and is used in the production of hydrogen using fuel cells.³

Ethanol from syngas

Syngas can be chemically converted to ethanol in the presence of an appropriate catalyst. The reaction involving this process can be represented as,



Ethanol production from syngas has been widely studied for more than 95 years.¹⁵ Despite this fact, there is currently no commercial process for the production of ethanol via this route, as the selectivity towards the desired ethanol product and overall conversion are still very low with current catalyst technologies. Much of the slow progress in developing improved catalysts for this reaction can be explained by the fact that the reaction kinetics are slow for the initial C-C bond formation to form C₂ species and fast for the carbon chain growth of C₂ intermediates. In other words, catalysts that are able to form the necessary C-C bonds to go from CO to ethanol are unlikely to stop at a simple two carbon chain, but instead will continue reacting to form longer hydrocarbons chains, mimicking the behavior of Fischer-Tropsch metal catalysts. Other by-products that are commonly encountered with syngas to ethanol production are methane, ethane, acetaldehyde and methanol.

Many transition metals have been studied as catalysts for the syngas to ethanol reaction. Thus far, the best catalyst for this reaction was found to be a supported rhodium catalyst.¹⁶ However, using rhodium as the active metal catalyst has its own disadvantages. First, rhodium is expensive and is not a widely abundant metal in nature. Secondly, when

rhodium is used as the catalyst its selectivity towards the desired product ethanol is still quite low. To overcome these disadvantages there is still a search for alternative catalysts that are more efficient and cost effective catalysts for the production of ethanol from syngas.¹⁷⁻²¹

Primary syngas to ethanol catalysts examined to-date:

The most common types of catalysts used for the conversion of syngas to ethanol can be classified in to four groups:

1. rhodium and rhodium based catalysts,
2. Mo based catalysts,
3. methanol synthesis catalysts, and
4. modified methanol synthesis catalysts with FT metals.

Rhodium and rhodium based catalysts

The syngas to ethanol conversion reaction has been of interest for more than 90 years. To implement this process a selective catalyst is needed. Rh based catalysts have thus far been the most selective towards ethanol production, and therefore, the most widely studied systems for ethanol synthesis from syngas. Previous experimental^{8,21-25} and theoretical studies^{26,27} indicate that rhodium is an ideal catalyst element for this reaction because it exhibits unique efficiency at inserting CO species into adsorbed Rh-C₁ bonds and the resulting species favor termination as alcohols instead of undergoing further hydrogenation and chain growth.

The type of support and promoter has also been shown to have influence on the conversion of CO and selectivity towards the desired ethanol product. Types of supports studied previously for Rh based catalysts are SiO_2 ^{8,16,22,24,28,29}, TiO_2 ²², SBA-15²⁵, Al_2O_3 ¹⁸ and cerium based ZrO_2 ²³. Most prior studies focused on SiO_2 as the support due to its high surface area, increased porosity and good stability. Also, SiO_2 is believed to improve CO adsorption owing to its high surface area. Guanzhong Lu et al. have proposed a combination of SiO_2 - TiO_2 as the catalyst support, combining the high surface area properties of SiO_2 with the promoter effects of TiO_2 , which favor the formation of C_2+ oxygenates.²² They have reported that SiO_2 - TiO_2 based Rh catalysts produce more C_2+ oxygenates compared to Rh on SiO_2 or TiO_2 supports alone. In related work, Guoqing Yuan et al.²⁵ used SBA-15 as the support material for rhodium. SBA-15 being a mesoporous molecular sieves with two-dimensional hexagonally ordered arrays of channels was selected as the catalyst support owing to its high thermal stability, appreciably large pore diameter, high pore volume and surface area. Fe promoted Rh on SBA-15 reduced methane formation thereby increasing selectivity towards the desired ethanol product.²⁵ Al_2O_3 was also employed as a support material for Rh based catalysts. José Luis G. Fierro et al. used Al_2O_3 in place of SiO_2 , they reported that for the syngas to ethanol conversion reaction the reactivity and activity of Rh based catalyst did not change appreciably when switching between Rh/ Al_2O_3 and Rh/ SiO_2 catalysts. The effect of supports was studied using ZrO_2 and SiO_2 as supports for Rh, Mn and Li were used as promoters in both cases. CO conversion remained same when RML/ SiO_2 or RML/ ZrO_2 were tested, but the

selectivity to C₂-oxygenates improved with ZrO₂. When RML was loaded on SiO₂-ZrO₂ mixed oxide both CO conversion and C₂-oxygenate selectivity increased.⁸ Yet another support, Ce based ZrO₂ was studied, CeO₂ promotes strong interactions between support and metal and generally improves overall catalyst performance. Rh supported on basic or neutral supports improved C₂-oxygenate formation, but excess acid sites decreased selectivity towards ethanol. Rh supported on basic supports promoted formation of mixed alcohols. NH₃-TPD and CO₂-TPD results on the Rh/Ce_{1-x}Zr_xO₂ catalyst revealed that the catalyst had both acid sites and base sites resulting in an increased CO conversion of 27.3% as compared to the 10.1% conversion found with the Rh/SiO₂ catalyst.²³

The primary disadvantages of rhodium based catalysts are the availability of rhodium and its price. To offset these disadvantages there are numerous studies on promoters for this reaction, including those using iron, zirconium, vanadium and lanthanum with rhodium-based catalysts.^{18,20,25,30-34} Specifically, Guoqing Yuan et al. showed the effect of iron loading on Rh/SBA-15. It was shown that as the iron loading on the catalyst increased, the active sites on the rhodium surface reduced; therefore, CO conversion also decreased. Increasing the iron loading from 0.5% to 2.5% significantly increased the ethanol selectivity from 3.6% to a maximum of 20.6%. When the iron loading was further increased to 10%, ethanol selectivity dropped to 14.6%.²⁵

In another paper, Stevens et al. utilized DFT calculations to investigate the performance of Rh-MN based catalysts. When manganese was used along with rhodium,

CO insertion energy barriers were reduced, improving selectivity towards the desired ethanol product. However, the presence of manganese did not affect the selectivity towards methane.²⁹ The effect of several promoters (M = Ir, Ga, V, Ti, Sc, Ca, and Li) on the CO insertion reaction over Rh/M alloy nanoparticles was also investigated. It was determined that the electronegativity difference between the promoter, M, and rhodium plays a key role. When the difference is 0.7, CO insertion barriers are lowered, and ethanol selectivity is found to be increased. This helps to explain the favorable activity of titanium doped materials, where the electronegativity difference between rhodium and titanium is found to be 0.7. The effect of manganese as a promoter was also reported by several researchers^{8,18,22}, and the resulting catalyst activity data showed that the selectivity towards ethanol increased when manganese is added as promoter. Additionally, other supports such as lanthanum, vanadium and iron were also reported to be favorable for the formation of C₂-oxygenates.^{24,28}

Molybdenum based catalysts

Molybdenum based catalysts have been widely studied because of their unique physical and chemical properties resembling that of noble metals. Additionally, Mo catalysts are generally low-cost, sulphur tolerant, and resistant to carbon deposition. When used for the catalytic conversion of CO, molybdenum based catalysts showed good hydrogenation activity with the formation of light hydrocarbons, where methane is the main product.^{30,35-37} Campoy et al. used alkali-Co doped molybdenum sulfide catalysts

to study the synthesis of higher alcohol production from syngas. In their study, methanol was recycled from the product stream, and the effect of methanol co-feeding was reported. A power law model was used to fit the data from experiments, which revealed that as the methanol content in the feed was increased, ethanol and higher alcohol production increased linearly. At the same time, hydrocarbon productivity increased exponentially.³⁵

Jensen et al. studied the production of higher alcohols from syngas on alkali doped Co-Mo-sulfide. These researchers also studied the effect of H₂S and process conditions like temperature and molar partial pressures of the reactants CO and H₂ on higher alcohol production. The addition of H₂S to the feed stream increased CO conversion, but the selectivity towards hydrocarbons increased and higher alcohol selectivity decreased. They showed that hydrocarbons have higher activation energies than alcohols indicating that increasing temperature favors higher CO conversions at the expense of increases in the production of hydrocarbons. It was also noted that selectivity and activity both increase with an increase in metal loading. However, rhodium based catalysts were found to be superior, leading to higher conversions of CO and a higher selectivity towards higher alcohols.³⁶

In another study published in 2013 by Hong et al. reported the use of Ni-Mo-K sulfide catalysts doped with carbon nanotubes (CNTs) for the conversion of syngas to ethanol and higher alcohols. When Ni_{0.5}Mo₁K_{0.5} 15%CNT was used as catalyst at reaction

conditions of 8 MPA and 593K, ethanol selectivity was higher than the case where CNTs were not present. Thus, CNTs were found to have promoting effects, increasing the alcohol production from syngas, but the cost and stability of these catalyst makes it unlikely that they will achieve commercial success.³⁰

Järås et al. studied the production of alcohols from syngas in the presence of K-Ni-MoS₂ catalysts; specifically examining the effects of operating parameters and the presence of catalyst promoters. It was found that, there is a correlation between CO conversion and selectivity towards higher alcohols. CO conversion increases with increases in temperature or decreased space velocity. As CO conversion increases hydrocarbon selectivity increases and selectivity towards ethanol and other higher alcohols decreases. The effect of promoters on alcohol production was also studied, and results indicate that the selectivity towards alcohols was increased in the presence of promoters.³⁷

Modified methanol catalysts

Syngas to ethanol processes have also been studied using traditional methanol synthesis catalysts. Copper is well known as a methanol synthesis catalyst and numerous studies with copper based catalysts are reported in the literature.^{32,34,38-43} Copper is inexpensive and widely available, which makes it an attractive alternative over noble metals. Also, when copper is used to produce methanol a small amount of higher alcohols was produced as a co-product. Copper based catalysts can be used to produce ethanol if

we can modify the catalyst with either support or by adding promoters such that the selectivity towards undesired products methane can be reduced. Most of the catalysts studied in this group are CuO-ZnO-Al₂O₃^{34,38}, Cu-ZnO^{39,41}, Cu /MCM-41³², Cu-Zn-Al⁴⁰, Cu based catalyst with alkali promoters⁴³ and Cu⁴².

Use of copper based catalysts for syngas to ethanol production was studied as early as 1988.³⁸ F. Pennella et al. used CuO/ZnO/Al₂O₃ catalysts to understand the syngas to ethanol reaction mechanism. This reaction was carried out in a fixed bed micro reactor where a small amount of methanol was added to feed. The amount of ethanol formed at zero contact time was found to be a function of methanol partial pressure in the feed. The isotopic distribution of the ethanolic carbon was consistent with a mechanism that involves a C1 species that is an intermediate in the formation of both ethanol and methanol. In yet another very recent (2016) study similar catalyst that were cobalt modified Cu/ZnO/Al₂O₃ was used, and the effect of sodium on the activity of catalyst was studied. Presence of cobalt in the catalyst has enhanced the sites for CO dissociation. Sodium acts as a dopant influencing catalytic activity. At low sodium loadings (less than 2%) the selectivity of ethanol increased but with high sodium loadings (0.8 wt%) catalyst underwent strong sintering of the metallic copper particles and thus Cu-Co interfacial sites were lost, thus ethanol selectivity dropped.³⁴

The addition of dimethyl ether (DME) into the feed was tested by G. Yang et al. In their report, a dual catalyst bed reactor was employed with H-MOR catalyst for

carbonylation of DME to methyl acetate, Cu/ZnO catalyst then hydrogenates methyl acetate to ethanol. The productivity and selectivity was reported to be enhanced in the presence of DME. When both the catalysts were used in the dual bed catalytic reactor the conversion of DME is reported to be as high as 56.3% with a selectivity of 55.3% methanol and 39.3% ethanol. When Cu/H-MOR was used in place of H-MOR the conversion of DME and CO both increased and the selectivity towards desired product ethanol also improved to 44.1%.³⁹

Various support materials were tested for copper-based catalysts. One such support is the meso-structured silica based support MCM-41³² which is attractive because of the supports high surface area of 1000 m²/g. High surface area improves the dispersion of active sites on the catalyst surface. Non-promoted Cu/MCM-41 catalyst favored methanol formation. The effect of the two promoters potassium and iron on Cu/MCM-41 catalyst indicated that when just potassium is added the selectivity towards methanol further increases, while the addition of promoter iron improves the hydrocarbon formation. But when both potassium and iron are added as promoters to Cu/MCM-41 catalysts the rate of formation of oxygenates increases, especially that of ethanol. This increase in ethanol formation is explained by the increase in reaction rate towards CO dissociation and CO non-dissociation steps.³²

Not surprisingly, syngas to ethanol experimental data suggests that the method of catalyst preparation influences the catalytic activity of copper-based catalysts. Y.-J. Liu et

al. prepared a complete liquid phase Cu-Zn-Al catalyst utilizing the sol-gel method. This liquid catalyst was found to have key Cu^+ and strong weak acid on the catalysts surface which was necessary for ethanol formation. The selectivity of ethanol with this catalyst was improved. Catalysts prepared from traditional methods such as incipient wetness impregnation method exhibited more conversion of CO and the major product was methanol (97% selectivity). This method of preparation has also stated that carbon chain growth can happen on liquid CuZnAl catalysts without the need of other promoters⁴⁰. J.J. Spivey et al. reported another novel method for the preparation of Cu-ZnO and Mn-Cu/ZnO based catalysts for higher alcohol formation. Nano porous polycarbonate membrane was used as a template for electro deposition of precursor metals from aqueous electrostatic solution containing $\text{Zn}(\text{NO}_3)_2$, $\text{Cu}(\text{NO}_3)_2$, $\text{Mn}(\text{NO}_3)_2$ and NH_4NO_3 . The resulting catalyst was in the form of nanotubes and nanowires. Addition of manganese improved the selectivity for higher alcohols by reducing methane and methanol formation. When Cu-ZnO nanowires was used as catalysts, selectivity towards ethanol was around 15.7% .^{40,41}

In the recent study performed by H. Zheng et al., density functional theory (DFT) was used to understand the mechanism of ethanol formation from syngas over a Cu [1 0 0] catalyst. Detailed mechanism is presented, where the two main products considered are methanol and ethanol. Ethanol formation proceeds via formation of intermediates CHO, CH_2O , CH_3O , CH_3 , and $\text{CH}_3\text{CH}_2\text{O}$. Further, the key intermediate was identified to be CH_3O . On a copper surface, CH_3O readily converts to CH_3OH therefore there is a need to

add promoters or supports which can help suppress the CH₃OH formation and/or maximize CH₃ formation.⁴²

Copper based catalysts Cu/ZnO or Cu/Al₂O₃ are known for their catalytic activity for methanol formation, and the addition of alkali metals as promoters was found to be promising for ethanol formation. Alkali promoters are suitable to neutralize the acidity of the catalysts, thus controlling the undesired reactions such as dehydration, isomerization, coke formation and methanation, improving the selectivity towards ethanol. Non-alkali promoters such as Mn, Ce, K, Na, and La₂O₃ also proved to significantly affect the product distribution. Irrespective of the kind of support used, physical parameters of temperature and pressure, addition of promoters in optimum amount enhances the ethanol formation.⁴³

Bimetallic Catalysts

Another important class of catalysts studied in recent years for ethanol synthesis is bimetallic catalysts. The metal combinations are designed so that one of the metals is used as a methanol synthesis catalyst (copper mostly) and the second metal is used as a FT-synthesis catalyst. Some combinations reported so far are Cu-X (X=Fe, Co, Ni)^{9,31,44-55} and Co-Pd⁵⁶. The presence of dual sites, CO insertion (copper) and CO dissociation (FT metal), is said to have synergetic effects in increasing selectivity towards the desired ethanol product.

Cu-Fe bimetallic catalysts are found to be very promising catalysts because both the metals are inexpensive. Cu-Fe catalysts are studied on SiO₂ based bimodal supports⁴⁹. The bimodal support was prepared by incipient wetness impregnation of silica gel with silica sol. Larger and smaller pores coexist in the bimodal derived catalyst, where larger pores of bimodal catalyst provide pathways for carbon chain growth of methanol and high diffusion efficiency of products and the smaller pores provided higher surface area and higher active metal dispersion, promoting the catalytic activity. However, the selectivity towards ethanol was low (less than 12%) when compared to C₄₊ alcohols. Effect of zinc and manganese as promoters on Cu-Fe catalyst was shown by Y. Lu et al.⁴⁶. It was shown that both zinc and manganese promoted the catalytic activity but they had different roles as promoters. ZnO improved the CO conversion rate, enhanced the stability of catalyst, and decreased selectivity towards higher alcohols whereas, manganese improved the BET surface area of catalyst and improved the dispersion of copper and iron. A CO conversion of 72% and ethanol selectivity of 24% were reported.⁴⁶ In order to understand the mechanism and intrinsic function of active metals unsupported Cu-Fe nanoparticles were tested by K. Xiao et al. Results indicated that mixing copper nanoparticles with iron nanoparticles has little to no effect on alcohol formation. An intimate contact between copper and iron are needed for alcohol formation. The selectivity towards ethanol remained low (less than 13%), favoring higher C₆₊ alcohols (up to 73.7%)⁴⁵.

Another class of bimetallic catalysts which is most studied for syngas to ethanol system is cobalt copper bimetallic catalyst. J. Wang et al. reported a series of Co-Cu

catalysts ranging from bare metals to bimetallic combinations. Catalyst combinations were prepared by the incipient wetness impregnation method on Al_2O_3 support. It was reported that when cobalt alone was used, the major product was methane and when copper alone is used the alcohol formation was favored. Addition of even small amounts of copper to cobalt based catalysts effected the product distribution. They have also reported that the presence of different types of active sites cobalt, mixed CoCu, and copper active sites resulted in increased selectivity towards ethanol.⁵³

The selectivity towards higher alcohols remains to be limited without the presence of promoters. Y.-T. Tsai et al. ⁵⁵reported Co-Cu-ZnO catalysts for the higher alcohol production from syngas. Detailed SSITKA studies on the Co-Cu-ZnO catalysts indicated that only combination of all three metals produced a catalyst with higher C_{2+} selectivity. The roles played by all three metals was explained, both cobalt and ZnO appear to decorate CO surface blocking the sites for methanation. With this three metal combination, selectivity towards alcohols increased but the presence of cobalt and ZnO on the surface of catalyst blocked the active sites and hence the activity of catalyst was shown to be low. It was reported that the high selectivities for alcohols are due to low concentration of active surface intermediates for hydrocarbons. ⁵⁵

Deactivation studies on CoCu/ TiO_2 were reported by Y. Yang et al in a recent 2016 study. The study reported that the activity of the catalyst was reduced but the selectivity towards alcohols remained the same. The constant selectivity is explained to be due to

the simultaneous reduction of capacity of catalyst to insert CO and dissociate CO. The selectivity towards hydrocarbons still remained high (~86%) when compared to selectivity towards alcohols (~11%).⁴⁸

Preparation method of the catalyst influences the product distribution. Preparation and use of Co-Cu nanoparticles for higher alcohol synthesis were reported^{47,48,53}. N.D. Subramanian et al. reported that the mixed nanoparticles are more selective to ethanol than their core shell counterparts, but the core shell nanoparticles exhibited higher activity. The composition of Co and Cu in the nanoparticles must be optimized to increase ethanol production. Maximum ethanol selectivity of 11.4% is reported for Co-Cu (1:24) catalyst⁵³.

The type of the support utilized also influences the ethanol selectivity. A perovskite type oxide LaFeO_3 was used to support Co-Cu nanoparticles. To improve the stability of the Co-Cu catalyst, LaFeO_3 was used as the support material as it exhibits higher stability in reducing atmospheres. Y.Z. Fang et al. reported a CO conversion of 56% with a 43% selectivity towards alcohols.⁵⁰ This catalyst was reported to have high activity, stability and selectivity towards alcohols. Deactivation studies of the Co-Cu/ ZrO_2 catalyst were also reported, and they demonstrated that deactivation was largely due to the volatilization of cobalt species, which resulted during reactions associated with the conversion of CO.⁴⁸

Finally, complex catalysts consisting of Co-Cu nanocrystals loaded on $\text{La}_{1-x}\text{Y}_x\text{Cu}_y\text{O}_3/\text{SiO}_2$ supports were prepared by Q. Yang et al. for ethanol synthesis from syngas. It was reported that the prepared catalyst showed good catalyst activity and selectivity for ethanol synthesis, but no data was provided for the stability or cost of the catalyst.⁵⁷

Dissertation objectives

The rational design of catalysts for syngas to ethanol conversion requires a thorough understanding of the complex reaction mechanism involved in the process. Density functional theory based simulations can provide molecular level insight about the key reactions, possible reaction pathways, and rate limiting steps for this reaction.

From previous experimental and theoretical studies, it can be inferred that to mimic the catalytic properties of rhodium metal, which catalyzes syngas to ethanol reactions, multiple metal sites will need to be present on the catalyst surface. This results from the fact that an effective and efficient catalyst must promote C-C chain elongation as well as alcohol formation steps. Studies to-date have shown that the presence of a promoter for C-C chain growth is necessary when modifying a methanol synthesis catalysts, such as Pt and Pd. Whereas, a promoter for CO insertion reactions is needed to modify Fischer-Tropsch catalysts so as to optimize the production of higher alcohols, including ethanol.

In this study, we use a bimetallic catalyst consisting of cobalt, which is a FT catalyst, and palladium, which is active for syngas to methanol reactions, to identify key

reactions and catalyst composition effects that influence the selective conversion of syngas to ethanol. To evaluate the syngas to ethanol reaction mechanism on Co-Pd catalysts a detailed reaction mechanism consisting of 24 intermediates was developed. To reduce the computational cost associated with studying faceted, extended catalyst surfaces, a nanocluster catalyst consisting of 13 atoms, seven cobalt and six palladium atoms, was created. The electronic character of the cobalt and palladium atoms are such that the most energetically favored cluster had a geometry where the metals are fully segregated. Therefore, this computational study examined both Co and Pd pure metal sites as well as the mixed metal interface sites generated at the boundaries between the segregated metals. Density functional theory was used to evaluate the minimum energy structures of adsorbed reactants and intermediates associated with the syngas to ethanol reaction process. This data provided the foundations for a detailed reaction model that can be used to identify optimal catalyst compositions.

This dissertation is laid out as follows, chapter two explains the basic concepts of density functional theory. Specifically, Schrodinger's equation and basic quantum chemistry is explained briefly. The chapter also presents the key input parameters used for all reported quantum simulations.

One of the first steps in ethanol formation from syngas is CO adsorption. Though CO is a small, widely studied molecule, adsorption of CO on the transition materials of interest is still not completely understood and is widely debated. In this dissertation, we

made an attempt to understand the CO adsorption on both cobalt and palladium metals. Further, this work details in Chapter 3 the influence of CO coverage on the overall reaction activity of neighboring catalyst atoms for a Co_7Pd_6 nanocluster.

The adsorption energies of 24 adsorbents important for the conversion of syngas to ethanol and related byproducts, are calculated for the three metals sites present on the CoPd nanocluster; specifically, the cobalt, palladium and cobalt palladium sites. A microkinetic model is developed for each of these surfaces assuming they are isolated from the other types of sites. A batch reactor was modeled, and the time evolution of products and intermediates is determined. Details of the microkinetic model results can be found in Chapter 4.

In Chapter 5, the microkinetic model is modified and extended to all Co_xPd_y bimetallic combinations. The ratios of number of sites of each type is varied and the time evolution of reactants, products and intermediates is evaluated. The 13 atom bimetallic cluster, which is considered as the catalyst element for this reaction has a diameter of approximately one nanometer. Given the very different reactivity of the metals in the Co_7Pd_6 cluster, it is important to consider the diffusion of intermediate species from one metal site to another, as evidenced by the preliminary results reported in earlier studies by the Bruce Group. The complete microkinetic model accounting for all three surface is the most complete reaction model developed to-date for the conversion of syngas to

ethanol, in part because it includes the initial carbon chain growth steps common to Fischer-Tropsch reactions but also because it includes key intersite diffusion processes.

It has been identified from the previous studies that the presence of two differing metals in close proximity influences the electronic structure of one another. To understand the electronic effects, a cobalt rich Co_9Pd_4 catalyst is used and the activation energies are compared to a related Co_7Pd_6 catalyst. Additionally, the activation energies of key reactions on the cobalt surface are measured as a function of the extent of CO coverage on the Pd surface of the cluster. Chapter 6 outlines the cluster composition effects and coverage effects on key reactions for ethanol formation from syngas.

In chapter seven, a detailed summary of conclusions from the study are presented along with the recommendations for further study.

This dissertation developed a detailed reaction model for syngas conversion to ethanol and higher hydrocarbons. This detailed reaction model enabled the elucidation of the primary reaction pathway for ethanol production as well as the electronic, composition, surface coverage, and diffusion effects on the product distribution. Although difficulties with synthesizing the ideal cobalt-palladium bimetallic catalyst may limit its use in commercial scale reactors, it did provide an excellent platform for elucidating the ethanol reaction mechanism and key reactions that should be considered for any de novo catalyst design efforts. Most importantly, the microkinetic model

developed herein can be extended to other more promising bimetallic cluster compositions, such as cobalt-copper and nickel-iridium.

References

1. Dresselhaus MS, Thomas IL. Alternative energy technologies. - *Nature*. 2001;414:- 332.
2. [Http://Www.eia.gov/todayinenergy/detail.php?id=26212](http://www.eia.gov/todayinenergy/detail.php?id=26212).
3. Subramani V, Gangwal SK. - A review of recent literature to search for an efficient catalytic process for the conversion of syngas to ethanol. - *Energy Fuels*. 2008;22(- 2):- 814. doi: - 10.1021/ef700411x.
4. Goldemberg J. - Ethanol for a sustainable energy future. - *Science*. 2007;315(- 5813):- 808.
5. Hu J, Wang Y, Cao C, Elliott DC, Stevens DJ, White JF. Conversion of biomass-derived syngas to alcohols and C2 oxygenates using supported rh catalysts in a microchannel reactor. - *Catalysis Today*. 2007;120(- 1):- 90. doi: - <http://dx.doi.org/10.1016/j.cattod.2006.07.006>.
6. Manochioa C, Andradea BR, Rodrigueza RP, Moraes BS. - Ethanol from biomass: A comparative overview. - *Renewable and Sustainable Energy Reviews*. 2017;80:- 743. doi: - <https://doi.org/10.1016/j.rser.2017.05.063>.

7. Mielenz JR. - Ethanol production from biomass: Technology and commercialization status. - *Current Opinion in Microbiology*. 2001;4(- 3):- 324. doi: - [https://doi.org/10.1016/S1369-5274\(00\)00211-3](https://doi.org/10.1016/S1369-5274(00)00211-3).
8. Han L, Mao D, Yu J, Guo Q, Lu G. - C2-oxygenates synthesis through CO hydrogenation on SiO₂-ZrO₂ supported rh-based catalyst: The effect of support. - *Applied Catalysis A: General*. 2013;454(-):- 81. doi: - <http://dx.doi.org/10.1016/j.apcata.2013.01.008>.
9. XIAO K, BAO Z, QI X, et al. - Advances in bifunctional catalysis for higher alcohol synthesis from syngas. - *Chinese Journal of Catalysis*. 2013;34(- 1):- 116. doi: - [http://dx.doi.org/10.1016/S1872-2067\(11\)60496-8](http://dx.doi.org/10.1016/S1872-2067(11)60496-8).
10. Khodakov AY, Chu W, Fongarland P. - Advances in the development of novel cobalt Fischer–Tropsch catalysts for synthesis of long-chain hydrocarbons and clean fuels. - *Chem Rev*. 2007;107(- 5):- 1692. doi: - 10.1021/cr050972v.
11. He J, Zhang W. Research on ethanol synthesis from syngas. - *Journal of Zhejiang University-SCIENCE A*. 2008;9(- 5):- 714. doi: - 10.1631/jzus.A071417.
12. Wilhelm DJ, Simbeck DR, Karp AD, Dickenson RL. - Syngas production for gas-to-liquids applications: Technologies, issues and outlook. - *Fuel Processing Technology*. 2001;71(- 1):- 139. doi: - [https://doi.org/10.1016/S0378-3820\(01\)00140-0](https://doi.org/10.1016/S0378-3820(01)00140-0).

13. Song C. - Global challenges and strategies for control, conversion and utilization of CO₂ for sustainable development involving energy, catalysis, adsorption and chemical processing. - *Catalysis Today*. 2006;115(- 1):- 2. doi: - <https://doi.org/10.1016/j.cattod.2006.02.029>.
14. Subramani V, Gangwal SK. - A review of recent literature to search for an efficient catalytic process for the conversion of syngas to ethanol. - *Energy Fuels*. 2008;22(- 2):- 814. doi: - 10.1021/ef700411x.
15. Emberga T, Uhiara F, Nwigwe C, Amadi R. Biomass conversion technologies. . 1923.
16. Mei D, Rousseau R, Kathmann SM, et al. - Ethanol synthesis from syngas over rh-based/SiO₂ catalysts: A combined experimental and theoretical modeling study. - *Journal of Catalysis*. 2010;271(- 2):- 325. doi: - <http://dx.doi.org/10.1016/j.jcat.2010.02.020>.
17. Hickman DA, Schmidt LD. Production of syngas by direct catalytic oxidation of methane. . 1993;259(- 5093):- 343.
18. Ojeda M, Granados ML, Rojas S, Terreros P, Garcia FJ, Fierro JL. Manganese-promoted rh/Al₂O₃ for C₂-oxygenates synthesis from syngas: Effect of manganese loading. - *Applied Catalysis A: General*. 2004;261(- 1):- 47. doi: - <http://dx.doi.org/10.1016/j.apcata.2003.10.033>.

19. Bwoker M. - On the mechanism of ethanol synthesis on rhodium. - *Catalysis Today*. 1992;15(- 1):- 77. doi: - [http://dx.doi.org/10.1016/0920-5861\(92\)80123-5](http://dx.doi.org/10.1016/0920-5861(92)80123-5).
20. Wang J, Zhang Q, Wang Y. - Rh-catalyzed syngas conversion to ethanol: Studies on the promoting effect of FeOx. - *Catalysis Today*. 2011;171(- 1):- 257. doi: - <http://dx.doi.org/10.1016/j.cattod.2011.03.023>.
21. Ojeda M, Rojas S, boutonnet,M,perez-Alonso, F.J., Garcia FJ, Fierro JL. - Synthesis of rh nano-particles by the microemulsion technology: Particle size effect on the CO+H₂ reaction. - *Applied Catalysis A: General*. 2004;274(- 1–2):- 33. doi: - <http://dx.doi.org/10.1016/j.apcata.2004.05.014>.
22. Han L, Mao DY,J., Guo Q, Lu G. - Synthesis of C₂-oxygenates from syngas over rh-based catalyst supported on SiO₂, TiO₂ and SiO₂–TiO₂ mixed oxide. - *Catalysis Communications*. 2012;23(-):- 20. doi: - <http://dx.doi.org/10.1016/j.catcom.2012.02.032>.
23. Liu y, Murata K, Inaba M, Takahara I, Okabe K. - Synthesis of ethanol from syngas over rh/Ce_{1-x}ZrxO₂ catalysts. - *Catalysis Today*. 2011;164(- 1):- 308. doi: - <http://dx.doi.org/10.1016/j.cattod.2010.10.087>.
24. - Mo X, - Gao J, - Umnajkaseam N, - Goodwin Jr JG. - La, V, and fe promotion of rh/SiO₂ for CO hydrogenation: Effect on adsorption and reaction. - *Journal of Catalysis*. (- 2):- 167.

25. Chena G, b, Cun-Yue Guo, Zhijun Huang a, Guoqing Yuan. - Synthesis of ethanol from syngas over iron-promoted rh immobilized on modified SBA-15 molecular sieve: Effect of iron loading. - *Chemical Engineering Research and Design*. (- 3):- 249. doi: - <http://dx.doi.org/10.1016/j.cherd.2010.07.014>.
26. Zhng J, Cao XM, Hu P, Zhong Z, Borgna A, Wu P. - Density functional theory studies of ethanol decomposition on rh(211). - *J Phys Chem C*. 2011;115(- 45):- 22429. doi: - [10.1021/jp206837z](http://dx.doi.org/10.1021/jp206837z).
27. Kapur N, Hyun J, Shan B, Nicholas JB, Cho K. - Ab initio study of CO hydrogenation to oxygenates on reduced rh terraces and stepped surfaces. - *J Phys Chem C*. 2010;114(- 22):- 10171. doi: - [10.1021/jp911903u](http://dx.doi.org/10.1021/jp911903u).
28. Subramanian ND, Gao J, Mob X, JGoodwinJr. Jg, Torres W, Spivey JJ. - La and/or V oxide promoted rh/SiO₂ catalysts: Effect of temperature, H₂/CO ratio, space velocity, and pressure on ethanol selectivity from syngas. - *Journal of Catalysis*. 2010;272(- 2):- 204. doi: - <http://dx.doi.org/10.1016/j.jcat.2010.03.019>.
29. Mei D, Rousseau R, Kathmann SM, et al. - Ethanol synthesis from syngas over rh-based/SiO₂ catalysts: A combined experimental and theoretical modeling study. - *Journal of Catalysis*. (- 2):- 325. doi: - <http://dx.doi.org/10.1016/j.jcat.2010.02.020>.
30. Wang JJ, Xie jR, Huang YH, Chen BH, Lin GL, Zhang HB. - An efficient Ni–Mo–K sulfide catalyst doped with CNTs for conversion of syngas to ethanol and higher alcohols. -

Applied Catalysis A: General. 2013;468(-):- 44. doi: -

<http://dx.doi.org/10.1016/j.apcata.2013.08.026>.

31. Song Z, Shib X, Ning H, Liu G, Zhong H, Liu Y. - Loading clusters composed of nanoparticles on ZrO₂ support via a perovskite-type oxide of La_{0.95}Ce_{0.05}Co_{0.7}Cu_{0.3}O₃ for ethanol synthesis from syngas and its structure variation with reaction time. - *Applied Surface Science*. 2017;405(-):- 1. doi: -

<http://dx.doi.org/10.1016/j.apsusc.2017.02.003>.

32. Lopez L, Montes V, Kušara H, Cabrer s, Boutonneta M, Järåsa S. - Syngas conversion to ethanol over a mesoporous cu/MCM-41 catalyst: Effect of K and fe promoters. -

Applied Catalysis A: General. 2016;526(-):- 77. doi: -

<http://dx.doi.org/10.1016/j.apcata.2016.08.006>.

33. Du H, Zhu H, Chen X, et al. - Study on CaO-promoted co/AC catalysts for synthesis of higher alcohols from syngas. - *Fuel*. 2016;182(-):- 42. doi: -

<http://dx.doi.org/10.1016/j.fuel.2016.05.089>.

34. Anton J, Nebel J, Song H, et al. - The effect of sodium on the structure–activity relationships of cobalt-modified cu/ZnO/Al₂O₃ catalysts applied in the hydrogenation of carbon monoxide to higher alcohols. - *Journal of Catalysis*. 2016;335(-):- 175. doi: -

<http://dx.doi.org/10.1016/j.jcat.2015.12.016>.

35. Portillo MA, Perales AL, Barrero FV, Campoy M. - A kinetic model for the synthesis of ethanol from syngas and methanol over an alkali-co doped molybdenum sulfide catalyst: Model building and validation at bench scale. - *Fuel Processing Technology*. 2016;151(-):- 19. doi: - <http://dx.doi.org/10.1016/j.fuproc.2016.05.027>.
36. Christensen JM, Mortensen PM, Trane R, Jensen PA, Jemsem AD. - Effects of H₂S and process conditions in the synthesis of mixed alcohols from syngas over alkali promoted cobalt-molybdenum sulfide. - *Applied Catalysis A: General*. 2009;366(- 1):- 29. doi: - <http://dx.doi.org/10.1016/j.apcata.2009.06.034>.
37. Andersson R, Boutonneta M, Järåsa S. - Correlation patterns and effect of syngas conversion level for product selectivity to alcohols and hydrocarbons over molybdenum sulfide based catalysts. - *Applied Catalysis A: General*. 2012;417-418(-):- 119. doi: - <http://dx.doi.org/10.1016/j.apcata.2011.12.033>.
38. Elliott DJ, Pennella F. - Mechanism of ethanol formation from synthesis gas over CuO/ZnO/Al₂O₃. - *Journal of Catalysis*. 1988;114(- 1):- 90. doi: - [http://dx.doi.org/10.1016/0021-9517\(88\)90011-5](http://dx.doi.org/10.1016/0021-9517(88)90011-5).
39. Yang G, San S, Jiang N, et al. - A new method of ethanol synthesis from dimethyl ether and syngas in a sequential dual bed reactor with the modified zeolite and cu/ZnO catalysts. - *Catalysis Today*. 2011;164(- 1):- 425. doi: - <http://dx.doi.org/10.1016/j.cattod.2010.10.027>.

40. Liu YJ, Zuo ZH, Li C, Deng X, Huang W. - Effect of preparation method on CuZnAl catalysts for ethanol synthesis from syngas. - *Applied Surface Science*. 2015;356(-):- 124. doi: - <http://dx.doi.org/10.1016/j.apsusc.2015.08.039>.
41. Gupta M, Spivey JJ. - Electrodeposited Cu–ZnO and Mn–Cu–ZnO nanowire/tube catalysts for higher alcohols from syngas. - *Catalysis Today*. 2009;147(- 2):- 126. doi: - <http://dx.doi.org/10.1016/j.cattod.2009.01.050>.
42. Zheng H, Zhang R, Li Z, Wang B. - Insight into the mechanism and possibility of ethanol formation from syngas on cu(1 0 0) surface. - *Journal of Molecular Catalysis A: Chemical*. 2015(-):- 115. doi: - <http://dx.doi.org/10.1016/j.molcata.2015.04.015>.
43. Gupta M, Smith ML, Spivey JJ. - Heterogeneous catalytic conversion of dry syngas to ethanol and higher alcohols on cu-based catalysts. - *ACS Catal*. 2011;1(- 6):- 641. doi: - [10.1021/cs2001048](http://dx.doi.org/10.1021/cs2001048).
44. Guo H, Zhang H, Peng F, et al. - Mixed alcohols synthesis from syngas over activated palygorskite supported Cu–Fe–Co based catalysts. - *Applied Clay Science*. 2015;111(-):- 83. doi: - <http://dx.doi.org/10.1016/j.clay.2015.03.009>.
45. XIAO K, BAO Z, QI X, et al. - Unsupported CuFe bimetallic nanoparticles for higher alcohol synthesis via syngas. - *Catalysis Communications*. 2013;40(-):- 154. doi: - <http://dx.doi.org/10.1016/j.catcom.2013.06.024>.

46. Lu Y, Yu F, Hu J, Liu j. - Catalytic conversion of syngas to mixed alcohols over zn-mn promoted cu-fe based catalyst. - *Applied Catalysis A: General*. 2012;429-430(-):- 48. doi: - <http://dx.doi.org/10.1016/j.apcata.2012.04.005>.
47. Liu GL, niu T, Cao A, Geng YX, Zhang Y, Liu Y. - The deactivation of Cu–Co alloy nanoparticles supported on ZrO₂ for higher alcohols synthesis from syngas. - *Fuel*. 2016;176(-):- 1. doi: - <http://dx.doi.org/10.1016/j.fuel.2016.02.057>.
48. Yang Y, Qi X, Wang X, et al. - Deactivation study of CuCo catalyst for higher alcohol synthesis via syngas. - *Catalysis Today*. 2016;270(-):- 101. doi: - <http://dx.doi.org/10.1016/j.cattod.2015.06.014>.
49. Ding M, Liu J, Zhang Q, Tsubaki N, Wang T, Ma L. - Preparation of copper-iron bimodal pore catalyst and its performance for higher alcohols synthesis. - *Catalysis Communications*. (-):- 138. doi: - <http://dx.doi.org/10.1016/j.catcom.2012.08.027>.
50. Fang YZ, Liu Y, Zhang LH. - LaFeO₃-supported nano co-cu catalysts for higher alcohol synthesis from syngas. - *Applied Catalysis A: General*. 2011;397(- 1–2):- 183. doi: - <http://dx.doi.org/10.1016/j.apcata.2011.02.032>.
51. Wang J, Chernavskii PA, Khodakov AY, Wang Y. - Structure and catalytic performance of alumina-supported copper–cobalt catalysts for carbon monoxide hydrogenation. - *Journal of Catalysis*. 2012;286(-):- 51. doi: - <http://dx.doi.org/10.1016/j.jcat.2011.10.012>.

52. Xiang y, Barbosa R, Li X, Kruse N. - Ternary Cobalt–Copper–Niobium catalysts for the selective CO hydrogenation to higher alcohols. - *ACS Catal.* 2015;5(- 5):- 2929. doi: - 10.1021/acscatal.5b00388.
53. Subramanian ND, Balaji G, Kumar CSSR, Spivey JJ. - Development of cobalt–copper nanoparticles as catalysts for higher alcohol synthesis from syngas. - *Catalysis Today.* 2009;147(- 2):- 100. doi: - <http://dx.doi.org/10.1016/j.cattod.2009.02.027>.
54. Mo X, Tsai YT, Gao J, Mao D, Goodwin Jr. JG. - Effect of component interaction on the activity of co/CuZnO for CO hydrogenation. - *Journal of Catalysis.* 2012;285(- 1):- 208. doi: - <http://dx.doi.org/10.1016/j.jcat.2011.09.033>.
55. Tsai YT, Mo X, Goodwin Jr. JG. - The synthesis of hydrocarbons and oxygenates during CO hydrogenation on CoCuZnO catalysts: Analysis at the site level using multiproduct SSITKA. - *Journal of Catalysis.* 2012;285(- 1):- 242. doi: - <http://dx.doi.org/10.1016/j.jcat.2011.09.038>.
56. Kumar N, Smith ML, Spivey JJ. - Characterization and testing of silica-supported cobalt–palladium catalysts for conversion of syngas to oxygenates. - *Journal of Catalysis.* 2012;289(-):- 218. doi: - <http://dx.doi.org/10.1016/j.jcat.2012.02.011>.
57. Hong Y, Yang Q, Kang N, Liu G, Liu Y. - Cu–Co alloy nano-particles supported on SiO₂ and modified by Ia and Y for ethanol synthesis from syngas. - *ChemistrySelect.* 2017;2(- 25):- 7580. doi: - 10.1002/slct.201701742.

CHAPTER TWO

INTRODUCTION TO DENSITY FUNCTIONAL THEORY

Introduction

Considerable advances have been made in quantum chemistry as well as computer capabilities during the last 20 years. There is an ever expanding research data base of more accurate and efficient quantum codes. Thus, quantum chemistry based tools, in particular density functional theory methods, have gained importance in understanding chemical reactions at the molecular level. DFT has gained popularity in calculating the energies of clusters, slabs, and molecules¹. The key to rational design of a catalyst lies in understanding elementary reaction mechanism of the reaction. DFT based codes are important to calculate kinetic and thermodynamic parameters for identifying the key reactions and the reaction pathway.

In this study, DFT is used to study the reaction mechanism of conversion of syngas to ethanol. There are two reactants, 24 intermediates and seven products of interest. A nanometer size bimetallic 13 atom icosahedra is used as the catalyst. Adsorption energies of reactants, intermediates and products on the surface of catalyst were calculated using density functional theory. Jaguar 7.0 was the software employed for these calculations, Jaguar an ab initio quantum chemistry software which uses the orbital theory approach.

This chapter aims at giving a brief introduction to quantum simulations with emphasis on density functional theory. Later, a brief explanation is given on input parameters given to Jaguar to calculate energies.

Density functional theory is rooted in concepts of quantum mechanics. In order to understand the foundations of DFT a brief introduction to quantum chemistry and the Schrödinger equation is presented. Quantum simulations emerged in the process of finding an approximate solution to the Schrödinger equation. The quantum state of the system is best described using Schrödinger equation. In its simplest form, which is time independent, nonrelativistic Schrödinger equation is represented by Equation 1².

$$\hat{H}\psi = E\psi \quad (1)$$

where, \hat{H} is the Hamiltonian operator, ψ is the wave function, and E is the proportionality constant for the energy of state. For a case that contains a collection of atoms, \hat{H} represents the total energy of the system and mathematically it represented as,

$$\hat{H} = -\frac{1}{2} \sum_{i=1}^N \nabla_i^2 - \frac{1}{2} \sum_{A=1}^M \frac{1}{MA} \nabla_A^2 - \sum_{i=1}^N \sum_{A=1}^M \frac{Z_A}{r_{iA}} + \sum_{i=1}^N \sum_{j>i}^N \frac{1}{r_{ij}} + \sum_{A=1}^M \sum_{B>A}^M \frac{Z_A Z_B}{R_{AB}} \quad (2)$$

where, i is the number of electrons which varies from 1 to N, A is the number of nuclei and varies from 1 to M.

For a system with M nuclei and N electrons total energy, the Hamiltonian is represented by equation 2. Each term in the above Equation 2 represents the kinetic energy of electrons, kinetic energy of nuclei, attractive electrostatic force between nuclei and electrons, repulsive electron-electron interaction, and repulsive interaction between nuclei respectively^{2,3}.

The Hamiltonian equation is complicated to solve; it can be simplified by the **Born-Oppenheimer approximation**. There is a significant difference between mass of a nucleus and mass of an electron. The nucleus is at least 1,800 times heavier than an electron. According to the Born-Oppenheimer approximation nucleus and electron interactions can be separated. Thus during calculation, the position of nuclei can be fixed at an equilibrium configuration, meaning that the kinetic energy of nuclei and repulsive interaction between nuclei are neglected. Applying this simplification, Equation 2 can be reduced and is represented as,

$$\widehat{H}_{elec} = -\frac{1}{2} \sum_{i=1}^N \nabla_i^2 - \sum_{i=1}^N \sum_{A=1}^M \frac{Z_A}{r_{iA}} + \sum_{i=1}^N \sum_{j>i}^N \frac{1}{r_{ij}} = \widehat{T} + \widehat{V}_{NE} + \widehat{V}_{EE} \quad (3)$$

For the case of fixed nuclei Equation 1 can be simplified to:

$$\widehat{H}_{elec} \psi_{elec} = E_{elec} \psi_{elec} \quad (4)$$

Equation 3 looks very simple, but even for a simple system calculating electron- electron interactions is complicated. Every molecule contains one nucleus and many electrons. Representing each of these electronic interactions and electron-nuclei interactions is very

cumbersome. Apart from this finding the position of an electron is a probability problem, and we need to consider the spin of electron. All these variables make solving the Schrödinger equation almost impossible. Another principle which further simplifies Schrodinger equation is the **Variational principle**. According to this principle, the lowest energy of the system is called ground state energy. This allows calculating approximate solution for the Schrödinger equation.

Density functional theory (Nobel prize 1998)

For the system of N electrons, the number of variables to be considered to solve the simplified Schrödinger equation is $3N$ (3 co-ordinates for each electron). As an example if we consider cobalt, it has 27 electrons and each of these electrons have three special coordinates x, y, & z. Therefore for a simple nanocatalyst containing 13 Cobalt atoms number of variables will be $3 \times 13 \times 27 = 1053$. Density functional theory simplifies the problem by reducing variables from $3N$ coordinates to 3. If we can calculate density of electrons at a particular position of space, we can calculate the probability of finding the electrons at particular coordinates, which further helps in calculating the wave function associated. Also it is easy to observe density unlike spatial coordinates of electrons.

DFT aims to replace the complicated N electron wave function with $3N$ spatial variables and N spin variables by simple quantity density which has 3 spatial variables. It is difficult to computationally solve $3N$ spatial variables and N spin variables of the wave

function. Further, it is not experimentally feasible to calculate the wave function of N electrons. On the other hand, with DFT, the number of variables is drastically reduced. Due to this it is computationally less expensive and the density of electrons can be experimentally determined, which makes it easy to visualize. Further, electron density reasonably estimates the molecular properties of the system. In short, DFT expresses the total energy of the system in terms of electronic density.

Hohenberg-Kohn's theorems

One of the founding pillars for the development of DFT are Hohenberg-Kohn theorems put forward in 1964^{4,5}. Hohenberg-Kohn have put forward two theories to prove the correctness of density functional theory.

The first theorem explains the concept of ground state energy. It states that electron density uniquely determines the Hamiltonian operator and thus determines all the properties of the system. According to this theorem ground state energy is a unique function of density, and external potential is also a unique function of density. Determining the external potential of the system will fix the Hamiltonian operator. With the simplified Schrödinger equation, we can determine all the properties of the system knowing the Hamiltonian operator. Hence, density of the system is key to determine all other properties of the system. Therefore, many particle ground state energies are sufficient to determine all the properties of the system⁴.

Hohenberg-Kohn's Second theorem states that the function that delivers ground state energy of the system (F_{HK}), delivers the lowest energy if, and only if, the input density is the true ground state density. From the first theorem we have seen that knowing the ground state energy determines the properties of the system. The second theorem explains how to make sure that the certain density is really the ground state density. Second theorem reestablishes variational principle.

Kohn-Sham's equations:

Hohenberg-Kohn's theorems tell us that there is a unique mapping between external potential of interacting system and ground state density of the system. However, these theorems don't make it clear on how to construct the function that delivers the ground state energy. It does not explain what kind of approximations should be used for unknown function.

Kohn-Sham published a second major paper on Density functional theory in 1965⁵. With the help of these equations one can determine the unknown functions. In other words, Kohn-Sham explained how to put Hohenberg-Kohn's equations to work. Kohn-Sham explain in their paper how to determine the kinetic energy term of the system. They have explained that most of the problems associated with the direct density functionals is connected with the way kinetic energy was calculated. Therefore, the better way to control accuracy of certain density functional is attained with a better method to calculate kinetic energy.

In Kohn-Sham's paper true kinetic energy of the system was formulated as a sum of non-interacting kinetic energy and exchange correlation energy. The concept of non-interacting reference system is put forth to determine the kinetic energy accurately. The energy of an interacting system is separated into energy of a non-interacting system and an exchange correlation term. The exchange and correlation terms are combined into exchange correlation energy. While the non-interacting kinetic energy, which is a major contribution to the kinetic energy term, can be determined with higher accuracy, the ambiguous terms are clubbed into exchange correlation functional.

Mathematically, universal functional $F[\rho(r)]$ is the sum of $T_s[\rho(r)]$, kinetic energy of non-interacting system with the same density as real interacting system, $J[\rho(r)]$ columbic interaction and $Exc([\rho(r)])$ which is exchange correlation energy.

$$F[\rho(r)] = T_s[\rho(r)] + J[\rho(r)] + E_{xc}([\rho(r)]) \quad (5)$$

Exchange correlation term is the sum of residual part of true kinetic energy $T_c(\rho)$ and non-classical electro static contributions $E_{ncl}(\rho)$.

$$Exc([\rho(r)]) = T_c(\rho) + E_{ncl}(\rho) \quad (6)$$

If we can determine the Exc term of the above equation, then we could determine the correct value of the energy that is Eigen value of the Hamiltonian in Schrödinger's equation. Therefore, the central goal of density functional theory is to find good approximations to exchange correlation functional.

Basis sets

If we go back to the time independent non relativistic Schrödinger equation, which is represented by Equation 1, we can see from previous discussions how a Hamiltonian can be determined. The next term that needs to be calculated is the wave function denoted by Ψ . The molecular wave function, Ψ , is unknown and is extremely complex. A basis set is a set of one particle functions used to build molecular orbitals. It is the approximate representation of the molecular orbitals. Molecular orbitals can be represented as a linear-combination-of-atomic-orbitals (LCAO).

There are different types of possible basis functions, where one of the earliest used is hydrogen-like orbitals. Atomic orbitals of one electron hydrogen atoms is well established. The knowledge of hydrogen orbitals can be used for LCAO method to determine molecular orbitals. Though the model is simple and has accurate data available, it had its own disadvantages. Most of the systems of interest have more than one electron and the LCAO of hydrogen atomic orbitals did not yield results with good accuracy.

Second type of basis set which can be used to represent molecular orbitals is Slater type orbitals. Slater type orbitals (STOs) are more accurate representations of atomic orbitals⁶. STOs decay exponentially with distance from the nuclei, accurately describing the long-range overlap between atoms, and reach a maximum at zero, well describing the

charge and spin at the nucleus. A disadvantage of using STOs is that it is computationally very expensive.

To overcome the disadvantage of STOs being very expensive, another type of basis set is introduced, which is Gaussian type orbitals (GTOs)⁷. Individual GTOs are not used as basis functions, instead a normalized linear combination of a few GTOs is used. GTOs are often used as approximations to STO's the advantage being that they are computationally more efficient. Different types of basis sets use different number of GTOs. Jargon used to represent number of GTOs used is often STO-NG. Where N is the number of primitive GTOs used.

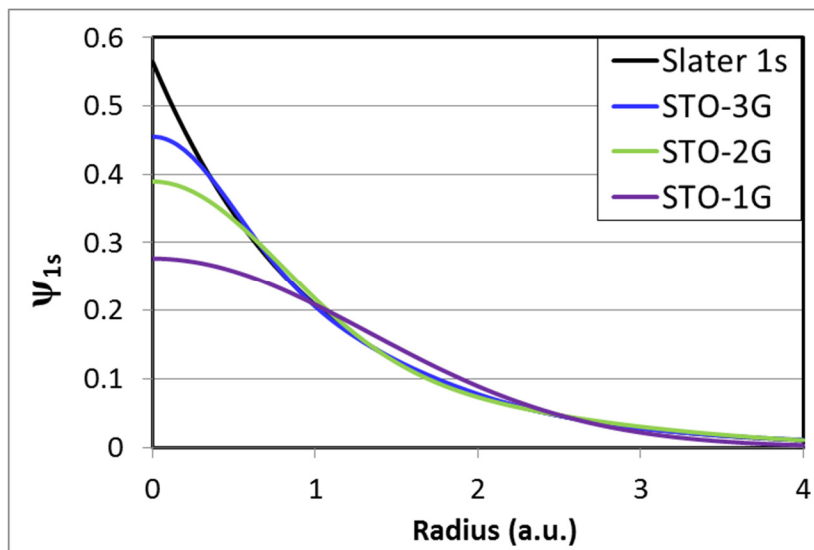


Figure 2. 1. Gaussian functions approximated by slater type orbitals (STOs)⁸

From the figure 2.1 it can be seen that Slater type 1s orbital can be approximated by a set of Gaussian type functions. It can be noted that as the number of Gaussian functions increases greater closeness of fit is obtained, that is, accuracy of representation increases.

STO-3G is the basis set with 3 primitive Gaussian functions. STO-3G basis functions have been developed for most of the elements in the periodic table. This is a popular starting point for calculations.

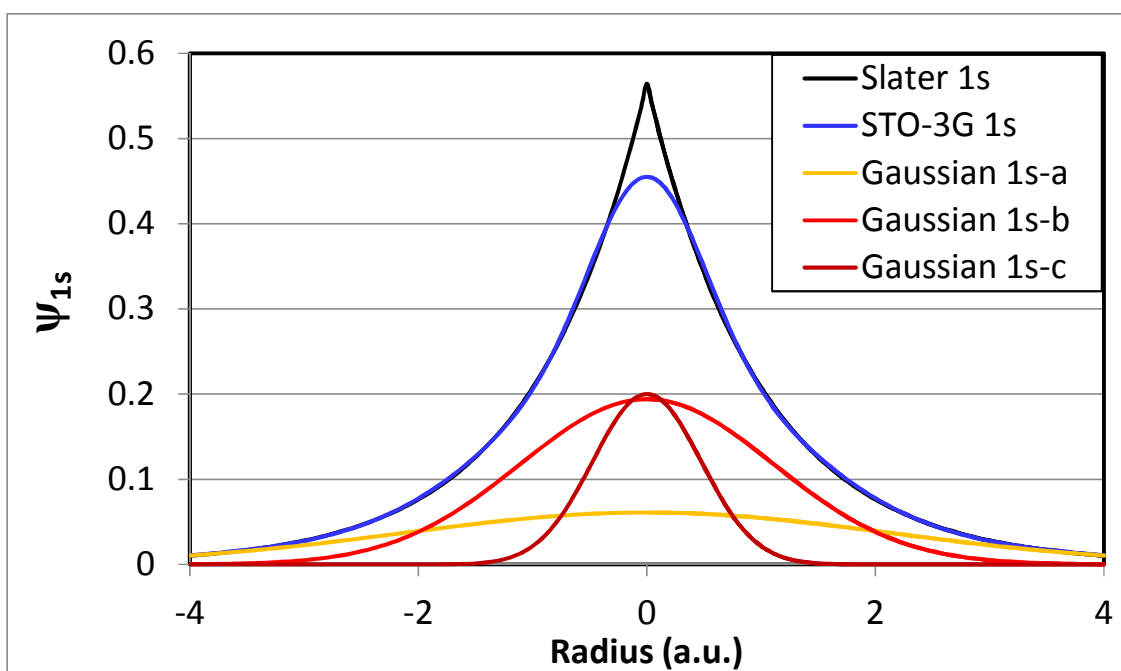


Figure 2. 2. STO-3G wave function used to represent the 1S orbital of Hydrogen atom. We can see that STO-3G cannot represent the cusp at $r=0$.⁸

Basis sets can also be classified based on the number of functions used to describe the atomic orbitals. Based on the number of functions used, they can be classified into; minimal basis sets, which use one function (STO or GTO) to describe AO. Double zeta which uses 2 functionals, triple zeta three basis functions for each AO. Split valence Basis sets are other class of basis sets used to approximate molecular orbitals. In this type of basis set, core and valence electrons are treated differently. It uses one basis function for each core AO and a larger basis function for valence AOs. They are developed to overcome

problems of inadequate description of anisotropic electronic distributions. Jargon used to represent these type of basis sets is K-LMG where K is the number of sp-type inner shell primitive GTOs, L is the number of s and p type primitive GTOs and M is the number of outer valence s and p type primitive GTOs. Examples of split valence basis sets are 3-21G and 6-311G.

Polarized basis sets are used to account for influence of distorted shape of molecular orbitals. In molecule formations, often the atomic orbitals get distorted in shape. Usually a '*' is used to represent a polarized basis set.

Example of a widely used basis set: 6-31G*+.

6-Inner core electrons described using 6 primitives contracted to a single contracted-Gaussian
3-Valence orbitals are described by 2 functions - a contracted-Gaussian composed of 3 primitives along with a single primitive.

1- Add wave functions for orbitals having higher angular momentum ($l+1$) than would normally be required for bonding (e.g., add a d orbital for oxygen bonding)

*- polarized to account for molecular orbital shape distortion

+ - Add diffuse wave functions to better describe van der Waals interactions

Figure 2. 3. Widely used 6-31G*+ basis set ⁸

For transition metal containing groups, the core is generally chemically inert and ab-initio effective core potentials are used to represent AO. Los Almos National

Laboratory has derived basis sets to treat transition metal containing groups. LANL2DZ (DZ represents double zeta) is applicable for a variety of atoms together. For example, it uses all electron basis set for light atoms and uses an effective core potential basis set for heavy atoms. It is a combination of ECP and valence basis sets.

Exchange correlation Functionals:

We can recall from Equation 6 that the exchange correlation functional (Exc) is a collection of electron-electron interactions along with correction for the self-interaction component and kinetic energy for the interacting system. Finding a good exchange correlation functional is the key to success in DFT calculations. The quality of DFT calculations depends on the accuracy of the exchange correlation functional used.

Functionals can be classified broadly into local density approximation (LDA), generalized gradient approximation (GGA,) and hybrid functionals. LDA is the simplest approximation to Exc, which is based upon the value of electron density at each point in space. LDA is derived based on the system containing homogenous electron gas. In this hypothetical system, the number of electrons and volume of gas is considered to be infinity. Density which is the ratio of mass to volume is thus finite and constant everywhere. Although LDA is the simplest approximation, it can be used in many situations as it can represent chemical bonds including covalent, metallic and ionic. But, LDA fails to describe physical interactions like van der Walls interactions and hydrogen

bonds. Also, the self-interaction problem (interaction of electrons with themselves) is not handled with this functional.

The next class of functional used in DFT is generalized gradient approximation (GGA). Although LDA is a reasonably good model to represent Exc term it considers density to be uniform. In a more realistic situation of atoms and molecules density undergoes rapid changes in space. In GGA density is supplemented by gradient of density at every point in space in order to account for non-homogeneity of electron density. Examples of widely used GGA models include PW91 (Perdew and Wang in 91) and BLYP (Becke Lee Yang Parr).

In exchange correlation, terms exchange contributions are significantly larger than the correlation counterpart. The success of finding the good approximation to Exc terms depends on finding an exact representation of exchange terms and approximating the correlation term. Hybrid functionals replace a fraction of exchange term with exact term. The exact exchange energy functional is rather described by KS orbitals rather than the density.

$$E_{xc} = E_x^{exact} + E_c \quad (7)$$

Most commonly used hybrid functions are B3LYP and PBE.

Another class of hybrid functionals is the Meta hybrid functionals. They are constructed by empirical fitting of their parameters, but constraining to uniform electron

gas. One advantage of these functionals is that they take into account dispersion forces, which is one of the biggest deficiencies of DFT. M06, M06-2X are examples of Meta hybrid functionals.

Commercial DFT software's

We have seen some basic principles of DFT and the theory behind it. In this section commercial software is used to implement DFT that are listed. Available codes can be classified based on if they follow atomic orbital approach or plane wave approach

In the atomic orbital approach, molecular orbitals are approximated by a linear combination of atomic orbitals. It is ideal for non-periodic systems and nanoclusters. In the Plane wave approach, atomic orbitals are approximated by a linear combination of plane waves which differ by reciprocal lattice vectors. The Plane wave approach is ideal for periodic systems.

This chapter provided a brief introduction to DFT. For further information consult references 9 and 10.^{9,10}

Atomic orbital codes: Jaguar¹¹; Gaussian 09¹²; CRYSTAL¹³; DMOL3¹⁴; Turbomole¹⁵; and NWChem¹⁶.

Plane wave codes: VASP¹⁷; CASTEP¹⁸; ABINIT¹⁹; and SIESTA²⁰.

References

1. Kohn W, Becke AD, Parr RG. - Density functional theory of electronic structure. - *J Phys Chem*. 1996;100(- 31):- 12974. doi: - 10.1021/jp960669l.
2. Koch W, Max C H, eds. *A chemist's guide to density functional theory*. ; 2001.
3. Neese F. - Prediction of molecular properties and molecular spectroscopy with density functional theory: From fundamental theory to exchange-coupling. - *Coordination Chemistry Reviews*. 2009;253(- 5):- 526. doi: - <https://doi.org/10.1016/j.ccr.2008.05.014>.
4. - Hohenberg P, Kohn W. - *Physical Review*. 1964;136(- 3B):- B864. doi: - 10.1103/PhysRev.136.B864.
5. - Kohn W. - *Physical Review*. (- 4A):- A1133. doi: - 10.1103/PhysRev.140.A1133.
6. - Slater JC. - *Physical Review*. (- 6):- 1498. doi: - 10.1103/PhysRev.94.1498.
7. Broclawik E, Salahub DR. - Density functional theory and quantum chemistry: Metals and metal oxides. - *Journal of Molecular Catalysis*. 1993;82(- 2):- 117. doi: - [https://doi.org/10.1016/0304-5102\(93\)80028-S](https://doi.org/10.1016/0304-5102(93)80028-S).
8. Bruce DA. Personal communication. .

9. Koch W. - *A chemist's guide to density functional theory*. Humbolt University Berlin: Wiley-VCH: Weinheim; 2001:- 2701. - 10.1021/ja004799q.

10. Parr RG, Yang W. - *Density-functional theory of atoms and molecules*. Newyork: Oxford University Press; 1989:- 101. - 10.1002/qua.560470107.

11. Bochevarov, A.D.; Harder, E.; Hughes, T.F.; Greenwood, J.R.; Braden, D.A.; Philipp, D.M.; Rinaldo, D.; Halls, M.D.; Zhang, J.; Friesner, R.A., "Jaguar: A high-performance quantum chemistry software program with strengths in life and materials sciences," Int. J. Quantum Chem., 2013, 113(18), 2110-2142

12. Gaussian 16, Revision B.01, Frisch, M. J.; Trucks, G. W.; Schlegel, H. B.; Scuseria, G. E.; Robb, M. A.; Cheeseman, J. R.; Scalmani, G.; Barone, V.; Petersson, G. A.; Nakatsuji, H.; Li, X.; Caricato, M.; Marenich, A. V.; Bloino, J.; Janesko, B. G.; Gomperts, R.; Mennucci, B.; Hratchian, H. P.; Ortiz, J. V.; Izmaylov, A. F.; Sonnenberg, J. L.; Williams-Young, D.; Ding, F.; Lipparini, F.; Egidi, F.; Goings, J.; Peng, B.; Petrone, A.; Henderson, T.; Ranasinghe, D.; Zakrzewski, V. G.; Gao, J.; Rega, N.; Zheng, G.; Liang, W.; Hada, M.; Ehara, M.; Toyota, K.; Fukuda, R.; Hasegawa, J.; Ishida, M.; Nakajima, T.; Honda, Y.; Kitao, O.; Nakai, H.; Vreven, T.; Throssell, K.; Montgomery, J. A., Jr.; Peralta, J. E.; Ogliaro, F.; Bearpark, M. J.; Heyd, J. J.; Brothers, E. N.; Kudin, K. N.; Staroverov, V. N.; Keith, T. A.; Kobayashi, R.; Normand, J.; Raghavachari, K.; Rendell, A. P.; Burant, J. C.; Iyengar, S. S.; Tomasi, J.; Cossi, M.; Millam, J. M.; Klene, M.; Adamo, C.; Cammi, R.; Ochterski, J. W.;

Martin, R. L.; Morokuma, K.; Farkas, O.; Foresman, J. B.; Fox, D. J. Gaussian, Inc., Wallingford CT, 2016.

13. Dovesi, R.; Erba, A.; Orlando, R.; Zicovich-Wilson, C. M.; Civalleri, B.; Maschio, L.; Rerat, M.; Casassa, S.; Baima, J.; Salustro, S.; Kirtman, B.
WIREs Comput Mol Sci., 2018, 8, e1360.

14. B. Delley (2000). "From molecules to solids with the DMol3 approach". *J. Chem. Phys.* 113 (18): 7756–7764.

15. Filipp Furche, Reinhart Ahlrichs, Christof Hättig, Wim Klopper, Marek Sierka, Florian Weigend WIREs Comput. Mol. Sci. 2013, DOI: 10.1002/wcms.1162.

16. M. Valiev, E.J. Bylaska, N. Govind, K. Kowalski, T.P. Straatsma, H.J.J. van Dam, D. Wang, J. Nieplocha, E. Apra, T.L. Windus, W.A. de Jong, "NWChem: a comprehensive and scalable open-source solution for large scale molecular simulations" *Comput. Phys.*

17. Hafner, J. (2008), *Ab-initio* simulations of materials using VASP: Density-functional theory and beyond. *J. Comput. Chem.*, 29: 2044-2078. doi:10.1002/jcc.21057 *Commun.* 181, 1477 (2010)

18. First principles methods using CASTEP", *Zeitschrift fuer Kristallographie* 220(5-6) pp. 567-570 (2005) S. J. Clark, M. D. Segall, C. J. Pickard, P. J. Hasnip, M. J. Probert, K. Refson, M. C. Payne

19. X. Gonze, B. Amadon, P.M. Anglade, J.-M. Beuken, F. Bottin, P. Boulanger, F. Bruneval, D. Caliste, R. Caracas, M. Cote, T. Deutsch, L. Genovese, Ph. Ghosez, M. Giantomassi, S. Goedecker, D. Hamann, P. Hermet, F. Jollet, G. Jomard, S. Leroux, M. Mancini, S. Mazevet, M.J.T. Oliveira, G. Onida, Y. Pouillon, T. Rangel, G.-M. Rignanese, D. Sangalli, R. Shaltaf, M. Torrent, M.J. Verstraete, G. Z  rah, J.W. Zwanziger. *Computer Physics Communications* 180, 2582-2615 (2009).

20. - Jos   M Soler and Emilio Artacho and Julian D Gale and Alberto Garc  a and Javier Junquera and Pablo Ordej  n and Daniel S  nchez-Portal. - The SIESTA method for ab initio order- N materials simulation. - *Journal of Physics: Condensed Matter*. (- 11):- 2745.

CHAPTER THREE

STUDY OF CO ADSORPTION AND COVERAGE EFFECTS ON CO₇PD₆ 13 ATOM

BIMETALLIC CATALYST CLUSTER

Introduction

The conversion of syngas to liquid products using heterogeneous catalysts is initiated by the adsorption of reactants from the gas phase onto the surface of the catalyst. Carbon monoxide or CO adsorption is a crucial early reaction step for syngas conversion. Hence, it is necessary to develop an understanding of the interaction between CO and transition metals so as to rationally design highly active catalysts with improved selectivity for the desired products.¹⁻⁶ CO adsorption on transition metal catalysts has been widely studied for many decades.²⁻⁹ This reaction garnered early interest as it is one of the first reactions in the Fischer-Tropsch gas to liquid fuels process to produce clean transportation fuels from coal; likewise, it is essential for syngas to ethanol fuel reactions.¹⁰⁻¹³ CO adsorption is also an important reaction for the industrial production of hydrogen using the water gas shift reaction. It is also important for ecofriendly processes, such as the removal of toxic CO from industrial and automotive exhausts and the production of H₂ feed gas with ultra-low levels of CO for fuel cell applications.¹⁴⁻¹⁵

There have been numerous theoretical^{5-9,16-25} and experimental studies^{2,3,26-32} of CO adsorption on transition metals. Some of these experiments sought to characterize the CO binding site and CO-metal bond strength using IR absorption methods.^{1,3} The

Blyholder model⁴ explains CO binding with the metal surface as a two-fold interaction, where there is a transfer of electrons from the carbon atom of the CO molecule to an empty orbital on the metal (the lowest unoccupied orbital or LUMO) via a sigma bonding interaction. This is followed by electron back donation from an occupied metal orbital to an unoccupied anti-bonding orbital on the CO molecule. This π back bonding interaction leads to a weakening of the CO carbon oxygen bond, which is observable via IR techniques as a change in the vibration wavelength of the CO bond.

With the increased availability of methane from shale gas reserves and bio-waste treatment processes there is a need to develop enhanced methane conversion technologies, especially those that generate liquid transportation fuels.³³⁻³⁵ One such reaction process is the conversion of methane derived syngas (a mixture of CO and H₂) to ethanol. To develop an optimal catalyst for this reaction it is essential to understand the reaction mechanism and the proper combination of transition metals that will most effectively catalyze the reaction. As part of this study, we are also interested in understanding the extent of CO surface coverage as a function of CO partial pressure and composition of the transition metal catalysts.

For the current reaction of syngas to ethanol, rhodium has been shown to be the most suitable catalytic element.³⁶ But, due to its low availability and high cost, it is desirable to find an alternative catalyst. When looking for a replacement catalyst it is important to find a metal or combination of metals that has the same ability to catalyze carbon chain

growth reactions as well as favor the formation of alcohol products from syngas. One promising catalyst alternative is a bimetallic catalyst consisting of cobalt and palladium. Cobalt is known to catalyze Fischer-Tropsch type reactions, which involve carbon chain elongation, and palladium is a good catalyst for methanol formation from syngas. Initial experimental testing of catalysts containing both metals (Co and Pd) has yielded promising results; however, it is still unclear what combination of metals will prove to be the most active and selective for ethanol formation.^{11,12,37,38}

In the current study of cobalt palladium bimetallic catalysts, density functional theory employing an atomic orbital approach was used to study both CO adsorption and coverage. The number of atoms in the studied bimetallic cluster was kept at the lowest stable magic number of atoms (i.e., 13 atoms) so as to ensure that the cluster structure was stable for all studied surface reactions.³⁹ The 13 atom bimetallic transition metal cluster containing cobalt (seven atoms) and palladium (six atoms) was considered the model catalyst. This simulation study of CO binding to the bimetallic cluster involves the calculation of adsorption energies, IR frequencies, metal-carbonyl bond lengths, carbon-oxygen bond lengths and the prediction of orbital densities and locations for the HOMO-LUMO metal orbitals as a function of CO coverage on the catalyst surface.

Experimental

A 13-atom cluster consisting of seven cobalt atoms and six palladium atoms (Co₇Pd₆) was used in this simulation study. All adsorption site optimizations (metal type and

number of surface bonds) and energy calculations were performed using density functional theory. DFT calculations were performed using Jaguar 7.0 software (Schrodinger, Inc.). Jaguar is an ab-initio simulation package that uses an atomic orbital approach to calculate system energies. Calculations were carried out using B3LYP and M06 hybrid exchange correlation functionals. Molecular orbitals are described using LACVP basis sets. Structures were built using Material Studio (Accelrys, Inc.). All calculations involving transition metals (cobalt and palladium) were spin polarized.

A thirteen-atom icosahedral structure consisting of nine cobalt and four palladium atoms was constructed. The catalyst structure was geometrically optimized using Jaguar, and optimum spin multiplicity was determined by calculating the minimum energy of the cluster at different spin states from 2 to 20. For these simulations, the geometry of the cluster was allowed to change. The cluster with the lowest energy was obtained at a spin state of 16.

Upon finding the optimum metal cluster geometry and spin state, DFT simulations of CO adsorption behavior were initiated. The atop, bridge and threefold adsorption sites were considered for CO adsorption on both cobalt and palladium metals. Surface coverage studies were performed by varying the number of adsorbed CO molecules from 1 to 6 on the surface of the metals. All atoms (including the metal atoms) were geometrically optimized in every simulation. The energy convergence criterion employed for all DFT optimizations was 10^{-5} Hartrees (0.03 KJ/mol).

The adsorption energy of CO is calculated as below.

$$E_{ads} = [E_{cluster-co} - E_{cluster} - n E_{co}] / n \quad (1)$$

where E_{ads} is the average adsorption energy of a CO molecule, $E_{cluster-co}$ is the energy of the 13-atom cluster with CO molecules on the surface, n is the number of CO molecules in the system and E_{co} is the energy of CO in the gas phase.

Finally, vibrational frequency and HOMO-LUMO calculations were also performed. A scaling factor of 0.9614 was used to correct vibrational frequencies obtained from the B3LYP functional⁴⁰ and a scaling factor of 0.9628 was used to correct vibrational frequencies obtained from the M06 functional⁴¹. Zero-point energy corrections were included in all calculations, and vibrational frequency calculations were used to calculate the zero-point energy correction factors. Atomic Fukui indices, derived from Mulliken populations for the HOMO-LUMO orbitals is computed using Jaguar.

Results and Discussion

Catalyst selection

Ethanol production from carbon monoxide and hydrogen involves a chain elongation step and an alcohol formation step. The overall ethanol production reaction is:



Figure 3.1 shows a subset of the periodic chart that includes rhodium and neighboring transition metals. The metals colored in red are active Fischer Tropsch catalysts and

metals colored in blue are efficient catalysts for methanol formation. Rhodium, colored yellow sits between the red and blue metals and has been proven to be an ideal catalyst for ethanol production.⁴² However, rhodium is a less than ideal catalysts because of the low availability and high cost of the metal; thus, there is a search for an alternative catalyst. We propose a bimetallic combination of cobalt (blue colored metal) and palladium (red colored metal). Cobalt is an active and selective catalyst for chain elongation types of reactions (Fisher Tropsche) and palladium is active for alcohol (methanol) formation reactions.^{38,43-45}

Cr	Mn	Fe	Co	Ni	Cu	<u>Syngas Products</u> ■ hydrocarbons ■ oxygenates ■ ethanol
Mo	Tc	Ru	Rh	Pd	Ag	
W	Re	Os	Ir	Pt	Au	

Figure 3. 1. Transition metals grouped as catalysts for carbon chain elongation (Red color) and alcohol formation reactions (Blue color)

To study reactions on cobalt-palladium bimetallic catalysts, a metal cluster was constructed using the minimum number of atoms necessary to form a stable cluster (13 atoms).³⁹ The optimized geometry is an icosahedral cluster with one cobalt atom at the center surrounded by six cobalt and six palladium atoms, see Figure 3.2. Given that cobalt and palladium atoms prefer to stay segregated, the resulting cluster has 3 types of active sites available on the surface of the catalyst: cobalt, palladium and mixed cobalt-palladium sites.

It was observed that as the number of atoms in the catalyst cluster is increased metal atoms tend to form a shell and core structure where palladium forms a shell surrounding core cobalt atoms.^{46,47} With the 38 atom cluster having near equally amount of palladium and cobalt (see Figure 3.3), metal segregation leads to their being only one type of site (palladium sites) on the catalyst surface. It is also observed that as the number of atoms increases in the system it is more computationally expensive to study reactions on this cluster. Therefore, in the current study a 13-atom cluster consisting of seven cobalt atoms and six palladium atoms is considered.

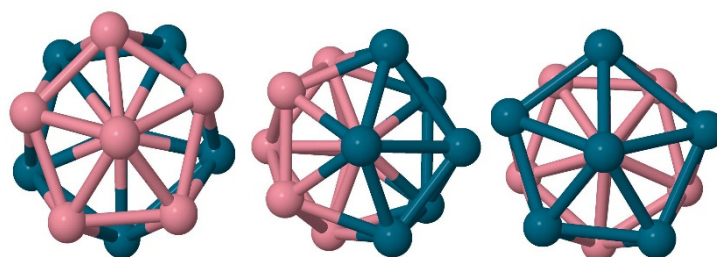


Figure 3. 2. 13 atom metal cluster containing 7 cobalt atoms and 6 palladium atoms. Cobalt and palladium are segregated.

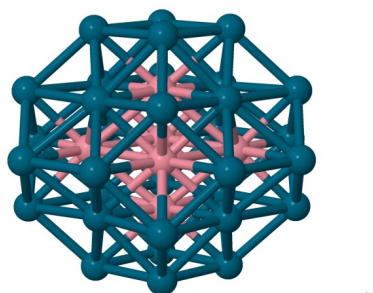


Figure 3. 3. Thirty-eight atom ($\text{Co}_6\text{Pd}_{32}$) cluster with cobalt atoms as core and palladium atoms in shell.

Because of the magnetic properties of the metal cluster, an optimum spin state must be determined. To find the optimum spin state a series of geometric optimizations were performed changing the number of unpaired electrons from 2 to 20 in multiples of 2. The total energy of the cluster was calculated at each spin state, and the minimum energy was observed for a spin state of 16. For later studied systems where CO molecules were bound to the cluster, spin states of 14, 16, and 18 were examined to verify that the optimal spin state did not change with the addition of CO molecules. A plot of system energy versus cluster spin multiplicity is shown in Figure 3.4. Also, the zero-point energy correction factor was used in all calculations.

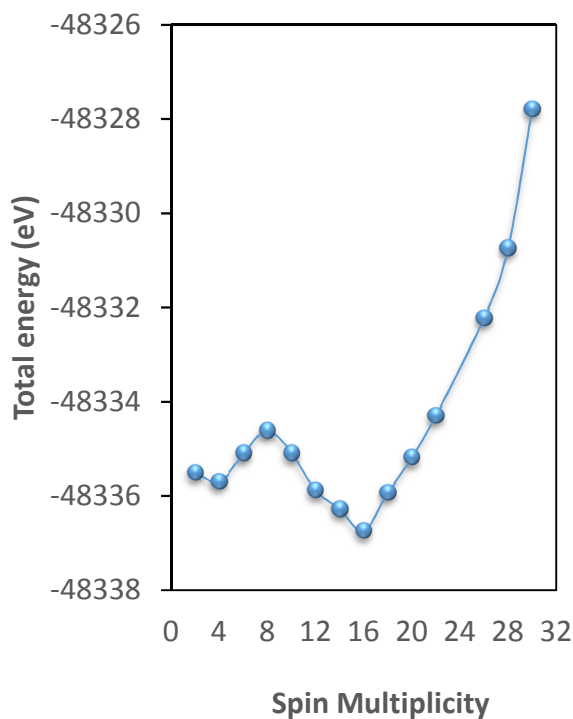


Figure 3. 4. Energy of Co_7Pd_6 cluster at different spin states.

CO Adsorption

CO adsorption on metal clusters is traditionally explained by the Blyholder model. As mentioned earlier, with the Blyholder model⁴ interactions between CO and a metal are twofold. Electrons are transferred from CO to the metal via a sigma forward donation and the metal back donates electron to an antibonding orbital of CO via π -bonding. This is in agreement with frontier orbital theory, where electrons are donated from CO to the lowest unoccupied molecular orbital (LUMO) on the metal and electrons are transferred from the highest occupied molecular orbital (HOMO) on the metal to CO (π back donation).

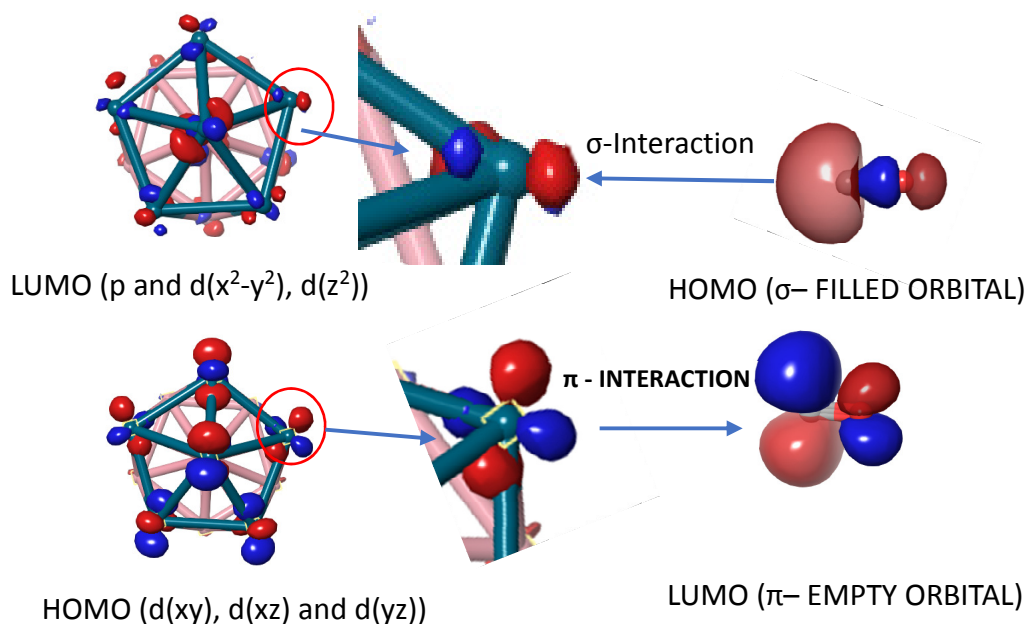


Figure 3. 5. Two fold electronic interactions between palladium atoms in the cluster and CO molecule (Blyholder model).

Two hybrid exchange correlation functionals B3LYP and M06 are considered for this study. B3LYP does considerably well at calculating energies for metal systems but fails to include dispersion effects that are important for CO binding. The M06 functional on the other hand includes dispersion effects but is computationally more expensive.^{40,48,49}

From prior CO adsorption experiments, it is understood that CO binds molecularly on both cobalt and palladium. CO also prefers to bind on atop, bridge, and threefold sites on palladium, while it prefers to adsorb only on atop sites on cobalt. There are eight different possible ways in which CO can bind to the Co₇Pd₆ cluster, adsorption energies are calculated for these eight configurations using the B3LYP and M06 functionals, see Table 3.1. From the data in Table 3.1, it can be inferred that the preferred CO adsorption site on the cluster is the bridge site on palladium atoms at the CoPd interface. It was observed that, CO adsorption energies are underestimated with the B3LYP functional; whereas, experimental values for CO adsorption on bulk metals compares well with M06 adsorption energies.

TABLE 3. 1. CO binding on Co₇Pd₆ cluster

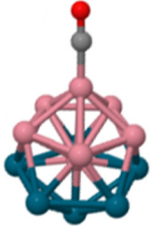
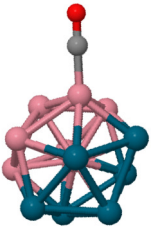
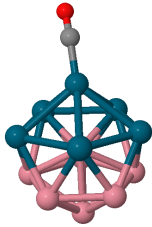
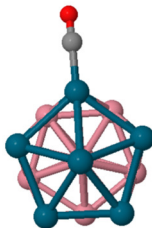
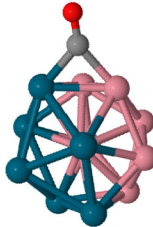
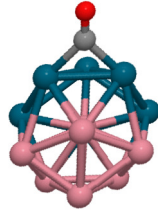
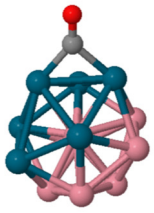
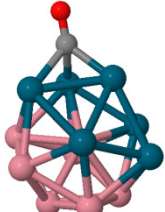
S.NO	Configuration	Geometry	Energy in eV		Bulk Experimental
			B3LYP	M06	
1	Atop on cobalt		-1.206	-1.32	-1.33 ⁵⁰
2	Atop on cobalt at CoPd interface		-1.21	-1.25	
3	Atop on palladium		-1.19	-1.22	
4	Atop on Pd at CoPd interface		-1.24	-1.29	
5	Bridge on CoPd interface		-1.23	-1.28	

Table 3.1. (Continued) CO binding on Co₇Pd₆ cluster.

S.NO	Configuration	Geometry	Energy in eV.		Bulk Experimental
			B3LYP	M06	
6	Bridge on palladium		-1.22	-1.27	
7	Bridge on Pd at CoPd interface		-1.35	-1.39	
8	Threefold on palladium		-1.18	-1.3	-1.3 ⁵⁰

CO adsorption calculations were also performed using the Vienna Ab Initio Simulation Package (VASP), which is a DFT method that employs plane waves to model the electron density in the system. VASP simulation using the PBE functional were used to model the 13 atom cluster of cobalt and palladium. For total energy calculations, we employed a plane wave cutoff energy of 400eV. With Calculated adsorption energies are compared in Table 3.2. It can be seen that PBE over estimates the adsorption energies as compared

to the experimental values. Of the three computational methods tested, the adsorption energies calculated using the M06 functional in Jaguar are closer to the experimental values.

TABLE 3. 2. Comparison of CO binding energies calculated from Jaguar and VASP⁴⁹

Configuration	JAGUAR (Molecular Orbital)		VASP (Plane wave)	Experimental
	B3LYP	M06	PBE	TDS
Threefold on Pd	-1.18	-1.3	-1.48	-1.3

CO coverage

To examine CO coverage effects on the Co₇Pd₆ cluster, the energy of the system was evaluated as a function of the number of CO molecules adsorbed to the cluster surface. The number of CO molecules was increased systematically from 1 to 10 on atop, bridge, and threefold sites, and the energy of the cluster with adsorbed CO molecules was calculated by DFT methods using B3LYP and M06 functionals. It was observed that CO molecules would adsorb on atop, bridge, and threefold palladium sites on the cluster; whereas, CO molecules only adsorbed on atop cobalt sites. For CO adsorption on palladium sites, the palladium atoms exhibited favorable bonding to one up to a maximum of two CO molecules. Also, CO binds more strongly to the palladium atom with only one cobalt neighbor (the Co atom at the core of the cluster) as compared to the

palladium atoms located at the CoPd interface, which are bonded to three cobalt atoms (see Figure 3.6). Energy calculations for CO binding on the palladium side of the cluster indicated that the maximum number of CO molecules that can be adsorbed is six with atop adsorption (i.e., one CO molecule adsorbed per palladium surface site), four with bridge adsorption, and two with threefold adsorption. The maximum number of CO molecules adsorbed on the cobalt side of the cluster is six atoms, which are bound to atop Co metal sites (i.e., one CO molecule adsorbed per cobalt surface site). Adsorption energy of each CO molecule on the cluster is calculated using Equation 1.

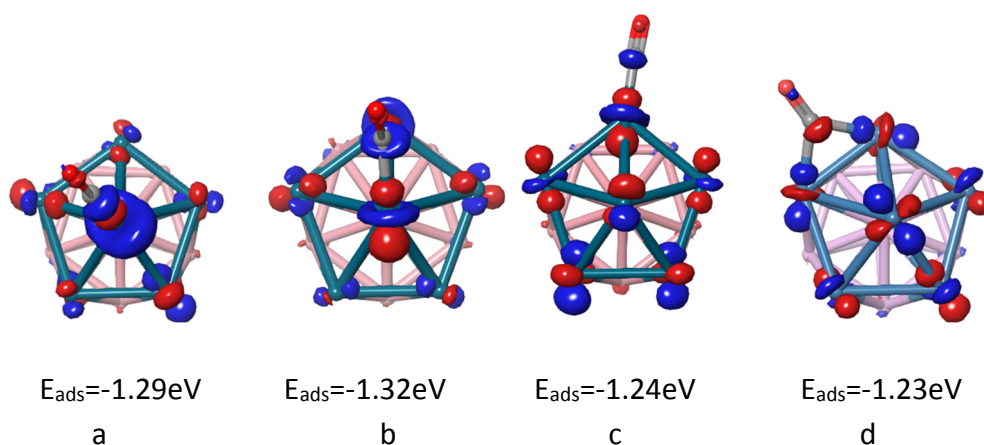


Figure 3. 6. CO binding energies on atop and bridge when center Pd atom is involved in binding vs. when center Pd atom is not involved.

- a. CO atop binding on center Pd atom
- b. CO bridge binding on center Pd atom
- c. CO atop binding on side Pd atom
- d. CO bridge binding on side Pd atom

CO adsorption on palladium side of Co₇Pd₆ cluster

The adsorption energy of CO as function of the number of adsorbed CO molecules on the surface of the cluster was estimated by DFT methods using B3LYP and M06 functionals, and these results are shown in Figure 3.7 & 3.8. From the graphs, it can be observed that the bond between palladium and CO becomes weaker and the adsorption energy decreases as the number of adsorbed CO molecules on the surface increases. When there is just one adsorbed CO on the cluster, the preferred adsorption site is a palladium bridge site, but as the number of CO molecules increases beyond three, the adsorption site preference changes from bridge to atop. Similar trends are observed with both B3LYP and M06 functionals.

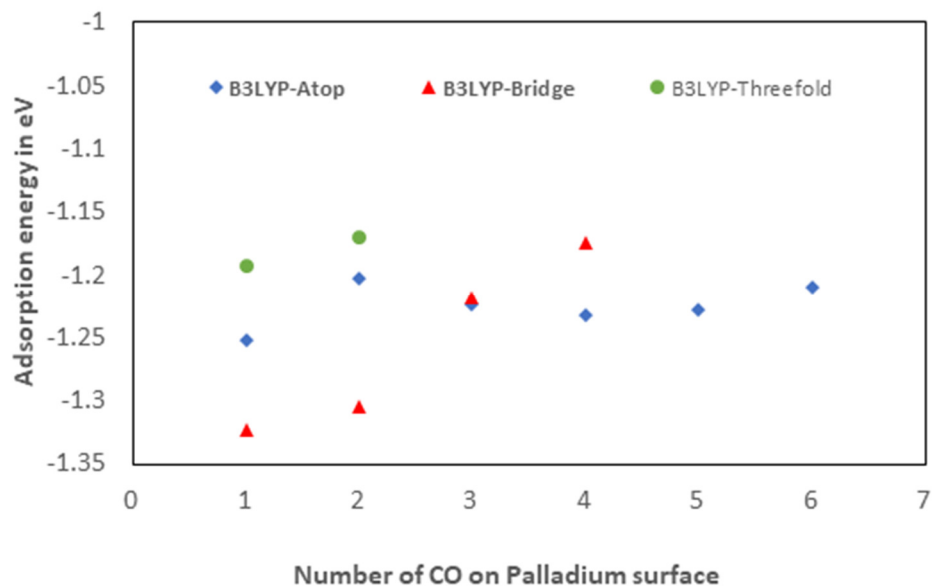


Figure 3. 7. Average adsorption energy for a CO molecule as a function of CO surface coverage on palladium sites of the Co₇Pd₆ cluster using DFT methods with B3LYP functionals.

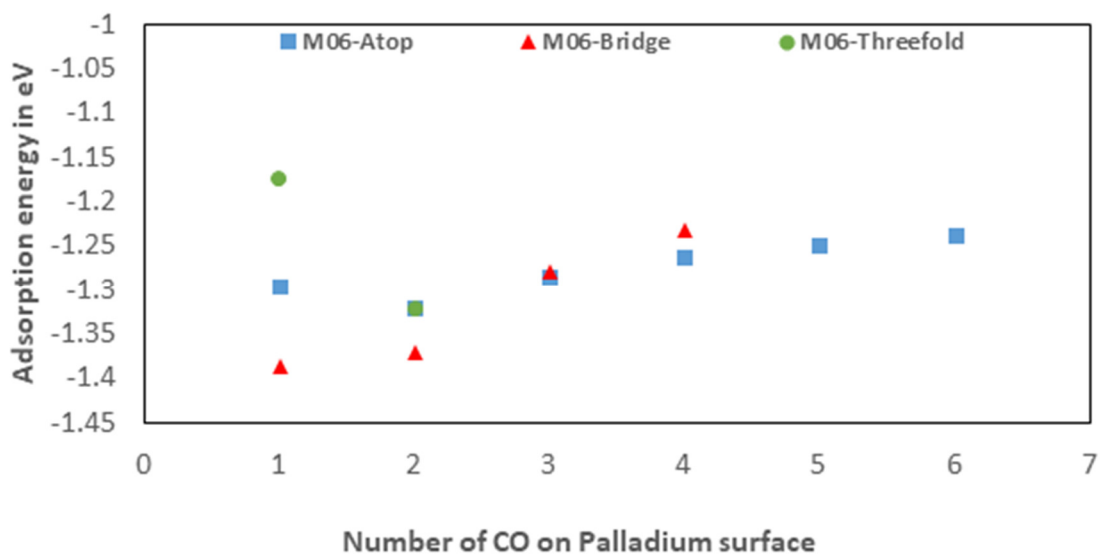


Figure 3. 8. Average adsorption energy for a CO molecule as a function of CO surface coverage on palladium sites of the Co_7Pd_6 cluster using DFT methods with MO6 functionals.

Why does the adsorption site preference for CO bonding on palladium change with CO loading?

On the 13-atom cluster of cobalt and palladium, when the number of CO molecules is increased beyond three, the adsorption site preference changes from bridge to atop on palladium sites. To understand this shift we looked at the highest occupied molecular orbitals (HOMO) on the metal cluster as a function of CO coverage. On the uncovered cluster, the HOMO is concentrated on the palladium side of the cluster. When the number of CO molecules binding in bridge configuration is increased beyond three there is a shift in the HOMO orbital from the Pd side to Co side. Whereas, when the

number of CO binding in the atop side is increased to three, the HOMO remains on the palladium side, allowing more CO to bind to the palladium surface.

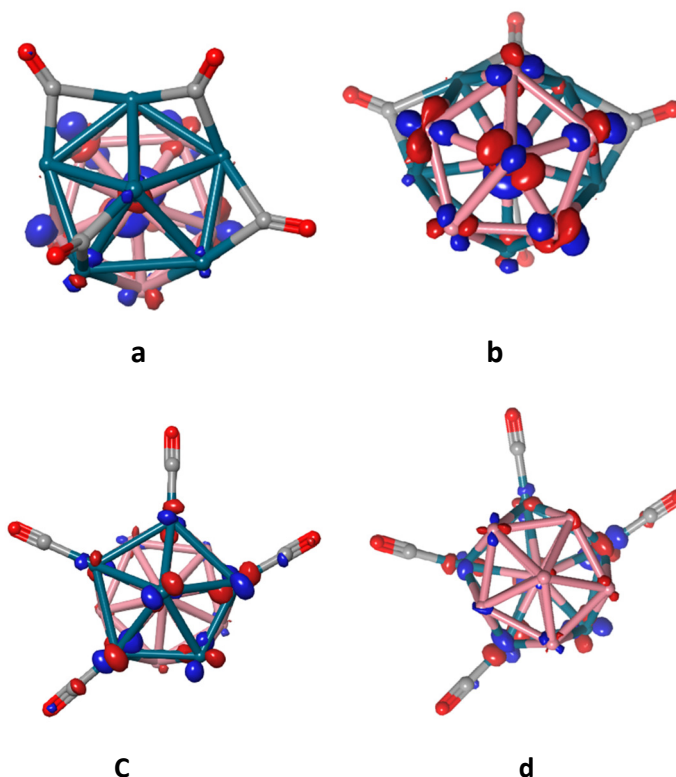


Figure 3. 9 HOMO shift from Pd side to Cobalt side when 4 atoms are bonded in bridge configuration.

- a. HOMO on Pd side with CO bridge binding b. HOMO on Co Side with CO bridge binding
 c. HOMO on Pd site with CO atop binding d. HOMO on Co side with CO atop binding

CO adsorption on Co side of Co₇Pd₆ cluster

CO prefers to adsorb only on the atop sites of cobalt atoms, with the maximum number of CO molecules that can adsorb equaling six for the six cobalt surface sites. In general, increasing the number of adsorbed CO species results in a decrease in the

average CO ligand bond strength, thereby reducing the average adsorption energy for a CO ligand on the cluster. Similar trends are observed with DFT energies calculated using both B3LYP and M06 functionals. The adsorption energies calculated using the M06 functionals are in the range of -1.3eV which correlates well with experimental values. However, it can be seen that the B3LYP functional underestimates the adsorption energy (see Figure 3.10 below).

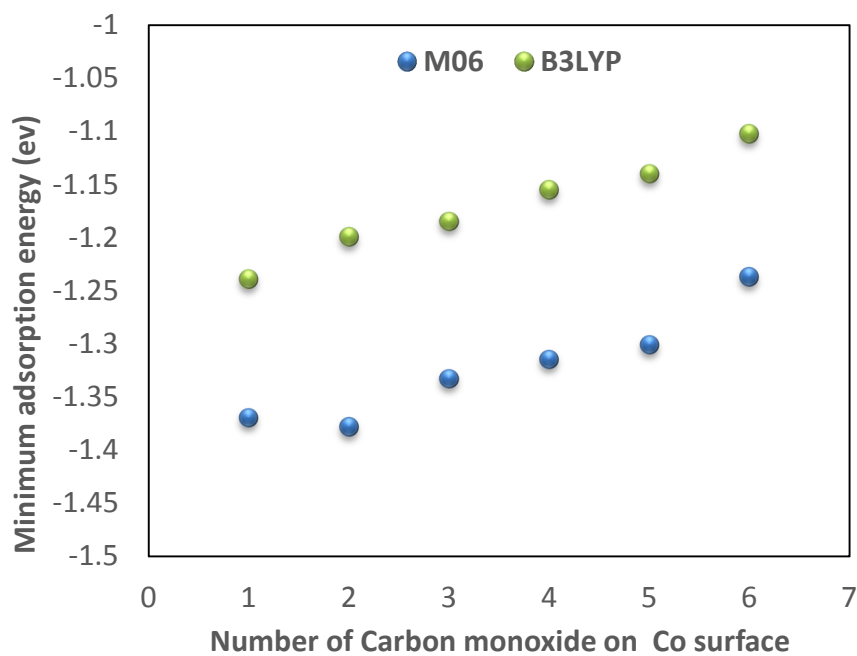


Figure 3. 10. Average CO adsorption energy change with the number of CO molecules adsorbed to Pd sites of the cluster using DFT methods employing B3LYP or M06 functionals.

Bond Lengths

Metal-carbon and carbon-oxygen bond lengths were calculated using DFT methods employing B3LYP and M06 functionals. A moderate change in bond lengths is observed as CO surface coverage increases. As the number of adsorbed CO molecules is increased, the bond length between palladium and carbonyl carbon atoms increases, suggesting that the bond is getting weaker with an increase in surface coverage. Similar observations are found with both B3LYP and M06 functionals. Bond lengths as a function of Co surface coverage are plotted in Figure 3.11. Predicted bond lengths for Pd-C and Co-C correlate well with the experimental values. Also, the bond length between Pd-C increases from atop, bridge to threefold as expected, demonstrating the effects of changes in carbon hybridization.

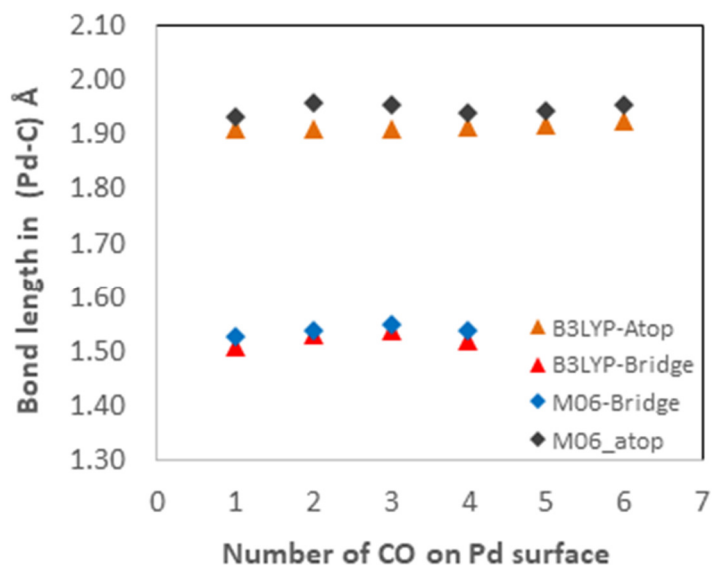


Figure 3. 11. Metal carbonyl bond lengths changing with number of CO on surface of Pd on CO₇Pd₆ cluster.

For CO carbon-oxygen bonds, as CO surface coverage increases, the bond length decreases, indicating that the C-O bond is getting stronger. This results from the cluster having less electron density to back donate to the C-O anti-bonding orbitals. It is also observed that metal-carbon bond lengths predicted by DFT methods using B3LYP functionals are shorter than the corresponding bonds modeled using DFT with M06 functionals. From the results it can be inferred that B3LYP is underestimating M-C bond lengths where as it is overestimating C-O bond lengths, this can be attributed to the fact that B3LYP does not include dispersion effects.

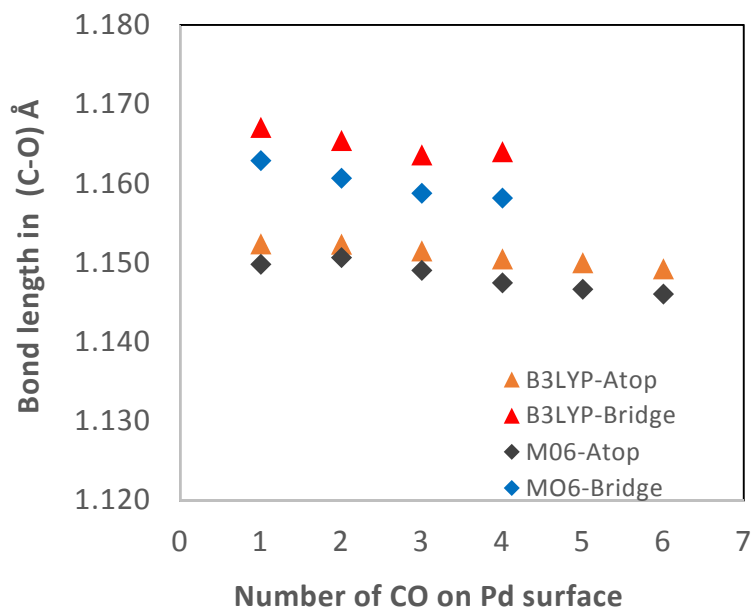


Figure 3. 12. Carbon-oxygen bond lengths changing with number of CO on surface of Pd

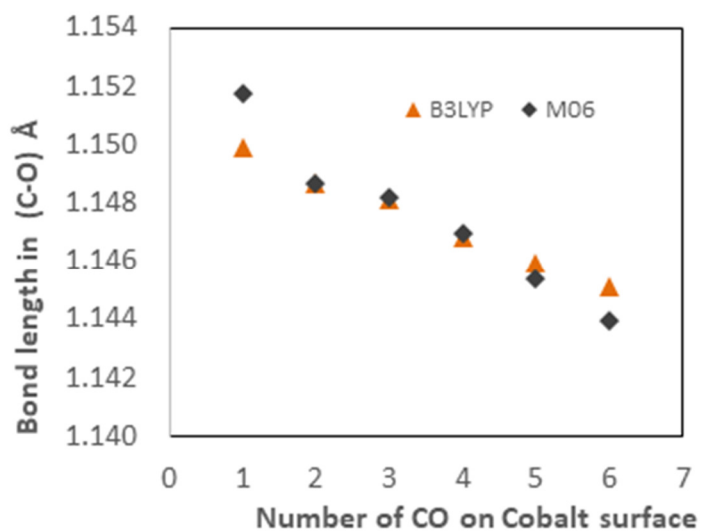


Figure 3. 13. Variations in carbon-oxygen bond lengths as a function of CO surface coverage on the cobalt sites of a Co_7Pd_6 cluster.

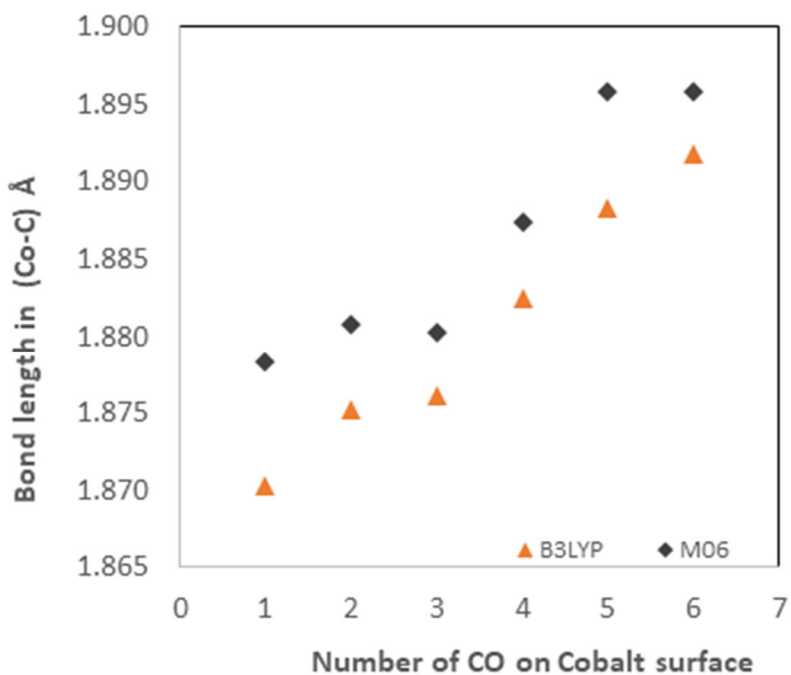


Figure 3. 14. Variations in cobalt-carbonyl carbon bond lengths as a function of CO surface coverage on the cobalt sites of a Co_7Pd_6 cluster.

Infrared spectra

Infrared (IR) absorption spectra were estimated via DFT methods as implemented in Jaguar (Schrodinger, Inc.) using a scaling factor of 0.9614 to correct vibrational frequencies errors that results from the use of the B3LYP³⁸ functional. Similarly, a scaling factor of 0.9628 was used to correct vibrational frequencies calculated from DFT methods using the M06 functional ³⁹. As the number of CO on the surface is increased, the vibrational frequency increases to a higher value indicating that the metal-carbon bond is getting weaker (see Figure 3.15). With CO binding on the atop site, the vibrational frequency is estimated to be between 2015-2065. For bridge site adsorption, the estimated vibrational frequency is between 1920-2000, and with threefold site adsorption, the vibrational frequency is between 2040 and 2100. These predicted vibrational frequencies correlate well with experimental values obtained using diffuse reflectance (DRIFTS) techniques with less than 5 percent error ²⁸ see Table 3.3).

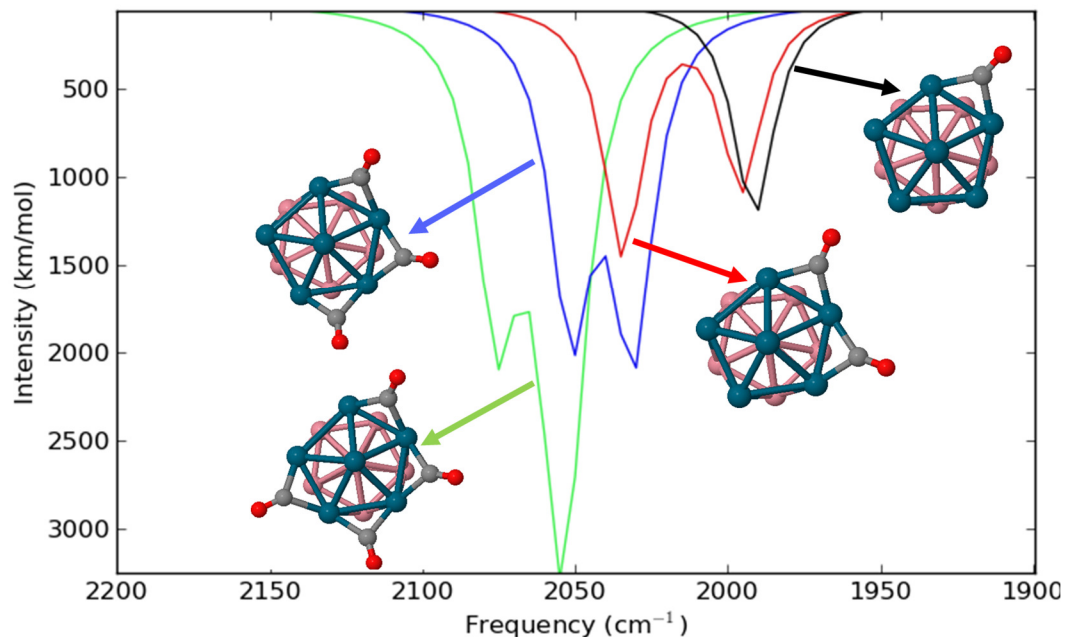


Figure 3. 15. Calculated shift in IR absorption frequency for CO vibrations as a function of Co surface coverage for CO molecules adsorbed on Pd bridge sites of the cluster.

TABLE 3. 3. Comparison of experimental and computational values for vibrational frequency

	Atop(Pd)	Bridge(Pd)	Atop (Co)
Experimental bulk²⁸	2049-2061	1909-1994	2010-2070
Co₇Pd₆ Cluster (M06 corrected)	2015-2065	1920-2000	2040-2100
% Error	less than 2.5	less than 5	less than 5

Conclusions

DFT simulation results for CO binding to the Co₇Pd₆ cluster follow expected trends and are in close agreement with experimental results. DFT methods employing B3LYP and

M06 functionals are able accurately estimate the CO adsorption energy, but B3LYP functional fails to include dispersion effects; hence, they overestimate CO adsorption energies. In terms of surface binding characteristics, CO prefers to bind on atop and bridge palladium sites or on atop cobalt sites. Additionally, the maximum number of CO molecules that can bind on the palladium sites of the cluster is six and likewise for the cobalt sites, which equates to a maximum surface coverage of CO equal to one CO per surface metal site. With only one CO on the surface, it prefers to bind on a palladium bridge site but as CO surface coverage increases beyond 0.5 CO molecules per surface metal, the adsorption site preference changes from bridge to atop. Change in the adsorption site preference can be explained by looking at the HOMO locations on the cluster as a function of Co surface coverage. As the number of CO on Pd bridge sites increases 0.5 Co per site, the HOMO shifts to the cobalt side of the cluster not allowing any more CO to bind to the palladium (unless the CO binding switches to atop configurations).

To discern how the reactivity of adsorbed CO molecules might change with increases in CO surface coverage, energy minimized adsorbate structures were used to calculate variations in bond lengths as a function of CO surface coverage. This data showed that metal-carbon bond lengths increase with an increase in the number of CO species on the surface; whereas, carbon-oxygen bond lengths decreases with the number of adsorbed CO. This suggests that increase in CO coverage would negatively impact CO hydrogenation reactions that ultimately lead to decreases in the CO bond length due to changes in

carbon hybridization from sp hybridized to sp² hybridization. However, from this data it is less clear how CO surface coverage would impact activation energies for CO insertion reactions.

This work also examined the ability of B3LYP and M06 functionals to accurately predict CO adsorption phenomena for the Co₇Pd₆ cluster. DFT methods using the B3LYP functional underestimated M-C bond lengths and overestimated C-O bond lengths. This can be attributed to its inability to address dispersion effects. Finally, predicted IR spectra for adsorbed CO species agree with experimental values measured using DRIFTS techniques; specifically, calculated values are within 5% of the experimental values.

References

1. - Ozensoy E, - Wayne Goodman D. - Vibrational spectroscopic studies on CO adsorption, NO adsorption CO + NO reaction on pd model catalysts. - *Phys Chem Chem Phys*. 2004;6(- 14):- 3765. doi: - 10.1039/B402302A.
2. Chen MS, Cai Y, Yan Z, Gath KK, Axnanda S, Wayne Goodman D. - Highly active surfaces for CO oxidation on rh, pd, and pt. - *Surface Science*. 2007;601(- 23):- 5326. doi: - <http://dx.doi.org/10.1016/j.susc.2007.08.019>.
3. Goyhenex C, Croci M, Claeys C, Henry CR. - FTIR studies of the adsorption of CO on supported metallic clusters PdMgO(100). - *Surface Science*. 1996;352-354(-):- 475. doi: - [http://dx.doi.org/10.1016/0039-6028\(95\)01182-X](http://dx.doi.org/10.1016/0039-6028(95)01182-X).

4. Sung S, Hoffmann R. - How carbon monoxide bonds to metal surfaces. - *J Am Chem Soc.* 1985;107(- 3):- 578. doi: - 10.1021/ja00289a009.
5. - Marek Gajdoš and Andreas Eichler and Jürgen Hafner. - CO adsorption on close-packed transition and noble metal surfaces: Trends from ab initio calculations. - *Journal of Physics: Condensed Matter.* (- 8):- 1141.
6. Feibelman PJ, Hammer B, Nørskov JK, et al. - The CO/pt(111) puzzle†. - *J Phys Chem B.* 2001;105(- 18):- 4018. doi: - 10.1021/jp002302t.
7. Fielicke A, Gruene P, Meijer G, Rayner DM. - The adsorption of CO on transition metal clusters: A case study of cluster surface chemistry. - *Surface Science.* 2009;603(- 10–12):- 1427. doi: - <http://dx.doi.org/10.1016/j.susc.2008.09.064>.
8. Föhlisch A, Nyberg M, Bennich P, et al. The bonding of CO to metal surfaces. *J Chem Phys.* 2000;112(4):1946-1958. doi: <http://dx.doi.org/10.1063/1.480773>.
9. Lischka M, Mosch C, Groß A. CO and hydrogen adsorption on pd(2 1 0). *Surf Sci.* 2004;570(3):227-236. doi: <http://dx.doi.org/10.1016/j.susc.2004.07.046>.
10. Dry ME. - The Fischer–Tropsch process: 1950–2000. - *Catalysis Today.* 2002;71(- 3–4):- 227. doi: - [http://dx.doi.org/10.1016/S0920-5861\(01\)00453-9](http://dx.doi.org/10.1016/S0920-5861(01)00453-9).

11. Cheng J, Hu P, Ellis P, French S, Kelly G, Lok CM. - A first-principles study of oxygenates on co surfaces in Fischer–Tropsch synthesis. - *J Phys Chem C*. 2008;112(-25):- 9464. doi: - 10.1021/jp802242t.
12. Khodakov AY, Chu W, Fongarland P. - Advances in the development of novel cobalt Fischer–Tropsch catalysts for synthesis of long-chain hydrocarbons and clean fuels. - *Chem Rev*. 2007;107(- 5):- 1692. doi: - 10.1021/cr050972v.
13. Tan KF, Xu J, Chang J, Borgna A, Saeys M. - Carbon deposition on co catalysts during Fischer–Tropsch synthesis: A computational and experimental study. - *Journal of Catalysis*. 2010;274(- 2):- 121. doi: - <https://doi.org/10.1016/j.jcat.2010.06.008>.
14. David N. - The water-gas shift reaction. - *Catalysis Reviews*. 1980;21(- 2):- 275. doi: - 10.1080/03602458008067535.
15. TAYLOR K. - Nitric oxide catalysis in automotive exhaust systems. - *Catalysis Reviews*. 1993;35(- 4):- 457. doi: - 10.1080/01614949308013915.
16. Cheng J, Hua P, Ellis P, French S, Kelly G, Martin C. - A DFT study of the transition metal promotion effect on ethylene chemisorption on co(0 0 0 1). - *Surface Science*. 2009;603(- 17):- 2752. doi: - <http://dx.doi.org/10.1016/j.susc.2009.07.012>.
17. Wanbayor R, Ruangpornvisuti V. - A periodic DFT study on binding of pd, pt and au on the anatase TiO₂ (0 0 1) surface and adsorption of CO on the TiO₂ surface-supported

pd, pt and au. - *Applied Surface Science*. 2012;258(- 7):- 3298. doi: - <http://dx.doi.org/10.1016/j.apsusc.2011.11.085>.

18. Lopez N, Nørskov J. - Catalytic CO oxidation by a gold nanoparticle: A density functional study. - *J Am Chem Soc*. 2002;124(- 38):- 11262. doi: - 10.1021/ja026998a.

19. Bakken V, Rytter E, Swang O. - Chemisorption on cobalt surfaces: The effect of subsurface rhenium atoms from quantum chemical cluster model calculations. - *Surface Science*. 2011;605(- 5–6):- 513. doi: - <http://dx.doi.org/10.1016/j.susc.2010.12.008>.

20. Pedersen F, Andersson MP. - CO adsorption energies on metals with correction for high coordination adsorption sites – A density functional study. - *Surface Science*. 2007;601(- 7):- 1747. doi: - <http://dx.doi.org/10.1016/j.susc.2007.01.052>.

21. Yudanov IV, Sahnoun R, Neyman KM, Rosch N. - CO adsorption on pd nanoparticles: Density functional and vibrational spectroscopy studies. - *J Phys Chem B*. 2003;107(- 1):- 255. doi: - 10.1021/jp022052b.

22. Zeinalipour-Yazdi CD, Cooksy AL, Efsthathiou AM. - CO adsorption on transition metal clusters: Trends from density functional theory. - *Surface Science*. 2008;602(- 10):- 1858. doi: - <http://dx.doi.org/10.1016/j.susc.2008.03.024>.

23. Yudanov IV, Genest A, Schauer mann S, Freund H. - Size dependence of the adsorption energy of CO on metal nanoparticles: A DFT search for the minimum value. - *Nano Lett.* 2012;12(- 4):- 2134. doi: - 10.1021/nl300515z.
24. Lopez N, Nørskov JK. Synergetic effects in CO adsorption on Cu–Pd(1 1 1) alloys. - *Surface Science.* 2001;477(- 1):- 59. doi: - [http://dx.doi.org/10.1016/S0039-6028\(01\)00706-3](http://dx.doi.org/10.1016/S0039-6028(01)00706-3).
25. Hammer B, Nørskov JK. - Theoretical surface science and catalysis—calculations and concepts. . 2000;45:- 71. doi: - [http://dx.doi.org/10.1016/S0360-0564\(02\)45013-4](http://dx.doi.org/10.1016/S0360-0564(02)45013-4).
26. Zheng H, Zhang R, Li Z, Wang B. Insight into the mechanism and possibility of ethanol formation from syngas on cu(100) surface. *Journal of Molecular Catalysis A: Chemical.* 2015;404-405(0):115. doi: <http://dx.doi.org/10.1016/j.molcata.2015.04.015>.
27. Guo X, Yates JT. Dependence of effective desorption kinetic parameters on surface coverage and adsorption temperature: CO on pd(111). *J Chem Phys.* 1989;90(11):6761-6766. doi: <http://dx.doi.org/10.1063/1.456294>.
28. Carlsson AF, Bäumer M, Risse T, Freund H-. Surface structure of Co–Pd bimetallic particles supported on Al₂O₃ thin films studied using infrared reflection absorption spectroscopy of CO. *J Chem Phys.* 2003;119(20):10885-10894. doi: <http://dx.doi.org/10.1063/1.1619943>.

29. Carlsson AF, Naschitzki M, Baumer M, Freund H-. - The structure and reactivity of Al₂O₃-supported Cobalt–Palladium particles: A CO-TPD, STM, and XPS study. - *J Phys Chem B*. 2003;107(- 3):- 778. doi: - 10.1021/jp021966v.
30. Murdoch A, Trant AG, Gustafson J, et al. - The influence of CO adsorption on the surface composition of cobalt/palladium alloys. - *Surface Science*. 2016;646(-):-31. doi: - <http://dx.doi.org/10.1016/j.susc.2015.08.004>.
31. Smith ML, Kumar N, Spivey JJ. - CO adsorption behavior of Cu/SiO₂, Co/SiO₂, and CuCo/SiO₂ catalysts studied by in situ DRIFTS. - *J Phys Chem C*. 2012;116(- 14):- 7931. doi: - 10.1021/jp301197s.
32. Carlsson AF, Naschitzki M, Baumer M, Freund H-. - Adsorption and reaction on pristine and oxidized Co–Pd bimetallic particles supported on Al₂O₃ thin films. - *Surface Science*. 2003;543(- 1–2):- 143. doi: - <http://dx.doi.org/10.1016/j.susc.2003.09.012>.
33. Kerr RA. - Natural gas from shale bursts onto the scene. - *Science*. 2010;328(- 5986):- 1624.
34. Wang Q, Chen X, Jha AN, Rogers H. - Natural gas from shale formation – the evolution, evidences and challenges of shale gas revolution in united states. - *Renewable and Sustainable Energy Reviews*. 2014;30:- 1. doi: - <https://doi.org/10.1016/j.rser.2013.08.065>.

35. Al-Douri A, Sengupta D, El-Halwagi MM. - Shale gas monetization – A review of downstream processing to chemicals and fuels. - *Journal of Natural Gas Science and Engineering*. 2017;45:- 436. doi: - <https://doi.org/10.1016/j.jngse.2017.05.016>.
36. - Spivey JJ, - Egbebi A. - Heterogeneous catalytic synthesis of ethanol from biomass-derived syngas. - *Chem Soc Rev*. 2007;36(- 9):- 1514. doi: - 10.1039/B414039G.
37. Schmid G. Developments in transition metal cluster chemistry — the way to large clusters. In: - *Clusters*. Vol 62. - Springer Berlin Heidelberg; 2005:- 51-85. - 10.1007/BFb0009185.
38. Scott AP, Radom L. - Harmonic vibrational frequencies: An evaluation of Hartree–Fock, Møller–Plesset, quadratic configuration interaction, density functional theory, and semiempirical scale factors. - *J Phys Chem*. 1996;100(- 41):- 16502. doi: - 10.1021/jp960976r.
39. Laury ML, Carlson MJ, Wilson AK. Vibrational frequency scale factors for density functional theory and the polarization consistent basis sets. *Journal of Computational Chemistry*. 2012;33(30):2380-2387. doi: 10.1002/jcc.23073.
40. Gupta M, Smith ML, Spivey JJ. - Heterogeneous catalytic conversion of dry syngas to ethanol and higher alcohols on cu-based catalysts. - *ACS Catal*. 2011;1(- 6):- 641. doi: - 10.1021/cs2001048.

41. Hanm HS, Lee WY. - Effects of promoters of palladium/silica catalysts for the synthesis of methanol. - *Applied Catalysis*. 1990;65(- 1):- 1. doi: - [https://doi.org/10.1016/S0166-9834\(00\)81583-3](https://doi.org/10.1016/S0166-9834(00)81583-3).
42. Ming H, Baker BG. - Characterization of cobalt fischer-tropsch catalysts I. unpromoted cobalt-silica gel catalysts. - *Applied Catalysis A: General*. 1995;123(- 1):- 23. doi: - [https://doi.org/10.1016/0926-860X\(94\)00220-7](https://doi.org/10.1016/0926-860X(94)00220-7).
43. Burghgraef H, Jansen APJ, Van Santen RA. - Electronic structure calculations and dynamics of methane activation on nickel and cobalt. - *The Journal of Chemical Physics*. 1994;101(- 12):- 11012. doi: - 10.1063/1.467852.
44. Fajula F, Anthony RG, Lunsford JK. - Methane and methanol synthesis over supported palladium catalysts. - *Journal of Catalysis*. 1982;73(- 2):- 237. doi: - [https://doi.org/10.1016/0021-9517\(82\)90098-7](https://doi.org/10.1016/0021-9517(82)90098-7).
45. - Gao W, - Zhao Y, - Chen H, et al. - Core-shell cu@(CuCo-alloy)/Al₂O₃ catalysts for the synthesis of higher alcohols from syngas. - *Green Chem.* (- 3):- 1525. doi: - 10.1039/C4GC01633E.
46. Wang L, JOhnson DD. - Predicted trends of Core–Shell preferences for 132 late transition-metal binary-alloy nanoparticles. - *J Am Chem Soc*. 2009;131(- 39):- 14023. doi: - 10.1021/ja903247x.

47. Schneebeli ST, Bochevarov A,D, Friesner RA. - Parameterization of a B3LYP specific correction for noncovalent interactions and basis set superposition error on a gigantic data set of CCSD(T) quality noncovalent interaction energies. - *J Chem Theory Comput.* 2011;7(- 3):- 658. doi: - 10.1021/ct100651f.

48. Sousa FA, Fernandes PA, Ramos MJ. - General performance of density functionals. - *J Phys Chem A.* 2007;111(- 42):- 10439. doi: - 10.1021/jp0734474.

49. - Marek Gajdoš and Andreas Eichler and Jürgen Hafner. - CO adsorption on close-packed transition and noble metal surfaces: Trends from ab initio calculations. - *Journal of Physics: Condensed Matter.* (- 8):- 1141.

CHAPTER FOUR

DFT AND MICROKINETIC MODELING STUDY OF SYNGAS TO ETHANOL CONVERSION ON ISOLATED SITES OF A BIMETALLIC CO₇PD₆ NANOCUSTER

Introduction:

Global energy demand continues to rise with increases in world population along with the rising urbanization, industrialization, and transportation demands of society. The International Energy Agency (IEA) projects that there will be 48% rise in world energy consumption by 2040.¹ To meet this ever-growing energy demand and to reduce dependence on non-renewable fossil fuels, there is a need to develop technologies for alternative renewable energy sources.

When we look at the total energy consumption in the United States, 29% of the energy is used for transportation. Currently, the primary energy sources for transportation are fossil fuels (diesel and petrol), biofuels (ethanol and biodiesel) and electricity produced from varied energy sources. For gasoline engines, ethanol is currently the only renewable fuel, which has been shown to reduce greenhouse gas emissions, that has achieved wide spread acceptance. Ethanol can be used as a fuel additive or as an alternative fuel by itself. Most of the ethanol produced today is from corn based biochemical processes, but the process is very energy intensive.¹⁻⁴

In this study, we are interested in developing an efficient, alternative chemical pathway to produce ethanol, especially from syngas as it can be derived from fossil or

renewable energy sources. Syngas describes mixtures of carbon monoxide (CO) and hydrogen (H₂). It is an important feedstock for many chemical processes, including the Fischer-Tropsch production of diesel fuel products. It can be also be produced from Methane by dry reforming⁵, steam reforming^{5,6} or partial oxidation processes^{6,7}, and can also be found in the exhaust from many industrial processes. The syngas to ethanol reaction has been widely studied for more than 95 years.⁸ Despite these efforts, there is still no commercial process for the production of ethanol via this route. Further, the reaction mechanism is not well understood, and the identification of highly selective catalysts for this reaction remains an elusive goal. The main chemical challenges faced in this process are low conversion of reactants and low selectivity towards ethanol, which can be explained by the fact that the reaction kinetics are slow for C-C bond formation and fast for the chain growth of C₂ intermediates. Other primary reaction by-products are methane, acetaldehyde and methanol.

The reaction mechanism for ethanol from syngas is complicated and to-date, several reaction mechanisms have been proposed. Most widely accepted reaction mechanisms for this reaction involve the following steps: CO adsorption, CO dissociation to form CH_x species, and CO insertion into CH_x species to form ethanol. Key CH_x intermediates can also undergo carbon chain growth to form higher alcohols or undergo further hydrogenation to form CH₄ or other higher hydrocarbons, all of which increase hydrogen demands and fail to yield the desired alcohol product.⁹ Thus, the key to successful ethanol formation is suppression of CH₄ formation from CH_x species as well as

a unique combination of carbon chain growth accompanied by the formation of hydroxyl functional groups.

Prior experimental studies showed that syngas is converted to ethanol in the presence of transition metal catalysts, especially supported rhodium catalysts.^{10,11} Numerous ethanol formation catalytic studies were performed on rhodium using different support materials and precursors, but ultimately the high cost and lower availability of rhodium have kept such processes from being commercialized. Thus, it is important to identify a lower cost alternative catalyst material.

Ethanol formation is a multi-step process consisting of carbon chain growth and alcohol formation reactions. It has been hypothesized that an appropriate combination of metals active for carbon chain growth, such as Co or Ni based Fisher-Tropsch catalysts¹²⁻¹⁴, and metals that effectively convert methane to methanol, such as Pd or Pt based catalysts¹⁵⁻¹⁷, might recreate the ethanol activity of rhodium, which is located in between these other groups of metals on the periodic chart. In this study, we examined the catalytic activity of a bimetallic catalyst consisting of cobalt and palladium, which has been shown to be experimentally active for syngas conversion to ethanol.

To understand the CoPd catalyzed syngas to ethanol reaction, a detailed reaction mechanism consisting of 46 reactions is proposed, and the energetics of the individual reactions were studied using density functional theory (DFT) calculations. The reaction mechanism involves three surfaces (Co, Pd, and CoPd), 46 reversible elementary reactions, two reactants (CO and H₂) and seven products, including ethanol. To reduce

the required computational time, the studied reaction sites are from a 13-atom nanometer sized icosahedral cobalt-palladium (CoPd) bimetallic cluster. This cluster size was selected because it is one of the smallest magic number clusters that are known to be stable. Further, the modeled bimetallic cluster consisted of seven cobalt and six palladium atoms (Co₇Pd₆). The small cluster size and near equal number of metals in the cluster ensures that all possible metal atom catalyst sites (Co, Pd, and CoPd) are exposed on the outer surface of the cluster, negating any issues that might have arisen from cluster compositions rich in Pd that might have favored the formation of a core shell structure devoid of Co containing surface sites.¹⁸

Adsorption energy, activation energy, entropy and heat of reactions for all the intermediates considered in the reaction network were calculated using atomic orbital based DFT methods (i.e., not plane wave approaches). Activation energies were calculated using DFT methods employing nudged elastic band theory. Multiple BEP relationships were created to reduce the overall computational time needed to study this large system of elementary reactions. Ultimately, a batch reactor microkinetic model was developed, so as to follow the time evolution of products and surface coverage of adsorbed reactants and intermediate species. Separate microkinetic models were developed for cobalt, palladium and cobalt-palladium catalyst sites to understand the intrinsic nature of the sites. Further, experimentally based coverage dependent sticking coefficients for CO adsorption were considered in the model.

Experimental

The catalyst simulated in the current study was a 13 atom cluster consisting of seven cobalt and six palladium atoms (Co_7Pd_6). The segregation of cobalt and palladium metal atoms in the cluster is the preferred arrangement of atoms. There are three different surface sites on the catalyst, pure Co sites, pure Pd sites and CoPd mixed sites at the interface (Figure 4.1). It is important to note that the pure metals sites studied are part of bimetallic cluster. The presence of two metals in such close proximity to one another will affect the electronic nature of one another. ¹⁹⁻²¹

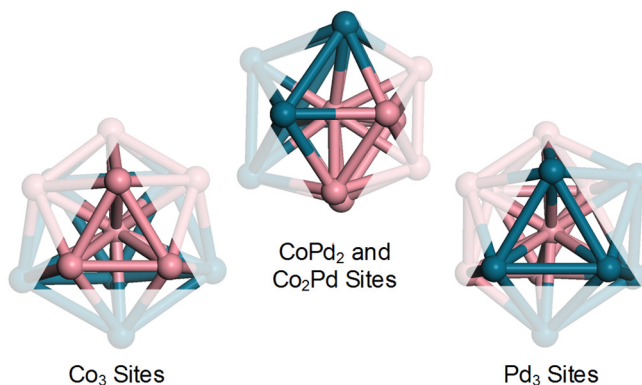


Figure 4. 1. Three-fold catalytic surface sites on the optimized Co_7Pd_6 catalyst: Co_3 , Pd_3 and mixed sites CoPd_2 and Co_2Pd sites. Cobalt and Palladium are represented in pink and blue, respectively.

Density Functional theory (DFT)

Geometries for the cluster, intermediate species, and gas phase molecules were built using Material Studio. DFT simulations of adsorption and surface reactions associated with the conversion of syngas to ethanol were carried out using Jaguar 7.0

(Schrodinger, Inc.). Jaguar is a quantum ab-initio simulation package, which employs density functional theory and an atomic orbital approach to evaluate the energetics of atomic and molecular systems. All electronic correlations were represented by the hybrid B3LYP functional, which is widely used for studying transition metal chemistry. Molecular orbitals were described using the LACVP basis sets. All calculations performed in this study were spin polarized, and an energy convergence of 10^{-5} Hartrees was employed for all total energy calculations. Vibrational frequencies were calculated, and these values were used to calculate the zero-point energy for each system. Finally, all reported total energies were zero point corrected.

The studied syngas to ethanol reaction mechanism included 24 intermediates and nine gas phase species (see Table 4.1). Atop, bridge and threefold catalyst sites were considered when finding the favorable binding site for each of these intermediate. The structures of all 24 intermediates on each of the Pd₃, Co₃ and CoPd sites of the catalyst were optimized.

Table 4. 1. List of intermediate species and gas phase reactants and products

Intermediates from the reaction mechanism									
1	CO*	6	CH*	11	CHCO*	16	CH ₂ COH*	21	OH*
2	H*	7	CH ₂ *	12	CH ₂ CO*	17	CH ₃ COH*	22	CHCH ₂ *
3	HCO*	8	CH ₃ *	13	CH ₃ CO*	18	CH ₂ CHOH*	23	CH ₂ CH ₂ *
4	CH ₂ O*	9	CHOH*	14	CHCHO*	19	CH ₃ CHOH*	24	CH ₃ CH ₂ *
5	CH ₃ O*	10	CH ₂ OH*	15	CH ₂ CHO*	20	O*		
gas phase species (Reactants and Products)									
1	CO(g)	3	CH ₄ (g)	5	CH ₃ CHO(g)	7	H ₂ O (g)	9	CH ₃ CH ₃ (g)
2	H ₂ (g)	4	CH ₃ OH (g)	6	CH ₃ CH ₂ OH (g)	8	CH ₂ CH ₂ (g)		

Adsorption, heat of reaction and activation energy

Jaguar 7.0 was used to calculate total energies of the stable intermediates on the catalyst surfaces. Adsorption energies of the intermediate species formed during reactions are calculated as,

$$E_{ads} = E_{adsorbate+cluster} - E_{cluster} - E_{ads(g)} \quad (1)$$

The climbing image nudged elastic band method (CI-NEB) was implemented to find the minimum energy path for all surface reactions. Eight images were used to connect the reactants and products of intermediate reactions. It is well known that B3LYP does not accurately predict absolute values for system energetics, but does routinely predict trends in energetics.^{22,23} Thus, from comparisons to experimental data, a scaling

factor of 0.7 was used to correct the DFT calculated adsorption energies on Co and Pd surface sites, whereas on CoPd sites, the energies were scaled by a factor of 0.53.

The number of reversible elementary reactions analyzed in this study was 46, considering the forward and reverse reactions separately and given the three distinct catalyst surfaces with this catalyst, total number of reactions is 276. To reduce the required computational time, Brønsted-Evans-Polanyi (BEP) relationships were developed for addition and dissociation reactions. BEP relations correlate the transition state energy of an elementary reaction step to the heat of reaction of that particular reaction.²⁴⁻²⁷ It is an efficient and computationally cost effective way to quantify reaction energetics for multi-reaction systems and allows one to calculate the activation energy of an elementary reaction, knowing only the adsorption energies of reactants and products along with their energies in the gas phase. Two linear relationships were developed, one for the association reactions, which leave an empty vacant site on the surface after reaction, and the other for dissociation type reactions, which consumes a vacant site for reaction (figure 4.2). BEP relationship is adopted from Ming's dissertation.²⁸

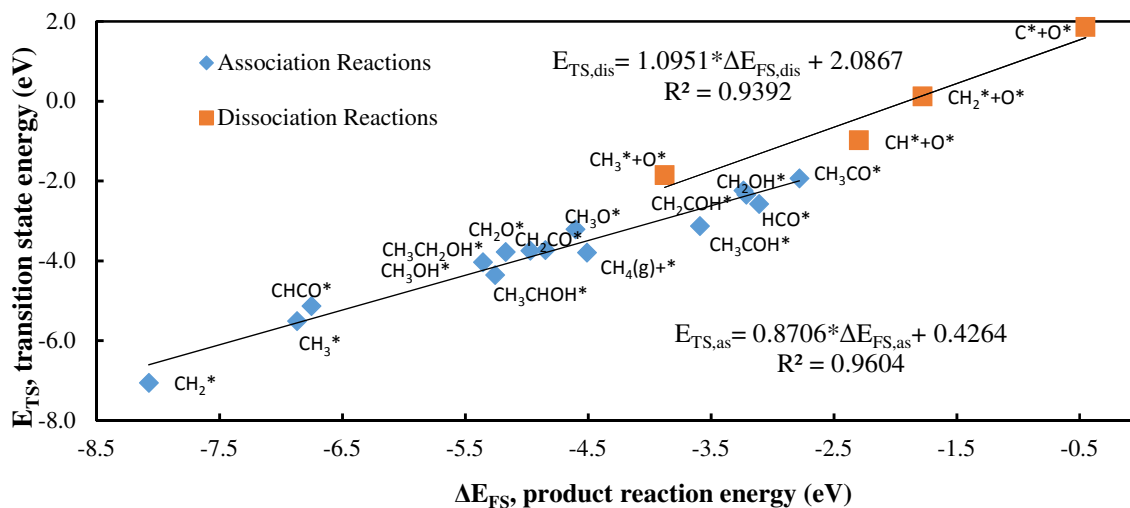


Figure 4. 2 BEP relationships for association and dissociation reactions obtained from DFT calculations on the Co₇Pd₆ catalyst ²⁸

- This graph is a TSS graph adopted from Ming’s dissertation.

The general formula for a BEP relationship is,

$$E_{TS} = \alpha \Delta E_{FS} + \beta \quad (2)$$

Where, E_{TS} is the transition energy and ΔE_{FS} is the final state enthalpy of the gas phase reactants combining with the vacant sites to form adsorbed products. Additional details of the BEP method are provided in the Appendix B.

Microkinetic Model

To quantitatively determine the conversion of reactants, the concentration of intermediates on the surface of the catalyst and selectivity towards products, a microkinetic model was developed. A batch reactor was modeled separately for each of the three catalyst sites: cobalt, palladium and CoPd sites on the catalyst. The reaction mechanism includes, adsorption and desorption of gas phase species, and elementary

reaction steps involving intermediate species on the surface. The detailed reaction mechanism is shown in Fig. 3, and includes reactions that are not necessarily important for all catalyst surfaces but do have some impact on the overall activity of at least one surface (e.g., carbon chain growth reactions). A system of 28 ordinary differential equations (ODE) were solved for time evolution of reactants (2), products (7) and intermediates (24). The microkinetic models included both forward and reverse reactions, which makes the total number of reactions to be 276. This system of ODEs was solved using Matlab R2016b software, and an inbuilt ODE solver (ODE15s) was implemented to quantify the time evolution of all gas phase and adsorbed species. Both absolute and relative tolerance were set to 10^{-8} , and the solution of ODEs was constrained to be non-negative. To check the accuracy of the solution, a material balance on the C, H and O species was performed at every time step.

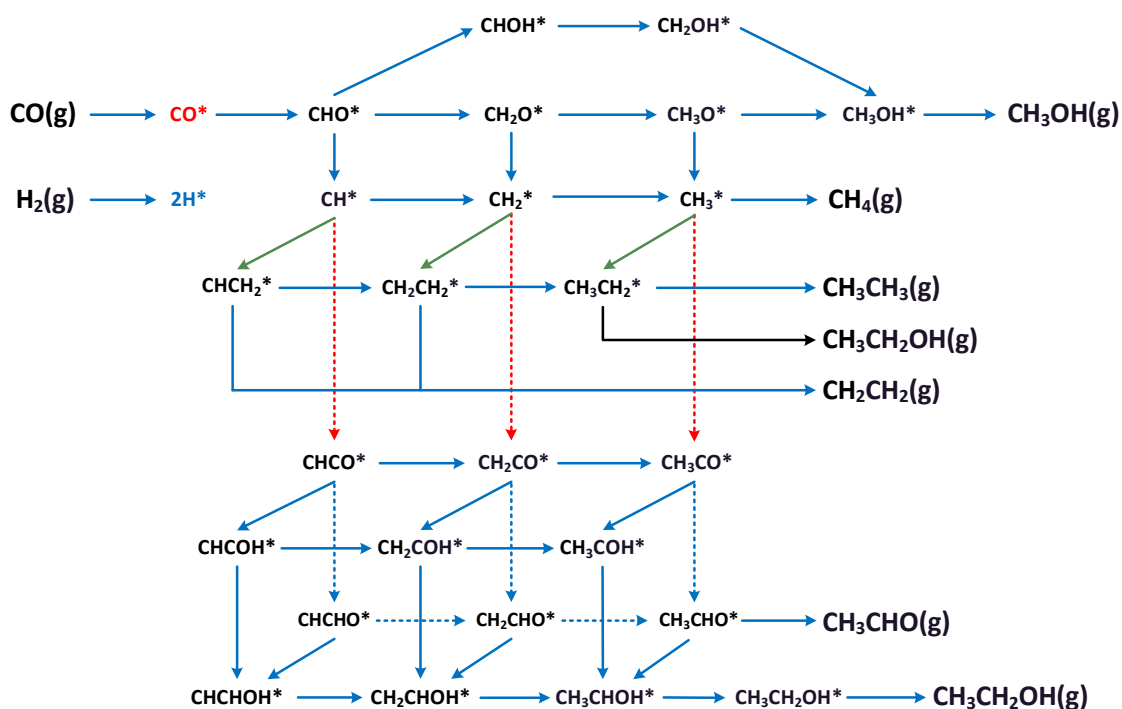


Figure 4. 3. Reaction mechanism for the conversion of syngas to ethanol and related products. Surface intermediates are represented by *. CO insertion reactions are shown with red arrows, hydroxylation reactions by black arrows, hydrogenation reactions by blue arrows, and Fischer-Tropsch type reactions by green arrows.

Adsorption and desorption processes

For adsorption and desorption reactions, the rate constants were determined using equilibrium rate constants and the collision theory of gases. The required equilibrium constants were determined using the entropy and enthalpy of reactions calculated using DFT simulations. Equilibrium constant is related to the Gibbs free energy by,

$$\ln K_{eq} = -\frac{\Delta G}{RT} \quad (3)$$

where, K_{eq} is the equilibrium constant, ΔG is the change in Gibbs free energy with reaction, R is the universal gas constant, and T is the temperature of the system.

The Gibbs free energy is related to enthalpy and entropy as follows,

$$\Delta G = \Delta H - T\Delta S \quad (4)$$

where, ΔH is the heat of reaction or enthalpy of reaction as determined from DFT simulations, and ΔS is the DFT derived entropy of the reaction. From equation 3 and 4 we can deduce equation 5.

$$\ln K_{eq} = -\frac{\Delta H - T\Delta S}{RT} \quad (5)$$

Heats of reaction are calculated as the difference of the enthalpy of the products minus the enthalpy of the reactants, and likewise for reactions entropy values.

Adsorption rate constants for gas phase species were determined using collision theory. In the work reported by Cortright and Dumesic,²⁹ it was shown that the rate constant for adsorption processes is,

$$r_{f,ads} = -\frac{w}{\sqrt{2\pi m_A k_B T}} \exp\left[\frac{-E_{f,ads}}{k_B T}\right] \sigma^0 (T, \theta) P_{A(g)} \quad (6)$$

Where, $r_{f,ads}$ is the rate of adsorption with units of coverage (molecules/active site) per time, m_A is the molecular weight of adsorbing species A, k_B is the Boltzmann constant, $E_{f,ads}$ is the activation energy for adsorption, w is the surface area per active site ($w= 1.57 \times 10^{-19} \text{ m}^2/\text{active site}$ for a nanocatalyst), $\sigma^0(T,\theta)$ is the sticking coefficient, which is measured as the probability that a collision of A with to the surface leads to adsorption , which is a function of temperature T and coverage θ , and. $P_{A(g)}$ is the partial pressure of the adsorbate A.

In this current work, adsorption processes are assumed to be barrier less, and thus, $E_{f, ads}$ are nearly zero and therefore neglected. At a given temperature, σ^0 is a function of coverage, and in this work, the sticking coefficient of CO is determined as a function of CO coverage. Sticking coefficients for other species were determined from experimental results reported previously.^{30,31} The rate of adsorption is therefore simplified as,

$$r_{f,ads} = -\frac{w}{\sqrt{2\pi m_A k_B T}} \sigma^0 (T, \theta) P_{A(g)} \quad (7)$$

Therefore, the adsorption rate constant is given by

$$k_{f,ads} = -\frac{w}{\sqrt{2\pi m_A k_B T}} \sigma^0 (T, \theta) \quad (8)$$

Desorption rate constants are determined as the ratio of adsorption rate constants (from equation 8) and equilibrium constants (from equation 5). Mathematically, desorption rate constants are given by,

$$k_{r,des} = \frac{k_{f,ads}}{K_{eq}} \quad (9)$$

Using equation 8 and 9, rate constants for the adsorption and desorption of reactants and products were determined.

Surface reactions

Rate constants for surface reactions involving intermediate species were determined using Arrhenius equations. Surface reaction rate constants for forward (k_f) and reverse (k_r) are determined as,

$$k_f = A \exp\left(\frac{-E_{a,f}}{RT}\right) \quad (10)$$

$$k_r = A \exp\left(\frac{-E_{a,r}}{RT}\right) \quad (11)$$

where, $E_{a,f}$ and $E_{a,r}$ are activation energies for forward and reverse reactions, respectively. A is the pre-exponential factor, which is calculated from the equation ($k_B T/h$), where h is Planck's constant. A constant value for A is used for all surface reactions in this model.^{32,33} R is ideal gas constant and T is the temperature.

Knowing the values for rate constants for both forward and reverse reactions the net rate of change in concentration of surface species with respect to time can be written as,

$$r_i = \frac{d\theta_i}{dt} = r_{\text{formation of species } i} - r_{\text{consumption of species } i} \quad (12)$$

Change in concentration of all 24 intermediate species is represented using equation 12.

The fraction of vacant sites is determined as,

$$\theta_o = 1 - \sum_i \theta_i \quad (13)$$

where, θ_o is the fraction of sites vacant during the reaction, and θ_i is the fraction of sites occupied by intermediate species i .

Reactor design

Though commercial production of ethanol from syngas would likely be carried out in a continuous flow reactor with solid catalysts, for simplicity, simulations examining catalyst performance over time were modeled in a batch reactor. For heterogeneous reactions the design expression for a batch reactor is given by,

$$\frac{dC_{A(g)}}{dt} = r_{A(g)} \quad (14)$$

Where, $r_{A(g)}$ is the rate of production of species A (mol A/g-cat), $C_{A(g)}$ is the concentration of A (mol A/m³), and t is time (sec).

The rate expression can also be represented in terms of the number of moles of species A $n_{A(g)}$ as,

$$\frac{dn_{A(g)}}{dt} = r_{A(g)} \left(\frac{s m_{cat}}{N_A \omega} \right) \quad (15)$$

where, s is the surface area per weight of catalyst (m^2/g), m_{cat} is the mass of catalyst in the reactor, N_A is the Avogadro's number, and ω is the approximate surface area per active site. Similar design equations were developed for each of the reactants and products.

A set of nine ODE's of the form of Eq. (14) for gas phase species and a set of twenty-four ODE's of the form Eq. (15) for intermediate species along with Eq. (13) are solved simultaneously to determine the rate of change in concentration of surface species and rate of formation or consumption of products and reactants respectively.

Results and discussion

In this study, 46 elementary reversible steps were investigated using DFT. Adsorption energies and preferred adsorption site for reactants and key intermediates are listed in Table 4.2. One of the essential and often disputed first steps in syngas conversion is CO adsorption. From DFT simulations, it was found that the adsorption energy of CO is relatively high (-1.82 eV) on the palladium surface, whereas it was lower on cobalt (-1.49 eV) and CoPd (-1.03 eV) surfaces. On the palladium surface CO prefers to adsorb on bridge sites, but on cobalt and cobalt-palladium surfaces it prefers to adsorb

on atop sites. Other intermediates, including H, HCO, CH₂O, CH₃O, O, CH, OH, CHOH, and CH₂OH, preferentially adsorb on hexagonally close packed (HCP) sites on all cluster surfaces (e.g., Co₃, Pd₃, CoPd₂, Co₂Pd). Additionally, CH₃CO was found to adsorb on bridge sites (Co₂, Pd₂, CoPd) and methyl (CH₃) species preferred to adsorb on atop sites, each forming a single bond with the underlying metal. In general, calculated adsorption energy data agrees reasonably with literature values.^{17,34,35}

Table 4. 2. Adsorption energies and preferred adsorption site of key intermediates on cobalt, CoPd and palladium surfaces

S.No.	Intermediate	Adsorption energy (eV)			Adsorption site
		Co	CoPd	Pd	
1	CO	-1.49	-1.03	-1.82	
2	H	-2.63	-2.82	-2.81	HCP
3	HCO	-1.87	-1.81	-1.64	HCP
4	CH ₂ O	-1.23	-0.91	-0.24	HCP
5	CH ₃ O	-3.45	-2.85	-1.85	HCP
6	O	-5.72	-4.61	-4.51	HCP
7	CH	-4.89	-4.41	-4.12	HCP
8	CH ₃	-2.10	-1.81	-1.76	Atop
9	CH ₃ CO	-2.03	-2.16	-1.65	Bridge
10	OH	-4.22	-3.53	-2.80	HCP
11	CHOH	-2.65	-2.50	-2.15	HCP
12	CH ₂ OH	-1.97	-2.01	-1.84	HCP

Activation energies

DFT derived transition state energies were calculated for select reactions using climbing image nudged elastic band theory (CI-NEB),^{36,37} which was implemented using an external program that interfaces with Jaguar. With this method, a series of eight intermediate surface structures between those of the reactants and products were used to identify the minimum energy path for the reaction. The initial transition states (TS) identified using CI-NEB were then further refined using the quadratic synchronous transit (QST) method implemented in Jaguar. Further, we ensured each local minimum had zero imaginary frequencies, and each transition state structure had exactly one imaginary frequency.

In this study, we have a complex reaction network with 46 reversible elementary reactions on three surfaces. It is computationally expensive to calculate the activation energies of all the reactions using DFT based CI-NEB calculations. To lessen this computational burden, linear BEP relationships were developed, one for association type reactions and another for dissociation reactions. A linearized regression of DFT derived transition states resulted in the BEP relationships shown earlier in Fig. 2. For the Co₇Pd₆ cluster, the linear BEP relationship for association reactions is

$$E_{TS,ass} = 0.8706\Delta E_{FS,ass} + 0.4364, R^2=0.96 \quad (16)$$

and for dissociation type of reactions, BEP relationship is

$$E_{TS,dis} = 1.0951\Delta E_{FS,ass} + 2.0867, R^2=0.94 \quad (17)$$

$E_{TS,ass}$ and $\Delta E_{FS,ass}$ are the transition state energy and final state energy of association type of reactions, respectively. Similarly, $E_{TS,dis}$ and $\Delta E_{FS,dis}$ are the transition state energy and final state energy of dissociation reactions, respectively. Further, activation energies calculated from DFT and BEP methods on Pd and Co surface are compared to literature values in Tables 4.3 and 4.4.

Table 4. 3. Activation energies on palladium surface compared to literature values³⁸⁻⁴⁰

S.NO	Reactions on Pd	Activation Energy (eV)			
		This work	Ref. 38	Ref. 39	Ref. 40
1	$\text{CO}^* + \text{H}^* \rightarrow \text{HCO}^* + ^*$	2.31	1.62		
2	$\text{HCO}^* + \text{H}^* \rightarrow \text{CH}_2\text{O}^* + ^*$	2.01	0.99	0.91	1.36
3	$\text{HCO}^* + ^* \rightarrow \text{CH}^* + \text{O}^*$	3.98	2.43	1.28	0.82
4	$\text{CH}_2\text{O}^* + ^* \rightarrow \text{CH}_2^* + \text{O}^*$	1.99	1.76		0.41
5	$\text{CH}_2\text{O}^* + \text{H}^* \rightarrow \text{CH}_3\text{O}^* + ^*$	0.66		1	
6	$\text{CH}^* + \text{H}^* \rightarrow \text{CH}_2^* + ^*$	0.53	0.83		
7	$\text{CH}_2^* + \text{H}^* \rightarrow \text{CH}_3^* + ^*$	0.99	0.57		
8	$\text{CH}_2\text{O}^* + \text{H}^* \rightarrow \text{CH}_2\text{OH}^* + ^*$	1.63		0.74	
9	$\text{HCO}^* + \text{H}^* \rightarrow \text{CHOH}^* + ^*$	2.41	1.27	0.8	
10	$\text{CHOH}^* + \text{H}^* \rightarrow \text{CH}_2\text{OH}^* + ^*$	0.62	1.23	0.99	
11	$\text{CH}_2\text{COH}^* + \text{H}^* \rightarrow \text{CH}_2\text{CHOH}^*$	0.94			
12	$\text{CH}_2\text{CHOH}^* + \text{H}^* \rightarrow \text{CH}_3\text{CHOH}^*$	1.38			
13	$\text{CH}_3\text{COH}^* + \text{H}^* \rightarrow \text{CH}_3\text{CHOH}^*$	0.75			

Although the activation energies predicted in this work for reactions on the Pd surface are significantly higher than those reported in the literature (see Table 4.3), the

relative energies from our data closely agree with the trends reported in the literature (i.e., heats of reaction are similar and comparisons of reaction rates follow similar trends). For reactions 1 and 2, it can be noted that the activation energy for the successive hydrogenation of CO is decreased as reported by Jorgensen et al.³⁸ When we look at reactions 3 and 4, the activation energy for CH₂O* dissociation is more favorable than dissociation of HCO*, and a similar pattern is observed with literature values from Jorgensen et al.³⁸ and Ye et al.⁴⁰. Hydrogenation of HCO to CHOH is unfavorable, but the successive hydrogenation of CHOH is favorable. Ye et al.⁴⁰ reported a similar behavior.

Table 4. 4. Activation energies on cobalt surface compared to literature values⁴¹⁻⁴⁵

S.NO	Reaction	Co	Ref. 41	Ref. 42	Ref. 43	Ref. 44	Ref. 45
1	$\text{CO}^* + \text{H}^* \rightarrow \text{HCO}^* + ^*$	1.85	1.59	1.31	1.18		1.09
2	$\text{HCO}^* + \text{H}^* \rightarrow \text{CH}_2\text{O}^* + ^*$	0.92	0.31	0.55			0.72
3	$\text{CH}_2\text{O}^* + \text{H}^* \rightarrow \text{CH}_3\text{O}^* + ^*$	0.66	0.50	0.86			0.89
4	$\text{HCO}^* + ^* \rightarrow \text{CH}^* + \text{O}^*$	1.20					
5	$\text{CH}_2\text{O}^* + ^* \rightarrow \text{CH}_2^* + \text{O}^*$	1.35	0.27				
6	$\text{CH}_3\text{O}^* + ^* \rightarrow \text{CH}_3^* + \text{O}^*$	1.66	1.32				0.62
7	$\text{CH}^* + \text{H}^* \rightarrow \text{CH}_2^* + ^*$	0.44	0.54	0.66	0.55	0.66	
8	$\text{CH}_2^* + \text{H}^* \rightarrow \text{CH}_3^* + ^*$	0.77	0.44	0.63	0.55	0.6	0.61
9	$\text{CH}_3^* + \text{H}^* \rightarrow \text{CH}_4(\text{g}) + 2^*$	1.24		1.09	0.99	0.96	1.28
10	$\text{CH}^* + \text{CO}^* \rightarrow \text{CHCO}^* + ^*$	1.25	0.83				
11	$\text{CH}_2^* + \text{CO}^* \rightarrow \text{CH}_2\text{CO}^* + ^*$	1.36	0.58				
12	$\text{CH}_3^* + \text{CO}^* \rightarrow \text{CH}_3\text{CO}^* + ^*$	1.71	1.13				0.86
13	$\text{CHCHO}^* + \text{H}^* \rightarrow \text{CH}_2\text{CHO}^* + ^*$	1.27	0.52				
14	$\text{CH}_2\text{OH}^* + \text{H}^* \rightarrow \text{CH}_3\text{OH}(\text{g}) + 2^*$	1.51		1.45			1.38
15	$\text{CH}_3\text{CO}^* + \text{H}^* \rightarrow \text{CH}_3\text{COH}^* + ^*$	1.54					0.86
16	$\text{CH}_3\text{COH}^* + \text{H}^* \rightarrow \text{CH}_3\text{CHOH}^* + ^*$	1.51		1.27			0.62
17	$\text{CH}_3\text{COH}^* + \text{H}^* \rightarrow \text{CH}_3\text{CH}_2\text{OH}(\text{g}) + ^*$	0.44					0.28
18	$\text{CH}^* + \text{CH}_2^* \rightarrow \text{CHCH}_2^* + ^*$	1.04		1.34	0.76		
19	$\text{CHCH}_2^* + \text{H}^* \rightarrow \text{CH}_2\text{CH}_2^* + ^*$	0.55					
20	$\text{H}_2^* + \text{CH}_2^* \rightarrow \text{CH}_2\text{CH}_2(\text{g}) + 2^*$	0.91		0.27	0.7		
21	$\text{CH}_3^* + \text{CH}_2^* \rightarrow \text{CH}_3\text{CH}_2^* + ^*$	1.49		0.76	1.11		
22	$\text{HCO}^* + \text{H}^* \rightarrow \text{CHOH}^* + ^*$	1.75		1.23			

Activation energies on the cobalt sites are higher from this study when compared to literature values (see Table 4.4). From our simulations it was observed that the dissociation of CH_xO^* species becomes unfavorable as x , number of hydrogen atoms increases, and Zhang et al.⁴¹ also observed a similar trend. Prior results by others Zhang et al.⁴¹, Cheng et al.⁴² and Zuo et al.⁴⁵ have shown that CO^* hydrogenation to HCO^* as well as HCO^* hydrogenation to CH_2O^* are favorable, but the activation energy for CH_2O^* hydrogenation to CH_3O^* is higher than either of the earlier hydrogenation steps. In contrast, our DFT results indicate a reduction in the activation energy for CH_2O hydrogenation reaction as compared to the activation energies for CO^* and HCO^* hydrogenation reactions.

Our DFT results for Co sites indicate that CH^* hydrogenations become more energy intensive with increase in the alkyl group saturation; specifically, the activation energy increases from 0.44 to 0.77 for CH^* hydrogenation and CH_2^* hydrogenation, respectively. A comparison of results from this study and those reported earlier Cheng et al.⁴², Liu et al.⁴³, and Gong et al.⁴⁴ indicate that activation energy for CH_3^* hydrogenation to form and desorb methane is high.

Together with the calculated adsorption energies and BEP relationships for adsorption and desorption reactions, heats of reaction and activation energies were calculated for each of the elementary reactions not explicitly examined by more rigorous ab initio methods.

Activation energies for forward and reverse reactions on Co, CoPd and Pd surfaces are presented in appendix B (Table B2, B3 and B4) respectively. Following key observations can be made from activation energies and equilibrium constants on Co, CoPd and Pd surfaces.

1. CO hydrogenation to form CH_xO species:

Successive CO hydrogenations to form HCO^* , CH_2O^* and CH_3O^* are more favorable as the degree of hydrocarbon saturation increases (see Table 4.5). A similar trend is observed on all three metal surfaces. In general, activation energies for surface reactions are higher on the Pd surface as compared to the Co and CoPd surfaces. The activation energies for the first two hydrogenation steps is similar on Co and CoPd sites, but further hydrogenation of CH_2O^* is more favorable on the CoPd surface. Similar trends can be observed with the reaction equilibrium constants. As the degree of carbon saturation increases, equilibrium favors the forward reaction, indicating that CH_3O^* is more stable than HCO^* and CH_2O^* . Equilibrium constants are relatively high for hydrogenation reactions on cobalt sites indicating that hydrogenation reactions are more favorable on cobalt sites. Whereas, the equilibrium constants for hydrogenation reactions are low on the other two surfaces making those reactions less favorable.

Table 4. 5. Activation energies and equilibrium constants of CO hydrogenation reactions

Reactions	Activation Energy(eV)			Equilibrium constants		
	Co	CoPd	Pd	Co	CoPd	Pd
$\text{CO}^* + \text{H}^* \leftrightarrow \text{HCO}^* + *$	1.3	1.31	1.62	1.39E-07	2.81E-09	1.31E-10
$\text{HCO}^* + \text{H}^* \leftrightarrow \text{CH}_2\text{O}^* + *$	0.64	0.60	1.41	1.02E+01	2.75E-01	6.41E-08
$\text{CH}_2\text{O}^* + \text{H}^* \leftrightarrow \text{CH}_3\text{O}^* + *$	0.46	0.37	0.60	8.08E+04	4.79E+01	5.38E-01

2. CH_xO^* dissociation to form CH_x^* species:

Dissociation of CH_xO^* species to CH_x^* and O^* species becomes more energy intensive as the degree of saturation of the alkyl group (i.e., the hydrogen content) in the CH_xO^* surface intermediate increases. Equilibrium constants for dissociation reactions are very low on CoPd surface. The existence of high activation energies and low equilibrium constants on CoPd surface makes dissociation reactions less favorable on this surface (see Table 4.6). Additionally, the equilibrium constant for HCO hydrogenation is extremely small for the the Pd surface, making this reaction highly unfavorable. However, CH_2O^* dissociation is favorable on the Pd surface. Finally, it is observed that the reaction activation energy increases for successive dissociations of CH_xO^* species on the Co surface, but high equilibrium constants for these reactions suggest that the reactions are still favorable on Co sites.

Table 4. 6. Activation energies and equilibrium constants of CH_xO dissociation reactions

Reactions	Activation Energy(eV)			Equilibrium constants		
	Co	CoPd	Pd	Co	CoPd	Pd
$\text{HCO}^* + \text{H}^* \leftrightarrow \text{CH}^* + \text{O}^*$	0.84	1.74	2.79	6.41E+00	3.38E-09	1.24E-13
$\text{CH}_2\text{O}^* + \text{H}^* \leftrightarrow \text{CH}_2^* + \text{O}^*$	0.95	1.22	1.39	4.98E+03	1.31E-02	2.96E+00
$\text{CH}_3\text{O}^* + \text{H}^* \leftrightarrow \text{CH}_3^* + \text{O}^*$	1.16	1.22	1.03	2.63E+02	5.12E-03	4.89E+02

3. CH hydrogenation to form CH_x species:

The reaction equilibrium constants for three hydrogenation reactions (see Table 4.7 below) are high on Co, Pd and CoPd surfaces indicating that the concentration of these intermediates on the catalyst surface are relatively low. Also, from an examination of the activation energies on all reaction surfaces, the activation energies for the successive hydrogenation of CH* species to CH₂* and CH₃* reduces as the hydrocarbon intermediate becomes more saturated.

Table 4. 7. Activation energies and equilibrium constants of CO hydrogenation reactions

Reactions	Activation Energy(eV)			Equilibrium constants		
	Co	CoPd	Pd	Co	CoPd	Pd
$\text{CH}^* + \text{H}^* \leftrightarrow \text{CH}_2^* + \text{H}^*$	0.31	0.33	0.37	7.93E+03	3.01E+04	1.31E+06
$\text{CH}_2^* + \text{H}^* \leftrightarrow \text{CH}_3^* + \text{H}^*$	0.54	0.52	0.69	4.98E+03	2.55E+00	8.90E+01
$\text{CH}_3^* + \text{H}^* \leftrightarrow \text{CH}_4(\text{g}) + 2\text{H}^*$	0.87	0.58	0.76	4.88E+03	6.73E+05	1.01E+04

CO adsorption and sticking coefficient

A preliminary microkinetic model was developed. In this model sticking coefficients were considered constant and obtained from literature.^{30,46-49} From preliminary microkinetic modeling results, it was observed that carbon monoxide adsorbed rapidly to cobalt, palladium, and cobalt-palladium surface sites. As a result of CO adsorption, the majority of the catalyst surface sites became effectively unavailable for other reactions; thus, the production of hydrogenated CO products was negligible. Experimentally, others have observed that the energetics for CO adsorption on metal surfaces becomes less favorable with higher CO surface coverage, until eventually reaching a maximum coverage of CO that is below full monolayer coverage. The experimental relationship between, CO adsorption, coverage, and the corresponding sticking coefficient on palladium and cobalt surfaces has been well discussed in the literature.^{30,31} As our initial adsorption model over predicted CO coverage on all catalyst surfaces, the adsorption behavior for CO in the final microkinetic model included an experimentally based model for CO coverage and the associated sticking coefficient, overcoming this complication. Similar experimentally based CO adsorption models were developed for cobalt and palladium surfaces; whereas, adsorption of CO on CoPd surfaces was modeled using a simple average of the values calculated for CO adsorption on the Co and Pd surface because there is currently no experimental data available for this system. Figures 4.4, 4.5 and 4.6 show how the sticking coefficient for CO adsorption on cobalt, palladium and cobalt-palladium sites, respectively, vary as a function of CO coverage.

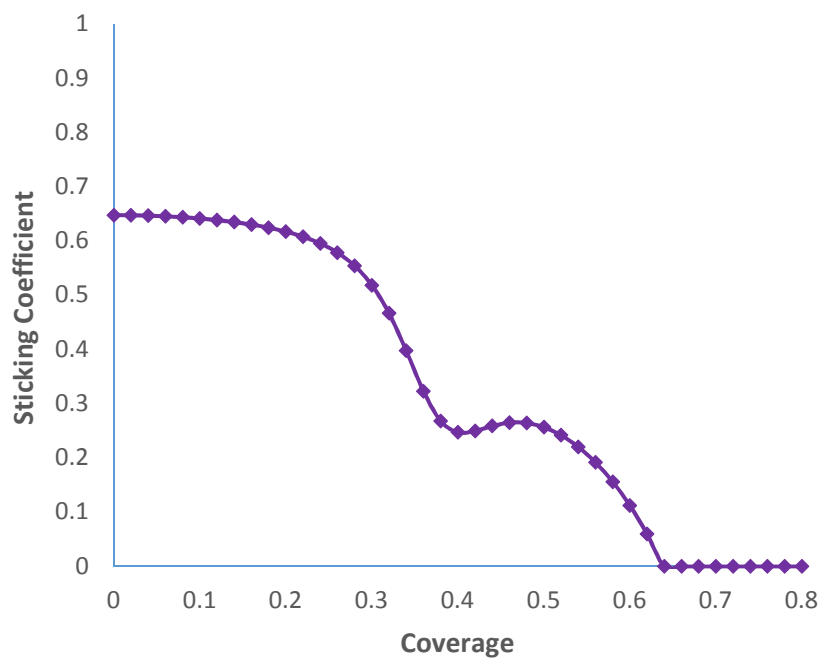


Figure 4. 4. Sticking coefficient as a function of coverage on cobalt surface

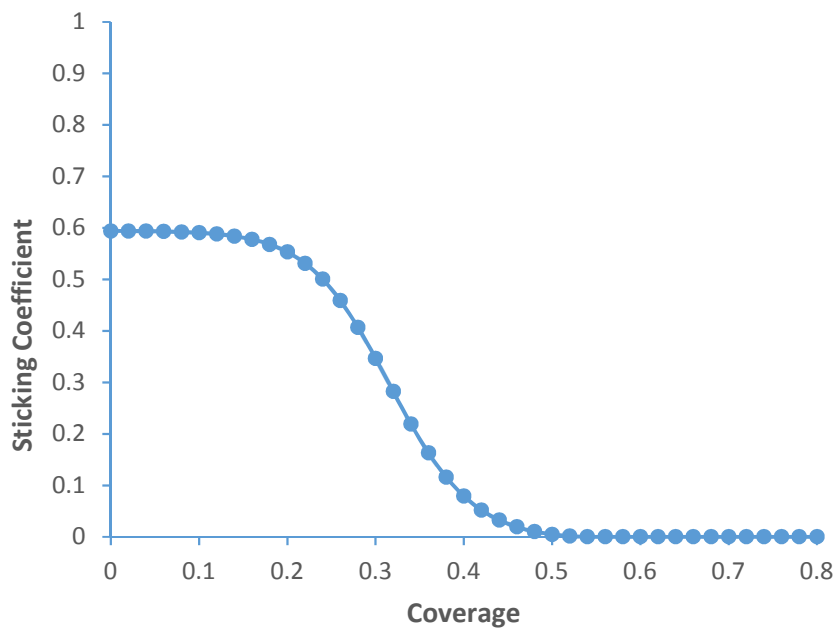


Figure 4. 5. Sticking coefficient as a function of coverage on palladium surface

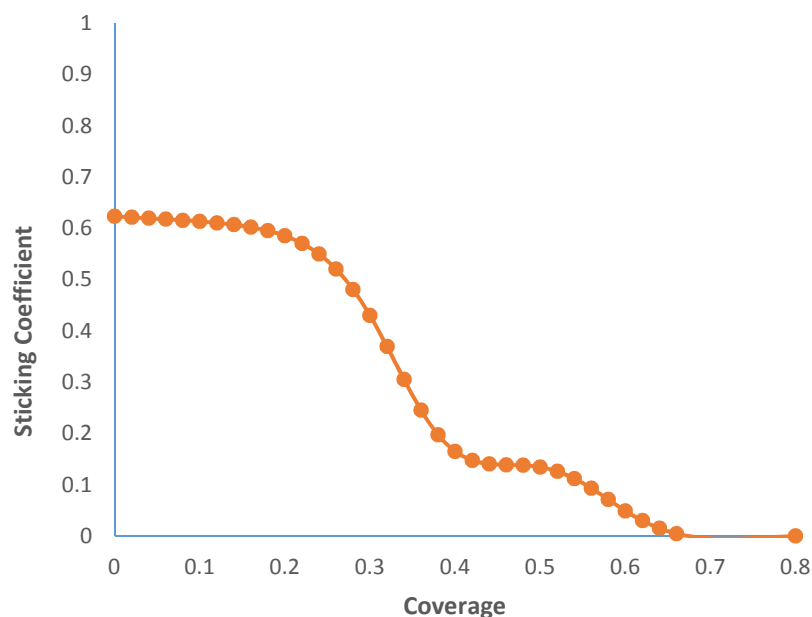


Figure 4. 6. Sticking coefficient as a function of coverage on cobalt-palladium surface reaction mechanism

There are two types of reaction mechanisms that have been proposed for syngas to ethanol formation, one in which CO dissociates to elemental carbon directly, followed by hydrogenation to form CH_x^* species and a second where adsorbed CO is hydrogenated to form HCO^* species, which subsequently undergo dissociation to form CH_x^* species. From our studies, we have seen that on both Co and Pd surfaces it is energetically more favorable to directly hydrogenate adsorbed CO as compared to the pathway involving dissociative CO adsorption. In this study, the primary pathway for the formation of CH_x^* species involves CO^* undergoing hydrogenation to form HCO^* , which upon further hydrogenation is converted to CH_2O^* and CH_3O^* species. These hydrogenated species then dissociate to form CH_x^* and O^* species. The reaction barriers for the necessary

hydrogenation and dissociation steps are low and feasible on all three metal surfaces; however, the activation barriers are lower on the cobalt surface as compared to the other two surfaces, indicating that the reactions happen faster on this surface.

Methane and Methanol

Most experimental efforts to produce ethanol from syngas have been plagued by side reactions that form methane and/or methanol. Thus, the microkinetic model developed herein also includes all reactions necessary to form these common byproducts. For example, the CH_x^* species formed by the dissociation of CH_xO^* species can be further hydrogenated to form methane. Production of methanol is somewhat more complicated as there are two accepted pathways for methanol formation,

1. CH_2O^* undergoes hydrogenation to form CH_2OH^* , which further forms CH_3OH .
2. Direct hydrogenation of CH_3O^* to CH_3OH

From our DFT and microkinetic model calculations it can be seen that majority of the methanol forms on palladium sites via direct hydrogenation of CH_3O^* . Figures 4.7, 4.8 and 4.9 show the reactions essential for methane and methanol formation pathways on palladium, cobalt and cobalt-palladium interfaces, respectively. From Figures 4.7, 4.8 and 4.9, we can deduce that on the palladium surface, hydrogenation of HCO^* to CH_2O^* and CH_3O^* species is favorable, but the dissociation of CH_xO^* species to CH_x^* species is unfavorable, suggesting that carbon chain growth reactions are unlikely to occur on palladium. The CH_2O^* and CH_3O^* species then follow both methanol formation pathways

to make methanol. In contrast, adsorbed CH_3O^* species readily dissociate to CH_3^* species on cobalt surfaces, and upon further hydrogenation the CH_3^* species are hydrogenated to form methane, which is then easily desorbed from the cobalt surface. At the CoPd interface, both HCO^* dissociation and CO insertion reactions are favored, combining the chemistry of palladium and cobalt metals. The calculated surface concentrations of CH_2^* and CH_3^* species are high on the CoPd surface, suggesting that the greater activity of the cobalt atoms plays a more dominate role on this mixed metal surface.

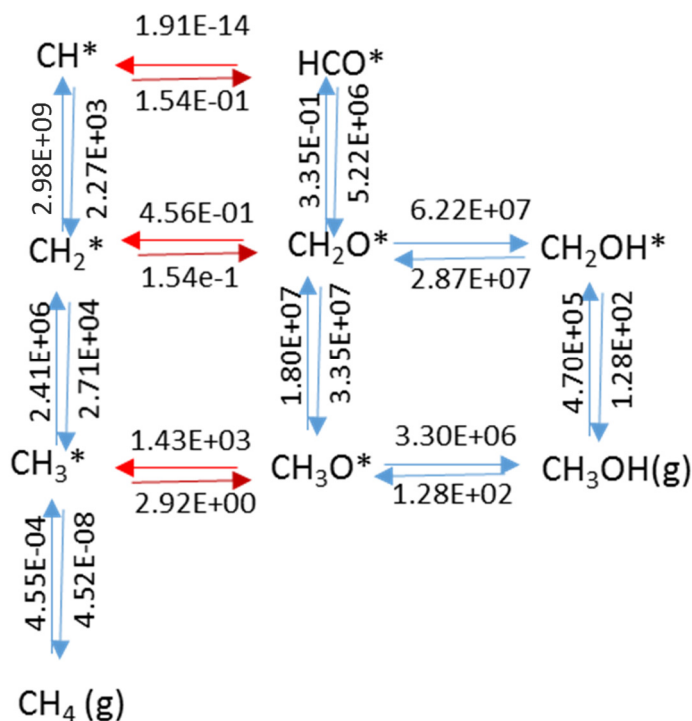


Figure 4. 7. Rate constants for important reactions for methane and methanol formation on palladium surface. CH_2O^* and CH_3O^* formation is favored compared to CH_x formation. CH_2O^* and CH_3O^* then undergo hydrogenation to form methanol.

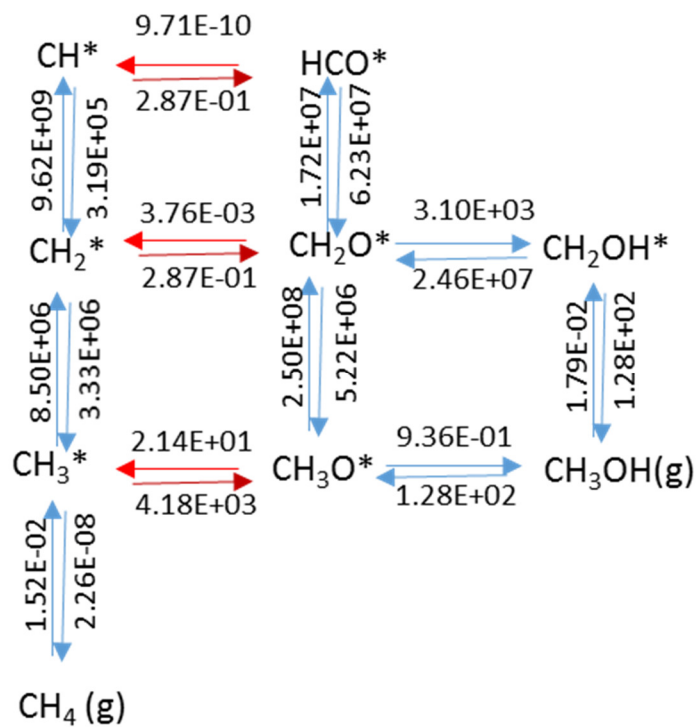


Figure 4. 8. Rate constants for important reactions for methane and methanol formation on Cobalt surface. CH_x^* formation is favored, concentration of CH_x^* is higher and favored product is methane.

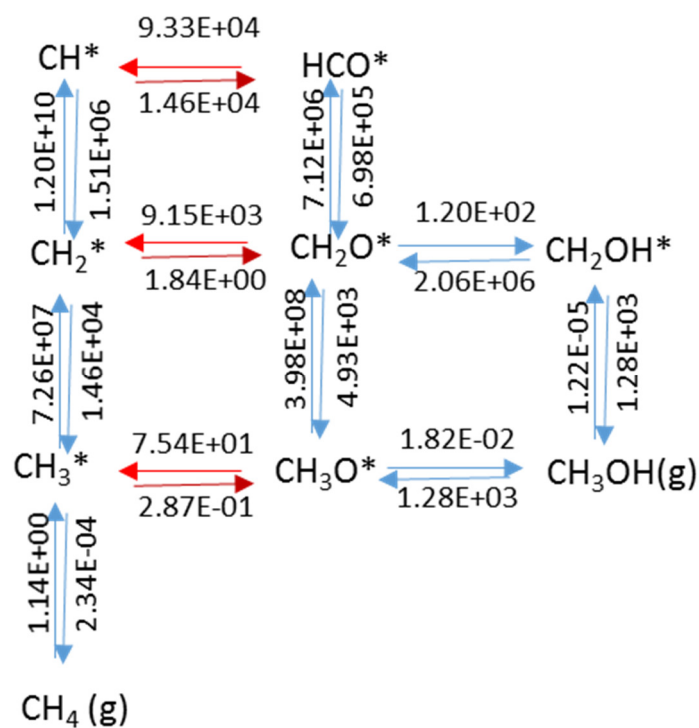


Figure 4. 9. Rate constants for important reactions for methane and methanol formation on cobalt-palladium surface. Both CH_xO^* formation CH_x^* and is favored, concentration of CH_x^* is higher.

Ethanol

In this study, there are three reaction pathways considered for ethanol formation:

1. CO insertion mechanism: adsorbed CO is inserted into CH_x^* species to form CH_xCO^* species, which are then hydrogenated to form CH_3CHOH^* species and upon further hydrogenation ethanol;
2. Hydroxycarbene mechanism: a methylene surface intermediate (CH_2^*) is inserted in CH_2O^* and upon rearrangement forms CH_3COH^* , which following successive hydrogenation reactions forms CH_3CHOH^* and later ethanol;

3. Hydroxylation mechanism: hydroxylation of adsorbed CH_3CH_2^* species leads directly to the formation of adsorbed ethanol.

Most of the ethanol formed on the CoPd cluster is generated on the combined cobalt-palladium surface. Rate constants for reactions leading to the formation of ethanol from all three pathways are shown in figure 4.10. Examination of these rate constants indicates that although ethanol formation is feasible via the CO insertion, hydroxycarbene, and hydroxylation pathways, only the CO insertion and hydroxycarbene pathways contribute appreciably to ethanol formation (i.e., direct hydroxylation of adsorbed alkyl intermediates is not favored). Further, ethanol synthesis via the CO insertion mechanism is the most favored as a result of the high surface concentration of adsorbed CO.

Another possible product formed by subsequent hydrogenation of CH_xCO^* species is acetaldehyde. Acetaldehyde can form from two possible pathways, hydrogenation of CH_3CO^* or CH_2CHO^* species. Simulation results from this study indicate that this is not a favored reaction product, which agrees with experimental results that did not indicate the formation of any acetaldehyde during syngas hydrogenation reactions using CoPd catalysts⁵⁰.

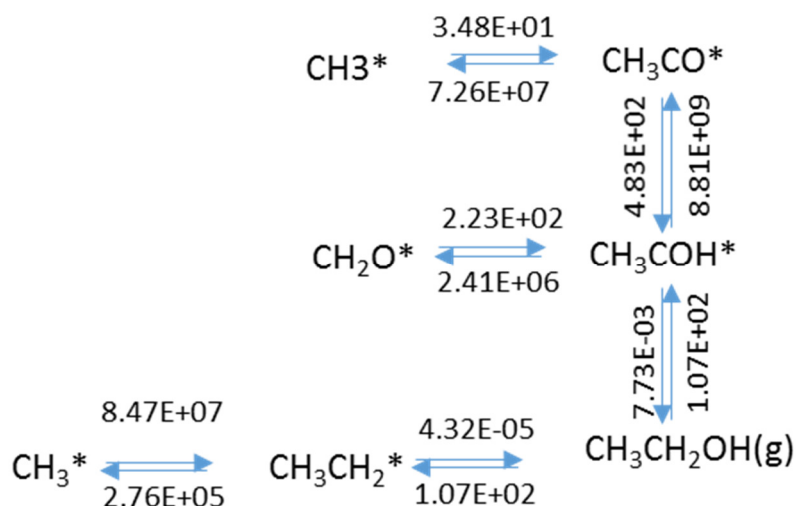


Figure 4. 10. Rate constants for reversible reactions leading to ethanol formation at CoPd interface.

Fischer-Tropsch products

It is well established that syngas can be converted to higher hydrocarbons and liquid fuels by Fischer-Tropsch synthesis (FTS) reactions^{42,51,52}. For completeness, the syngas to ethanol reaction mechanism considered in this study also includes Fischer-Tropsch reactions (see reactions 38 to 45). This is a unique aspect of this work as other syngas to ethanol studies did not examine the impact of carbon chain growth reactions on the overall product selectivity. However, for computational efficiency reasons we have limited our study to only the formation of C₂ hydrocarbons. Thus, our data showing the formation of ethane should be interpreted to mean ethane or higher molecular weight FT type hydrocarbons. Again, the focus of this study was on ethanol production but the intention to include FTS reactions is to show that there is a possibility that CH_x^{*} species convert to higher hydrocarbons rather than forming just methane. Additionally, the

inclusion of higher molecular weight hydrocarbon intermediates allowed us to investigate the direct hydroxylation pathway for ethanol synthesis.

For the Fischer-Tropsch mechanism, CH_x^* species formed on the metal surfaces can undergo further CH_2^* insertion reactions to form ethylene and upon hydrogenation, ethane is formed. From the microkinetic model results it has been observed that FTS reactions are not favorable on palladium due to low concentrations of CH_x^* species on the surface. On this surface, CH_x^* species are immediately converted to intermediates leading to methanol formation. Whereas, activation barriers for FTS reactions are very low on Co surfaces when compared to the other two palladium containing surfaces indicating that FTS reactions are favored on the Co surface. Further, the major products desorbing from the Co surface are methane and ethane, which is in good agreement with numerous experimental results showing that cobalt is an excellent FT catalyst^{13,42,51,53}.

Microkinetic model for separate reaction sites

To understand the chemistry on each of the three different catalytic surfaces on the cluster, a separate microkinetic model was developed for each of these surfaces. Although the preferred product is ethanol, other products methane, ethane, ethylene, methanol, acetaldehyde, and, water were considered in the model. Along with the gas phase products and reactants, 24 unique surface intermediates were also considered. The number of reversible reactions considered was 46, which means 92 reactions were examined on each of the metal surfaces, making a total of 276 reactions. Formation of

C₂+ hydrocarbons and oxygenates is neglected in this model for computational efficiency reasons. A batch reactor is modeled, and the time evolution of products is obtained. Reaction conditions are maintained closely to experimental conditions, the ratio of CO to H₂ is maintained at 2, the temperature is held constant at 523 K, and differential equations for the concentration of intermediates on each site are considered along with the differential equations for change for the number of moles of products with time. The model included a total of 33 ordinary differential equations (ODEs): nine ODE's of the type represented by equation 14 (for 2 reactants and 7 products) and 24 ODE's of the type represented by equation 15 (for 24 intermediates). The Matlab ODE solver ODE15s was used to solve the 33 ODE's simultaneously to yield data for the time evolution of products and the rate of change in concentration of reactants. We constrained the solution to be non-negative. A material balance on all elements, including carbon, hydrogen and oxygen, was performed to check the accuracy of the microkinetic model.

Product distribution

The time evolution of products on pure palladium, cobalt and cobalt-palladium sites are shown in Figures 4.11, 4.12 and 4.13, respectively. It can be seen that Pd₃ sites produces methanol as the primary product, Co₃ sites produce methane and ethane confirming FTS reactions on the cobalt surface, and on the CoPd surface, the major product is ethanol. It is interesting to note that the ethanol concentration is negligible on pure palladium and cobalt sites but it is the major product on the CoPd mixed sites.

Selectivities of major products methane, ethane, methanol, acetaldehyde and ethanol are compared to experimental values in Table 4.8.

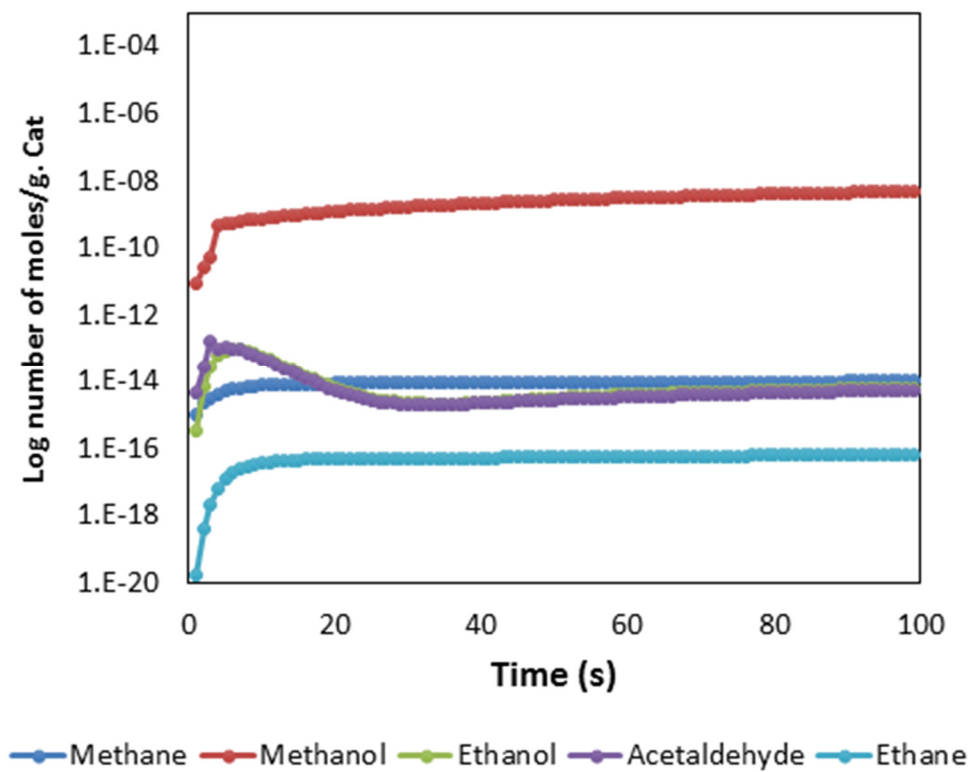


Figure 4. 11. Time evolution of products on palladium rich surfaces

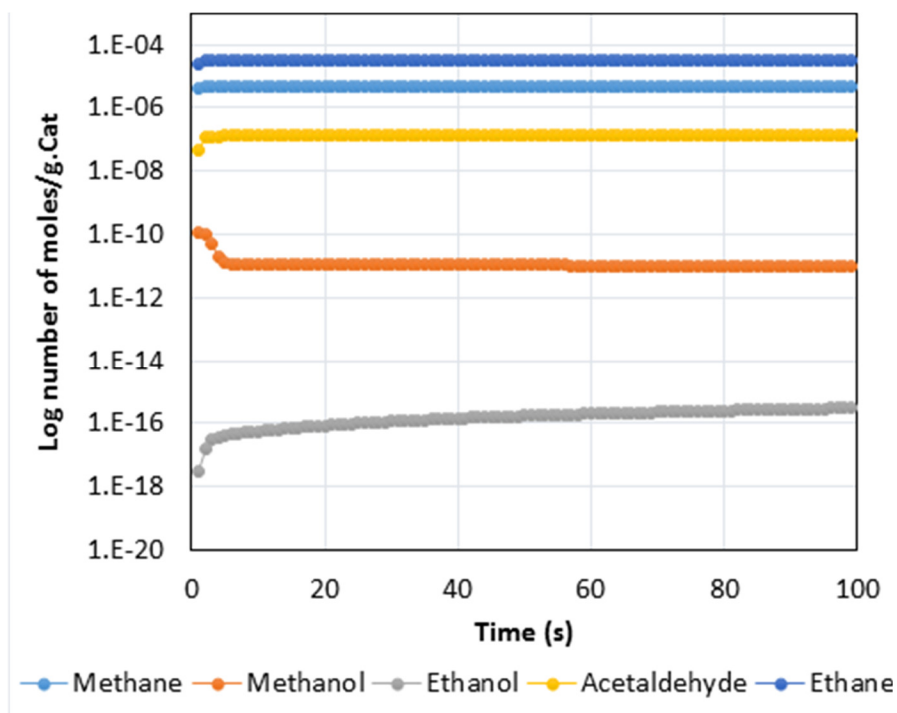


Figure 4.12. Time evolution of products on cobalt rich surface

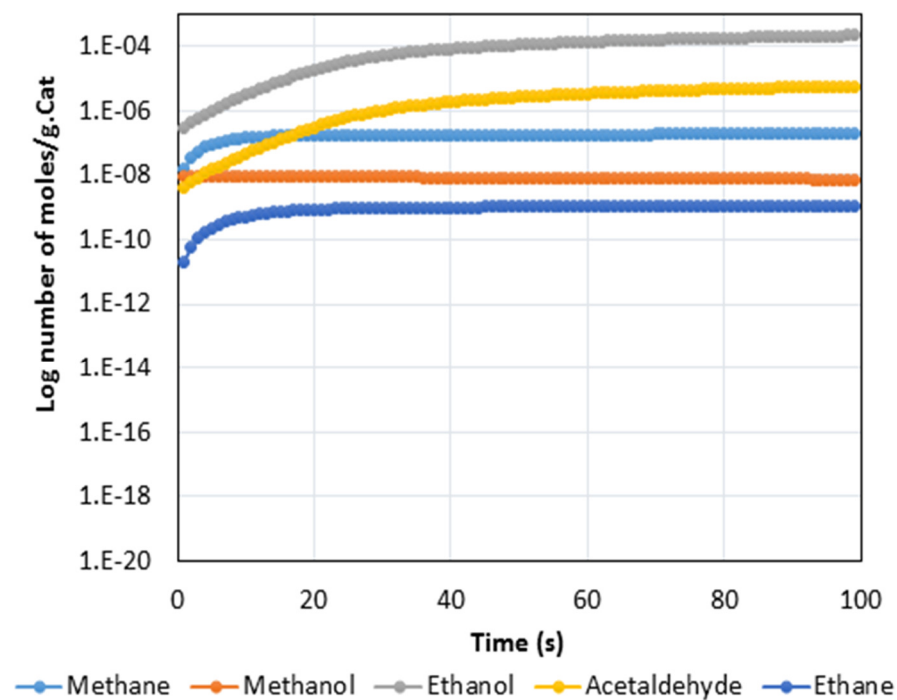


Figure 4.13. Time evolution of products on cobalt-palladium interface

Table 4. 8. Product distributions observed for syngas conversion using the present microkinetic model and experiments using supported metal catalysts.

Predicted product selectivity from microkinetic model				
Site	Total Hydrocarbons (Methane, Ethane)	Methanol	Ethanol	Acetaldehyde
Palladium	0.00	100	0.00	0.00
Cobalt	99.67 (12.26, 87.41)	0.00	0.00	0.33
CoPd	0.13 (0.13, 0.00)	0.01	97.43	2.43
Product selectivity from experiments				
Site	Methane Ethane	Methanol	Ethanol	Acetaldehyde
Pd(5)/Al ₂ O ₃	20	79.7	0.03	0.00
Co(5)/Al ₂ O ₃	97.2	2.0	0.3	0.6

All microkinetic model simulations used a reaction temperature and partial pressures of reactants that are matched to experimental data. The reactor temperature was maintained at 523 K, and the syngas feed contained a 2:1 molar ratio of H₂ to CO. The partial pressure of H₂ and CO reactants in the reactor feed were 1.2 and 0.6 atm, respectively.

Overall product selectivity for major products was computed as the ratio of number of moles of desired product to summation of number of moles of all products formed. Results from the microkinetic model match well with the experimental data. Further, at a reactor time of 1 min, our model predicts that on Pd₃ sites, methanol is the primary product with a product selectivity of 100 percent, indicating that the other

products are formed in negligible quantities. Experimental data also predicts that methanol is the primary product with a selectivity of 79.7%. On the cobalt rich surface, the microkinetic model predicts a product distribution of 12.26% methane, 87.41% ethane and 0.33% acetaldehyde; whereas, the experimental results indicate 97.2% methane, 2% methanol, 0.6 % Acetaldehyde and 0.2% ethanol. Thus, the major product from both experimental and theoretical work for cobalt rich surfaces consists primarily of C1 and higher molecular weight hydrocarbons. For the catalyst containing mixed CoPd sites, ethanol is the major product with a selectivity of 97.43%. Selectivity towards methane and acetaldehyde was 0.13% and 2.43%, respectively. To-date, there is no experimental data available for a pure CoPd surface; thus, not comparison to experimental data is possible.

The relatively minor difference in product selectivities for the microkinetic model and experimental observations is the result of numerous factors. First and foremost, it should be recognized that the pure metal sites studied herein are actually part of a bimetallic catalyst. Thus, the presence of two metals in such close proximity will certainly affect the electronic behavior of each other.¹⁹⁻²¹ Also, the cluster is nanometer size in diameter, which means that the number of coordinated metals to any given site is like that of a step or edge site in a larger catalyst particle, and these sites are known to be more reactive than metals in a terrace surface site. This type of phenomena is part of the explanation for experimental results showing that the catalytic nature of metals changes at nanometer scale.^{47,54-57} It is also important to consider that the catalyst used in the

experimental study are not pure metals, but instead both cobalt and palladium are supported on alumina, and it is a well-known fact in catalysis that the product distribution is influenced by the presence of the support material.

From the microkinetic model results on Co, Pd and CoPd sites we can note that ethanol was formed only from the CoPd sites. This can be explained by looking at the activation energies for the key intermediate reactions. It was discussed before that the most favorable path for ethanol formation is via CO insertion to form CH_xCO^* species on the surface; therefore, the key reactions for ethanol formation are CO insertion reactions. When we look at the activation energies for five important CO insertion and hydrogenation reactions leading to CH_xCO^* species (see Table 4.9 below), it can be noted that the activation energies are very high on Pd and Co surfaces, making them less favorable for ethanol formation. Whereas, the activation energies on CoPd sites are lower than other two surfaces. Thus, ethanol formation takes place only on CoPd catalyst sites.

Table 4. 9. Activation energies of key CO insertion and hydrogenation reactions

R.No.	Reaction	Activation Energy(eV)		
		Co	CoPd	Pd
1	$\text{CH}^* + \text{CO}^* \leftrightarrow \text{CHCO}^* + *$	0.88	0.73	2.80
2	$\text{CH}_2^* + \text{CO}^* \leftrightarrow \text{CH}_2\text{CO}^* + *$	0.95	0.88	0.78
3	$\text{CH}_3^* + \text{CO}^* \leftrightarrow \text{CH}_3\text{CO}^* + *$	1.20	0.86	1.42
4	$\text{CHCO}^* + \text{H}^* \leftrightarrow \text{CH}_2\text{CO}^* + *$	0.71	0.27	2.80
5	$\text{CH}_2\text{CO}^* + \text{H}^* \leftrightarrow \text{CH}_3\text{CO}^* + *$	0.73	0.55	1.06

Conclusions

Combined DFT and microkinetic model is used in this study to understand the reaction mechanism on a 13 atom cobalt-palladium bimetallic catalysts. The reaction mechanism studied here is comprehensive with 46 reversible reactions on three surfaces, making the total number of reactions studied 276. To reduce the computational time in evaluating the transition state energies for this complex system of reactions, BEP relationships were developed for association and dissociation type of reactions. Transition state energies from BEP and DFT were used to calculate the activation energies for all reactions not explicitly evaluated by CI-NEB methods employing ab initio techniques. Our microkinetic model includes surface coverage effects of carbon monoxide that are based on experimentally observed behavior. A batch reactor is designed, and the time evolution of products and intermediates are followed to determine product selectivities and evaluate the favored pathway(s) for product formation.

Separate microkinetic models were generated for cobalt, palladium and CoPd surfaces. The results from the microkinetic model are in good agreement with experimental data. One important observation from this study is that ethanol formation takes place only on the CoPd sites on this catalyst. Pure cobalt or palladium sites are incapable of generating ethanol by themselves, but when combined a synergetic effect between Co and Pd is responsible for ethanol formation.

The reaction mechanism for product formation can be explained as follows, CO adsorbs strongly on all of the metal surfaces making the direct dissociation not feasible on this catalyst. The pathway for ethanol formation begins with CO adsorbing on the catalyst surface to form CO^* . Hydrogenation of adsorbed CO^* yields HCO^* , which then undergoes successive hydrogenation reactions to form CH_3O^* species. On the palladium surface, CH_3O^* species undergo further hydrogenation to form methanol, while with the cobalt and CoPd sites, CH_3O^* undergoes further dissociation to form CH_3^* . On the cobalt surface CH_3^* species undergo further hydrogenation and follows FTS reactions to make higher hydrocarbons, while on CoPd sites, the CH_3^* species undergo CO insertion reactions to form ethanol. To improve the product selectivities for ethanol production, the number of mixed CoPd sites should be a maximum. From this study, we can conclude that the key for ethanol formation is formation of CH_3^* species on the surface and suppression of FTS reactions on the catalyst. Ethanol formation happens only when the activation energy for CO insertion reactions is minimum. This study provides a complete treatment for syngas conversion to products using a microkinetic model for a batch reactor, with special treatment for CO adsorption and coverage that is based on experimental observations. This model can be extended to other types of bimetallic clusters and other continuous reactors such as continuous stirred tank reactor and PFR, enabling the design of optimum catalysts and reactor for the conversion of syngas to ethanol.

References

1. [Http://Www.eia.gov/todayinenergy/detail.php?id=26212](http://www.eia.gov/todayinenergy/detail.php?id=26212).
2. Mielenz JR. - Ethanol production from biomass: Technology and commercialization status. - *Current Opinion in Microbiology*. 2001;4(- 3):- 324. doi: - [https://doi.org/10.1016/S1369-5274\(00\)00211-3](https://doi.org/10.1016/S1369-5274(00)00211-3).
3. Maddipati P, Atiyeh HK, Bellmer DD, Huhnke RL. Ethanol production from syngas by clostridium strain P11 using corn steep liquor as a nutrient replacement to yeast extract. . 2011;102.
4. Manochioa C, Andradea BR, Rodrigueza RP, Moraes BS. - Ethanol from biomass: A comparative overview. - *Renewable and Sustainable Energy Reviews*. 2017;80:- 743. doi: - <https://doi.org/10.1016/j.rser.2017.05.063>.
5. Garzon FP, Pakhare D, Spivey JJ, Bruce DA. - Dry reforming of methane on rh-doped pyrochlore catalysts: A steady-state isotopic transient kinetic study. - *ACS Catal*. 2016;6(- 6):- 3826. doi: - 10.1021/acscatal.6b00666.
6. Vita A, Cristiano G, Italiano C, Pino L, Specchia S. - Syngas production by methane oxy-steam reforming on me/CeO₂ (Me=Rh, pt, ni) catalyst lined on cordierite monoliths. - *Applied Catalysis B: Environmental*. 2015;162:- 551. doi: - <https://doi.org/10.1016/j.apcatb.2014.07.028>.

7. Luo Z, Kriz DA, Miao R, et al. - TiO₂ supported gold–palladium catalyst for effective syngas production from methane partial oxidation. - *Applied Catalysis A: General*. 2018;554:- 54. doi: - <https://doi.org/10.1016/j.apcata.2018.01.020>.
8. Emberga T, Uhiara F, Nwigwe C, Amadi R. Biomass conversion technologies. . 1923.
9. Subramani V, Gangwal SK. - A review of recent literature to search for an efficient catalytic process for the conversion of syngas to ethanol. - *Energy Fuels*. 2008;22(- 2):- 814. doi: - 10.1021/ef700411x.
10. Schmid G. Developments in transition metal cluster chemistry — the way to large clusters. In: - *Clusters*. Vol 62. - Springer Berlin Heidelberg; 2005:- 51-85. - 10.1007/BFb0009185.
11. - Spivey JJ, - Egbibi A. - Heterogeneous catalytic synthesis of ethanol from biomass-derived syngas. - *Chem Soc Rev*. 2007;36(- 9):- 1514. doi: - 10.1039/B414039G.
12. Khodakov AY, Chu W, Fongarland P. - Advances in the development of novel cobalt Fischer–Tropsch catalysts for synthesis of long-chain hydrocarbons and clean fuels. - *Chem Rev*. 2007;107(- 5):- 1692. doi: - 10.1021/cr050972v.
13. Ming H, Baker BG. - Characterization of cobalt fischer-tropsch catalysts I. unpromoted cobalt-silica gel catalysts. - *Applied Catalysis A: General*. 1995;123(- 1):- 23. doi: - [https://doi.org/10.1016/0926-860X\(94\)00220-7](https://doi.org/10.1016/0926-860X(94)00220-7).

14. Saib AM, Claeys M, van Steen E. - Silica supported cobalt Fischer–Tropsch catalysts: Effect of pore diameter of support. - *Catalysis Today*. 2002;71(- 3):- 395. doi: - [https://doi.org/10.1016/S0920-5861\(01\)00466-7](https://doi.org/10.1016/S0920-5861(01)00466-7).
15. Hanm HS, Lee WY. - Effects of promoters of palladium/silica catalysts for the synthesis of methanol. - *Applied Catalysis*. 1990;65(- 1):- 1. doi: - [https://doi.org/10.1016/S0166-9834\(00\)81583-3](https://doi.org/10.1016/S0166-9834(00)81583-3).
16. Zhang Q, Li X, Fujimoto K. - Pd-promoted cr/ZnO catalyst for synthesis of methanol from syngas. - *Applied Catalysis A: General*. 2006;309(- 1):- 28. doi: - <https://doi.org/10.1016/j.apcata.2006.04.026>.
17. Poutsma ML, Elek LF, Ibarbia PA, Rabo JA. - Selective formation of methanol from synthesis gas over palladium catalysts. - *Journal of Catalysis*. 1978;52(- 1):- 157. doi: - [https://doi.org/10.1016/0021-9517\(78\)90131-8](https://doi.org/10.1016/0021-9517(78)90131-8).
18. Wang L, JOhnson DD. - Predicted trends of Core–Shell preferences for 132 late transition-metal binary-alloy nanoparticles. - *J Am Chem Soc*. 2009;131(- 39):- 14023. doi: - 10.1021/ja903247x.
19. - Sakong S, - Mosch C, - Gro[German sz ligature] A. - CO adsorption on cu-pd alloy surfaces: Ligand versus ensemble effects. - *Phys Chem Chem Phys*. (- 18):- 2216. doi: - 10.1039/B615547B.

20. Chen W, Kim J, Sun S, Chen S. - Composition effects of FePt alloy nanoparticles on the electro-oxidation of formic acid. - *Langmuir*. 2007;23(- 22):- 11303. doi: - 10.1021/la7016648.
21. Greeley J, Mavrikakis M. Alloy catalysts designed from first principles. - *Nature Materials*. 2004:- 810.
22. Schneebeli ST, Bochevarov A,D, Friesner RA. - Parameterization of a B3LYP specific correction for noncovalent interactions and basis set superposition error on a gigantic data set of CCSD(T) quality noncovalent interaction energies. - *J Chem Theory Comput*. 2011;7(- 3):- 658. doi: - 10.1021/ct100651f.
23. Rinalso D, Tian L, Garvey JN, Friesner RA. - Density functional localized orbital corrections for transition metals. - *The Journal of Chemical Physics*. 2008;129(- 16):- 164108. doi: - 10.1063/1.2974101.
24. Chen Y, Saliccioli M, Vlachos DG. - An efficient reaction pathway search method applied to the decomposition of glycerol on platinum. - *J Phys Chem C*. 2011;115(- 38):- 18707. doi: - 10.1021/jp205483m.
25. Michaelides A, Liu ZP, Zhang CJ, Alavi A, King DA, Hu P. - Identification of general linear relationships between activation energies and enthalpy changes for dissociation reactions at surfaces. - *J Am Chem Soc*. 2003;125(- 13):- 3704. doi: - 10.1021/ja027366r.

26. Liu C, Cundari TR, Wilson AK. - CO₂ reduction on transition metal (fe, co, ni, and cu) surfaces: In comparison with homogeneous catalysis. - *J Phys Chem C*. 2012;116(- 9):- 5681. doi: - 10.1021/jp210480c.
27. Ferrin P, Simonetti D, Kandoi S, et al. - Modeling ethanol decomposition on transition metals: A combined application of scaling and Brønsted–Evans–Polanyi relations. - *J Am Chem Soc*. 2009;131(- 16):- 5809. doi: - 10.1021/ja8099322.
28. He M. *A computational approach for the rational design of bimetallic clusters for ethanol formation from syn-gas.* ; 2013.
29. Cortright RD, Dumesic JA. - Kinetics of heterogeneous catalytic reactions: Analysis of reaction schemes. . 2001;46:- 161. doi: - [https://doi.org/10.1016/S0360-0564\(02\)46023-3](https://doi.org/10.1016/S0360-0564(02)46023-3).
30. Behm RJ, Christmann K, Ertl G. - Adsorption of CO on pd(100). - *The Journal of Chemical Physics*. 2008;73(- 6):- 2984. doi: - 10.1063/1.440430.
31. Lahtinen J, Kauraala KK. - Adsorption and structure dependent desorption of CO on co(0001). - *Surface Science*. 1998;418(- 3):- 502. doi: - [https://doi.org/10.1016/S0039-6028\(98\)00711-0](https://doi.org/10.1016/S0039-6028(98)00711-0).

32. Grabow LC, Gokhale AA, Evans ST, Dumesic JA, Mavrikakis M. - Mechanism of the water gas shift reaction on pt: First principles, experiments, and microkinetic modeling. - *J Phys Chem C*. 2008;112(- 12):- 4608. doi: - 10.1021/jp7099702.
33. Dooling DJ, Rekoske JE, Broadbelt LJ. - Microkinetic models of catalytic reactions on nonuniform surfaces: Application to model and real systems. - *Langmuir*. 1999;15(- 18):- 5846. doi: - 10.1021/la981376h.
34. Lischka M, Mosch C, Gro A. - CO and hydrogen adsorption on pd(210). - *Surface Science*. 2004;570(- 3):- 227. doi: - <https://doi.org/10.1016/j.susc.2004.07.046>.
35. Neurock M. First-principles analysis of the hydrogenation of carbon monoxide over palladium. - *Topics in Catalysis*. 1999;9(- 3):- 135. doi: - 10.1023/A:1019179009796.
36. Hratchian HP, Schlegel HB. - Chapter 10 - finding minima, transition states, and following reaction pathways on ab initio potential energy surfaces A2 - dykstra, clifford E. . 2005:- 195. doi: - <https://doi.org/10.1016/B978-044451719-7/50053-6>.
37. Henkelman G. - A climbing image nudged elastic band method for finding saddle points and minimum energy paths. - *The Journal of Chemical Physics*. 2000;113(- 22):- 9901. doi: - 10.1063/1.1329672.

38. Jørgensen M, Grönbeck H. - First-principles microkinetic modeling of methane oxidation over pd(100) and pd(111). - *ACS Catal.* 2016;6(- 10):- 6730. doi: - 10.1021/acscatal.6b01752.
39. Jiang R, Guo W, Li M, Fu D, Dhan H. - Density functional investigation of methanol dehydrogenation on pd(111). - *J Phys Chem C.* 2009;113(- 10):- 4188. doi: - 10.1021/jp810811b.
40. Ye J, Liu C, Mei D, Ge Q. - Methanol synthesis from CO₂ hydrogenation over a Pd₄/In₂O₃ model catalyst: A combined DFT and kinetic study. - *Journal of Catalysis.* 2014;317:- 44. doi: - <https://doi.org/10.1016/j.jcat.2014.06.002>.
41. Zhang R, Kang L, He L, Wang B. - Insight into the CC chain growth in fischer-tropsch synthesis on HCP co(10-10) surface: The effect of crystal facets on the preferred mechanism. - *Computational Materials Science.* 2018;145:- 263. doi: - <https://doi.org/10.1016/j.commatsci.2018.01.013>.
42. Cheng J, Hu P, Ellis P, French S, Kelly G, Lok CM. - A first-principles study of oxygenates on co surfaces in Fischer–Tropsch synthesis. - *J Phys Chem C.* 2008;112(- 25):- 9464. doi: - 10.1021/jp802242t.
43. Liu JX, Su HY, Li WX. - Structure sensitivity of CO methanation on co (0001), (1 0 1 2) and (1 1 2 0) surfaces: Density functional theory calculations. - *Catalysis Today.* 2013;215:- 36. doi: - <https://doi.org/10.1016/j.cattod.2013.04.024>.

44. Gong XQ. - CH_x hydrogenation on co(0001): A density functional theory study. - *The Journal of Chemical Physics*. 2005;122(- 2):- 024711. doi: - 10.1063/1.1829257.
45. Zuo ZJ, Peng F, Huang W. Efficient synthesis of ethanol from CH₄ and syngas on a Cu-co/TiO₂ Catalyst using a stepwise reactor. - *Scientific Reports*. 2016;6:- 34670.
46. Lundstrom KI, Shivaraman MS, Svensson CM. - A hydrogen-sensitive Pd-gate MOS transistor. - *Journal of Applied Physics*. 1975;46(- 9):- 3876. doi: - 10.1063/1.322185.
47. Stotz H, Deutschmann O. Methane oxidation over palladium: On the mechanism in fuel-rich mixtures at high temperatures. - *Topics in Catalysis*. 2017;60(- 1):- 83. doi: - 10.1007/s11244-016-0717-5.
48. Bowker M, Holroyd RP, Sharpe RG, Corneille JS, Francis SM, Goodman DW. - Molecular beam studies of ethanol oxidation on Pd(110). - *Surface Science*. 1997;370(- 2):- 113. doi: - [https://doi.org/10.1016/S0039-6028\(96\)00959-4](https://doi.org/10.1016/S0039-6028(96)00959-4).
49. Lisowski W. - Kinetics and thermodynamics of hydrogen interaction with thin cobalt films. - *Applied Surface Science*. 1989;35(- 3):- 399. doi: - [https://doi.org/10.1016/0169-4332\(89\)90022-6](https://doi.org/10.1016/0169-4332(89)90022-6).
50. Kumar N, Smith ML, Spivey JJ. - Characterization and testing of silica-supported cobalt–palladium catalysts for conversion of syngas to oxygenates. - *Journal of Catalysis*. 2012;289(-):- 218. doi: - <http://dx.doi.org/10.1016/j.jcat.2012.02.011>.

51. Khodakov AY, Chu W, Fongarland P. - Advances in the development of novel cobalt Fischer–Tropsch catalysts for synthesis of long-chain hydrocarbons and clean fuels. - *Chem Rev.* 2007;107(- 5):- 1692. doi: - 10.1021/cr050972v.
52. Tan KF, Xu J, Chang J, Borgna A, Saeys M. - Carbon deposition on co catalysts during Fischer–Tropsch synthesis: A computational and experimental study. - *Journal of Catalysis.* 2010;274(- 2):- 121. doi: - <https://doi.org/10.1016/j.jcat.2010.06.008>.
53. Dowlati M, Siyavashi N, Azizi HR. Sintering and coking: Effect of preparation methods on the deactivation of CoCo–Ni/TiO₂Ni/TiO₂ in Fischer–Tropsch synthesis. - *Arabian Journal for Science and Engineering.* 2018;43(- 5):- 2441. doi: - 10.1007/s13369-017-2845-z.
54. Tang L, Han B, Persson K, et al. - Electrochemical stability of nanometer-scale pt particles in acidic environments. - *J Am Chem Soc.* 2010;132(- 2):- 596. doi: - 10.1021/ja9071496.
55. Cuenya BR. - Metal nanoparticle catalysts beginning to shape-up. - *Acc Chem Res.* 2013;46(- 8):- 1682. doi: - 10.1021/ar300226p.
56. Burda C, Lou Y, Chen X, Samia ACS, Stout J, Gole JL. - Enhanced nitrogen doping in TiO₂ nanoparticles. - *Nano Lett.* 2003;3(- 8):- 1049. doi: - 10.1021/nl034332o.

57. El-Sayed MA. - Some interesting properties of metals confined in time and nanometer space of different shapes. - *Acc Chem Res.* 2001;34(- 4):- 257. doi: - 10.1021/ar960016n.

CHAPTER FIVE

ETHANOL SYNTHESIS FROM SYNGAS: COMBINED MICROKINETIC MODEL ON CO_xPD_y CLUSTER, STUDY OF DIFFUSION EFFECTS ON PRODUCT DISTRIBUTION

Introduction

Identification of abundant shale gas reserves in the United States and the rest of the world¹⁻³ have increased attention on developing technologies to convert shale gas to value added chemicals, such as liquid fuels.^{4,5} Additionally, growing concerns over the use of fossil fuels have increased efforts to synthesize a renewable fuel replacement for transportation fuels, such as gasoline. In both cases, there is a need to identify efficient processes to convert methane, which is the primary constituent of shale gas and a readily synthesized biofuel, into a high-energy density transportation fuel that can readily be incorporated into the existing liquid fuels infrastructure. Given the intractable nature of direct methane conversion processes, it is easier to first convert methane to syngas,⁶⁻⁸ a reactive mixture of carbon monoxide (CO) and hydrogen (H₂), which can further be converted to liquid fuels, including ethanol. Thus, the main focus of this study is to develop a comprehensive reaction model for the conversion of syngas to ethanol.

Ethanol has been identified as an alternative renewable fuel, which can be used both as fuel by itself or as an additive to gasoline fuels.^{9,10} Ethanol also exhibits lower emissions during combustion when compared to traditional fuels (gasoline), and these

characteristics have heightened efforts to develop efficient technologies for its production.¹¹

Multiple studies have reported on the direct catalytic conversion of syngas to ethanol.¹²⁻¹⁶ Despite this fact, there is currently no commercial process for the production of ethanol from syngas via any direct route.^{12,13,17-21} The main problem areas are, identifying economical catalyst material that can produce the desired ethanol product with high selectivity. Thus far, the best catalyst for this reaction was found to be a supported rhodium catalyst.^{15,22-24} However, using rhodium as a catalyst for this reaction has its own disadvantages. Specifically, rhodium is expensive, not in high abundance in nature, and despite significant research to-date, the available rhodium catalysts still have relatively low selectivity for the production of ethanol.

The key step for the rational design of any catalyst is to understand the reaction mechanism for product formation. There are two theories put forward to explain the ethanol formation on rhodium surfaces. One theory involves CO and H₂ adsorbing on the surface of catalyst, followed by CO* hydrogenation to form HCO*, which is further hydrogenated to form CH₃O*. The CH₃O* surface species then undergoes a CO insertion reaction to form an acyl species CH_xCO*, which upon further hydrogenation leaves the surface as ethanol. Second theory explains ethanol formation via direct CO dissociation followed by CO insertion and hydrogenation. In both the theories, the key intermediate was identified as CH_x* species on the surface. CH_x* species can either be hydrogenated to

form CH₄ or undergo further chain growth to form higher hydrocarbons. CH_x* can also undergo CO insertion to form ethanol. Therefore, the ideal catalyst for ethanol formation from syngas would be the one that yields high concentrations of CH_x* species on the surface, while simultaneously suppressing the hydrogenation of CH_x* species to form methane or higher alkanes.^{19,23,25-27}

In this study, we propose a bimetallic catalyst consisting of cobalt and palladium. Cobalt is a commonly used Fischer-Tropsch catalyst²⁸⁻³⁰, which promotes carbon chain growth via the insertion of adsorbed CH_x* species into cobalt-alkyl bonds; whereas, palladium is an ideal methanol catalyst³¹⁻³³ that promotes CO insertion reactions. The combination of these two metals provides the necessary surface chemistry for ethanol formation.

The main focus of this chapter is to extend the microkinetic model from chapter four so as to identify optimal catalyst compositions for ethanol formation. In chapter four, microkinetic models were developed for isolated cobalt, palladium and CoPd sites, so as to understand the intrinsic nature of each catalyst site. In this chapter, we describe a more comprehensive microkinetic model that includes the diffusion of surface species between catalyst sites of differing composition. Additionally, the ratio of the number of sites of a given type (cobalt, cobalt-palladium and palladium) was varied so that catalyst composition effects on the overall catalyst selectivity can be quantified and evaluated

with respect to the proposed mechanisms for syngas to ethanol formation on Co_xPd_y catalysts.

Experimental

Catalyst geometry:

An icosahedral 13 atom cluster consisting of seven cobalt atoms and six palladium atoms was used in this computational study. Initial Density Functional Theory (DFT) studies of spin optimized clusters confirmed that the cobalt and palladium preferred to stay segregated in the cluster. For the Co_7Pd_6 cluster, there are three different types of catalyst sites: pure cobalt sites (Co_3), pure palladium sites (Pd_3) and mixed CoPd sites (Co_2Pd and CoPd_2 sites). For the studied 13 atom cluster, there are five Co_3 sites, five Pd_3 sites and 10 CoPd sites.

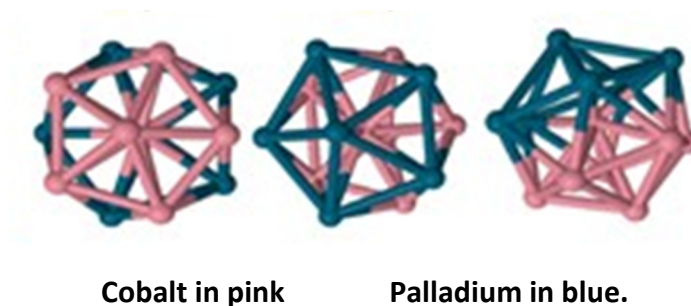


Figure 5. 1. Thirteen atom metal cluster of seven cobalt atoms and six palladium atoms.

Adsorption energy calculations:

Density functional theory (DFT) simulations were carried out to understand the reaction mechanism for the conversion of syngas, a mixture of carbon-monoxide and hydrogen, to the desired ethanol product. To understand the reaction mechanism in detail, a complex reaction network consisting of forty-six reversible elementary reactions was studied. The studied syngas to ethanol mechanism included 24 intermediates and nine gas phase species. DFT simulations were carried out using Jaguar 7.0 (Schrodinger, Inc.). Jaguar is a quantum ab-initio simulation package, which employs density functional theory and an atomic orbital approach to evaluate the energetics of atomic and molecular systems. All electronic correlations were represented by the hybrid B3LYP functional, which is widely used for studying transition metal chemistry. Molecular orbitals were described using the LACVP basis sets. All calculations performed in this study were spin polarized, and an energy convergence of 10^{-5} Hartrees was employed for all total energy calculations. Vibrational frequencies were calculated, and these values were used to calculate the zero-point energy for each system. Finally, all reported total energies were zero point corrected.

Materials Studio software (Accelrys, Inc.) was used to build all initial chemical structures. For reaction intermediates bound to the catalyst surface, three types of sites, atop, bridge and threefold catalyst sites, were considered when finding the most

favorable binding site. Adsorption energies were determined for the optimum binding site for all twenty-four intermediates on the three types of surface sites (Co, Pd and CoPd).

Adsorption energies of the intermediate species formed during reactions were calculated by,

$$E_{ads} = E_{adsorbate+cluster} - E_{cluster} - E_{ads(g)} \quad (1)$$

where $E_{adsorbate + cluster}$ is the energy of the optimized adsorbate structure on the cluster, $E_{cluster}$ is the energy of a pristine cluster and $E_{ads(g)}$ is the energy of the adsorbate in the gas phase.

Activation energies:

To determine the activation energies of elementary reactions, we need to determine the transition state energies. This is because the activation energy is the difference between the energy of reactants and the transition state energy. For this study, the climbing image nudged elastic band method (CI-NEB) was implemented to find the minimum energy path for all surface reactions. Eight images were used to connect the reactants and products of intermediate reactions.³⁴

The number of reversible elementary reactions analyzed in this study was forty-six, and given the three different types of catalyst sites (Co, Pd, CoPd), the total number of reactions requiring evaluation was 276 (i.e., 46 x 2 x 3). To reduce the required computational time, Brønsted-Evans-Polanyi (BEP) relationships were developed for

addition and dissociation reactions. BEP relations correlate the transition state energy of an elementary reaction step to the heat of reaction of that particular reaction.³⁵⁻³⁸ It is an efficient and computationally cost effective way to quantify reaction energetics for multi-reaction systems and allows one to calculate the activation energy of an elementary reaction, knowing only the adsorption energies of reactants and products along with their energies in the gas phase. Two linear relationships were developed, one for the association reactions, which leave an empty vacant site on the surface after reaction, and the other for dissociation type reactions, which consume a vacant site during reaction (see Figure 4.2). The BEP relationship used in this study was developed by a Dr. Ming He, a former doctoral student in the Bruce Research Group.³⁹ From comparisons with experimental data, a scaling factor of 0.7 was used to correct the DFT calculated adsorption energies on Co and Pd surface sites; whereas, the DFT energies were scaled by a factor of 0.53 on the CoPd sites.^{40,41}

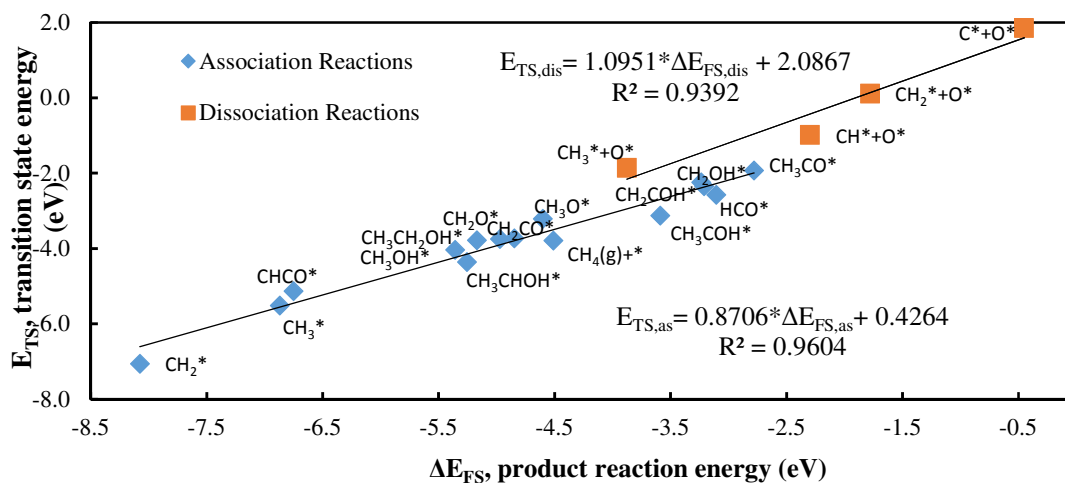


Figure 5. 2. BEP relationships for association and dissociation reaction types obtained from DFT calculations for the Co_7Pd_6 catalyst. Transition state energies are related to final product reaction energies for gas phase reactants combining with vacant site(s) to form adsorbed products.³⁹

- This graph is a TSS graph adopted from Ming’s dissertation.

Arrhenius equation

Rate constants for surface reactions involving intermediate species were determined using Arrhenius equations, where the temperature dependence of the rate constant for a given surface reaction (k) is given by the exponential function,

$$k = A \exp\left(\frac{-E_a}{RT}\right) \quad (2)$$

where E_a is the activation energy, R is the ideal gas constant, T is temperature in units of K, and A is the pre-exponential factor, which generally describes the frequency of a molecular event (collision, vibration, etc.) that could lead to product formation. In this

study, a constant value of A was used for all surface reactions,^{42,43} and this value is calculated from the equation,

$$A = \frac{k_B T}{h} \quad (3)$$

where k_B is the Boltzmann constant, and h is Planck's constant. Given that the reactions are reversible, the rate for a given forward reaction (as written) is represented by k_f , whereas the reverse reaction is described by the symbol k_r .

Adsorption and desorption reactions

Reactions involving gas phase species, including the adsorption of reactants and desorption of products, must be modeled differently than surface reactions involving only surface bound species. This is because the kinetics of a surface site reaction with a gas phase moiety are impacted by the properties of the gas, including the kinetic energy, density, and collision diameter of the reactive gas molecule. All adsorption and desorption reactions were assumed to be at equilibrium. Further, DFT derived entropy and enthalpy values were used to determine equilibrium constants.

The equilibrium constant relating the ratio of forward and reverse rate constants can be represented in terms of the entropy and enthalpy of reaction by,

$$\ln K_{eq} = -\frac{\Delta H - T\Delta S}{RT} \quad (4)$$

where ΔH is the heat of reaction, and ΔS is the entropy of reaction.

Rate constants for adsorption processes were determined using the collision theory for gases. In the work authored by Cortright and Dumesic⁴⁴, it was shown that the rate of adsorption of a gas phase species is given by,

$$r_{f,ads} = -\frac{w}{\sqrt{2\pi m_A k_B T}} \exp\left[\frac{-E_{f,ads}}{k_B T}\right] \sigma^0(T, \theta) P_{A(g)} \quad (5)$$

where $r_{f,ads}$ is the rate of adsorption with units of coverage (molecules/active site) per time, m_A is the molecular weight of the adsorbing species A , $E_{f,ads}$ is the activation energy for adsorption, w is the area per active site ($w= 1.57e-19$ m²/active site for the nanocatalyst), $\sigma^0(T, \theta)$ is the sticking coefficient, which is measured as the probability that a collision of A on to the surface leads to adsorption. This latter term is a function of temperature T , metal coverage θ , and $P_{A(g)}$, which is the partial pressure of the adsorbate A .

In this work, adsorption processes were assumed to be barrier less, which makes $E_{f,ads}$ nearly zero and is therefore neglected. Additionally, at a given temperature, σ^0 is a function of coverage. As our initial adsorption model over predicted CO coverage on all catalyst surfaces, the adsorption behavior for CO in the final microkinetic model included an experimentally based model for CO coverage and the associated sticking coefficient (see Chpt. 4 Experimental), overcoming this complication. Similar experimentally based CO adsorption models were developed for cobalt and palladium surfaces; whereas, adsorption of CO on CoPd surfaces was modeled using a simple average of the values

calculated for CO adsorption on the Co and Pd surface because there is currently no experimental data available for this system (refer to Appendix C for sticking coefficients).

The rate of adsorption can be simplified as,

$$r_{f,ads} = -\frac{W}{\sqrt{2\pi m_A k_B T}} \sigma^0 (T, \theta) P_{A(g)} \quad (6)$$

Therefore, the adsorption rate constant is given by

$$k_{f,ads} = -\frac{W}{\sqrt{2\pi m_A k_B T}} \sigma^0 (T, \theta) \quad (7)$$

The desorption rate constant is defined as the ratio of the adsorption rate constant (from Eqn. 7) and the equilibrium constant (from Eqn. 4) for a specified single-step reaction process,

$$k_{r,des} = \frac{k_{f,ads}}{K_{eq}} \quad (8)$$

Surface concentration of intermediate species

For intermediate species, the net change of surface coverage with respect to time is given by,

$$r_i = \frac{d\theta_i}{dt} = r_{\text{formation of species } i} - r_{\text{consumption of species } i} \quad (9)$$

There are three types of sites under consideration. Change in surface coverage of species on three surfaces, Co, CoPd and Pd was used to calculate the net rate of change in concentration of intermediate surface species.

$$r_{Pd,i} = \frac{d\theta_{Pd,i}}{dt} = r_{\text{formation of species } i \text{ on Pd sites}} - r_{\text{consumption of species } i \text{ on Pd sites}} \quad (10)$$

$$r_{CoPd,i} = \frac{d\theta_{CoPd,i}}{dt} = r_{\text{formation of species } i \text{ on CoPd sites}} - r_{\text{consumption of species } i \text{ on CoPd sites}} \quad (11)$$

$$r_{Co,i} = \frac{d\theta_{Co,i}}{dt} = r_{\text{formation of species } i \text{ on Co sites}} - r_{\text{consumption of species } i \text{ on Co sites}} \quad (12)$$

The net rate of formation of component i was calculated as the sum of the rates of formation for each catalyst surface using Eqns. 10, 11 and 12,

$$r_{net,i} = r_{Pd,i} + r_{CoPd,i} + r_{Co,i} \quad (13)$$

Equations of this type were written for all twenty-four intermediate species on the surface.

The Fraction of vacant sites can be defined as,

$$\theta^* = 1 - \sum_i \theta_i \quad (14)$$

where θ^* is the fraction of sites vacant during the reaction, and θ_i is the fraction of sites occupied by any of the 24 intermediate species i .

The fraction of vacant Pd₃ sites is calculated as

$$\theta_{Pd}^* = n_{Pd} - \sum_i \theta_{Pd,i} \quad (15)$$

where θ_{Pd}^* is the fraction of vacant sites on the palladium surface, $\theta_{Pd,i}$ is the fraction of palladium sites occupied by intermediate species i , and n_{Pd} is the total number of Pd₃ sites on the catalyst. Similar equations are defined for the CoPd and Co₃ type of sites,

$$\theta_{CoPd}^* = n_{CoPd} - \sum_i \theta_{CoPd,i} \quad (16)$$

$$\theta_{Co}^* = n_{Co} - \sum_i \theta_{Co,i} \quad (17)$$

The intermediates and gas phase species used in this model are listed in Table

5.1.

Table 5. 1. List of intermediate species and gas phase reactants and products

Intermediates from the reaction mechanism									
1	CO*	6	CH*	11	CHCO*	16	CH ₂ COH*	21	OH*
2	H*	7	CH ₂ *	12	CH ₂ CO*	17	CH ₃ COH*	22	CHCH ₂ *
3	HCO*	8	CH ₃ *	13	CH ₃ CO*	18	CH ₂ CHOH*	23	CH ₂ CH ₂ *
4	CH ₂ O*	9	CHOH*	14	CHCHO*	19	CH ₃ CHOH*	24	CH ₃ CH ₂ *
5	CH ₃ O*	10	CH ₂ OH*	15	CH ₂ CHO*	20	O*		
gas phase species (Reactants and Products)									
1	CO(g)	3	CH ₄ (g)	5	CH ₃ CHO(g)	7	H ₂ O (g)	9	CH ₃ CH ₃ (g)
2	H ₂ (g)	4	CH ₃ OH (g)	6	CH ₃ CH ₂ OH (g)	8	CH ₂ CH ₂ (g)		

Considering all the intermediates from Table 5.1, Equations 15, 16 and 17 can be expanded as,

$$\begin{aligned}
\theta_{Pd}^* = & n_{Pd} - \theta_{CO_Pd} + \theta_{H_Pd} + \theta_{HCO_Pd} + \theta_{CH_2O_Pd} + \theta_{CH_3O_Pd} + \theta_{CH_Pd} + \theta_{CH_2_Pd} \\
& + \theta_{CH_3_Pd} + \theta_{CHOH_Pd} + \theta_{CH_2OH_Pd} + \theta_{CHCO_Pd} + \theta_{CH_2CO_Pd} + \theta_{CH_3CO_Pd} + \theta_{CHCHO_Pd} \\
& + \theta_{CH_2CHO_Pd} + \theta_{CH_2COH_Pd} + \theta_{CH_3COH_Pd} + \theta_{CH_2CHOH_Pd} + \theta_{CH_3CHOH_Pd} + \theta_{O_Pd} + \theta_{OH_Pd} \\
& + \theta_{CHCH_2_Pd} + \theta_{CH_2CH_2_Pd} + \theta_{CH_3CH_2_Pd}
\end{aligned} \tag{18}$$

$$\begin{aligned}
\theta_{CoPd}^* = & n_{CoPd} - \theta_{CO_CoPd} + \theta_{H_CoPd} + \theta_{HCO_CoPd} + \theta_{CH_2O_CoPd} + \theta_{CH_3O_CoPd} + \theta_{CH_CoPd} \\
& + \theta_{CH_2_CoPd} + \theta_{CH_3_CoPd} + \theta_{CHOH_CoPd} + \theta_{CH_2OH_CoPd} + \theta_{CHCO_CoPd} + \theta_{CH_2CO_CoPd} \\
& + \theta_{CH_3CO_CoPd} + \theta_{CHCHO_CoPd} + \theta_{CH_2CHO_CoPd} + \theta_{CH_2COH_CoPd} + \theta_{CH_3COH_CoPd} + \\
& \theta_{CH_2CHOH_CoPd} + \theta_{CH_3CHOH_CoPd} + \theta_{O_CoPd} + \theta_{OH_CoPd} + \theta_{CHCH_2_CoPd} + \theta_{CH_2CH_2_CoPd} \\
& + \theta_{CH_3CH_2_CoPd}
\end{aligned} \tag{19}$$

$$\begin{aligned}
\theta_{Co}^* = & n_{Co} - \theta_{CO_Co} + \theta_{H_Co} + \theta_{HCO_Co} + \theta_{CH_2O_Co} + \theta_{CH_3O_Co} + \theta_{CH_Co} + \theta_{CH_2_Co} \\
& + \theta_{CH_3_Co} + \theta_{CHOH_Co} + \theta_{CH_2OH_Co} + \theta_{CHCO_Co} + \theta_{CH_2CO_Co} + \theta_{CH_3CO_Co} + \theta_{CHCHO_Co} \\
& + \theta_{CH_2CHO_Co} + \theta_{CH_2COH_Co} + \theta_{CH_3COH_Co} + \theta_{CH_2CHOH_Co} + \theta_{CH_3CHOH_Co} + \theta_{O_Co} + \theta_{OH_Co} \\
& + \theta_{CHCH_2_Co} + \theta_{CH_2CH_2_Co} + \theta_{CH_3CH_2_Co}
\end{aligned} \tag{20}$$

The sum of the fractional number of sites for each catalyst surface must also sum to one,

$$n_{Co} + n_{CoPd} + n_{Pd} = 1 \tag{21}$$

In Chapter 4, microkinetic model was run at three points

1. $n_{Pd}=1; n_{Co}=n_{CoPd}=0$; (Palladium rich surface)
2. $n_{CoPd}=1; n_{Pd}=n_{Co}=0$; (CoPd rich surface)
3. $n_{Co}=1; n_{Pd}=n_{CoPd}=0$; (Cobalt rich surface)

To extend microkinetic model, n_{Co} , n_{CoPd} and n_{Pd} was varied from 0.01 to 1 with a step size of 0.01 and the microkinetic model code was run at more than 4500 data points.

Design equations for the batch reactor

Though commercial production of ethanol from syngas would likely be carried out in a continuous flow reactor with solid catalysts, for simplicity, simulations examining catalyst performance over time were modeled in a batch reactor. For heterogeneous reactions the design expression for a batch reactor is given by

$$\frac{dn_{A(g)}}{dt} = r_{A(g)} \left(\frac{s m_{cat}}{N_A \omega} \right) \quad (22)$$

where, s is the catalyst surface area per weight of catalyst (m^2/g), m_{cat} is the mass of catalyst in the reactor, N_A is the Avogadro's number and ω is the approximate surface area per active site.

The rate of change in number of moles produced on Co, CoPd and Pd sites can be written separately as,

$$\frac{dn_{A(g),Co}}{dt} = r_{A(g),Co} \left(\frac{s m_{cat}}{N_A \omega} \right) \quad (23)$$

$$\frac{dn_{A(g),CoPd}}{dt} = r_{A(g),CoPd} \left(\frac{s m_{cat}}{N_A \omega} \right) \quad (24)$$

$$\frac{dn_{A(g),Pd}}{dt} = r_{A(g),Pd} \left(\frac{s m_{cat}}{N_A \omega} \right) \quad (25)$$

where $r_{A(g),Co}$, $r_{A(g),CoPd}$, $r_{A(g),Pd}$ are the rates of production of species A on cobalt sites, CoPd sites and palladium sites, respectively.

The net rate of change in number of moles of species A is written as a summation overall all three surfaces,

$$\frac{dn_{A(g),net}}{dt} = r_{A(g),Co} \left(\frac{sm_{cat}}{N_A \omega} \right) + r_{A(g),CoPd} \left(\frac{sm_{cat}}{N_A \omega} \right) + r_{A(g),Pd} \left(\frac{sm_{cat}}{N_A \omega} \right) \quad (26)$$

Differential mole balances similar to Eqn. 26 were written for all gas phase components, including all reactants and products yielding 9 equations.

Diffusion processes

In this study, diffusion is modeled as an elementary reaction step between adsorbed species on one surface (Co, Pd, or CoPd) and an empty site on a differing surface (Co, Pd, or CoPd). Each of the diffusion reactions is modeled as an elementary reaction. Activation energies for all diffusion processes was calculated using the CI-NEB method, which was previously employed to calculate the activation energies for elementary reaction steps.

Rates of diffusion of species from one site to another site is represented similarly to the rate of change in concentration of surface species as a result of a chemical reaction. Thus, the diffusion rate is defined as,

$$r_{D,i} = \frac{d\theta_{D,i}}{dt} = r_{(\text{decrease in concentration of } i \text{ on one surface})} - r_{(\text{increase in concentration of } i \text{ on another surface})} \quad (27)$$

where $r_{D,i}$ is the rate of diffusion of species i from one surface site to another. When species i is diffusing from one surface to another, the concentration of species i is reduced on one surface and increased on another surface. $r_{D,i}$ is the rate of change in concentration of species due to diffusion. Similar equations are written all 22 diffusion processes included in this model. It should be noted that for computational efficiency only those diffusion processes that impacted the final product selectivity were included in the final microkinetic model. Finally, the net rate of formation of component i represented in Eqn. 13 is modified to include diffusion reactions,

$$r_{net,i} = \frac{d\theta_i}{dt} = r_{Co,i} + r_{CoPd,i} + r_{Pd,i} + r_{D,i} \quad (28)$$

Diffusion rates were calculated only for key species as mentioned before; therefore, for all other species, $r_{D,i}=0$.

A set of twenty four ordinary differential equations (ODE's) of the form of Eqn. 28 for twenty four intermediate species and a set of nine ODE's of the form of Eqn. 28 for gas phase species were solved simultaneously with Eqns. 18, 19, and 20 to determine the rate of change in concentration of surface species and the rate of formation or consumption of gas phase products and reactants, respectively. The inbuilt ODE solver in Matlab (ODE 15s) was used to solve all 33 differential equations simultaneously. Solutions

from the ODE solver were constrained to be non-negative, so as to avoid any concentrations or number of moles of a given species being negative.

Results and discussion

Carbon monoxide coverage

From preliminary microkinetic modeling results, it was observed that carbon monoxide adsorbed rapidly to cobalt, palladium, and cobalt-palladium surface sites. As a result of CO adsorption, the majority of the catalyst surface sites became effectively unavailable for other reactions; thus, the production of hydrogenated CO products was negligible. Experimentally, others have observed that the energetics for CO adsorption on metal surfaces becomes less favorable with higher CO surface coverage, until eventually reaching a maximum coverage of CO that is below full monolayer coverage. The experimental relationship between, CO adsorption, coverage, and the corresponding sticking coefficient on palladium and cobalt surfaces has been well discussed in the literature.^{45,46} As our initial adsorption model over predicted CO coverage on all catalyst surfaces, the adsorption behavior for CO in the final microkinetic model included an experimentally based model for CO coverage and the associated sticking coefficient, overcoming this complication. Similar experimentally based CO adsorption models were developed for cobalt and palladium surfaces; whereas, adsorption of CO on CoPd surfaces was modeled using a simple average of the values calculated for CO adsorption on the Co and Pd surface because there is currently no experimental data available for this system.

Figures 5.3, 5.4, and 5.5 show how the sticking coefficient for CO adsorption on cobalt, palladium and cobalt-palladium sites, respectively, vary as a function of CO coverage.

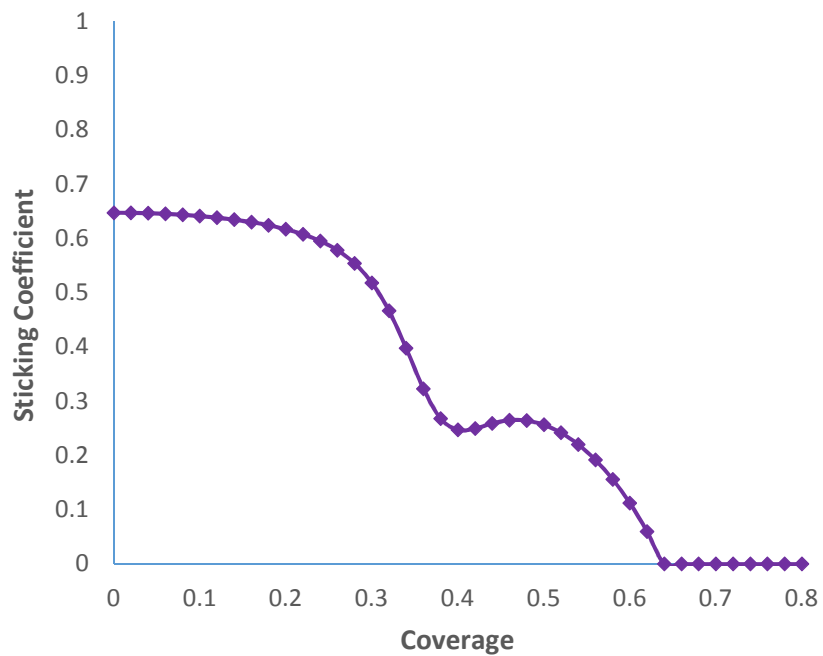


Figure 5. 3. Sticking coefficient as a function of coverage on cobalt surface

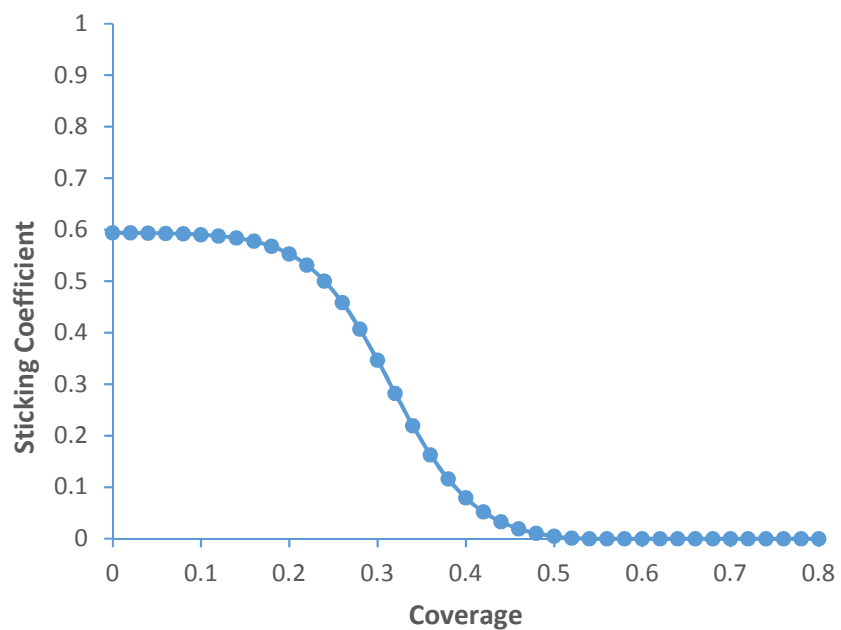


Figure 5. 4. Sticking coefficient as a function of coverage on palladium surface

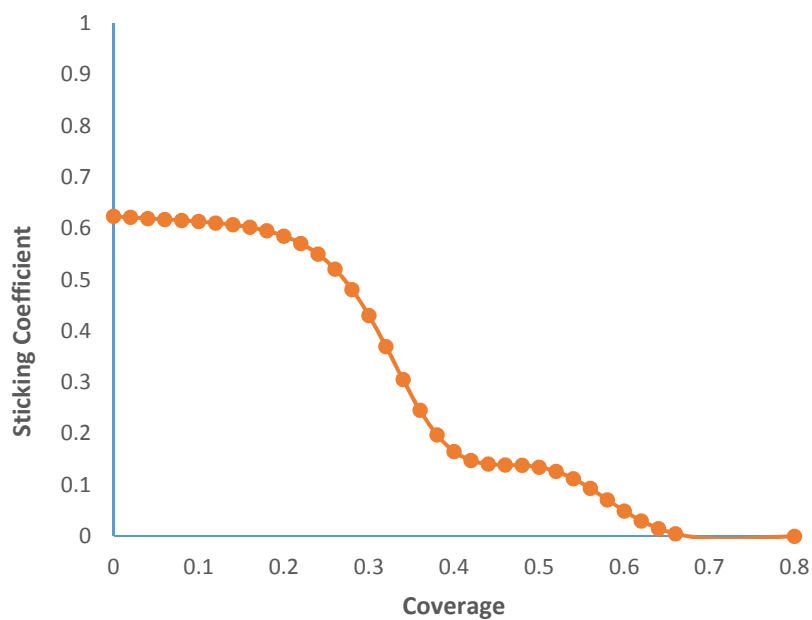


Figure 5. 5 Sticking coefficient as a function of coverage on cobalt-palladium surface

Reaction mechanism

Production of ethanol from syngas involves a complex reaction network. Although, this reaction has been studied extensively, the reaction mechanism is still unclear as of today. One of the primary objectives of this study was to understand the reaction mechanism, which is complex as it contains two reactants (CO and H₂), seven products (CH₄, CH₃OH, CH₃CHO, CH₃CH₃, CH₃CH₂OH, H₂O and CH₂CH₂) and 24 intermediate species. We considered 46 elementary reversible reactions involving reactants, products and intermediates. The detailed reaction mechanism considered for the production of ethanol and related byproducts from syngas is shown in Figure 5.6, and includes all gas phase reactants, surface intermediates, and products considered in this study.

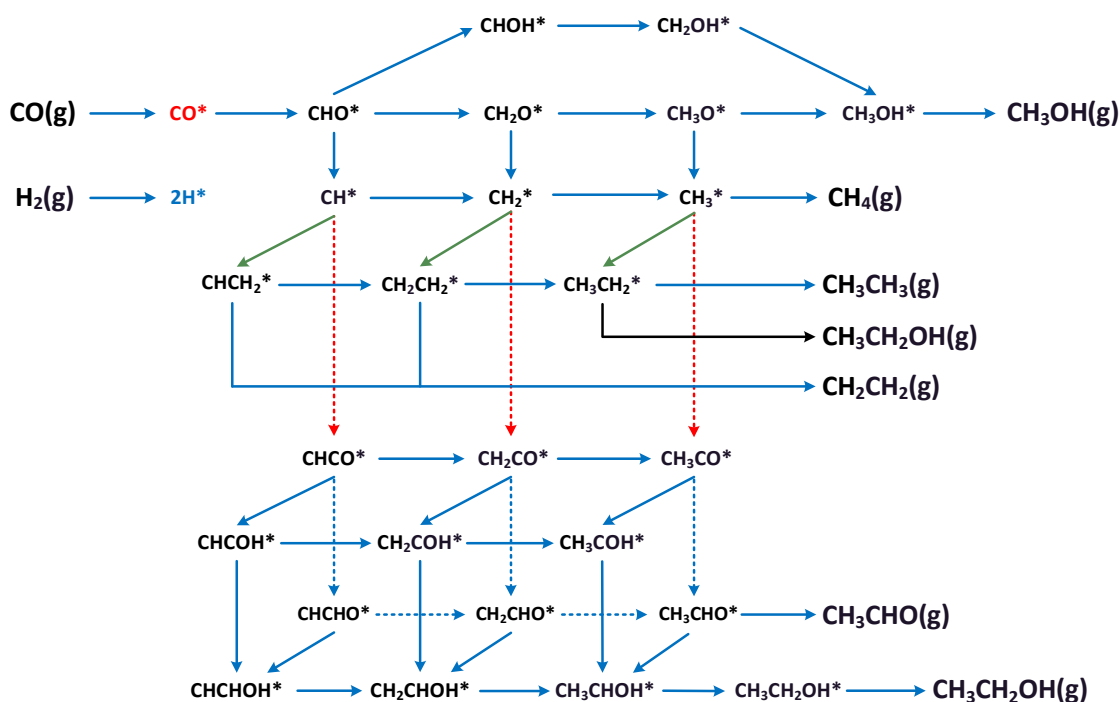


Figure 5. 6. Reaction mechanism of syngas to ethanol conversion. Although ethanol is desired product other products methanol, methane, ethane, ethylene and acetaldehyde are formed as byproducts. Intermediates on surface of the catalyst are represented by $*$. Color of the arrows indicate the type of reaction. CO insertion reactions are shown with red arrows, hydroxylation reaction by black arrows, hydrogenation reactions by blue arrows, and CH_2 insertion reactions are represented in green.

In this study, a bimetallic catalyst consisting of cobalt and palladium is considered. The catalyst structure and number of active sites were shown previously in Fig. 5.1. For the studied Co_7Pd_6 nanocatalyst, cobalt and palladium prefer to be segregated from one another, with one cobalt atom at the center of the icosahedral structure and the 12 surface sites occupied by an equal number of segregated cobalt and palladium atoms (6 of each metal). When separate microkinetic models were used to describe the cobalt, palladium and CoPd sites, there were four major products formed: methane, ethane,

methanol and ethanol. The product distribution from the separate models was discussed in Chpt. 4 and is shown in Table 5.2. The primary products formed on cobalt only sites are methane and ethane, whereas palladium sites largely yield methanol as the primary product. On CoPd mixed-metal sites, the synergetic effects of cobalt and palladium lead to ethanol being formed as the major product. These microkinetic modeling results are in close agreement with the experimental data for syngas conversion over supported cobalt and palladium single-metal catalysts. To identify the catalyst composition that maximizes ethanol product selectivity, the microkinetic model for syngas conversion was modified so that it could evaluate multiple catalyst compositions having varying levels of cobalt, palladium and CoPd catalyst sites.

Table 5. 2. Product distribution from separate Microkinetic models

Type of site	Product selectivity (%)			
	Methane +Ethane	Methanol	Ethanol	Acetaldehyde
Palladium	0.00	100	0.00	0.00
Cobalt	99.67 (12.26+87.41)	0.00	0.00	0.33
CoPd	0.13 (0.13+0.00)	0.01	97.43	2.43

In the multisite microkinetic model, the total fraction of sites is considered equal to one and equals the sum of the cobalt, palladium and CoPd catalyst site fractions.

Numerous multisite microkinetic models were solved with the catalyst site fractions for

each surface varied from 0.01 to 0.98 with a step size of 0.01. The number of moles of reactant consumed and product formed on each type of site was summed to find the change in total number of moles of gas phase species with respect to time.

For each gas phase component, a rate equation describing adsorption processes was developed for each surface. For carbon monoxide, the elementary reaction describing CO adsorption is



The rate of reaction for this adsorption process on a palladium surface is then described by the equation,

$$r_{CO_Pd} = -k_{1f_Pd} \left(P_{CO(g)} \theta_{Pd}^* - \frac{\theta_{CO_Pd}}{K_{CO_Pd}} \right) \quad (30)$$

where k_{1f_Pd} and K_{CO_Pd} are the forward rate and equilibrium constants for the reaction, respectively, θ_{Pd}^* is the fraction of empty sites on the Pd surface, θ_{CO_Pd} is the fraction of sites covered with CO on the Pd surface. Similar rate expressions can be written for the Co and CoPd sites. For the cobalt surface, the rate of consumption of CO is given by,

$$r_{CO_Co} = -k_{1f_Co} \left(P_{CO(g)} \theta_{Co}^* - \frac{\theta_{CO_Co}}{K_{CO_Co}} \right) \quad (31)$$

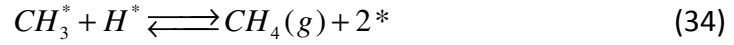
whereas, on the CoPd surface, the rate of consumption of CO is given by,

$$r_{CO_CoPd} = -k_{1f_CoPd} \left(P_{CO(g)} \theta_{CoPd}^* - \frac{\theta_{CO_CoPd}}{K_{CO_CoPd}} \right) \quad (32)$$

Summing the reaction rates for each surface, the net rate of consumption of carbon monoxide is then

$$r_{CO} = \frac{dn_{CO}}{dt} = r_{CO_Pd} + r_{CO_CoPd} + r_{CO_Co} \quad (33)$$

Similar equations can be written for the hydrogen reactant as well as for the product gases. As an example, the elementary reaction leading to methane (CH₄) formation is



The rate of formation of methane on the palladium surface is represented by,

$$r_{CH_4_Pd} = k_{11f_Pd} \left(\theta_{CH_3_Pd} \theta_{H_Pd} - \frac{P_{CH_4(g)} \theta_{Pd}^* \theta_{Pd}^*}{K_{CH_4_Pd}} \right) \quad (35)$$

Likewise, the rate of formation of methane on the cobalt surface is,

$$r_{CH_4_Co} = k_{11f_Co} \left(\theta_{CH_3_Co} \theta_{H_Co} - \frac{P_{CH_4(g)} \theta_{Co}^* \theta_{Co}^*}{K_{CH_4_Co}} \right) \quad (36)$$

On CoPd surface, the rate of CH₄ consumption is,

$$r_{CH_4_CoPd} = k_{11f_CoPd} \left(\theta_{CH_3_CoPd} \theta_{H_CoPd} - \frac{P_{CH_4(g)} \theta_{CoPd}^* \theta_{CoPd}^*}{K_{CH_4_CoPd}} \right) \quad (37)$$

Then, net CH₄ formation is given by

$$r_{CH_4} = \frac{dn_{CH_4}}{dt} = r_{CH_4_Pd} + r_{CH_4_CoPd} + r_{CH_4_Co} \quad (38)$$

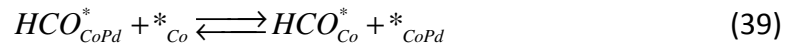
Similar equations for the net rate of change in number of moles are written for other products, including methanol, ethanol, acetaldehyde, ethane, water and ethylene.

Diffusion processes

One of the most important phenomena often neglected with DFT based multisite microkinetic models is the diffusion of intermediates from one type of reaction site to another. The importance of diffusion processes in the overall reaction mechanism of chemical processes at elevated temperatures is well established experimentally,⁴⁷⁻⁵⁰ but due to the added complexity and additional computational effort needed to address these issues, multisite microkinetic reaction models seldom incorporate diffusion processes. The catalyst cluster considered in this study is sub-nanometer in size. With such a small size, the distance between differing catalyst sites is small, and the diffusion of intermediates between reaction sites is more frequent. It is therefore important for this study to include surface diffusion phenomena to make the reaction mechanism and thus the predicted product selectivities more accurate.

Given the complexity of the reaction system modeled herein and to reduce the overall level of computations, diffusion reactions are only considered for select species important to the overall reaction selectivity. The selection of species for diffusion processes was screened using the following criterion. All intermediates having very high adsorption energies on all three surfaces should have very high activation barriers to

diffusion; therefore, diffusion should not play an important role for these species, hence diffusion rates for these species are ignored. Diffusion rates for species that are easily adsorbed and desorbed from the catalyst surface were also ignored because these species can move from one catalyst site to another via gas phase transfer processes. This screening process reduced the number of important diffusion reactions to twenty-two. Important intermediates considered for diffusion calculations are HCO^* , CH_2O^* , CH_3O^* , CH_3CO^* , CH_2CHO^* , CH_3COH^* , CH_3CHOH^* , OH^* , CH_2^* , CH_3CH_2^* and CH_3^* . The diffusion of these intermediates was treated as a reaction between the diffusing species and an active site on a different catalyst surface. For example, if we consider the diffusion of HCO^* species from a CoPd site to a Co_3 site, it can be considered as a reaction between HCO on CoPd site and empty Co_3 active site, and this diffusion reaction can be written as,



The rate of diffusion r_D can be written as,

$$r_D = k_{fD} \theta_{\text{HCO}_{\text{CoPd}}} \theta_{\text{Co}}^* - k_{rD} \theta_{\text{HCO}_{\text{Co}}} \theta_{\text{CoPd}}^* \quad (40)$$

where k_{fD} and k_{rD} are diffusion rate constants calculated similar to reaction rate constants. The activation energies for diffusion reactions were calculated using the CI-NEB method. Additionally, the diffusion barrier for CH_3CH_2^* was assumed identical to that of a methyl group. In total, there are twenty-two reversible diffusion reactions considered in the microkinetic model. Diffusion reactions and activation energies for diffusion

processes are presented in Table 5.3. The uncorrected activation energies measured by DFT methods for diffusion processes D1-D20 were previously calculated by Dr. M. He. ³⁹

Table 5. 3. Activation energies for key diffusion reactions D1 to D22 corrected by a factor of 0.7

S.NO	Reaction	Eaf	Ear
D1	$\text{HCO}^*_{\text{CoPd}+\text{Co}} \leftrightarrow \text{HCO}^*_{\text{Co}+\text{CoPd}}$	0.83	0.41
D2	$\text{HCO}^*_{\text{CoPd}+\text{Pd}} \leftrightarrow \text{HCO}^*_{\text{Pd}+\text{CoPd}}$	0.88	1.53
D3	$\text{CH}_2\text{O}^*_{\text{CoPd}+\text{Co}} \leftrightarrow \text{CH}_2\text{O}^*_{\text{Co}+\text{CoPd}}$	0.53	0.22
D4	$\text{CH}_2\text{O}^*_{\text{CoPd}+\text{Pd}} \leftrightarrow \text{CH}_2\text{O}^*_{\text{Pd}+\text{CoPd}}$	0.20	0.70
D5	$\text{CH}_3\text{O}^*_{\text{CoPd}+\text{Co}} \leftrightarrow \text{CH}_3\text{O}^*_{\text{Co}+\text{CoPd}}$	0.27	0.56
D6	$\text{CH}_3\text{O}^*_{\text{CoPd}+\text{Pd}} \leftrightarrow \text{CH}_3\text{O}^*_{\text{Pd}+\text{CoPd}}$	0.44	1.23
D7	$\text{CH}_3\text{CO}^*_{\text{CoPd}+\text{Co}} \leftrightarrow \text{CH}_3\text{CO}^*_{\text{Co}+\text{CoPd}}$	0.87	0.95
D8	$\text{CH}_3\text{CO}^*_{\text{CoPd}+\text{Pd}} \leftrightarrow \text{CH}_3\text{CO}^*_{\text{Pd}+\text{CoPd}}$	1.07	0.95
D9	$\text{CH}_3\text{COH}^*_{\text{CoPd}+\text{Co}} \leftrightarrow \text{CH}_3\text{COH}^*_{\text{Co}+\text{CoPd}}$	1.29	0.61
D10	$\text{CH}_3\text{COH}^*_{\text{CoPd}+\text{Pd}} \leftrightarrow \text{CH}_3\text{COH}^*_{\text{Pd}+\text{CoPd}}$	1.69	1.77
D11	$\text{CH}_3\text{CHOH}^*_{\text{CoPd}+\text{Co}} \leftrightarrow \text{CH}_3\text{CHOH}^*_{\text{Co}+\text{CoPd}}$	0.96	0.74
D12	$\text{CH}_3\text{CHOH}^*_{\text{CoPd}+\text{Pd}} \leftrightarrow \text{CH}_3\text{CHOH}^*_{\text{Pd}+\text{CoPd}}$	0.55	0.37
D13	$\text{OH}^*_{\text{CoPd}+\text{Co}} \leftrightarrow \text{OH}^*_{\text{Co}+\text{CoPd}}$	0.25	0.69
D14	$\text{OH}^*_{\text{CoPd}+\text{Pd}} \leftrightarrow \text{OH}^*_{\text{Pd}+\text{CoPd}}$	0.76	1.15
D15	$\text{CH}_2\text{CHO}^*_{\text{CoPd}+\text{Co}} \leftrightarrow \text{CH}_2\text{CHO}^*_{\text{Co}+\text{CoPd}}$	1.04	1.30
D16	$\text{CH}_2\text{CHO}^*_{\text{CoPd}+\text{Pd}} \leftrightarrow \text{CH}_2\text{CHO}^*_{\text{Pd}+\text{CoPd}}$	0.57	1.10
D17	$\text{CH}_2^*_{\text{CoPd}+\text{Co}} \leftrightarrow \text{CH}_2^*_{\text{Co}+\text{CoPd}}$	0.35	0.39
D18	$\text{CH}_2^*_{\text{CoPd}+\text{Pd}} \leftrightarrow \text{CH}_2^*_{\text{Pd}+\text{CoPd}}$	1.03	0.46
D19	$\text{CH}_3^*_{\text{CoPd}+\text{Co}} \leftrightarrow \text{CH}_3^*_{\text{Co}+\text{CoPd}}$	0.29	0.29
D20	$\text{CH}_3^*_{\text{CoPd}+\text{Pd}} \leftrightarrow \text{CH}_3^*_{\text{Pd}+\text{CoPd}}$	2.80	2.80
D21	$\text{CH}_3\text{CH}_2^*_{\text{CoPd}+\text{Co}} \leftrightarrow \text{CH}_3\text{CH}_2^*_{\text{Co}+\text{CoPd}}$	0.29	0.29
D22	$\text{CH}_3\text{CH}_2^*_{\text{CoPd}+\text{Pd}} \leftrightarrow \text{CH}_3\text{CH}_2^*_{\text{Pd}+\text{CoPd}}$	2.80	2.80

Effect of diffusion on product distribution

To understand the effects of diffusion on the overall selectivity towards the product formation, a multisite microkinetic model for the conversion of syngas to ethanol was run with and without the diffusion steps being included in the model. The reaction conditions were set to common experimental conditions. The temperature was maintained constant at 523 K, and the partial pressures of the reactants was $P_{\text{H}_2} = 6$ atm and $P_{\text{CO}} = 3$ atm, yielding an initial CO to H₂ molar ratio of reactants of 2 ($n_{\text{CO}}/n_{\text{H}_2}=2$). Microkinetic model results with and without diffusion

processes are compared in Table 5.4. The ratio of catalyst sites for this run was similar to the model catalyst that is $n_{Pd}=0.25$, $n_{CoPd}=0.50$ and $n_{Co}=0.25$. Selectivities were determined at a reaction time of 60 seconds.

Table 5. 4. Microkinetic model results with and without diffusion reactions compared to experimental results on CoPd catalyst

Product selectivities					
	Methane	Ethane	Methanol	Ethanol	Acetaldehyde
Without Diffusion	1.69	2.77	0.14	92.99	2.41
With diffusion	60.68	27.54	11.77	0	0
Experimental ²¹	41.1	25.8	18.8	5.6	-

From an examination of the data in Table 5.4, it is clear that surface diffusion processes have a significant impact on product selectivity. When the diffusion of intermediate species is not included, selectivity towards ethanol is highest at 92.99% indicating that ethanol was the major product; whereas, when the diffusion of the intermediate species was considered, ethanol formation is negligible. Further, the multisite microkinetic model results for a system with surface diffusion between sites compares well with the experimental data indicating that the major products formed on this catalyst are hydrocarbons.

The product distribution observed from the multisite microkinetic model with diffusion processes included is consistent with the activation energies of key reactions and the following reaction mechanism for ethanol formation. Specifically, key reaction

steps for ethanol formation include CO adsorption, followed by hydrogenation to HCO^* , which on further hydrogenation forms CH_2O^* and CH_3O^* species. The CH_xO^* species then dissociate to form CH_x^* species. The adsorbed CH_x^* intermediate then undergoes CO insertion and additional hydrogenation reactions to make ethanol. An ideal catalyst for ethanol formation must favor the formation of CH_x^* species, and should suppress further hydrogenation of CH_x^* species to form hydrocarbons. How each of the catalyst surfaces contributes to this mechanism is described in further detail below.

Palladium Sites

When isolated on an appropriate catalyst support, palladium metal sites would primarily catalyze syngas conversion to methanol (deduced from the results in Table 5.1). From the simulation results presented in Table 5.4 for syngas conversion *without* diffusion between catalysts sites, methanol accounts for less than 1% of the products formed. This low yield of methanol can be explained by looking at the activation energies of key reactions. Most reactions have very high activation energies on the palladium surface as compared to the other two surfaces (see Appendix C). For example, if we look at the reaction where HCO^* is hydrogenated to form CH_2O^* , the activation energy for the reaction on the Pd surface is 1.41 eV as compared to values of 0.64 eV and 0.6 eV on the cobalt and CoPd surfaces, respectively. Due to the high activation energies on this surface, most of the key reactions are not favorable; thus, methanol selectivity is low.

On the other hand, when surface intermediates are allowed to diffuse between catalyst sites, the rate of production of methanol is significantly higher. This results from the CH_2O^* intermediate being able to readily diffuse to Pd sites with only a 0.20 eV diffusion barrier from CoPd sites, where it is more favorably generated. The palladium bound CH_2O^* species then undergoes further hydrogenation to make methanol, which explains how the production of methanol increases from 0.14% to 11.77% when surface diffusion is allowed between catalyst sites. Further, the dissociation of CH_xO^* is not favorable on Pd sites; therefore, ethanol is not synthesized in appreciable amounts on palladium sites.

Cobalt-Palladium Interface Sites

By excluding surface diffusion processes with the Co_7Pd_6 cluster, the microkinetic model predicts that the major syngas reaction product is ethanol with a yield of 92.99%, and this is due to multiple factors. First, the activation energies for key reactions on the CoPd surface are comparable if not less than the respective activation energies on cobalt and palladium single-metal sites. Additionally, hydrogenation and CO insertion reactions are more favorable on CoPd sites when compared to the other two reaction sites. CoPd sites meet both the conditions for making an ideal catalyst for ethanol formation, favors the dissociation of CH_xO^* to CH_x^* species as well as CO insertion reactions. Finally, with the model Co_7Pd_6 catalyst, the ratio of Co, Pd and CoPd sites is 0.25, 0.25 and 0.5,

respectively. Thus, the greater number of CoPd sites leads to increased ethanol production.

With diffusion reactions included, the surface intermediates and reactions that are essential for ethanol formation are shown to occur on the CoPd surface, but with the activation energies of key diffusion processes being low for species transferring from CoPd sites to other surface sites, diffusion rates are faster than reaction rates on CoPd. Thus, the ethanol selectivity is almost zero for the mixed site catalyst undergoing diffusion.

Cobalt sites

Cobalt is an excellent catalyst for Fischer-Tropsch reactions leading to the production of longer-chain hydrocarbons. A close examination of the results shown in Table 5.1 reveals that when only cobalt sites are present the major products are methane and ethane (and likely higher hydrocarbons not modeled in this study). In the combined model containing all the three kinds of sites but lacking diffusion between sites, the rate at which CoPd sites make ethanol is faster than that of cobalt sites making hydrocarbons. Therefore, the selectivity towards hydrocarbons is less than 5%.

Inclusion of diffusion reactions into the multisite microkinetic model enables all of the key reaction intermediates formed on CoPd sites, CH_3O^* , CH_2^* , CH_3^* , and CH_3CH_2^* , to diffuse from the CoPd surface to neighboring cobalt sites. Upon diffusing to the cobalt sites, these intermediates are rapidly hydrogenated to methane and ethane

hydrocarbons, as the activation energy for hydrogenation reactions is low on cobalt sites. Thus, the inclusion of surface diffusion processes increases the hydrocarbon selectivity for the catalyst, and the percentage of hydrocarbon products increase from 5% to 88%. This results suggests that any ethanol selective catalyst should minimize the number of pure cobalt sites available for reaction either through catalyst synthesis or selective catalyst poisoning.

Microkinetic reaction model with varying catalyst composition

To understand catalyst composition effects on the final product distribution, the DFT-based multisite microkinetic model was used to simulate reaction outcomes for a range of catalyst compositions. Specifically, the catalysts modeled in this syngas conversion study contained three types of sites, Co, Pd and CoPd, where the surface fraction of each type was varied from 0.01 to 0.98, yielding approximately 4500 simulations. The results from these multisite microkinetic modeling studies are plotted on ternary diagrams, where the axes describe the surface fraction of the three types of sites (Co, Pd and CoPd). A separate ternary diagrams is shown for each of the four major products, methane, methanol, ethanol and ethane (see Figures 5.7 and 5.8). From these graphs it is evident that the product distribution is greatly affected by catalyst composition and by the inclusion of surface diffusion processes. A comparison of results with and without diffusion processes included in the model clearly shows that for small

mixed metal clusters, the accuracy of the microkinetic model (as compared to experimental data) was improved with the addition of surface diffusion processes.

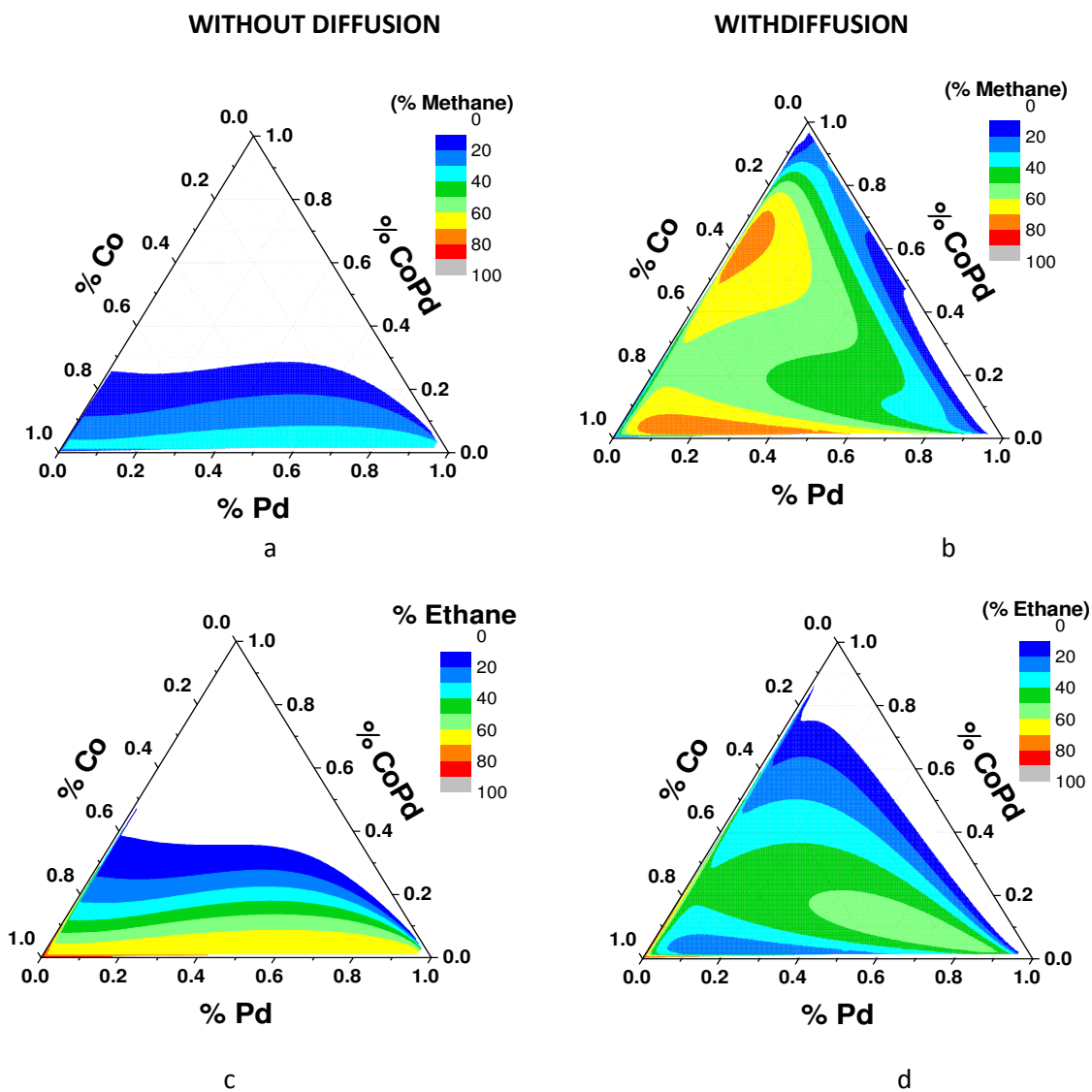


Figure 5. 7. Ternary diagrams for product selectivity with and without diffusion reactions included in the model. Product selectivity in (mol%) a) methane without diffusion, b) methane with diffusion, c) ethane without diffusion, d) ethane with diffusion Axis x, y and z represent concentrations of metal sites Pd, CoPd, Co sites respectively

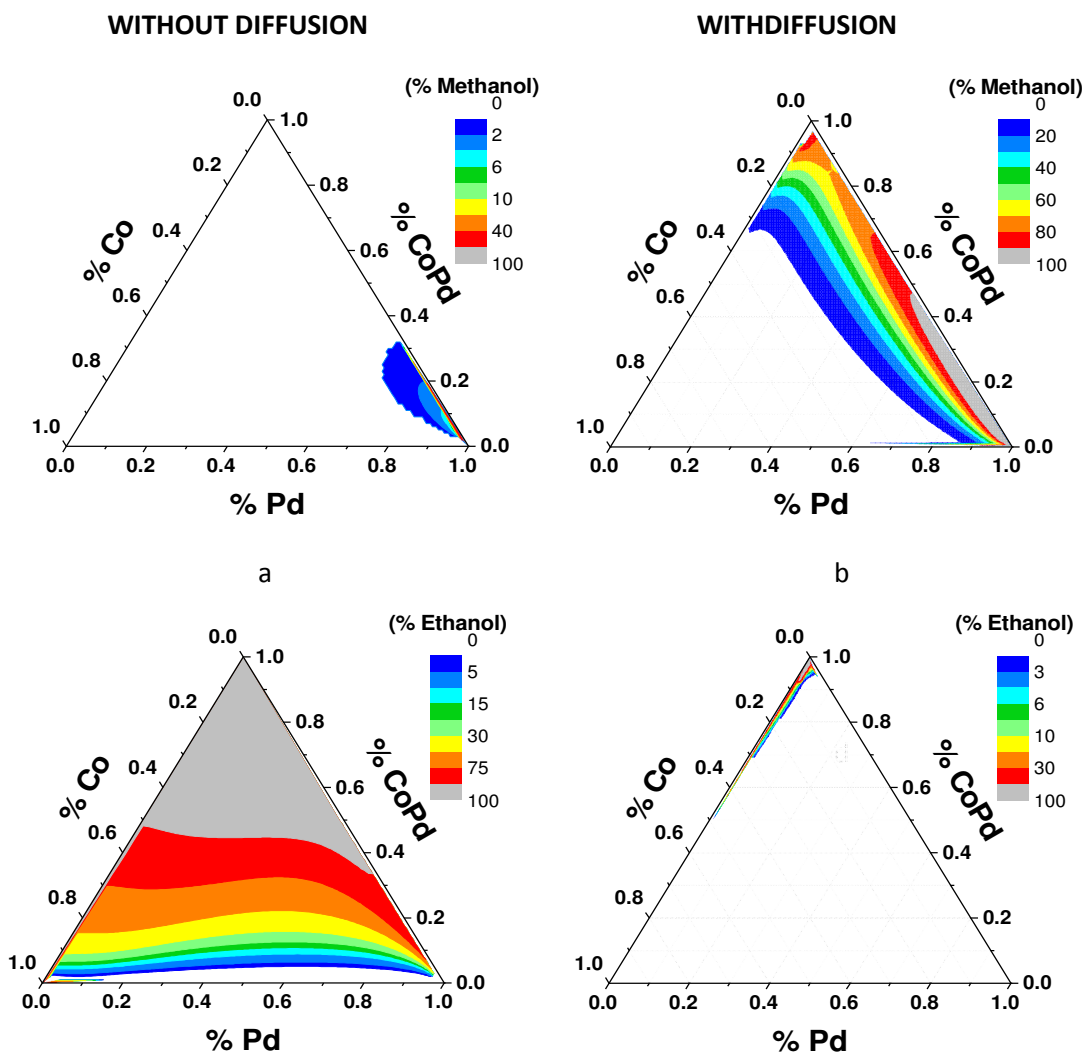


Figure 5. 8. Ternary diagrams for product selectivity with and without diffusion reactions included in the model. Product selectivity in (mol%) a) methanol with diffusion, b) methanol without diffusion, c) ethanol without diffusion, and d) ethanol with diffusion. Axis x, y and z represent concentrations of metal sites Pd, CoPd, Co sites respectively. Note that the scale for a and d is different

Hydrocarbons

The methane and ethane product fractions predicted by the microkinetic models with and without surface diffusion phenomena for syngas conversion over Co-Pd catalysts with varying composition are shown in Figure 5.7. Examination of the product

distributions with surface diffusion processes included indicate that the dominant products are hydrocarbons for most Co-Pd catalyst compositions. The concentrations of methane and ethane are low only when the catalyst contains more than 90% Pd sites.

Methanol

As the concentration of Pd in the catalyst increases, the selectivity towards methanol increases. At catalyst compositions consisting largely of palladium, methanol is nearly the sole product generated. Additionally, the concentration of cobalt sites should be less than 40% for the catalyst to make any methanol, and higher concentrations of methanol are seen at lower concentration of Co sites.

Ethanol

The microkinetic model predictions for ethanol product formation are shown in Figure 5.8. The maximum concentration of ethanol product is seen only when the CoPd site concentration is greater than 95%. Thus, to improve the selectivities of the catalyst, it is important to have more bimetallic sites on the catalyst. As the number of atoms in a Co-Pd catalyst particle increases, the bimetallic particles prefer to make core shell structures, reducing the number of bimetallic sites accessible on the catalyst. From this study it is evident that increasing the number of bimetallic active sites on the catalyst leads to greater ethanol selectivity.

How to improve ethanol selectivity?

Analysis of the syngas conversion reaction mechanism shown in Figure 5.6 shows that there are three reaction pathways to produce ethanol: the CO insertion, the hydroxycarbene, and the direct hydroxylation of CH_3CH_2^* pathways. The most favorable pathway is the CO insertion route due to the high concentration of CO on the surface of the catalyst. Thus, the activation energies for CO insertion steps heavily influence product selectivities.

Microkinetic model simulations for syngas conversion on separate catalyst sites predicted that ethanol would account for more than 95% of the observed products on CoPd sites, indicating that there is a synergetic effect between the metals contributing to an increase ethanol formation. Therefore, it is essential to have mixed metal (CoPd) sites for greater selectivity towards the desired ethanol product.

Simulations of syngas conversion over a range of catalysts having varying ratios of Co, Pd and CoPd sites using the multisite microkinetic model with diffusion between sites clearly showed that the reactivity and diffusion behavior associated with cobalt sites dominates the overall catalyst behavior, making hydrocarbons the favored reaction product. This is due to the low activation energies for most reactions on cobalt sites, especially hydrogenation reactions. It is observed that on the Co_7Pd_6 thirteen atom catalyst ethanol formation proceeds via CO adsorption, followed by hydrogenation, to form CH_x^* surface species. Thus, it is very important to have high concentrations of CH_x^* species to improve ethanol selectivity.

Although the concentration of CH_x^* species is high on cobalt sites, the activation energies for the necessary CO insertion reactions for ethanol formation are high compared to hydrogenation and CH_x^* insertion reactions favoring the FTS pathway. Thus, the other important ingredient for improving the ethanol selectivity of a Co-Pd catalyst is suppressing further hydrogenation of CH_x^* species. Given the difficulty of selective catalyst poisoning of cobalt metal sites and not CoPd mixed metal sites, the only viable strategy to create an ethanol selective CoPd catalyst is to synthesize a catalyst that largely contains CoPd mixed metal sites. It should also be noted that Pd only sites are not necessary for ethanol production, but the presence of palladium in the CoPd mixed metal sites is essential.

In summary, to achieve a high ethanol selectivity from the conversion of syngas over Co-Pd metal catalysts it is essential to have a very high concentration of mixed metal sites on the catalyst surface. In particular, the creation of large cobalt domains should be avoided. Further, the main pathway for ethanol formation on these mixed metal sites is through the CO insertion pathway. To improve the product selectivity towards ethanol, it is important to lower activation energies for CO insertion reactions and reduce CO adsorption strength so as to decrease the coverage of CO on the surface making more catalyst sites available for key reactions. The primary undesirable reactions in the ethanol reaction mechanism are hydrogenation reactions, where CH_x^* and CH_3CH_2^* species are hydrogenated to methane and ethane, respectively. Thus, suppression of these hydrocarbon formation reactions is a key fundamental for improved ethanol selectivity.

Conclusions

In this study, an extensive reaction network consisting of more than 250 elementary reactions was used to understand the syngas to ethanol reaction mechanism and the role of bimetallic sites on product selectivity. The multisite microkinetic model used in this study includes CO coverage effects as well as surface diffusion processes. A batch reactor is modeled, and the time evolution of product formation and concentration of intermediates is quantified for each type of catalyst surface site.

Results from the multisite microkinetic model presented herein are in good agreement with experimental results in part because the model accounted for CO coverage effects and the surface diffusion of intermediates between catalyst sites. In fact, the results from microkinetic models without diffusion yielded results that were very inconsistent with experimental data. Additionally, the concentration of intermediates on the surface of the catalyst at any time during the reaction can be determined from the microkinetic model, which enables one to more easily understand the interplay between adsorbed intermediates on differing catalyst sites. The time evolution of products from this model also compared well with experimental data from flowing reactor systems that more closely resemble the commercial reactors that would likely be used for the conversion of syngas to ethanol.

The uniqueness of this syngas to ethanol simulation study is derived from the inclusion of surface diffusion phenomena, CO coverage effects and Fischer-Tropsch type

reactions into a multisite microkinetic model for Co-Pd catalysts. The simulations showed that to significantly increase ethanol production it is imperative to have a high concentration of mixed CoPd sites, and a very low presence of cobalt only domains. It was also observed that the main reaction pathway for ethanol production is the CO insertion pathway. Finally, it is important to suppress Fischer-Tropsch type hydrocarbon forming reactions to improve the selectivity towards desired ethanol product.

References

1. Kerr RA. - Natural gas from shale bursts onto the scene. - *Science*. 2010;328(- 5986):- 1624.
2. Wang Q, Chen X, Jha AN, Rogers H. - Natural gas from shale formation – the evolution, evidences and challenges of shale gas revolution in united states. - *Renewable and Sustainable Energy Reviews*. 2014;30:- 1. doi: - <https://doi.org/10.1016/j.rser.2013.08.065>.
3. Chen S, Zhu Y, Wang H, Liu H, Fang J. - Shale gas reservoir characterisation: A typical case in the southern sichuan basin of china. - *Energy*. 2011;36(- 11):- 6609. doi: - <https://doi.org/10.1016/j.energy.2011.09.001>.
4. Al-Douri A, Sengupta D, El-Halwagi MM. - Shale gas monetization – A review of downstream processing to chemicals and fuels. - *Journal of Natural Gas Science and Engineering*. 2017;45:- 436. doi: - <https://doi.org/10.1016/j.jngse.2017.05.016>.

5. He C, You F. - Toward more cost-effective and greener chemicals production from shale gas by integrating with bioethanol dehydration: Novel process design and simulation-based optimization. - *AIChE Journal*. 2014;61(- 4):- 1209. doi: - 10.1002/aic.14713.
6. Peña MA, J.P.Gómez JP, Fierro JLG. - New catalytic routes for syngas and hydrogen production. - *Applied Catalysis A: General*. 1996;144(- 1):- 7. doi: - [https://doi.org/10.1016/0926-860X\(96\)00108-1](https://doi.org/10.1016/0926-860X(96)00108-1).
7. Garzon FP, He M, Bruce DA. - Ab initio derived reaction mechanism for the dry reforming of methane on rh doped pyrochlore catalysts. - *Journal of Catalysis*. 2016;333:- 59. doi: - <https://doi.org/10.1016/j.jcat.2015.10.017>.
8. Hickman DA, Schmidt LD. Production of syngas by direct catalytic oxidation of methane. . 1993;259(- 5093):- 343.
9. Goldemberg J. - Ethanol for a sustainable energy future. - *Science*. 2007;315(- 5813):- 808.
10. Agarwal AK. - Biofuels (alcohols and biodiesel) applications as fuels for internal combustion engines. - *Progress in Energy and Combustion Science*. 2007;33(- 3):- 233. doi: - <https://doi.org/10.1016/j.pecs.2006.08.003>.

11. Yüksel F, Yüksel B. - The use of ethanol–gasoline blend as a fuel in an SI engine. - *Renewable Energy*. 2004;29(- 7):- 1181. doi: - <https://doi.org/10.1016/j.renene.2003.11.012>.
12. Subramani V, Gangwal SK. - A review of recent literature to search for an efficient catalytic process for the conversion of syngas to ethanol. - *Energy Fuels*. 2008;22(- 2):- 814. doi: - 10.1021/ef700411x.
13. Wang JJ, Xie jR, Huang YH, Chen BH, Lin GL, Zhang HB. - An efficient Ni–Mo–K sulfide catalyst doped with CNTs for conversion of syngas to ethanol and higher alcohols. - *Applied Catalysis A: General*. 2013;468(-):- 44. doi: - <http://dx.doi.org/10.1016/j.apcata.2013.08.026>.
14. Liu YJ, Zuo ZH, Li C, Deng X, Huang W. - Effect of preparation method on CuZnAl catalysts for ethanol synthesis from syngas. - *Applied Surface Science*. 2015;356(-):- 124. doi: - <http://dx.doi.org/10.1016/j.apsusc.2015.08.039>.
15. Haider MA, Gogate MR, Davis RJ. - Fe-promotion of supported rh catalysts for direct conversion of syngas to ethanol. - *Journal of Catalysis*. 2009;261(- 1):- 9. doi: - <https://doi.org/10.1016/j.jcat.2008.10.013>.
16. Wang J, Zhang Q, Wang Y. - Rh-catalyzed syngas conversion to ethanol: Studies on the promoting effect of FeOx. - *Catalysis Today*. 2011;171(- 1):- 257. doi: - <http://dx.doi.org/10.1016/j.cattod.2011.03.023>.

17. Portillo MA, Perales AL, Barrero FV, Campoy M. - A kinetic model for the synthesis of ethanol from syngas and methanol over an alkali-co doped molybdenum sulfide catalyst: Model building and validation at bench scale. - *Fuel Processing Technology*. 2016;151(-):- 19. doi: - <http://dx.doi.org/10.1016/j.fuproc.2016.05.027>.
18. Han L, Mao D, Yu J, Guo Q, Lu G. - C2-oxygenates synthesis through CO hydrogenation on SiO₂-ZrO₂ supported rh-based catalyst: The effect of support. - *Applied Catalysis A: General*. 2013;454(-):- 81. doi: - <http://dx.doi.org/10.1016/j.apcata.2013.01.008>.
19. Fan Z, Chen W, Pan X, Bao X. - Catalytic conversion of syngas into C2 oxygenates over rh-based catalysts—Effect of carbon supports. - *Catalysis Today*. 2009;147(- 2):- 86. doi: - <https://doi.org/10.1016/j.cattod.2009.03.004>.
20. Lu Y, Yu F, Hu J, Liu j. - Catalytic conversion of syngas to mixed alcohols over zn-mn promoted cu-fe based catalyst. - *Applied Catalysis A: General*. 2012;429-430(-):- 48. doi: - <http://dx.doi.org/10.1016/j.apcata.2012.04.005>.
21. Kumar N, Smith ML, Spivey JJ. - Characterization and testing of silica-supported cobalt–palladium catalysts for conversion of syngas to oxygenates. - *Journal of Catalysis*. 2012;289(-):- 218. doi: - <http://dx.doi.org/10.1016/j.jcat.2012.02.011>.
22. Hu J, Wang Y, Cao C, Elliott DC, Stevens DJ, White JF. - Conversion of biomass-derived syngas to alcohols and C2 oxygenates using supported rh catalysts in a

microchannel reactor. - *Catalysis Today*. 2007;120(- 1):- 90. doi: -
<https://doi.org/10.1016/j.cattod.2006.07.006>.

23. Mei D, Rousseau R, Kathmann SM, et al. - Ethanol synthesis from syngas over rh-based/SiO₂ catalysts: A combined experimental and theoretical modeling study. - *Journal of Catalysis*. 2010;271(- 2):- 325. doi: -
<https://doi.org/10.1016/j.jcat.2010.02.020>.

24. Subramanian ND, Gao J, Mob X, JGoodwinJr. Jg, Torres W, Spivey JJ. - La, V, and Fe promotion of rh/SiO₂ for CO hydrogenation: Effect on adsorption and reaction. - *Journal of Catalysis*. 2010;272(- 2):- 167. doi: - <https://doi.org/10.1016/j.jcat.2009.08.007>.

25. Subramani V, Gangwal SK. - A review of recent literature to search for an efficient catalytic process for the conversion of syngas to ethanol. - *Energy Fuels*. 2008;22(- 2):- 814. doi: - 10.1021/ef700411x.

26. Choi YM, Liu P. - Mechanism of ethanol synthesis from syngas on rh(111). - *J Am Chem Soc*. 2009;131(- 36):- 13054. doi: - 10.1021/ja903013x.

27. Gupta M, Smith ML, Spivey JJ. - Heterogeneous catalytic conversion of dry syngas to ethanol and higher alcohols on Cu-based catalysts. - *ACS Catal*. 2011;1(- 6):- 641. doi: - 10.1021/cs2001048.

28. Yates IC, Satterfield CN. - Intrinsic kinetics of the fischer-tropsch synthesis on a cobalt catalyst. - *Energy Fuels*. 1991;5(- 1):- 168. doi: - 10.1021/ef00025a029.
29. Khodakov AY, Chu W, Fongarland P. - Advances in the development of novel cobalt Fischer–Tropsch catalysts for synthesis of long-chain hydrocarbons and clean fuels. - *Chem Rev*. 2007;107(- 5):- 1692. doi: - 10.1021/cr050972v.
30. Iglesia E. - Design, synthesis, and use of cobalt-based fischer-tropsch synthesis catalysts. - *Applied Catalysis A: General*. 1997;161(- 1):- 59. doi: - [https://doi.org/10.1016/S0926-860X\(97\)00186-5](https://doi.org/10.1016/S0926-860X(97)00186-5).
31. Fajula F, Anthony RG, Lunsford JK. - Methane and methanol synthesis over supported palladium catalysts. - *Journal of Catalysis*. 1982;73(- 2):- 237. doi: - [https://doi.org/10.1016/0021-9517\(82\)90098-7](https://doi.org/10.1016/0021-9517(82)90098-7).
32. Kelly KP, Tatsumi T, Uematsu T, Driscoll DJ, Lunsford JH. - Methanol synthesis over palladium supported on silica. - *Journal of Catalysis*. 1986;101(- 2):- 396. doi: - [https://doi.org/10.1016/0021-9517\(86\)90267-8](https://doi.org/10.1016/0021-9517(86)90267-8).
33. Yasuo K, Setsuko K, Shuichi N, Takaharu O, Kenzi T. - Selective methanol formation from atmospheric co and h₂ over novel palladium catalysts. - *Chem Lett*. 1981;9(- 9):- 1249. doi: - 10.1246/cl.1981.1249.

34. Henkelman G. - A climbing image nudged elastic band method for finding saddle points and minimum energy paths. - *The Journal of Chemical Physics*. 2000;113(- 22):- 9901. doi: - 10.1063/1.1329672.
35. Chen Y, Saliccioli M, Vlachos DG. - An efficient reaction pathway search method applied to the decomposition of glycerol on platinum. - *J Phys Chem C*. 2011;115(- 38):- 18707. doi: - 10.1021/jp205483m.
36. Michaelides A, Liu ZP, Zhang CJ, Alavi A, King DA, Hu P. - Identification of general linear relationships between activation energies and enthalpy changes for dissociation reactions at surfaces. - *J Am Chem Soc*. 2003;125(- 13):- 3704. doi: - 10.1021/ja027366r.
37. Liu C, Cundari TR, Wilson AK. - CO₂ reduction on transition metal (fe, co, ni, and cu) surfaces: In comparison with homogeneous catalysis. - *J Phys Chem C*. 2012;116(- 9):- 5681. doi: - 10.1021/jp210480c.
38. Ferrin P, Simonetti D, Kandoi S, et al. - Modeling ethanol decomposition on transition metals: A combined application of scaling and Brønsted–Evans–Polanyi relations. - *J Am Chem Soc*. 2009;131(- 16):- 5809. doi: - 10.1021/ja8099322.
39. He M. *A computational approach for the rational design of bimetallic clusters for ethanol formation from syn-gas.* ; 2013.

40. Rinalso D, Tian L, Garvey JN, Friesner RA. - Density functional localized orbital corrections for transition metals. - *The Journal of Chemical Physics*. 2008;129(- 16):- 164108. doi: - 10.1063/1.2974101.
41. Schneebeli ST, Bochevarov A,D, Friesner RA. - Parameterization of a B3LYP specific correction for noncovalent interactions and basis set superposition error on a gigantic data set of CCSD(T) quality noncovalent interaction energies. - *J Chem Theory Comput*. 2011;7(- 3):- 658. doi: - 10.1021/ct100651f.
42. Dooling DJ, Rekoske JE, Broadbelt LJ. - Microkinetic models of catalytic reactions on nonuniform surfaces: Application to model and real systems. - *Langmuir*. 1999;15(- 18):- 5846. doi: - 10.1021/la981376h.
43. Grabow LC, Gokhale AA, Evans ST, Dumesic JA, Mavrikakis M. - Mechanism of the water gas shift reaction on pt: First principles, experiments, and microkinetic modeling. - *J Phys Chem C*. 2008;112(- 12):- 4608. doi: - 10.1021/jp7099702.
44. Cortright RD, Dumesic JA. - Kinetics of heterogeneous catalytic reactions: Analysis of reaction schemes. . 2001;46:- 161. doi: - [https://doi.org/10.1016/S0360-0564\(02\)46023-3](https://doi.org/10.1016/S0360-0564(02)46023-3).
45. Behm RJ, Christmann K, Ertl G. - Adsorption of CO on pd(100). - *The Journal of Chemical Physics*. 2008;73(- 6):- 2984. doi: - 10.1063/1.440430.

46. Lahtinen J, Kauraala KK. - Adsorption and structure dependent desorption of CO on co(0001). - *Surface Science*. 1998;418(- 3):- 502. doi: - [https://doi.org/10.1016/S0039-6028\(98\)00711-0](https://doi.org/10.1016/S0039-6028(98)00711-0).
47. Winterlin J, Volkering S, Janssens TVW, Zambelli T, Ertl G. - Atomic and macroscopic reaction rates of a surface-catalyzed reaction. - *Science*. 1997;278(- 5345):- 1931.
48. Lombardo SJ, Bell AT. - A review of theoretical models of adsorption, diffusion, desorption, and reaction of gases on metal surfaces. - *Surface Science Reports*. 1991;13(- 1):- 3. doi: - [https://doi.org/10.1016/0167-5729\(91\)90004-H](https://doi.org/10.1016/0167-5729(91)90004-H).
49. Shiang K-, Wei CM, Tsong TT. - A molecular dynamics study of self-diffusion on metal surfaces. - *Surface Science*. 1994;301(- 1):- 136. doi: - [https://doi.org/10.1016/0039-6028\(94\)91295-5](https://doi.org/10.1016/0039-6028(94)91295-5).
50. - Winterlin J. Existence of a "Hot" atom mechanism for the dissociation of O₂ on pt(111). *PhysRevLett*. 1996;77(- 1):- 123. doi: - 10.1103/PhysRevLett.77.123.

CHAPTER SIX

COMPOSITION EFFECTS OF COBALT – PALLADIUM BIMETALLIC CATALYSTS FOR ETHANOL SYNTHESIS FROM SYNGAS (CO+H₂)

Introduction

Though today crude oil remains the primary feedstock for transportation fuels, these resources are limited, may have deleterious effects on the environment, and are not uniformly available throughout the world. These various factors help drive efforts to identify alternative fuels that can be readily introduced into the existing transportation infrastructure and are ideally derived from widely available renewable sources. Ethanol is one such alternative liquid fuel, and it is presently derived from biological sources such as sugarcane and corn. These biological sources are difficult to transport and the final fermentation product is an azeotropic mixture of ethanol and water, which requires energy intensive processes to isolate the fuel grade ethanol product. Given the shortcomings of the existing ethanol production methods, it would be useful to identify alternative methods of ethanol production that are faster and could make use of a more diverse renewable feedstock. One such example would be a process for converting bio-derived methane into ethanol, and the most promising approach involves the methane gas first being converted into syngas, which can then later be reacted over an appropriate transition metal catalyst to yield ethanol with minimal side products.

Direct catalytic conversion of syngas to ethanol involves two steps, chain elongation to form a C-C bond and alcohol formation. Studies have shown that rhodium is an ideal catalyst for this conversion process, but the high cost and limited availability of this metal limits its use in large scale commercial processes. A lower cost alternative catalyst might be a bimetallic catalyst, with one metal that aids C-C bond formation (e.g., Co and Ni) and another metal that selectively forms alcohol products (e.g., Pt and Pd). In this study, cobalt and palladium bimetallic catalysts are considered as an alternative to rhodium for ethanol synthesis.

The reaction mechanism involves forty-six reversible reactions occurring on a thirteen atom cobalt-palladium catalysts (Co_7Pd_6) that contains a near equimolar ratio of metals. From the forty-six reactions studied, several key or rate limiting reactions were identified, and they are, CO adsorption on to the surface of the metal, followed by CO^* hydrogenation to form CH_3O^* , which then undergoes dissociation to form CH_3^* species. These CH_3^* species can either be hydrogenated to form hydrocarbons or undergo CO insertion to form ethanol. These key reactions are represented in Figure 6.1.

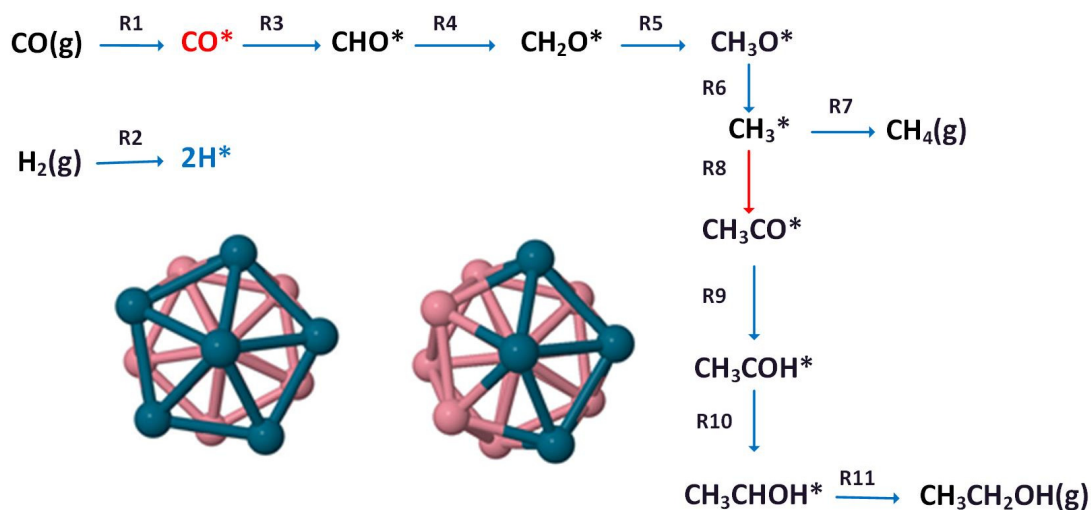


Figure 6. 1. Key reactions identified for the synthesis of ethanol from syngas and structures of the geometry optimized Co_7Pd_6 and Co_9Pd_4 clusters.

DFT modeling of syngas to ethanol reactions on the Co_7Pd_6 bimetallic catalyst indicate that the activation energies of key reactions are relatively high on palladium. Therefore, the primary role of palladium atoms is to provide CoPd mixed sites, which are key for ethanol formation. Also, adsorption studies from Chapter 3 indicate that CO the adsorption energy is high on the palladium surface as compared to the Co and CoPd surfaces, and due to this high adsorption energy, it is believed that most of the Pd sites are covered with CO. Results from the microkinetic model also indicate that most of the Pd surface sites are CO covered. The Chapter 3 CO adsorption studies also showed that the maximum number of CO atoms that can adsorb on Pd sites is six with atop configurations. In this chapter, we show the impact of CO coverage of the palladium surface on adsorption energies of key species on Co surfaces. Specifically, the Pd side of

the cluster is covered with six CO atoms, and the activation energies of the identified key reactions is calculated on Co side of the cluster.

Previous theoretical and experimental studies of metal alloy nanoparticles indicate that changes in catalyst composition alter the chemical and electro-chemical properties of the nanocluster, often termed as a ligand effect.¹⁻⁵ Therefore, the rational design of an optimal ethanol production catalysts requires a deep understanding of the composition and coverage effects that determine the catalyst properties.⁶⁻⁹ To gain this understanding, apart from coverage effects, we also studied the effects of cluster composition on the DFT calculated activation energies for key ethanol formation reactions.

To understand the coverage and composition effects on activation energies of key reactions, we recalculated these activation energies for two scenarios. Initially, to understand composition effect, the cluster composition was changed by increasing the number of cobalt atoms to nine from the initial number of seven, which changed the cluster composition from Co_7Pd_6 to Co_9Pd_4 . All activation energies were calculated using combined DFT and BEP methods. Secondly, to understand the coverage effects, Pd sites on the Co_7Pd_6 cluster were completely covered with CO, and the activation energies of identified key reactions on cobalt sites were calculated using the combined DFT and BEP methods discussed in Chapter 4.

Experimental

Initial structures were built using Material Studio. First principles DFT calculations were performed using Jaguar 7.0 with a combination of B3LYP hybrid functionals and the LACVP basis set. All of the DFT calculations involving metals were spin polarized and zero-point energy corrected. The energy convergence criterion for calculating energy changes was set to 10^{-5} Hartrees (0.03 KJ/mol).

a) Composition effects:

Initially, a thirteen-atom icosahedral structure consisting of nine cobalt and four palladium atoms was constructed. The catalyst structure was geometrically optimized using Jaguar, and the result was a cluster with segregated cobalt and palladium atoms. The optimum spin multiplicity was determined by calculating the minimum energy of the cluster at different spin states of 2 to 20. For these simulations, the geometry of the cluster was allowed to change. The cluster with the lowest energy was obtained at spin state 18.

Later simulations examined the adsorption behavior of nine intermediates, CO^* , H^* , CHO^* , CH_2O^* , CH_3O^* , CH_3^* , O^* , CH_3CO^* , CH_3COH^* , and CH_3CHOH^* , which were previously identified as being important for the formation of ethanol as well as possible side products, such as methane and methanol. For each intermediate, optimum binding site (e.g., atop, bridge, or 3-fold site) and spin state were determined, and the zero-point energy corrected total energy was calculated.

Heats of reaction for 11 key reactions were calculated as the difference between the minimum energy of the adsorbed products and reactants. The final activation energies for the key reactions were calculated using the linear BEP relationships described in Chapters 4 and 5.

b) Coverage effects on activation energies:

To understand CO coverage effects on the activation energies of key reactions, all palladium sites included atop bound CO ligands. With six CO molecules on the palladium surface, the geometries of nine key intermediates were optimized on the cobalt sites. From the total energy data, heats of reaction for the 11 key reactions is calculated and is shown in Figure 6.1 were calculated. A BEP relationship was then used to determine the activation energies for the 11 key reactions. The structure of the Co_7Pd_6 cluster with six CO ligands on palladium sites is represented in Figure 6.2.

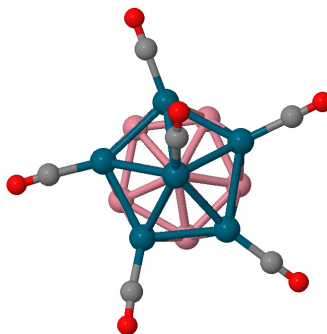


Figure 6. 2. Co_7Pd_6 cluster with CO ligands bound to each Pd surface site.

Results and Discussion

The key reactions for ethanol formation from syngas start with CO and H adsorption to the surface of the catalyst. These adsorption processes are then followed by the spontaneous hydrogenation of CO to form HCO^* , which further undergoes successive hydrogenations to form CH_3O^* on the surface. The CH_3O^* can undergo hydrogenation to form methanol, or it can dissociate to form CH_3^* and O^* species. The CH_3^* thus formed can either be hydrogenated and desorb from the surface as methane or undergo CO insertion to yield CH_3CO^* . Further hydrogenation of CH_3CO^* forms the desired ethanol product.

To further elaborate on the calculations performed in this study, we will use the hydrogenation of adsorbed CO^* ($\text{CO}^* + \text{H}^* \rightarrow \text{CHO}^* + *$) as an example. For this reaction, the heat of reaction is calculated as the difference in the enthalpy of the products and reactants,

$$\Delta H_r = \{\text{Energy of } \text{CHO}^* \text{ on cluster} + \text{Energy of empty cluster}\} - \{\text{Energy of } \text{CO}^* \text{ on cluster} + \text{Energy of } \text{H}^* \text{ on cluster}\} \quad (1)$$

For the Co_7Pd_6 cluster, the linear BEP relationship for association type reactions is

$$E_{\text{TS,ass}} = 0.8706 \Delta E_{\text{FS,ass}} + 0.4364, \quad R^2 = 0.96 \quad (2)$$

For dissociation type reactions, such as the dissociation of CHO^* to form adsorbed CO and hydrogen ($\text{CHO}^* + * \rightarrow \text{CO}^* + \text{H}^*$), the linear BEP relationship is

$$E_{TS,dis} = 1.0951 \Delta E_{FS,dis} + 2.0867, \quad R^2=0.94 \quad (3)$$

$E_{TS,ass}$ and $\Delta E_{FS,ass}$ are the transition state energy and final state energy of association type of reactions, respectively, and similarly, $E_{TS,dis}$ and $\Delta E_{FS,dis}$ are the transition state energy and final state energy of dissociation type of reactions, respectively. Using the calculated heats of reaction and gas phase energies, activation energies of key reactions were determined using BEP relationships represented by equation 2 and 3.

a. Cluster composition effects, a comparison of Co₉Pd₄ and Co₇Pd₆ bimetallic catalysts:

The activation energies of eleven key reactions on the Co₇Pd₆ bimetallic catalyst are compared with the activation energies observed for the same reactions on the cobalt rich Co₉Pd₄ catalysts, and these results are shown in Table 6.1. From an examinations of these results, it is clearly evident that activation energies are effected by change in cluster composition. For example, the reactants CO and H₂ both bond more strongly to the Co surface with the cobalt rich cluster. Specifically, the energy for CO adsorption is increased from 1.49 eV to 1.66 eV, and the energy for dissociative adsorption for H₂ is increased from 0.59 to 1.43 eV. Increased adsorption energies indicate stronger bonding between metal and adsorbent, potentially suggesting that it would be easier for the Co surface to become covered with the reactants making vacant active sites less available for other reactions.

Table 6. 1. Cluster composition effects, a comparison of activation energies of key syngas to ethanol reactions on Co₇Pd₆ and Co₉Pd₄ catalysts.

Rxn. #	Reactions	Co ₇ Pd ₆ ΔE _a (eV)	Co ₉ Pd ₄ ΔE _a (eV)
R1	CO(g)+*→CO*	-1.49	-1.66
R2	H ₂ (g)+2*→2H*	-0.59	-1.43
R3	CO*+H*→CHO*+*	1.85	2.08
R4	CHO*+H*→CH ₂ O*+*	0.92	1.20
R5	CH ₂ O*+H*→CH ₃ O*+*	0.29	0.85
R6	CH ₃ O*→CH ₃ *+O*	1.36	1.56
R7	CH ₃ *+H*→CH ₄ (g)+2*	1.24	1.05
R8	CH ₃ *+CO*→CH ₃ CO*+*	1.71	1.57
R9	CH ₃ CO*+H*→CH ₃ COH*+*	1.97	2.68
R10	CH ₃ COH*+H*→CH ₃ CHOH*+*	1.51	1.26
R11	CH ₃ CHOH*+H*→CH ₃ CH ₂ OH(g)+2*	0.43	1.07

Activation energies for reactions involving the successive hydrogenation of CO are also increased for the Co₉Pd₄ cluster, making them less favorable. Additionally, the activation energies for both CH₃* hydrogenation to form methane and CO insertion to make alcohols are less on the cobalt rich cluster compared to Co₇Pd₆ cluster. However, the energy for CH₄ formation is more favorable than that for the CO insertion reaction, indicating that the cobalt rich catalyst favors methane and higher hydrocarbon formation rather than ethanol formation.

In general, as the fraction of Co atoms in the catalyst cluster increases, the activation energies for most of the key reactions needed for ethanol production are increased, suggesting that electronic effects from neighboring palladium

atoms induce changes in the orbital energy levels on cobalt atoms in a way that favors the production of methane.

Table 6. 2. Activation energy trends for different types of reaction on Co rich surface and Co₇Pd₆ surface

S.NO	Reactions	ΔE_a (ev)	
		Co ₉ Pd ₄	Co ₇ Pd ₆
Hydrogenation			
1	CO*+H*→CHO*+*	2.08	1.85
2	CHO*+H*→CH ₂ O*+*	1.20	0.92
3	CH ₂ O*+H*→CH ₃ O*+*	0.85	0.29
Hydrogenation			
4	CH*+H*→CH ₂ *+*	1.49	0.44
5	CH ₂ *+H*→CH ₃ *+*	1.31	0.77
6	CH ₃ *+H*→CH ₄ (g)+2*	1.05	1.24
CO insertion			
7	CH*+CO*→CHCO*+*	1.39	0.94
8	CH ₃ *+CO*→CH ₃ CO*+*	1.57	1.71
Dissociation			
9	CHO*+*→CH*+O*	1.35	1.75
10	CH ₂ O*+*→CH ₂ *+O*	1.26	1.37
11	CH ₃ O*+*→CH ₃ *+O*	1.56	1.36
Hydrogenation			
12	CH ₃ CO*+H*→CH ₃ COH*+*	2.68	1.97
13	CH ₃ COH*+H*→CH ₃ CHOH*+*	1.26	1.51
14	CH ₃ CHOH*+H*→CH ₃ CH ₂ OH(g)+2*	1.07	0.43

The following key observations can be made from the activation energies for forward reactions on cobalt rich Co₉Pd₄ cluster and equimolar Co₇Pd₆ surfaces, which are presented in Table 6.2.

1. Activation energies for most Co catalyzed reactions are higher on catalysts enriched with cobalt, indicating that the selectivity towards ethanol is reduced

with increases in the cobalt content of the catalyst. This could be due to the electronic effects from neighboring palladium atoms induce changes in the orbital energy levels on cobalt atoms in a way that favors the production of methane.

2. Based on the data in Table 6.2, it can be noted that successive hydrogenations of CO become more favorable as the hydrogen saturation of the intermediate is increased, irrespective of catalyst composition.
3. As the weight fraction of cobalt in the bimetallic catalyst increases, there is a significant increase in the activation energy for CO* insertion reactions and CH₃CO* hydrogenation reactions, making the Co rich catalyst less favorable for ethanol formation.
4. Activation energies for CH_x* dissociation to make CH* and CH₂* species are reduced when the catalyst is enriched with cobalt. Further, the increased surface concentrations of CH_x* species favors methane formation on cobalt rich catalysts.

b. CO Coverage effects for the Co₇Pd₆ bimetallic catalyst

We have seen from Chapter 3 that as the number of CO atoms on the Pd sites increases, the binding site preferences for CO change from bridge to atop so as to accommodate a maximum number of CO molecules on the palladium surface. The limit for CO adsorption capacity on palladium equals one CO per palladium surface atom or six CO molecules adsorbed on the Co₇Pd₆ cluster. To

understand how reactions on Co sites are influenced by CO coverage on the palladium sites of the cluster, activation energies for the 11 key reactions on cobalt sites were calculated for conditions where the palladium surface was saturated with adsorbed CO species. The results of these simulation are presented in Table 6.3.

Table 6. 3. CO coverage effects, a comparison of activation energies of key syngas to ethanol reactions on a pristine Co_7Pd_6 cluster and a $\text{Co}_7\text{Pd}_6(\text{CO})_6$ cluster having Pd sites saturated with CO.

S.NO	Reactions	Co_7Pd_6 ΔE_a (eV)	With coverage ΔE_a (eV)
R1	$\text{CO}(\text{g})+\ast \rightarrow \text{CO}^\ast$	-1.49	-0.91
R2	$\text{H}_2(\text{g})+2\ast \rightarrow 2\text{H}^\ast$	-0.59	-0.78
R3	$\text{CO}^\ast+\text{H}^\ast \rightarrow \text{CHO}^\ast+\ast$	1.85	1.87
R4	$\text{CHO}^\ast+\text{H}^\ast \rightarrow \text{CH}_2\text{O}^\ast+\ast$	0.92	0.88
R5	$\text{CH}_2\text{O}^\ast+\text{H}^\ast \rightarrow \text{CH}_3\text{O}^\ast+\ast$	0.29	0.83
R6	$\text{CH}_3\text{O}^\ast \rightarrow \text{CH}_3^\ast+\text{O}^\ast$	1.36	1.56
R7	$\text{CH}_3^\ast+\text{H}^\ast \rightarrow \text{CH}_4(\text{g})+2\ast$	1.24	0.31
R8	$\text{CH}_3^\ast+\text{CO}^\ast \rightarrow \text{CH}_3\text{CO}^\ast+\ast$	1.71	0.45
R9	$\text{CH}_3\text{CO}^\ast+\text{H}^\ast \rightarrow \text{CH}_3\text{COH}^\ast+\ast$	1.97	2.04
R10	$\text{CH}_3\text{COH}^\ast+\text{H}^\ast \rightarrow \text{CH}_3\text{CHOH}^\ast+\ast$	1.51	0.63
R11	$\text{CH}_3\text{CHOH}^\ast+\text{H}^\ast \rightarrow \text{CH}_3\text{CH}_2\text{OH}(\text{g})+2\ast$	0.43	0.89

It was noted from earlier studies that as the surface coverage on a given metal surface increases, the adsorption energy decreases.¹ This could be due to crowding effect or electron withdrawing effects. The same holds true for atoms experiencing some type of electronic interaction with neighboring metal atoms. Specifically, for the Co_7Pd_6 cluster, the adsorption energy for CO on cobalt sites

are decreased when CO coverage on the cluster palladium sites increases. The decrease in adsorption energy could be due to the electronic effects resulting from having transition metals in close proximity. Although, the CO coverage did not affect the activation energies of hydrogenation of CO^* to HCO^* and then to CH_2O^* , the activation energy for further hydrogenation to CH_3O^* is increased. For CH_3^* hydrogenation reaction (R6), the activation energy is reduced from 1.24 eV to 0.31 eV, favoring methane formation. Additionally, the activation energy for the CO insertion reaction with CH_3O^* is also reduced from 1.71 eV to 0.54, favoring the reaction, but the activation energy for the hydrogenation of CH_3CHOH^* (R11) is very high, making the catalyst less favorable to ethanol formation. It can be observed that the activation energies for most of the key syngas to ethanol reactions are reduced by CO coverage on Pd sites.

Table 6. 4. Activation energy trends for different types of reaction on Co₇Pd₆ surface at high and low coverage

S.NO	Reactions	ΔE_a (ev)	
		With coverage	No coverage
Hydrogenation			
1	$\text{CO}^* + \text{H}^* \rightarrow \text{CHO}^* + ^*$	1.87	1.85
2	$\text{CHO}^* + \text{H}^* \rightarrow \text{CH}_2\text{O}^* + ^*$	0.88	0.92
3	$\text{CH}_2\text{O}^* + \text{H}^* \rightarrow \text{CH}_3\text{O}^* + ^*$	0.83	0.29
Hydrogenation			
4	$\text{CH}^* + \text{H}^* \rightarrow \text{CH}_2^* + ^*$	0.91	0.89
5	$\text{CH}_2^* + \text{H}^* \rightarrow \text{CH}_3^* + ^*$	1.17	0.77
6	$\text{CH}_3^* + \text{H}^* \rightarrow \text{CH}_4(\text{g}) + 2^*$	0.31	1.24
CO insertion			
7	$\text{CH}^* + \text{CO}^* \rightarrow \text{CHCO}^* + ^*$	0.57	0.94
8	$\text{CH}_2^* + \text{CO}^* \rightarrow \text{CH}_2\text{CO}^* + ^*$	0.73	1.36
9	$\text{CH}_3^* + \text{CO}^* \rightarrow \text{CH}_3\text{CO}^* + ^*$	0.45	1.71
Dissociation			
10	$\text{CHO}^* + ^* \rightarrow \text{CH}^* + \text{O}^*$	2.23	1.75
11	$\text{CH}_2\text{O}^* + ^* \rightarrow \text{CH}_2^* + \text{O}^*$	1.81	1.37
12	$\text{CH}_3\text{O}^* + ^* \rightarrow \text{CH}_3^* + \text{O}^*$	1.56	1.36
Hydrogenation			
13	$\text{CH}_3\text{CO}^* + \text{H}^* \rightarrow \text{CH}_3\text{COH}^* + ^*$	2.04	1.97
14	$\text{CH}_3\text{COH}^* + \text{H}^* \rightarrow \text{CH}_3\text{CHOH}^* + ^*$	0.63	1.51
15	$\text{CH}_3\text{CHOH}^* + \text{H}^* \rightarrow \text{CH}_3\text{CH}_2\text{OH}(\text{g}) + 2^*$	0.89	0.43

The following key observations can be made from the activation energies for forward reactions on Co₇Pd₆ surfaces at high and low Co surface coverages, which are presented in Table 6.4

1. Activation energies for hydrogenation and dissociation reactions were found to be consistently higher with coverage. Most strikingly, the activation energy for CH_2^* hydrogenation increased by 1 eV with monolayer CO coverage on Pd sites.
2. Activation energies for CO^* hydrogenation to form HCO^* and CH_3CO^* hydrogenation to form CH_3CO^* are invariant with CO coverage.
3. CO undergoes successive hydrogenations to form CH_2O^* and CH_3O^* species, and these reactions are favorable on Co sites independent of the CO coverage on Pd sites.
4. Monolayer coverage of Pd sites with CO leads to the activation energy for CH_3^* hydrogenation to CH_4 to decreased by nearly 1 eV, suggesting that the selectivity towards methane is highly favorable under conditions with high CO coverage on the catalyst surface.
5. CO insertion reactions are less energy intensive when Pd catalyst sites are saturated with CO.
6. Dissociation of CH_xO^* species is less favorable at high surface coverages of CO, which reduces the concentrations of CH_x^* species on the catalyst surface, making it less favorable for ethanol to be formed in appreciable amounts.

Conclusions

The influence of composition effects and CO adsorption effects on the CoPd bimetallic 13 atom catalyst were investigated using first principles based DFT calculations.

On the Co rich surface, the adsorption energy for both CO and H increased, although the geometry of the adsorbed species was unaffected, indicating local surface electronic effects with a change in the catalyst composition. Activation energies for most of the key reactions also increased. From the relative activation energies of R7 and R8 reactions, it can be concluded that increasing the percentage of Co in the 13 atom cluster increases selectivity towards the undesired methane product. As the number of cobalt atoms is increased, activation energies of key syngas to ethanol reactions are increased; thus, the overall rate of reactions on Co sites are reduced.

In contrast, coverage of Pd sites on the Co_7Pd_6 cluster with six CO atoms reduced the activation energies of most of the reactions, which could be due to the reduced adsorption strength with increased number of molecules on the surface of the catalyst. For example, CO adsorption energy is decreased from -1.49 eV to -0.91 eV, and the activation energy for CH_3^* hydrogenation is reduced from 1.24 eV to 0.31 eV favoring the methane formation. This latter observation suggests that active sites from metals other than cobalt are essential to convert syngas to methanol. It also has implications for the size of the metal cluster. For the specific case examined herein, Co and Pd can segregate into a core-shell structure with cobalt on the outside of the cluster; thus, it would be important to maintain the cluster size and composition such that some palladium atoms could be exposed, else methane would likely be the primary product.

References

1. Das KN, Shoji T. - Adsorption and diffusion of H and O on an ni(111) surface containing different amounts of cr. - *Applied Surface Science*. 2018;445:- 217. doi: - <https://doi.org/10.1016/j.apsusc.2018.03.134>.
2. Chen W, Kim J, Sun S, Chen S. - Composition effects of FePt alloy nanoparticles on the electro-oxidation of formic acid. - *Langmuir*. 2007;23(- 22):- 11303. doi: - [10.1021/la7016648](https://doi.org/10.1021/la7016648).
3. Liu P, Logadottir A, Norskov JK. - Modeling the electro-oxidation of CO and H₂/CO on pt, ru, PtRu and Pt₃Sn. - *Electrochimica Acta*. 2003;48(- 25):- 3731. doi: - [https://doi.org/10.1016/S0013-4686\(03\)00538-3](https://doi.org/10.1016/S0013-4686(03)00538-3).
4. - Sakong S, - Mosch C, - Gro[German sz ligature] A. - CO adsorption on cu-pd alloy surfaces: Ligand versus ensemble effects. - *Phys Chem Chem Phys*. (- 18):- 2216. doi: - [10.1039/B615547B](https://doi.org/10.1039/B615547B).
5. Rodriguez JA, Chaturvedi S, Kuhn M. - The adsorption of sulfur on rh(111) and cu/rh(111) surfaces. - *The Journal of Chemical Physics*. 1997;108(- 7):- 3064. doi: - [10.1063/1.475697](https://doi.org/10.1063/1.475697).
6. Besenbacher F, Chorkendorff I, Clausen BS, et al. - Design of a surface alloy catalyst for steam reforming. - *Science*. 1998;279(- 5358):- 1913.

7. Greeley J, Mavrikakis M. Alloy catalysts designed from first principles. - *Nature Materials*. 2004;- 810.
8. - Ismail R, - Johnston RL. - Investigation of the structures and chemical ordering of small pd-au clusters as a function of composition and potential parameterisation. - *Phys Chem Chem Phys*. (- 30):- 8607. doi: - 10.1039/C004044D.
9. Pašti I, Mentus S. - Electronic properties of the $Pt_xMe_{1-x}/Pt(111)$ (Me=Au, bi, in, pb, pd, sn and cu) surface alloys: DFT study. - *Materials Chemistry and Physics*. 2009;116(- 1):- 94. doi: - <https://doi.org/10.1016/j.matchemphys.2009.02.053>.

CHAPTER SEVEN

CONCLUSIONS AND RECOMMENDATIONS

Conclusions

Direct synthesis of ethanol from syngas using chemical catalysts is an attractive, alternative method for ethanol production, which can use fossil or renewable fuel feed stocks. In this study, a sub-nanometer sized thirteen-atom bimetallic cluster, consisting of cobalt and palladium (Co_7Pd_6) was investigated as a possible catalyst for ethanol synthesis. A detailed microkinetic model based on ab initio quantum calculations was developed to understand the overall reaction mechanism, quantify the relative amounts of products, and discern how catalyst composition impacts product selectivity.

The syngas to ethanol reaction mechanism developed in this study consists of 46 reversible elementary reactions consisting of twenty-four intermediates, two reactants and seven products. A differentiating aspect of this model was the inclusion of Fischer-Tropsch and multiple alcohol generating reactions. Density functional theory was used to determine the adsorption energies of twenty-four intermediates on three types of surface sites: cobalt, palladium and CoPd. Heats of reaction and entropies of reaction were also determined using DFT methods.

One of the first and important elementary steps in the syngas to ethanol reaction mechanism is the adsorption of CO. The energetics of CO binding as a function of CO

surface coverage on cobalt and palladium surface were modeled using DFT. It was determined that CO prefers to adsorb molecularly on both cobalt and palladium. On palladium surface, CO prefers to bind via a bridge configuration at low surface loadings, but at higher surface coverages, CO prefers an atop geometry. This study also confirms that the adsorption energy for CO decreases as number of adsorbed CO ligands on the surface increases up to three, and then it remains relatively constant. Additionally, the DFT modeling results included a comparison of two different functionals: the more accurate M06 model, which includes dispersion effects, and the widely used and computationally efficient B3LYP model. Although B3LYP performs reasonably well in describing CO binding, the inclusion of dispersion effects in the M06 models enables it to more accurately describe CO bonding, which includes back donation of electrons from the metal adsorption site to the CO ligand antibonding orbitals. However, for the larger syngas to ethanol reaction model, the B3LYP model was considerably more efficient and of sufficient accuracy that it was selected for this larger study. Theoretical vibrational frequencies obtained from Jaguar using the M06 functional also agree well with experimental values with less than 5% error.

DFT derived activation energies combined with linear BEP relationships allowed us to determine the activation energy of all 46 reversible elementary reactions included in the syngas to ethanol model. It was also observed that the activation energies from our study are uniformly high when compared to similar DFT studies and the limited experimental data available. Therefore, a scaling factor of 0.7 was used to scale activation

energies on Co and Pd sites, whereas activation energies on CoPd bimetallic sites were scaled by a factor of 0.53.

A microkinetic model was built to quantify product distributions and intermediate surface concentrations. This model also included carbon chain growth reactions important to Fischer-Tropsch reaction chemistry as well as all known reaction models for ethanol synthesis. Thus, this model is the first to be able to evaluate catalyst selectivities for both higher alcohol and higher alkane products. Initial microkinetic modeling used adsorption models based on the collision theory for syngas binding to the catalyst surface. This early model predicted that CO species occupied all available surface sites making other surface reactions impossible, which is obviously incorrect, given the general syngas reactivity of the metals involved. To model the system more accurately, coverage dependent sticking coefficients derived from experimental data were used to describe the CO adsorption process. Results from separate models for each type of catalyst site, Co, Pd, and CoPd indicated that cobalt surfaces catalyzed the conversion of syngas to methane and other higher hydrocarbons, while palladium yields methanol as the primary product, and ethanol is only produced on CoPd mixed sites. Results from these microkinetic models correlate well with the available experimental data.

Though these separate models helped us to understand the intrinsic nature of each of the sites, a combined reaction model is required to understand the reaction mechanism on the CoPd bimetallic catalyst. Specifically, it is important to include surface

diffusion processes along with surface reaction and adsorption/desorption phenomena into the microkinetic model. To reduce the computational time, diffusion processes were only considered for key species. The uniqueness of this study lies in designing a complete microkinetic model that includes both coverage effects and diffusion of species, which is very rare due to the complexity of the reaction mechanism for syngas to ethanol.

Results from the combined model indicated that the major syngas conversion products from a Co_7Pd_6 catalyst are hydrocarbons (methane and ethane). This product mix arises from the fact that cobalt surface sites are considerably more active (higher turnover rates) than the Pd or CoPd sites. Additionally, key ethanol synthesis intermediates produced on the CoPd sites, such as CH_3^* and CH_3O^* , were more likely to diffuse to cobalt sites rather than undergo further reactions to form ethanol. Finally, the microkinetic model was extended, this time to examine syngas conversion selectivity as a function of catalyst composition. Specifically, Co_xPd_y catalysts of differing cobalt and palladium ratios were examined. Results from the microkinetic model indicate that appreciable ethanol formation only takes place when the concentration of CoPd sites is greater than 95%.

Though recent experimental data suggest that CoPd catalysts may not be the ideal catalyst for ethanol formation due to the poor selectivity towards ethanol and the difficulty associated with synthesizing a pure CoPd phase. However, this study does

provide keen insight into important factors that must be considered in order to optimize syngas to ethanol production. Some of the key factors that control ethanol formation are:

1. A need to maximize the presence of CoPd interface sites. As Co and Pd prefer to stay segregated, one possibility is to isolate sub-nanometer clusters that contain an equimolar ratio of Co and Pd or use thin nano sheets of alternating Co metal and Pd metal to increase interface sites;
2. Identify a catalyst surface that yields high concentrations of the CH_x species on the surface that are needed to form ethanol, but somehow suppress the hydrogenation of CH_3^* to form methane;
3. Identify a surface with a low activation barrier for CO insertion reactions; and
4. Optimize the CO adsorption energy so as to reduce the surface coverage of CO, which leads to the poisoning of active surface sites, especially on noble metal surface.

Recommendations

The focus of this study was on developing a comprehensive reaction model for the production of ethanol and related products on bimetallic transition metal catalysts. This work built upon earlier models but significantly expanded the number of reactions included in the model and examined the effects of surface coverage on reactivity. Specifically, the Microkinetic model developed as a part of this work expands the ethanol reaction network to include Fischer-Tropsch reactions, provides greater

understanding of Co binding and coverage effects, and incorporates the diffusion of species between different reactive sites. However, the scope of the study was restricted to one bimetallic catalyst CoPd and did not include detailed quantum analysis of all reactions. Given these limitations and others, there still exist many topics related to this project that require future study.

Choice of functional

In the current study, most of the DFT calculations were performed using the B3LYP functional. Although B3LYP is the most popular functional used, it has its own disadvantages. It fails to accurately describe non-chemical interactions, such as van der Waals interactions, in transition metal systems¹⁻³. B3LYP also includes errors arising from the self-interaction of electrons. Newer classes of hybrid functionals that represent Meta hybrid functionals are constructed by empirical fitting of their parameters, but constraining to a uniform electron gas. These functionals take in to account non-covalent interactions and overcome errors associated with hybrid functionals like B3LYP. M06 and M06-2X are examples of these Meta hybrid functionals.⁴

In the CO adsorption studies (Chapter 3), adsorption energies were calculated using B3LYP and M06 functionals. The results of these studies demonstrate how B3LYP underestimates metal carbon bond lengths and over estimates the CO bond length in part because B3LYP does not include van der Waals interactions. Because of the complexity of the reaction network studied, to reduce computational time all of the data represented

in the later chapters is derived using B3LYP functional. One way to reduce the errors from B3LYP functional is using functionals that explicitly take long range dispersion forces into consideration. Therefore, in order to better describe the system energetics, M06 type functionals or the Bayesian error estimation functional with van der Waals (BEEF-vdw) can be used.^{5,6}

Other clusters

Ethanol production on bimetallic Cobalt-Palladium can be extended to other promising catalysts for this reaction. From previous studies in the Bruce research group, the important catalyst combinations that are identified as promising catalysts for the reaction are Ni₇Pt₆, Ni₇Cu₆, Fe₇Cu₆, Ru₇Pd₆, Ru₇Cu₆, and Co₇Cu₆. Significant research has been focused on cobalt-copper catalyst. There are both experimental and theoretical works reported on the catalyst. One interesting possibility of future work is to extend this study to other bimetallic nanoclusters mentioned above. Additionally, CO coverage effects could be extended to other transition metals so as to accurately identify favorable binding sites and binding energy under high coverage conditions that more closely match reaction conditions.

Reaction network

The syngas to ethanol reaction network developed in this study considers 46 elementary reversible reactions. Though this reaction network is extensive, there are still some reactions that can be added to make it more thorough and complete.

One of the prime concerns with heterogeneous catalytic reactions is catalyst deactivation⁷⁻¹⁰. In cobalt-palladium bimetallic catalysts, there is the likely possibility that sites containing multiple cobalt species can occur, and cobalt is a well-known Fischer-Tropsch (FT) catalyst. Thus, hydrocarbons formed by Fischer-Tropsch reactions may accumulate and be converted to carbon or coke. This coke then blocks active sites on the catalyst surface, and the catalyst eventually needs to be replaced. This process is called coking and can severely limit the effectiveness and longevity of a catalyst. The present model could be further improved by expanding the number of FT and coking or carbon formation reactions – enabling the study of catalyst deactivation.

Microkinetic model

The importance of including diffusion steps is noted from Chapter 5. Although the current microkinetic model includes surface diffusion steps for many of the reaction intermediates, the diffusion of Fischer-Tropsch species is not included in the present reaction model. It would be useful to add diffusion steps for all species in the reaction network.

The microkinetic model developed in this work includes several assumptions. One of the major assumptions is that the sticking coefficient for CO on the catalyst surface is defined as a function of coverage. Using this assumption, the concentration of CO remains the same after it reaches maximum coverage on the surface. It is questionable as to the accuracy of this assumption, but attempts to model the adsorption process by more

traditional approaches yielded surfaces of very low activity as a result of near complete coverage with adsorbed reaction gases. A detailed study of CO adsorption processes on metals may yield an adsorption model that does not require the use of experimental adsorption information.

In the present microkinetic model, rate constants are calculated using the Arrhenius equations. As an assumption, a constant pre-exponential factor of $k_B T/h$ (1×10^{13}) is used for all elementary reactions.¹¹ DFT derived pre-exponential factors can be determined and used to improve the accuracy of the model.

For simplification, the present microkinetic model is designed for a batch reactor but it can be extended to flow reactors (PFR and CSTR)^{6,12} that more accurately resemble those used commercially for the conversion of syngas to liquid products.

Reaction conditions

Results from the MKM are shown at experimental conditions of temperature 525K and molar ratio of reactants CO:H₂ at 2:1. This work can also be extended to study the effect of temperature, mole ratio and pressure.

Key assumptions in this dissertation

DFT calculations and microkinetic model used in this study are based on several assumptions. Below is a list of some key assumptions.

1. For surface reaction rates modeled using Arrhenius Law, a constant pre-exponential factor (A) of 10^{13} was used to determine the rate constants (k). For a similar system studied by Dr. Ming He¹³, DFT derived pre-exponential factors varied from 10^{11} to 10^{13} . Thus, assuming a constant pre-exponential factor could impact the model predictions; however, it was more commonly observed that errors in the pre-exponential factor were less impactful than errors in the reaction activation energy.
2. The BEP relationships used to calculate many of the activation energies for surface reactions were based on the assumption that there is a linear relationship between the activation energies and gas phase energies. It was noticed that the difference in activation energies between DFT and BEP values for select reactions was as high as 0.3 eV. Such an error in activation energy might significantly impact the observed product distributions from microkinetic models, especially if the reactions impacted are any of the rate limiting processes for making products. An improvised microkinetic model would include activations energies calculated using rigorous DFT-nudged elastic band methods. Alternatively, BEP relationships for each reaction type could be developed (e.g., carbon hydrogenation, CO insertion, oxygen hydrogenation, etc.).
3. The microkinetic model built in this work uses coverage dependent sticking coefficients for CO adsorption. Hydrogen is the second component after CO having high coverages on three surface types of sites. Coverage dependent adsorption

- energies for all reactants (including hydrogen) and products would further improve the accuracy of the microkinetic model.
4. Activation energies for all studied reactions were calculated using the assumption that all reactions happen on a fresh catalyst surface. It was observed from initial DFT studies of CO adsorption and coverage that the adsorption energy of CO changes with coverage. Therefore, improved accuracy would be achieved using a coverage dependent model for activation energies.
 5. For Co_xPd_y catalysts, activation energies on a specific sites type were assumed to be independent of catalyst composition. This assumption may not be valid, but initial modeling suggests it will not have a significant effect on overall catalyst site behavior.
 6. Sticking coefficients for gas phase components are obtained from literature for pure Co and Pd surfaces; however, the catalyst considered in this study is a bimetallic nanocluster. Therefore, the presence of metals in such close proximity could affect the electronic distributions of one another effecting the adsorption behavior.
 7. Collision theory based rate constants are calculated based on the assumption that the adsorption and desorption of gas phase species were barrier less processes. This assumption may not be valid for all species.
 8. In designing the diffusion equations it was assumed that the intermediate is always close to the metal-metal interface sites, thereby facilitating the diffusion

- in a single step. In reality, intermediates could be sitting in the pool of one type of metal atoms (Co, Pd or CoPd) making diffusion a multi-step process.
9. It is well known that catalyst structure, i.e., the presence of step edges, defect sites and corners, can significantly impact the reactivity of a given catalyst. These effects were not studied for this catalyst.
 10. DFT modeling results presented in this work indicate that the MO6 functional more accurately describes the energetics for the studied system, but the potentially less accurate B3LYP functional was used to develop the microkinetic model due to computational expediency. Reevaluating all adsorption and activation energies using the MO6 (or a related model) might improve the accuracy of the model.

References

1. Burke K. - Perspective on density functional theory. - *The Journal of Chemical Physics*. 2012;136(- 15):- 150901. doi: - 10.1063/1.4704546.
2. Sousa FA, Fernandes PA, Ramos MJ. - General performance of density functionals. - *J Phys Chem A*. 2007;111(- 42):- 10439. doi: - 10.1021/jp0734474.
3. - Cramer CJ, - Truhlar DG. - Density functional theory for transition metals and transition metal chemistry. - *Phys Chem Chem Phys*. (- 46):- 10757. doi: - 10.1039/B907148B.

4. Zhao Y, Truhlar DG. - Density functionals with broad applicability in chemistry. - *Acc Chem Res.* 2008;41(- 2):- 157. doi: - 10.1021/ar700111a.
5. - Wellendorff J. Density functionals for surface science: Exchange-correlation model development with bayesian error estimation. - *Physical Review B.* 2012;85(- 23):- 235149. doi: - 10.1103/PhysRevB.85.235149.
6. Deshmukh SR, Mhadeshwar AB, Vlachos DG. - Microreactor modeling for hydrogen production from ammonia decomposition on ruthenium. - *Ind Eng Chem Res.* 2004;43(- 12):- 2986. doi: - 10.1021/ie030557y.
7. Argyle MD, Bartholomew CH. - Heterogeneous catalyst deactivation and regeneration: A review. - *Catalysts (2073-4344).* 2015;5(- 1):- 145.
8. Wilhelm DJ, Simbeck DR, Karp AD, Dickenson RL. - Syngas production for gas-to-liquids applications: Technologies, issues and outlook. - *Fuel Processing Technology.* 2001;71(- 1):- 139. doi: - [https://doi.org/10.1016/S0378-3820\(01\)00140-0](https://doi.org/10.1016/S0378-3820(01)00140-0).
9. - *Arabian Journal for Science and Engineering.* (- 5):- 2441. doi: - 10.1007/s13369-017-2845-z.
10. Tan KF, Xu J, Chang J, Borgna A, Saeys M. - Carbon deposition on co catalysts during Fischer–Tropsch synthesis: A computational and experimental study. - *Journal of Catalysis.* 2010;274(- 2):- 121. doi: - <https://doi.org/10.1016/j.jcat.2010.06.008>.

11. Perez GB, Alvarez-Idaboy JR, Jimenez AG, Cruz-Torres A. - Quantum chemical and conventional TST calculations of rate constants for the OH+alkane reaction. - *Chemical Physics*. 2005;310(- 1):- 213. doi: - <https://doi.org/10.1016/j.chemphys.2004.10.031>.
12. - Dix ST, - Scott JK, - Getman RB, - Campbell CT. - Using degrees of rate control to improve selective n-butane oxidation over model MOF-encapsulated catalysts: Sterically-constrained Ag₃Pd(111). - *Faraday Discuss.* (- 0):- 21. doi: - [10.1039/C5FD00198F](https://doi.org/10.1039/C5FD00198F).
13. He M. *A computational approach for the rational design of bimetallic clusters for ethanol formation from syn-gas.* ; 2013.

APPENDICES

APPENDIX A

DFT ENERGIES AND XYZ CO-ORDINATES OF KEY STRUCTURES

1. Energy of reactants, intermediates and products in gas phase. Energies are calculated using Jaguar, functional used for calculations is B3LYP.

Table A1. Energy of species in gas phase

S.No.	Gas phase species	Energy (Ha) (Zero point energy corrected)
1	CO	-113.304
2	C	-37.8453
3	H	-0.50027
4	H ₂	-1.16837
5	O	-75.0595
6	CH	-38.4745
7	CH ₂	-39.1361
8	CH ₃	-39.8132
9	CH ₄	-40.4791
10	CHOH	-114.389
11	CH ₂ OH	-115.023
12	CH ₃ OH	-115.673
13	HCO	-113.839
14	CH ₂ O	-114.477
15	CH ₃ O	-115.017
16	CHCO	-151.906
17	CH ₂ CO	-152.57
18	CH ₃ CO	-153.14
19	CHCHO	-152.46
20	CH ₂ CHO	-153.133
21	CH ₃ CHO	-153.78

22	CHCOH	-152.507
23	CH ₂ COH	-153.09

Table A1 (Continued)

S.No.	Gas phase species	Energy (Ha) (Zero point energy corrected)
24	CH ₃ COH	-153.693
25	CH ₃ CHOH	-154.321
26	CH ₃ CH ₂ OH	-154.966
27	OH	-75.7201
28	H ₂ O	-76.3984
29	CH ₂ CHOH	-153.757
30	CH ₃ CH ₃	-79.7637
31	CH ₂ CH ₂	-78.5426
32	CHCH ₂	-77.8696
33	CH ₃ CH ₂	-79.1057

2. Pd sites of Co₇Pd₆ cluster are covered with CO and adsorption energies of key species is calculated on Co sites. Energies are calculated using Jaguar, functional used for calculations is B3LYP.

Table A2. Energy of species on Co sites of Co₇Pd₆ cluster with six CO on Pd sites

S.NO	Intermediate	Optimized spin	Adsorption site preference	Energy (Ha) (Zero point energy corrected)
1	Cluster+6CO	16		-2456.358065
2	CO	16	Terminal	-2569.695761
3	H	15	Threefold	-2456.956578
4	CHO	15	Threefold	-2570.253036
5	CH ₂ O	16	Threefold	-2570.853571
6	CH ₃ O	13	Threefold	-2571.452423
7	CH ₃	17	Terminal	-2496.20943
8	O	16	Threefold	-2531.608761
9	CH ₃ CO	15	Bridge	-2609.556835
10	CH ₃ COH	14	Terminal	-2610.110559
11	CH ₃ CHOH	15	Bridge	-2610.723941
12	CH ₃ CH ₂ OH	16	Terminal	-2611.339138
13	CH	15	Threefold	-2494.993658
14	CH ₂	16	Threefold	-2495.610491
15	CHCO	15	Bridge	-2608.354269
16	CH ₂ CO	16	Threefold	-2608.957607

3. Energies of key species on Co₉Pd₄ cluster. Energies are calculated using Jaguar, functional used for calculations is B3LYP. All energies are zero point energy corrected and spin polarized.

Table A3. Energy of species on Co sites of Co₉Pd₄ cluster

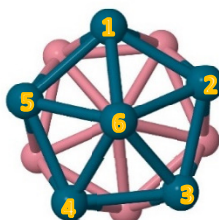
S.NO	Intermediate	Optimized spin	Adsorption site preference	Energy (Ha) (Zero point energy corrected)
1	Co ₉ Pd ₄	16		-1812.941144
2	CO	16	Terminal	-1926.306458
3	H	15	Threefold	-1813.551538
4	CHO	15	Threefold	-1926.872321
5	CH ₂ O	16	Threefold	-1927.478342
6	CH ₃ O	13	Threefold	-1928.09642
7	CH ₃	17	Terminal	-1852.836016
8	O	16	Threefold	-1888.220266
9	CH ₃ CO	15	Bridge	-1966.174254
10	CH ₃ COH	14	Terminal	-1966.719743
11	CH ₃ CHOH	15	Bridge	-1967.324216
12	CH ₃ CH ₂ OH	16	Terminal	-1967.946133
13	CH	15	Threefold	-1851.610747
14	CH ₂	16	Threefold	-1852.22182
15	CHCO	15	Bridge	-1964.973275

4. CO adsorption and coverage data on Pd sites. Energies are calculated using Jaguar, functional used for calculations is B3LYP. All energies are zero point energy corrected and spin polarized.

Table A4. CO Coverage on Pd sites of CoPd

S.NO.	Number of carbon monoxide	Position	Energy (Ha) (Zero point energy corrected)
1	1	Bridge-16	-1889.695491
2	2	Bridge-12,23	-2003.033737
3	2	Bridge-16,12	-2003.037661
4	2	Bridge-12,34	-2003.038189
5	3	Bridge-12,23,34	-2116.379403
6	3	Bridge-12,23,45	-2116.381698
7	3	Bridge-12,23,56	-2116.389855
8	4	Bridge-12,23,34,56	-2229.564654
9	1	Atop 6	-1889.694151
10	2	Atop1,2	-2003.036929
11	2	Atop1,3	-2003.032662
12	2	Atop1,6	-2003.039621
13	3	Atop1,2,3	-2116.385596
14	3	Atop1,2,4	-2116.388119
15	3	Atop1,2,6	-2116.390518
16	3	Atop1,3,6	-2116.390299
17	4	Atop1,2,3,6	-2229.739477
18	4	Atop1,2,3,4	-2229.741037
19	5	Atop1,2,3,4,5	-2343.089846
20	6	Atop1,2,3,4,5,6	-2456.435116

- Numbers 1 to 6 in position indicate the site on which CO is adsorbed



5. Energies of intermediates adsorbed on three sites of Co₇Pd₆ cluster, calculated using B3LYP functional. All energies are zero point energy corrected.

Table A5. Energy of species adsorbed on the cluster in (Hartrees)
All energies are zero point corrected

	Co ₃	Co ₂ Pd, CoPd ₂	Pd ₃	Adsorption site preference
Cluster	-1776.32321			
CO	-1889.6825	-1889.69145	-1889.6946	Terminal
CO	-1889.6824	-1889.66451	-1889.6808	Bridge
CO	N/A	-1889.68417	-1889.66356	Threefold
H ₂	-1777.5134	-1777.5144	-1777.51544	Terminal
C	-1814.3256	-1814.31713	-1814.30339	Threefold
O	-1851.5921	-1851.5512	-1851.54747	Threefold
H	-1776.9205	-1776.92731	-1776.92696	Threefold
OH	-1852.1986	-1852.17329	-1852.14652	Threefold
HCO	-1890.2421	-1890.24412	-1890.2339	Threefold
CH ₂ O	-1890.845	-1890.83397	-1890.80854	Threefold
CH ₃ O	-1891.4692	-1891.44725	-1891.41069	Threefold
CH	-1814.9775	-1814.95976	-1814.94936	Threefold
CH ₂	-1815.5962	-1815.59591	-1815.58669	Threefold
CH ₃	-1816.2135	-1816.20292	-1816.20104	Terminal
CHOH	-1890.8099	-1890.80458	-1890.79163	Threefold
CH ₂ OH	-1891.419	-1891.42062	-1891.4142	Threefold
CHCO	-1928.3502	-1928.32187	-1928.34523	Bridge
CH ₂ CO	-1928.9448	-1928.94196	-1928.94345	Threefold
CH ₃ CO	-1929.5383	-1929.543	-1929.52444	Bridge
CHCHO	-1928.9606	-1928.94313	-1928.92115	Threefold
CH ₂ CHO	-1929.563	-1929.55616	-1929.5357	Threefold
CH ₂ COH	-1929.5272	-1929.51575	-1929.51191	Threefold
CH ₃ COH	-1930.0959	-1930.09423	-1930.09255	Terminal
CH ₂ CHOH	-1930.1179	-1930.11629	-1930.12402	Bridge
CH ₃ CHOH	-1930.6737	-1930.6953	-1930.70939	Terminal
CHCH ₂	-1854.27149	-1854.26995	-1854.255949	Bridge
CH ₂ CH ₂	-1854.88957	-1854.908011	-1854.891384	Terminal
CH ₃ CH ₂	-1855.47329	-1855.46617	-1855.466721	Terminal

*Adopted from Appendix C of Dr.Ming He dissertation

6. Geometric xyz coordinates of optimized structures obtained from output xyz files

Table A6. Geometric xyz coordinates of important intermediates

Structure	Coordinates			
Cluster	Co	0.0271649778	-0.0571206447	2.4470774242
	Co	-1.7444668310	-1.3634928554	1.1280792206
	Co	-1.7977788231	1.2298876720	1.1140871123
	Co	0.7262013339	-2.1682341349	1.0615635655
	Co	0.6307695045	2.0807153009	1.1413847398
	Co	2.2003194626	0.0180659620	1.1733398019
	Co	0.0089856058	-0.0361695472	-0.1878903114
	Pd	-2.4082731601	-0.0723632465	-1.0534012854
	Pd	-0.6852533988	-2.3074219300	-1.0887918299
	Pd	-0.7684867680	2.2399912079	-1.0497147608
	Pd	2.0131347779	-1.3944234216	-1.0371182016
	Pd	1.9343192850	1.4434011519	-1.0127485548
	Pd	0.0499904573	-0.0039982915	-2.6111734443
	CH ₂ on Pd sites	Co	0.1561515213	0.2749071958
Co		-2.0187977521	-0.5000871628	1.3112655808
Co		-1.2558917182	1.9619287651	1.0178421338
Co		0.1663392335	-2.0118013497	1.3656143661
Co		1.3584011539	2.0023339573	0.9029088659
Co		2.2724104572	-0.4200340337	0.9952421971
Co		0.0410109152	0.0845183617	-0.0493100055
Pd		-2.3080694592	0.6914904532	-1.0098132523
Pd		-1.5042831862	-2.0359607788	-0.7858967153
Pd		-0.0915221201	2.3850792328	-1.2397746047
Pd		1.4075424976	-1.9221881566	-0.9417491350
Pd		2.1735595292	0.7660744594	-1.3251094931
Pd		-0.2140218337	-0.3144896899	-2.5595386185
C		-1.4352659117	-1.8415342814	-2.7742264331
H		-2.3618688597	-1.5227129471	-3.2669760154
H		-0.8974974487	-2.6341600721	-3.3107525508

Table A6. Continued

Structure	Coordinates			
CH ₂ on Co sites	Co	0.0451227979	-0.0724730670	2.4384965629
	Co	-1.7446200440	-1.3588095401	1.1597118970
	Co	-1.8158042019	1.2970356071	1.0182991730
	Co	0.7521430400	-2.1610510203	1.2207991897
	Co	0.6009233950	2.1265392489	1.0994584611
	Co	2.2767503121	0.2253217881	1.0670492121
	Co	0.0559064632	0.0017578376	-0.1472167521
	Pd	-2.3875829149	-0.1606035403	-1.0125828328
	Pd	-0.6542590501	-2.3355841466	-1.0241510529
	Pd	-0.7985347387	2.2093192013	-1.1462837001
	Pd	1.9993220567	-1.4074768053	-0.9045655744
	Pd	1.9048269774	1.5222258116	-1.1126944824
	Pd	0.0097200725	-0.1437759010	-2.5747390268
	C	-0.7368443005	-2.1414400655	2.6421428335
	H	-0.7900492706	-3.2448113797	2.5774230358
	H	-0.8406125506	-1.8790691586	3.7071356926
CH ₂ on CoPd sites	Co	-0.0691632068	-0.2141522527	2.4580131586
	Co	-2.1041245211	-1.0003432455	1.0660612266
	Co	-1.4406599038	1.5578902068	1.1667545281
	Co	0.1581448139	-2.3094324575	0.9928661558
	Co	1.1734649930	1.8229997079	1.2034757849
	Co	2.1050038931	-0.6190640790	1.1390271920
	Co	0.0219739178	-0.0268710695	-0.0365646882
	Pd	-2.3495216580	0.5771525547	-1.1260134096
	Pd	-1.2408086958	-1.9820765077	-1.1570067621
	Pd	-0.1387636071	2.3637758157	-0.9538013437
	Pd	1.5396753784	-1.7867984788	-1.1343659148
	Pd	2.2224723986	0.9607752573	-0.9584790809
	Pd	0.1001308074	0.1035020983	-2.5474522605
	C	-3.2050473355	-1.2028449739	-0.6428038696
	H	-4.0014448503	-0.9642225370	0.1096181776
	H	-3.7287063672	-1.5247220147	-1.5545846175

Table A6. Continued

Structure	Coordinates			
CH ₃ on Co sites	Co	0.0099623481	0.3325643450	2.7841904821
	Co	-1.6585817385	-1.0851184042	1.3282885600
	Co	-1.7924965015	1.4460218409	1.0840158878
	Co	0.7672085368	-1.8914555064	1.3862391779
	Co	0.6476144264	2.2172210598	0.9541539597
	Co	2.1694675728	0.1939305605	1.1618912698
	Co	0.0239078257	0.0357728166	-0.1671437028
	Pd	-2.4225024684	-0.0969605921	-0.9505308538
	Pd	-0.7184119823	-2.4118275214	-0.7176017909
	Pd	-0.7827785849	2.2595653645	-1.2267380236
	Pd	2.0494303473	-1.5074546956	-0.8470001931
	Pd	2.0055480555	1.4185204719	-1.1453311128
	Pd	0.0449214559	-0.2508237542	-2.6172490229
	C	-0.0264564283	0.5794726161	4.7622087286
	H	-0.9985588581	0.2398529941	5.1432417405
	H	0.1263801240	1.6269348918	5.0459694776
H	0.7654490663	-0.0367254017	5.2083161370	
CH ₃ on Pd sites	Co	-0.0895738733	-0.8013588334	2.2712485536
	Co	-1.8432600968	-1.6000195974	0.6273930358
	Co	-1.7713623366	0.9486343850	1.2684707166
	Co	0.6021140962	-2.4337293164	0.3654627312
	Co	0.7041943145	1.5635298646	1.6283958277
	Co	2.1826101245	-0.4996575996	1.0442997267
	Co	0.0225356173	-0.0294618452	-0.2102437376
	Pd	-2.3896355482	0.2975421256	-1.1241915957
	Pd	-0.8011602701	-1.9148206748	-1.7732554551
	Pd	-0.6083761172	2.3903385568	-0.5424840725
	Pd	1.9206046755	-1.1434257821	-1.4815683088
	Pd	2.0390486432	1.5114295004	-0.6178077998
	Pd	0.0591534923	0.5499105812	-2.6748777804
	C	0.4218073167	-0.5376482882	-4.3529037344
	H	0.4278641900	0.2480103608	-5.1188773862
	H	1.3882980389	-1.0476034825	-4.3064061667
H	-0.3854742383	-1.2539019422	-4.5348901058	

Table A6. Continued

Structure	Coordinates			
CH ₃ on CoPd sites	Co	0.3721101272	-0.1183332258	2.3812307705
	Co	-1.5910784846	-1.3319428485	1.1554081899
	Co	-1.4701317092	1.2133576345	1.2350414405
	Co	0.7807988439	-2.1779809885	0.9213134764
	Co	0.9576460058	1.9545474608	0.9837653207
	Co	2.5702558726	-0.1304592359	0.9942582702
	Co	0.0960628768	-0.0716694896	-0.2842458400
	Pd	-2.5103070944	0.0332493974	-0.8587133393
	Pd	-0.8587057896	-2.3251033785	-1.1304259151
	Pd	-0.6899211288	2.2953642303	-1.0123142587
	Pd	2.0081192545	-1.5194608165	-1.2508073051
	Pd	2.0711981166	1.3236547843	-1.2511434519
	Pd	-0.1592218963	0.0172650450	-2.7277431914
	C	3.8803018915	-0.0861572853	2.4888370863
	H	3.7641133132	0.8114229266	3.1068695043
	H	3.7759641042	-0.9738712335	3.1241222019
H	4.8796558634	-0.0825979960	2.0336036730	
CH ₃ O on Co sites	Co	-0.1501277199	0.1092968482	2.3356177913
	Co	-1.8344843598	-1.3486256544	0.9531351134
	Co	-1.9447715345	1.1474140177	0.7956025614
	Co	0.7715078497	-1.9353858634	1.0779341307
	Co	0.5208009919	2.1337936546	0.9300139798
	Co	2.1376993437	0.2835851185	1.2404592536
	Co	0.0755649642	-0.0142981070	-0.3193972536
	Pd	-2.3407612035	-0.2007036596	-1.3999616791
	Pd	-0.5203272786	-2.3968291526	-1.0991665433
	Pd	-0.8487552204	2.2334394524	-1.2602794689
	Pd	2.2572055673	-1.2394502233	-0.9269938187
	Pd	2.0476242449	1.5816255888	-1.0884286074
	Pd	0.3136998218	-0.0415733872	-2.7613725167
	O	-2.3064559158	0.0384677472	2.4735882515
	C	-3.3060266021	-0.0224086050	3.4907391314
	H	-3.1154993302	-0.8649713676	4.1687979273
H	-3.3101371433	0.8986955782	4.0877328440	
H	-4.3046933312	-0.1531522429	3.05444468694	

Table A6. Continued

Structure	Coordinates			
CH ₃ O on Pd sites	Co	-0.0838089365	-0.2549044704	2.4559588416
	Co	-1.8500499398	-1.4075519851	0.8813050600
	Co	-1.7776072590	1.2116051645	0.9982006526
	Co	0.6306734571	-2.2091893154	0.9742415547
	Co	0.6794791634	1.9367136004	1.2495342052
	Co	2.2139700295	-0.1776883857	1.1418412001
	Co	0.0260777246	-0.0753792609	-0.0711795082
	Pd	-2.3786711860	-0.0136230938	-1.2136550087
	Pd	-0.6751994122	-2.3016803372	-1.2905666556
	Pd	-0.6501152295	2.3087330950	-0.9975227580
	Pd	2.0446022532	-1.5299748587	-1.0764744505
	Pd	2.0969688587	1.3435787563	-0.8821198879
	Pd	0.1392091266	0.0039771532	-2.5353055500
	C	0.9234847195	2.7169637782	-3.9574827882
	H	1.2891690107	3.7335526717	-3.7558926463
	O	0.7877534887	2.0180471622	-2.7358521361
	H	-0.0370758204	2.7914765192	-4.4833291656
H	1.6510077410	2.2212733839	-4.6140323746	
CH ₃ CO on CoPd sites	Co	0.1663485231	0.0777108861	2.5341539376
	Co	-1.8211119360	-0.9839357085	1.2400615698
	Co	-1.4655094230	1.5426804854	0.9534465447
	Co	0.4815149778	-2.1061857320	1.2311983349
	Co	1.0595639744	1.9933034920	1.0145181446
	Co	2.2883620724	-0.3001942247	1.0059101977
	Co	0.0584023842	-0.0732095435	-0.2062058991
	Pd	-2.3220912972	0.1765141418	-1.0742317174
	Pd	-1.0244600611	-2.2912200606	-0.9052696266
	Pd	-0.3256966537	2.2272769791	-1.2352170282
	Pd	1.7763752270	-1.7768089488	-1.0317159177
	Pd	2.1618905590	1.0884701443	-1.1646332110
	Pd	0.0623023241	-0.2306795985	-2.6464457425
	C	1.6316511391	3.7935043469	3.3544022333
	C	1.0119740686	2.4984984383	2.8860180803
	H	2.7018052643	3.7875035883	3.1152599821
	O	0.4897325154	1.7515413353	3.7413897686
H	1.4974101186	3.9339727828	4.4316030736	
H	1.1961933196	4.6361404843	2.8075221827	

Table A6. Continued

Structure	Coordinates			
CH ₂ OH on Pd sites	Co	-1.0618509444	-0.3730990552	2.0462199722
	Co	-1.7314716173	-1.7719422921	0.0589881275
	Co	-2.3417541186	0.6971469416	0.2575470225
	Co	0.5901735709	-2.0476646829	1.0994270273
	Co	-0.3891808039	1.9465114157	1.3634221672
	Co	1.3891269707	0.2133877013	1.9007672076
	Co	0.0376070718	0.0006941248	-0.1125062007
	Pd	-1.7173823190	-0.3397340592	-2.0848754865
	Pd	0.3652419889	-2.2805869005	-1.4774495036
	Pd	-0.7773672730	2.3032123244	-1.1596383936
	Pd	2.5437918382	-0.8815350222	-0.2177692984
	Pd	1.8755668881	1.9362378424	0.0061490086
	Pd	1.0367655124	0.4742841525	-2.4475682870
	C	0.0367703831	0.8402084565	-4.2318360976
	H	0.5919226858	1.6679520015	-4.6843668514
	O	0.2216485152	-0.3087202398	-4.9913917823
	H	-0.3194928514	-1.0096228302	-4.6031859965
H	-1.0218864951	1.1084175488	-4.0747170976	
CH ₃ CHOH on CoPd sites	Co	0.7582486962	0.0356330208	2.0691881494
	Co	-1.0530966084	-1.5416060326	1.2742876425
	Co	-1.5423701261	0.9731239864	1.2499197641
	Co	1.3412801519	-1.8974454969	0.6523866676
	Co	0.6413701078	2.0636531578	0.5868022183
	Co	2.4673782721	0.2855156655	0.2513032411
	Co	0.0997186651	-0.1421243074	-0.3363162809
	Pd	-2.5112558456	-0.5534651023	-0.6466096054
	Pd	-0.5099235604	-2.6639527997	-1.0422880394
	Pd	-1.2569967844	2.0087877924	-1.1758110017
	Pd	1.9732230260	-1.3845526751	-1.8027233512
	Pd	1.5994280890	1.5224207168	-1.8409658508
	Pd	-0.5311870887	-0.2896935421	-2.7508142241
	C	3.7596744312	3.2686226217	-1.0475772479
	C	3.5826012496	1.7735045865	-1.2350590600
	H	3.2970593000	3.8382161835	-1.8614748367
	O	4.1876015178	1.4185276895	-2.4817723702
H	3.3178333254	3.5915556781	-0.1018191182	
H	4.8295182996	3.5202061041	-1.0391012112	
H	4.0826551605	0.4606985381	-2.5987918417	
H	4.1603846911	1.3168015050	-0.3948695469	

Table A6. Continued

Structure	Coordinates			
CHCH ₂ on Co sites	Co	-0.2874469377	-0.2297255173	2.5053424503
	Co	-2.0049101333	-1.3861041420	0.8556053146
	Co	-2.0106981393	1.1615651140	0.9210256279
	Co	0.6480475964	-2.2700064653	1.2010602830
	Co	0.3456773447	2.0597203171	1.2532523787
	Co	2.0172472789	0.1419433705	1.3521099603
	Co	-0.0503975955	0.0010292323	-0.1679212084
	Pd	-2.3765401373	-0.0402128104	-1.3885394793
	Pd	-0.5687317916	-2.3921013172	-1.0530193902
	Pd	-0.8463336759	2.3357594899	-1.1114448846
	Pd	2.0843685760	-1.3485878663	-0.7717208183
	Pd	1.9344506807	1.6059660349	-0.8330163348
	Pd	0.2527052717	0.0578275193	-2.6058740297
	C	0.7654380418	-2.1598246991	3.2035253877
	H	1.7460682645	-2.0354156840	3.6791935682
	C	-0.2856266696	-2.1090992387	4.0742692937
	H	-0.1648243831	-1.9800701697	5.1533126270
	H	-1.3126446016	-2.3085884852	3.7586897659
CH ₂ CH ₂ on Co sites	Co	0.3824527583	0.5220753765	2.3173211770
	Co	-1.1982814971	-1.5144979261	1.7907441728
	Co	-1.8599507621	1.0524399160	1.1707581652
	Co	1.5242197326	-1.5131205150	1.2897513451
	Co	0.2596151777	2.4498168098	0.5937659272
	Co	2.3110492616	0.8860448939	0.6581226048
	Co	0.0472099897	-0.0060302455	-0.1889547738
	Pd	-2.3723333066	-0.8299382481	-0.5385484132
	Pd	-0.1146409023	-2.5789757027	-0.4236993639
	Pd	-1.4446232660	1.8361058091	-1.3084741830
	Pd	2.2216219416	-1.0046146011	-1.1830556755
	Pd	1.4399365547	1.7727838321	-1.6405029342
	Pd	-0.2502670770	-0.5032983858	-2.5828500228
	C	-1.5201231518	-2.9285926251	3.3978219853
	H	-1.7897506307	-3.8324021775	2.8556638726
	H	-0.6007414806	-2.9704317992	3.9748649875
	C	-2.4210933605	-1.9021958330	3.5588682803
	H	-3.4256434189	-1.9659175548	3.1473229516
H	-2.2435741162	-1.0985202135	4.2677114750	

Table A6. Continued

Structure	Coordinates			
CH ₃ CH ₂ on Co sites	Co	-0.0784273872	0.3527504496	2.4528954013
	Co	-2.1155401228	-0.6883412890	1.1251992697
	Co	-1.5539448479	1.7838165284	0.7963424076
	Co	0.1957333873	-1.9378946798	1.6179299850
	Co	0.9614470789	2.1739105745	0.8254456286
	Co	2.1428921694	-0.0369110057	1.1928930145
	Co	-0.0250343762	0.0214165510	-0.2269263013
	Pd	-2.3800104227	0.3028946726	-1.2735372900
	Pd	-1.1091625103	-2.3062959400	-0.6478944087
	Pd	-0.3476789139	2.3518242224	-1.4567954224
	Pd	1.7195206814	-1.8785501089	-0.5502456187
	Pd	2.1634028371	0.9845510374	-1.2206880199
	Pd	0.0601509935	-0.4172555810	-2.6359228528
	C	0.4535081475	-1.8430569469	3.6475529778
	H	1.4809510403	-2.2221400800	3.7573621348
	H	0.4636119749	-0.8748911148	4.1920276385
	C	-0.5573990402	-2.7851034065	4.3244810580
	H	-0.5628467653	-3.7767615147	3.8539954994
	H	-1.5803043369	-2.3956281097	4.2646077974
	H	-0.3319287224	-2.9427210941	5.3890213091

APPENDIX B

Micro kinetic modelling

Supporting documentation for chapter 4

1. Microkinetic model is built using Matlab R2016b, a batch reactor is modeled to obtain the time dependent concentrations of reactants and products. Table B1 has a list of constants and tunable parameters in the model.

Table B1. Constants used in this model

Boltzmann constant (k_b)	1.3806488 e-23	J/K
Universal gas constant (R)	8.3144621	J/mol K
Planks constant (h)	6.62606957e-34	J*s
Avogadro number (N_a)	6.02214129e23	molecules/mol
Temperature (T)	523	K
Surface area of catalyst /mass of it (s)	1e ⁶	m ² /kg
Surface area / active site (ω)	1.57 x 10 ⁻¹⁹	m ² /active site
Mass of catalyst (mcat)	9e-7	mg
Initial moles of CO (n_{CO})	7 x 10 ⁻⁵	moles
Initial moles of H ₂ (n_{H_2})	14 x 10 ⁻⁵	moles
Volume of the reactor (vol)	1e-6	m ³
Mass of carbon monoxide (mco)	4.6512e-26	Kg
Mass of hydrogen (mh2)	3.3538e-27	Kg
Mass of methane (mch4)	2.6635e-26	Kg
Mass of methanol (mch3oh)	5.3204e-26	Kg
Mass of acetaldehyde (mch3cho)	7.314e-26	Kg
Mass of ethanol (mch3ch2oh)	7.6443e-26	Kg

Table B1 Continued

Mass of water (mh ₂ o)	2.9923e-26	Kg
Mass of ethane (mch ₃ ch ₃)	4.9925e-26	Kg
Mass of ethylene (mch ₂ ch ₂)	4.6579e-26	Kg

2. Activation energies of 44 reactions calculated from BEP and NEB combined.

Activation energies on cobalt surface are represented in B2, on CoPd surface are represented in B3 and activation energies on palladium surface are represented in table B4.

Table B2 . Activation energies on cobalt surface

R.No.	Reaction	Activation energy on Cobalt	
		E _{af}	E _{ar}
R1	CO(g)+* \leftrightarrow CO*	0.00	0.00
R2	H ₂ (g)+2* \leftrightarrow 2H*+*	0.00	0.00
R3	CO*+H* \leftrightarrow HCO*+*	1.30	0.58
R4	HCO*+H* \leftrightarrow CH ₂ O*+*	0.64	0.75
R5	CH ₂ O*+H* \leftrightarrow CH ₃ O*+*	0.46	0.97
R6	HCO*+* \leftrightarrow CH*+O*	0.84	0.92
R7	CH ₂ O*+* \leftrightarrow CH ₂ *+O*	0.95	1.33
R8	CH ₃ O*+* \leftrightarrow CH ₃ *+O*	1.16	1.41
R9	CH*+H* \leftrightarrow CH ₂ *+*	0.31	0.71
R10	CH ₂ *+H* \leftrightarrow CH ₃ *+*	0.54	0.92
R11	CH ₃ *+H* \leftrightarrow CH ₄ (g)+2*	0.87	0.71

Table B2 Continued

R.No.	Reaction	Activation energy on Cobalt	
		E _{af}	E _{ar}
R12	$\text{CH}^* + \text{CO}^* \leftrightarrow \text{CHCO}^* + ^*$	0.88	1.13
R13	$\text{CH}_2^* + \text{CO}^* \leftrightarrow \text{CH}_2\text{CO}^* + ^*$	0.95	0.74
R14	$\text{CH}_3^* + \text{CO}^* \leftrightarrow \text{CH}_3\text{CO}^* + ^*$	1.20	0.54
R15	$\text{CHCO}^* + \text{H}^* \leftrightarrow \text{CH}_2\text{CO}^* + ^*$	0.71	0.66
R16	$\text{CH}_2\text{CO}^* + \text{H}^* \leftrightarrow \text{CH}_3\text{CO}^* + ^*$	0.73	0.66
R17	$\text{CH}_3\text{CO}^* + \text{H}^* \leftrightarrow \text{CH}_3\text{CHO}(\text{g}) + 2^*$	1.25	0.64
R18	$\text{CH}_3\text{CO}^* + \text{H}^* \leftrightarrow \text{CH}_3\text{COH}^* + ^*$	1.08	0.32
R19	$\text{CH}_3\text{COH}^* + \text{H}^* \leftrightarrow \text{CH}_3\text{CHOH}^* + ^*$	1.06	0.69
R20	$\text{CH}_3\text{CHOH}^* + \text{H}^* \leftrightarrow \text{CH}_3\text{CH}_2\text{OH}(\text{g}) + 2^*$	0.30	0.66
R21	$\text{CH}_2\text{O}^* + \text{H}^* \leftrightarrow \text{CH}_2\text{OH} + ^*$	1.14	0.70
R22	$\text{CH}_2\text{CO}^* + \text{H}^* \leftrightarrow \text{CH}_2\text{COH}^* + ^*$	0.91	0.63
R23	$\text{CH}_2\text{COH}^* + \text{H}^* \leftrightarrow \text{CH}_3\text{COH}^* + ^*$	1.30	0.75
R24	$\text{CHCO}^* + \text{H}^* \leftrightarrow \text{CHCHO}^* + ^*$	0.62	0.87
R25	$\text{CH}_2\text{CO}^* + \text{H}^* \leftrightarrow \text{CH}_2\text{CHO}^* + ^*$	0.32	0.71
R26	$\text{CHCHO}^* + \text{H}^* \leftrightarrow \text{CH}_2\text{CHO}^* + ^*$	0.89	0.99
R27	$\text{CH}_2\text{CHO}^* + \text{H}^* \leftrightarrow \text{CH}_3\text{CHO}(\text{g}) + 2^*$	1.74	0.66
R28	$\text{CH}_2\text{O}^* + \text{CH}_2^* \leftrightarrow \text{CH}_3\text{COH}^* + ^*$	1.11	0.69
R29	$\text{O}^* + \text{H}^* \leftrightarrow \text{OH}^* + ^*$	0.98	1.16
R30	$\text{OH}^* + \text{H}^* \leftrightarrow \text{H}_2\text{O}(\text{g}) + ^*$	1.39	0.83
R31	$\text{CH}_2\text{COH}^* + \text{H}^* \leftrightarrow \text{CH}_2\text{CHOH}^* + ^*$	0.93	0.81
R32	$\text{CH}_2\text{CHOH}^* + \text{H}^* \leftrightarrow \text{CH}_3\text{CHOH}^* + ^*$	1.32	0.53
R33	$\text{CH}_2\text{CHO}^* + \text{H}^* \leftrightarrow \text{CH}_2\text{CHOH}^* + ^*$	1.50	0.69
R34	$\text{CH}_2\text{OH}^* + \text{H}^* \leftrightarrow \text{CH}_3\text{OH}(\text{g}) + 2^*$	1.05	0.67
R35	$\text{HCO}^* + \text{H}^* \leftrightarrow \text{CHOH}^* + ^*$	1.42	0.86
R36	$\text{CH}_3\text{O}^* + \text{H}^* \leftrightarrow \text{CH}_3\text{OH}(\text{g}) + 2^*$	1.48	0.13
R37	$\text{CHOH}^* + \text{H}^* \leftrightarrow \text{CH}_2\text{OH}^* + ^*$	0.58	0.81

Table B2 Continued

R.No.	Reaction	Activation energy on Cobalt	
		E _{af}	E _{ar}
R38	$\text{CH}^* + \text{CH}_2^* \leftrightarrow \text{CHCH}_2^* + ^*$	0.73	1.13
R39	$\text{CHCH}_2^* + \text{H}^* \leftrightarrow \text{CH}_2\text{CH}_2^* + ^*$	0.39	0.78
R40	$\text{CHCH}_2^* + \text{H}^* \leftrightarrow \text{CH}_2\text{CH}_2(\text{g}) + 2^*$	0.78	0.72
R41	$\text{CH}_2^* + \text{CH}_2^* \leftrightarrow \text{CH}_3\text{CH}_2^* + ^*$	1.04	0.79
R42	$\text{CH}_3\text{CH}_2^* + \text{H}^* \leftrightarrow \text{CH}_3\text{CH}_3(\text{g}) + 2^*$	0.37	0.69
R43	$\text{CH}_2\text{CH}_2^* + \text{H}^* \leftrightarrow \text{CH}_3\text{CH}_2^* + ^*$	0.82	0.56
R44	$\text{CH}_2^* + \text{CH}_2^* \leftrightarrow \text{CH}_2\text{CH}_2^* + ^*$	0.63	1.02
R45	$\text{CHCH}_2^* + ^* \leftrightarrow \text{CH}_2\text{CH}_2(\text{g}) + 2^*$	0.75	0.30
R46	$\text{CH}_3\text{CH}_2^* + \text{OH}^* \leftrightarrow \text{CH}_3\text{CH}_2\text{OH}(\text{g}) + 2^*$	1.76	0.64

Table B3 . Activation energies on cobalt- palladium surface

R.No.	Reaction	Activation energy on CoPd	
		E _{af}	E _{ar}
R1	$\text{CO}(\text{g}) + ^* \leftrightarrow \text{CO}^*$	0.00	0.00
R2	$\text{H}_2(\text{g}) + 2^* \leftrightarrow 2\text{H}^* + ^*$	0.00	0.00
R3	$\text{CO}^* + \text{H}^* \leftrightarrow \text{HCO}^* + ^*$	1.31	0.42
R4	$\text{HCO}^* + \text{H}^* \leftrightarrow \text{CH}_2\text{O}^* + ^*$	0.60	0.55
R5	$\text{CH}_2\text{O}^* + \text{H}^* \leftrightarrow \text{CH}_3\text{O}^* + ^*$	0.37	0.50
R6	$\text{HCO}^* + ^* \leftrightarrow \text{CH}^* + \text{O}^*$	1.74	1.07
R7	$\text{CH}_2\text{O}^* + ^* \leftrightarrow \text{CH}_2^* + \text{O}^*$	1.22	1.07
R8	$\text{CH}_3\text{O}^* + ^* \leftrightarrow \text{CH}_3^* + \text{O}^*$	1.22	0.98
R9	$\text{CH}^* + \text{H}^* \leftrightarrow \text{CH}_2^* + ^*$	0.33	0.78

Table B3 Continued

R.No.	Reaction	Activation energy on CoPd	
		E _{af}	E _{ar}
R10	$\text{CH}_2^* + \text{H}^* \leftrightarrow \text{CH}_3^* + ^*$	0.52	0.68
R11	$\text{CH}_3^* + \text{H}^* \leftrightarrow \text{CH}_4(\text{g}) + 2^*$	0.58	0.54
R12	$\text{CH}^* + \text{CO}^* \leftrightarrow \text{CHCO}^* + ^*$	0.73	0.64
R13	$\text{CH}_2^* + \text{CO}^* \leftrightarrow \text{CH}_2\text{CO}^* + ^*$	0.88	0.56
R14	$\text{CH}_3^* + \text{CO}^* \leftrightarrow \text{CH}_3\text{CO}^* + ^*$	0.86	0.46
R15	$\text{CHCO}^* + \text{H}^* \leftrightarrow \text{CH}_2\text{CO}^* + ^*$	0.27	0.50
R16	$\text{CH}_2\text{CO}^* + \text{H}^* \leftrightarrow \text{CH}_3\text{CO}^* + ^*$	0.55	0.50
R17	$\text{CH}_3\text{CO}^* + \text{H}^* \leftrightarrow \text{CH}_3\text{CHO}(\text{g}) + 2^*$	1.11	0.49
R18	$\text{CH}_3\text{CO}^* + \text{H}^* \leftrightarrow \text{CH}_3\text{COH}^* + ^*$	1.23	0.47
R19	$\text{CH}_3\text{COH}^* + \text{H}^* \leftrightarrow \text{CH}_3\text{CHOH}^* + ^*$	0.60	0.56
R20	$\text{CH}_3\text{CHOH}^* + \text{H}^* \leftrightarrow \text{CH}_3\text{CH}_2\text{OH}(\text{g}) + 2^*$	0.64	0.50
R21	$\text{CH}_2\text{O}^* + \text{H}^* \leftrightarrow \text{CH}_2\text{OH} + ^*$	0.75	0.45
R22	$\text{CH}_2\text{CO}^* + \text{H}^* \leftrightarrow \text{CH}_2\text{COH}^* + ^*$	0.89	0.46
R23	$\text{CH}_2\text{COH}^* + \text{H}^* \leftrightarrow \text{CH}_3\text{COH}^* + ^*$	0.93	0.56
R24	$\text{CHCO}^* + \text{H}^* \leftrightarrow \text{CHCHO}^* + ^*$	0.38	0.63
R25	$\text{CH}_2\text{CO}^* + \text{H}^* \leftrightarrow \text{CH}_2\text{CHO}^* + ^*$	0.38	0.53
R26	$\text{CHCHO}^* + \text{H}^* \leftrightarrow \text{CH}_2\text{CHO}^* + ^*$	0.60	0.74
R27	$\text{CH}_2\text{CHO}^* + \text{H}^* \leftrightarrow \text{CH}_3\text{CHO}(\text{g}) + 2^*$	1.32	0.50
R28	$\text{CH}_2\text{O}^* + \text{CH}_2^* \leftrightarrow \text{CH}_3\text{COH}^* + ^*$	0.70	0.52
R29	$\text{O}^* + \text{H}^* \leftrightarrow \text{OH}^* + ^*$	0.51	0.77
R30	$\text{OH}^* + \text{H}^* \leftrightarrow \text{H}_2\text{O}(\text{g}) + ^*$	0.87	0.63
R31	$\text{CH}_2\text{COH}^* + \text{H}^* \leftrightarrow \text{CH}_2\text{CHOH}^* + ^*$	0.66	0.60
R32	$\text{CH}_2\text{CHOH}^* + \text{H}^* \leftrightarrow \text{CH}_3\text{CHOH}^* + ^*$	0.80	0.44
R33	$\text{CH}_2\text{CHO}^* + \text{H}^* \leftrightarrow \text{CH}_2\text{CHOH}^* + ^*$	1.16	0.52
R34	$\text{CH}_2\text{OH}^* + \text{H}^* \leftrightarrow \text{CH}_3\text{OH}(\text{g}) + 2^*$	0.86	0.50

Table B3 Continued

R35	$\text{HCO}^* + \text{H}^* \leftrightarrow \text{CHOH}^* + ^*$	1.02	0.48
R36	$\text{CH}_3\text{O}^* + \text{H}^* \leftrightarrow \text{CH}_3\text{OH}(\text{g}) + 2^*$	1.31	0.51
R37	$\text{CHOH}^* + \text{H}^* \leftrightarrow \text{CH}_2\text{OH}^* + ^*$	0.44	0.60
R38	$\text{CH}^* + \text{CH}_2^* \leftrightarrow \text{CHCH}_2^* + ^*$	0.31	0.85
R39	$\text{CHCH}_2^* + \text{H}^* \leftrightarrow \text{CH}_2\text{CH}_2^* + ^*$	0.14	0.63
R40	$\text{CHCH}_2^* + \text{H}^* \leftrightarrow \text{CH}_2\text{CH}_2(\text{g}) + 2^*$	0.67	0.55
R41	$\text{CH}_2^* + \text{CH}_2^* \leftrightarrow \text{CH}_3\text{CH}_2^* + ^*$	0.72	0.59
R42	$\text{CH}_3\text{CH}_2^* + \text{H}^* \leftrightarrow \text{CH}_3\text{CH}_3(\text{g}) + 2^*$	0.28	0.52
R43	$\text{CH}_2\text{CH}_2^* + \text{H}^* \leftrightarrow \text{CH}_3\text{CH}_2^* + ^*$	1.08	0.41
R44	$\text{CH}_2^* + \text{CH}_2^* \leftrightarrow \text{CH}_2\text{CH}_2^* + ^*$	0.24	0.81
R45	$\text{CHCH}_2^* + ^* \leftrightarrow \text{CH}_2\text{CH}_2(\text{g}) + 2^*$	0.83	0.23
R46	$\text{CH}_3\text{CH}_2^* + \text{OH}^* \leftrightarrow \text{CH}_3\text{CH}_2\text{OH}(\text{g}) + 2^*$	0.87	0.49

Table B4. Activation energies on palladium surface

R.No.	Reaction	Activation energy on Palladium	
		E _{af}	E _{ar}
R1	$\text{CO(g)} + * \leftrightarrow \text{CO}^*$	0.00	0.00
R2	$\text{H}_2(\text{g}) + 2* \leftrightarrow 2\text{H}^* + *$	0.00	0.00
R3	$\text{CO}^* + \text{H}^* \leftrightarrow \text{HCO}^* + *$	1.62	0.59
R4	$\text{HCO}^* + \text{H}^* \leftrightarrow \text{CH}_2\text{O}^* + *$	1.41	0.66
R5	$\text{CH}_2\text{O}^* + \text{H}^* \leftrightarrow \text{CH}_3\text{O}^* + *$	0.60	0.57
R6	$\text{HCO}^* + * \leftrightarrow \text{CH}^* + \text{O}^*$	2.79	1.44
R7	$\text{CH}_2\text{O}^* + * \leftrightarrow \text{CH}_2^* + \text{O}^*$	1.39	1.44
R8	$\text{CH}_3\text{O}^* + * \leftrightarrow \text{CH}_3^* + \text{O}^*$	1.03	1.31
R9	$\text{CH}^* + \text{H}^* \leftrightarrow \text{CH}_2^* + *$	0.37	1.01
R10	$\text{CH}_2^* + \text{H}^* \leftrightarrow \text{CH}_3^* + *$	0.69	0.90
R11	$\text{CH}_3^* + \text{H}^* \leftrightarrow \text{CH}_4(\text{g}) + 2*$	0.76	0.71
R12	$\text{CH}^* + \text{CO}^* \leftrightarrow \text{CHCO}^* + *$	2.80	3.27
R13	$\text{CH}_2^* + \text{CO}^* \leftrightarrow \text{CH}_2\text{CO}^* + *$	0.78	0.74
R14	$\text{CH}_3^* + \text{CO}^* \leftrightarrow \text{CH}_3\text{CO}^* + *$	1.42	0.50
R15	$\text{CHCO}^* + \text{H}^* \leftrightarrow \text{CH}_2\text{CO}^* + *$	2.80	2.70
R16	$\text{CH}_2\text{CO}^* + \text{H}^* \leftrightarrow \text{CH}_3\text{CO}^* + *$	1.06	0.62
R17	$\text{CH}_3\text{CO}^* + \text{H}^* \leftrightarrow \text{CH}_3\text{CHO}(\text{g}) + 2*$	1.11	0.64
R18	$\text{CH}_3\text{CO}^* + \text{H}^* \leftrightarrow \text{CH}_3\text{COH}^* + *$	1.30	0.62
R19	$\text{CH}_3\text{COH}^* + \text{H}^* \leftrightarrow \text{CH}_3\text{CHOH}^* + *$	0.38	0.78
R20	$\text{CH}_3\text{CHOH}^* + \text{H}^* \leftrightarrow \text{CH}_3\text{CH}_2\text{OH}(\text{g}) + 2*$	1.11	0.66
R21	$\text{CH}_2\text{O}^* + \text{H}^* \leftrightarrow \text{CH}_2\text{OH}^* + *$	0.54	0.58
R22	$\text{CH}_2\text{CO}^* + \text{H}^* \leftrightarrow \text{CH}_2\text{COH}^* + *$	1.25	0.59
R23	$\text{CH}_2\text{COH}^* + \text{H}^* \leftrightarrow \text{CH}_3\text{COH}^* + *$	1.18	0.74
R24	$\text{CHCO}^* + \text{H}^* \leftrightarrow \text{CHCHO}^* + *$	2.80	2.27
R25	$\text{CH}_2\text{CO}^* + \text{H}^* \leftrightarrow \text{CH}_2\text{CHO}^* + *$	0.87	0.65
R26	$\text{CHCHO}^* + \text{H}^* \leftrightarrow \text{CH}_2\text{CHO}^* + *$	2.80	3.00
R27	$\text{CH}_2\text{CHO}^* + \text{H}^* \leftrightarrow \text{CH}_3\text{CHO}(\text{g}) + 2*$	1.34	0.66

Table B4 Continued

R.No.	Reaction	Activation energy on Palladium	
		E _{af}	E _{ar}
R28	CH ₂ O*+CH ₂ * \leftrightarrow CH ₃ COH*+*	0.29	0.69
R29	O*+H* \leftrightarrow OH*+*	1.04	0.95
R30	OH*+H* \leftrightarrow H ₂ O(g)+*	0.71	0.82
R31	CH ₂ COH*+H* \leftrightarrow CH ₂ CHOH*+*	0.66	0.82
R32	CH ₂ CHOH*+H* \leftrightarrow CH ₃ CHOH*+*	0.97	0.62
R33	CH ₂ CHO*+H* \leftrightarrow CH ₂ CHOH*+*	1.00	0.71
R34	CH ₂ OH*+H* \leftrightarrow CH ₃ OH(g)+2*	1.09	0.67
R35	HCO*+H* \leftrightarrow CHOH*+*	1.69	0.62
R36	CH ₃ O*+H* \leftrightarrow CH ₃ OH(g)+2*	1.04	0.68
R37	CHOH*+H* \leftrightarrow CH ₂ OH*+*	0.43	0.80
R38	CH*+CH ₂ * \leftrightarrow CHCH ₂ *+*	0.27	1.09
R39	CHCH ₂ *+H* \leftrightarrow CH ₂ CH ₂ *+*	0.18	0.79
R40	CHCH ₂ *+H* \leftrightarrow CH ₂ CH ₂ (g)+2*	0.61	0.72
R41	CH ₂ *+CH ₂ * \leftrightarrow CH ₃ CH ₂ *+*	0.74	0.78
R42	CH ₃ CH ₂ *+H* \leftrightarrow CH ₃ CH ₃ (g)+2*	0.37	0.69
R43	CH ₂ CH ₂ *+H* \leftrightarrow CH ₃ CH ₂ *+*	1.09	0.55
R44	CH ₂ *+CH ₂ * \leftrightarrow CH ₂ CH ₂ *+*	0.24	1.51
R45	CHCH ₂ *+* \leftrightarrow CH ₂ CH ₂ (g)+2*	0.78	0.30
R46	CH ₃ CH ₂ *+OH* \leftrightarrow CH ₃ CH ₂ OH(g)+2*	0.66	0.64

Notes for tables B2, B3 and B4:

- a) In tables B2, B3 and B4 the values in bold are derived from extensive DFT calculations. Other values are derived from BEP relationships.
- b) Activation energies obtained from DFT and BEP are scaled by a factor of 0.7 on Co and Pd surfaces, whereas scaling factor for CoPd surface is 0.53.

3. Entropy of reactions is calculated using DFT. Selecting Vibrational frequencies in the Properties tab requests calculations of frequencies, infrared (ir) intensities, and thermochemical properties: heat capacity, entropy, enthalpy, and Gibbs free energy.

Table B5. DFT derived entropy of reaction for reactions involving gas phase species on three surfaces.

Entropy of reactions in J/mol K				
S.No.	Reactions	Cobalt	CoPd	Palladium
1	$\text{CO(g)}+2^* \leftrightarrow \text{CO}^*+^*$	-134.51	-133.35	-102.53
2	$\text{H}_2\text{(g)}+2^* \leftrightarrow \text{H}^*+\text{H}^*$	-135.26	-145.10	-114.96
3	$\text{CH}_3^*+\text{H}^* \leftrightarrow \text{CH}_4\text{(g)}+2^*$	143.35	159.63	131.54
4	$\text{CH}_2\text{OH}^*+\text{H}^* \rightarrow \text{CH}_3\text{OH(g)}+2^*$	232.02	222.98	208.00
5	$\text{CH}_3\text{CO}^*+\text{H}^* \rightarrow \text{CH}_3\text{CHO(g)}+2^*$	143.12	179.68	167.71
6	$\text{CH}_3\text{CHOH}^*+\text{H}^* \rightarrow \text{CH}_3\text{CH}_2\text{OH(g)}+2^*$	160.72	150.50	143.45
7	$\text{OH}^*+\text{H}^* \rightarrow \text{H}_2\text{O(g)}+2^*$	166.04	163.00	152.36
8	$\text{CH}_2\text{CHO}^*+\text{H}^* \rightarrow \text{CH}_3\text{CHO(g)}+2^*$	204.19	214.82	197.97
9	$\text{CH}_3\text{O}^*+\text{H}^* \rightarrow \text{CH}_3\text{OH(g)}+2^*$	220.42	219.21	213.67
10	$\text{CHCH}_2^*+\text{H}^* \rightarrow \text{CH}_2\text{CH}_2\text{(g)}+2^*$	154.15	169.57	144.00
11	$\text{CH}_3\text{CH}_2^*+\text{H}^* \rightarrow \text{CH}_3\text{CH}_3\text{(g)}+2^*$	144.93	129.69	126.89
12	$\text{CH}_2\text{CH}_2^*+^* \rightarrow \text{CH}_2\text{CH}_2\text{(g)}+2^*$	134.70	142.59	144.16
13	$\text{CH}_3\text{CH}_2^*+\text{OH}^* \rightarrow \text{CH}_3\text{CH}_2\text{OH(g)}+2^*$	145.63	117.50	134.20

4. Enthalpy of reactions is calculated using DFT derived adsorption energies. All adsorption energies used to calculate enthalpies are zero point energy corrected and obtained using B3LYP.

Table B6. DFT derived enthalpy of reaction for reactions involving gas phase species on three surfaces.

Enthalpy of reactions in eV				
S.No.	Reactions	Cobalt	CoPd	Palladium
1	$\text{CO(g)}+2^* \leftrightarrow \text{CO}^*+^*$	-1.494	-1.736	-1.82
2	$\text{H}_2\text{(g)}+2^* \leftrightarrow \text{H}^*+\text{H}^*$	-0.593	-0.621	-0.65
3	$\text{CH}_3^*+\text{H}^* \leftrightarrow \text{CH}_4\text{(g)}+2^*$	0.231	0.00129	0.12
4	$\text{CH}_2\text{OH}^*+\text{H}^* \rightarrow \text{CH}_3\text{OH(g)}+2^*$	2.455	1.786	0.601
5	$\text{CH}_3\text{CO}^*+\text{H}^* \rightarrow \text{CH}_3\text{CHO(g)}+2^*$	0.875	1.189	0.674
6	$\text{CH}_3\text{CHOH}^*+\text{H}^* \rightarrow \text{CH}_3\text{CH}_2\text{OH(g)}+2^*$	1.49	0.272	0.646
7	$\text{OH}^*+\text{H}^* \rightarrow \text{H}_2\text{O(g)}+2^*$	1.94	1.519	0.78
8	$\text{CH}_2\text{CHO}^*+\text{H}^* \rightarrow \text{CH}_3\text{CHO(g)}+2^*$	1.547	1.547	0.78
9	$\text{CH}_3\text{O}^*+\text{H}^* \rightarrow \text{CH}_3\text{OH(g)}+2^*$	1.92	1.51	0.506
10	$\text{CHCH}_2^*+\text{H}^* \rightarrow \text{CH}_2\text{CH}_2\text{(g)}+2^*$	0.078	0.222	-0.167
11	$\text{CH}_3\text{CH}_2^*+\text{H}^* \rightarrow \text{CH}_3\text{CH}_3\text{(g)}+2^*$	-0.45	-0.455	-0.449
12	$\text{CH}_2\text{CH}_2^*+^* \rightarrow \text{CH}_2\text{CH}_2\text{(g)}+2^*$	0.645	1.146	0.694
13	$\text{CH}_3\text{CH}_2^*+\text{OH}^* \rightarrow \text{CH}_3\text{CH}_2\text{OH(g)}+2^*$	1.59	0.73	0.016

5. Terminology used in MKM model for writing rate expressions and developing ODE equations is represented in table below.

Table B7. Symbols used in rate expressions and differential equations

Intermediates	On active sites
Empty Sites	γ_0
θ_{CO}	γ_1
θ_H	γ_2
θ_{HCO}	γ_3
θ_{CH_2O}	γ_4
θ_{CH_3O}	γ_5
θ_{CH}	γ_6
θ_{CH_2}	γ_7
θ_{CH_3}	γ_8
θ_{CHOH}	γ_9
θ_{CH_2OH}	γ_{10}
θ_{CHCO}	γ_{11}
θ_{CH_2CO}	γ_{12}
θ_{CH_3CO}	γ_{13}
θ_{CHCHO}	γ_{14}
θ_{CH_2CHO}	γ_{15}
θ_{CH_2COH}	γ_{16}
θ_{CH_3COH}	γ_{17}
θ_{CH_2CHOH}	γ_{18}
θ_{CH_3CHOH}	γ_{19}
θ_O	γ_{20}
θ_{OH}	γ_{21}
θ_{CHCH_2}	γ_{22}
$\theta_{CH_2CH_2}$	γ_{23}
$\theta_{CH_3CH_2}$	γ_{24}

Table B7 Continued

Gas Phase species	Number of moles
$n_{\text{CO}} \text{ (g)}$	Y25
$n_{\text{H}_2} \text{ (g)}$	Y26
$n_{\text{CH}_4} \text{ (g)}$	Y27
$n_{\text{CH}_3\text{OH}} \text{ (g)}$	Y28
$n_{\text{CH}_3\text{CH}_2\text{OH}} \text{ (g)}$	Y29
$n_{\text{CH}_3\text{CHO}} \text{ (g)}$	Y30
$n_{\text{H}_2\text{O}} \text{ (g)}$	Y31
$n_{\text{CH}_2\text{CH}_2} \text{ (g)}$	Y32
$n_{\text{CH}_3\text{CH}_3} \text{ (g)}$	Y33)

6. Sticking coefficients for CO on cobalt and palladium surface are modeled as a function of coverage. A sixth order quadratic equation is fitted to represent the dependency of sticking coefficients. Equations and constants for the sticking coefficients is represented below. For CoPd surface, an average values obtained from Co and Pd surfaces is used.

Coverage dependent sticking coefficients:

- a. Equation relating sticking coefficient and coverage of carbon monoxide on palladium surface

$$S_{\text{Co}} = (a_1 + c_1 y_1^2 + e_1 y_1^4) / (1 + b_1 y_1^2 + d_1 y_1^4 + f_1 y_1^6)$$

Where,

$$a_1 = 0.593999221$$

$$b_1 = -5.360127273$$

$$c_1 = -3.434120556$$

$$d_1 = 19.47053542$$

$$e_1 = 4.722521824$$

$$f_1 = 353.3218192$$

- b. Equation relating sticking coefficient and coverage of carbon monoxide on CoPd surface

Sticking Coefficients on CoPd surface are obtained by taking average of sticking coefficients on CO and Pd surfaces)

$$SC_{Co} = (a_2 + c_2 y_1^2 + e_2 y_1^4 + g_2 y_1^6) / (1 + b_2 y_1^2 + d_2 y_1^4 + f_2 y_1^6)$$

Where,

$$a_2 = 0.627374526$$

$$b_2 = -14.42835968$$

$$c_2 = -9.938044222$$

$$d_2 = 67.4470774$$

$$e_2 = 49.78140341$$

$$f_2 = -65.08072897$$

$$g_2 = -71.83630315$$

- c. Equation relating sticking coefficient and coverage of carbon monoxide on cobalt surface

$$SC_{Co} = (a_3 + c_3 y_1^2 + e_3 y_1^4 + g_3 y_1^6) / (1 + b_3 y_1^2 + d_3 y_1^4 + f_3 y_1^6)$$

Where,

$$a_3 = 0.647374526$$

$$b_3 = -14.42835968$$

$$c_3 = -9.938044222$$

$$d_3 = 67.4470774$$

$$e_3 = 49.78140341$$

$$f_3 = -65.08072897$$

$$g_3 = -71.83630315$$

7. Rate of the surface reactions is represented as a product of rate constants and concentration of reactants. For reactions involving gas phase species, rates are represented in terms of DFT derived equilibrium constants.

Table B8. Rate expressions for surface reactions

R.No.	Reaction	Rate Expression
R1	$\text{CO(g)} + * \leftrightarrow \text{CO}^*$	$k_f(1)(P_{\text{CO}}^{y_0} y_0^{-y_1} / K_{\text{CO}})$
R2	$\text{H}_2(\text{g}) + 2* \leftrightarrow 2\text{H}^* + *$	$K_f(2)(P_{\text{H}_2}^{y_0} y_0^{-y_2} y_2^2 / K_{\text{H}_2})$
R3	$\text{CO}^* + \text{H}^* \leftrightarrow \text{HCO}^* + *$	$k_f(3) y_1 y_2 - k_r(3) y_3 y_0$
R4	$\text{HCO}^* + \text{H}^* \leftrightarrow \text{CH}_2\text{O}^* + *$	$k_f(4) y_2 y_3 - k_r(4) y_4 y_0$
R5	$\text{CH}_2\text{O}^* + \text{H}^* \leftrightarrow \text{CH}_3\text{O}^* + *$	$k_f(5) y_4 y_2 - k_r(5) y_5 y_0$
R6	$\text{HCO}^* + * \leftrightarrow \text{CH}^* + \text{O}^*$	$k_f(6) y_3 y_0 - k_r(6) y_6 y_2^0$
R7	$\text{CH}_2\text{O}^* + * \leftrightarrow \text{CH}_2^* + \text{O}^*$	$k_f(7) y_0 y_4 - k_r(7) y_7 y_2^0$
R8	$\text{CH}_3\text{O}^* + * \leftrightarrow \text{CH}_3^* + \text{O}^*$	$k_f(8) y_5 y_0 - k_r(8) y_8 y_2^0$
R9	$\text{CH}^* + \text{H}^* \leftrightarrow \text{CH}_2^* + *$	$k_f(9) y_6 y_2 - k_r(9) y_7 y_0$
R10	$\text{CH}_2^* + \text{H}^* \leftrightarrow \text{CH}_3^* + *$	$k_f(10) y_7 y_2 - k_r(10) y_8 y_0$
R11	$\text{CH}_3^* + \text{H}^* \leftrightarrow \text{CH}_4(\text{g}) + 2*$	$k_f(11) y_2 y_8 - k_f(11) P_{\text{H}_2}^{y_0} y_0 / K_{\text{H}_2}$
R12	$\text{CH}^* + \text{CO}^* \leftrightarrow \text{CHCO}^* + *$	$k_f(12) y_1 y_6 - k_r(12) y_{11} y_0$
R13	$\text{CH}_2^* + \text{CO}^* \leftrightarrow \text{CH}_2\text{CO}^* + *$	$k_f(13) y_1 y_7 - k_r(13) y_{12} y_0$
R14	$\text{CH}_3^* + \text{CO}^* \leftrightarrow \text{CH}_3\text{CO}^* + *$	$k_f(14) y_1 y_8 - k_r(14) y_{13} y_0$
R15	$\text{CHCO}^* + \text{H}^* \leftrightarrow \text{CH}_2\text{CO}^* + *$	$k_f(15) y_2 y_{11} - k_r(15) y_{12} y_0$
R16	$\text{CH}_2\text{CO}^* + \text{H}^* \leftrightarrow \text{CH}_3\text{CO}^* + *$	$k_f(16) y_{12} y_2 - k_r(16) y_{13} y_0$
R17	$\text{CH}_3\text{CO}^* + \text{H}^* \leftrightarrow \text{CH}_3\text{CHO}(\text{g}) + 2*$	$k_f(17)(y_{13} y_2 - P_{\text{CH}_3\text{CHO}}^{y_0} y_0 / K_{\text{H}_2})$
R18	$\text{CH}_3\text{CO}^* + \text{H}^* \leftrightarrow \text{CH}_3\text{COH}^* + *$	$k_f(18) y_{13} y_2 - k_r(18) y_{17} y_0$
R19	$\text{CH}_3\text{COH}^* + \text{H}^* \leftrightarrow \text{CH}_3\text{CHOH}^* + *$	$k_f(19) y_{17} y_2 - k_r(19) y_{19} y_0$
R20	$\text{CH}_3\text{CHOH}^* + \text{H}^* \leftrightarrow \text{CH}_3\text{CH}_2\text{OH}(\text{g}) + 2*$	$k_f(20)((y_{19} y_2) - P_{\text{CH}_3\text{CH}_2\text{OH}}^{y_0} y_0 / K_{\text{CH}_3\text{CH}_2\text{OH}})$
R21	$\text{CH}_2\text{O}^* + \text{H}^* \leftrightarrow \text{CH}_2\text{OH}^* + *$	$k_f(21) y_2 y_4 - k_r(21) y_{10} y_0$
R22	$\text{CH}_2\text{CO}^* + \text{H}^* \leftrightarrow \text{CH}_2\text{COH}^* + *$	$k_f(22) y_2 y_{12} - k_r(22) y_{16} y_0$
R23	$\text{CH}_2\text{COH}^* + \text{H}^* \leftrightarrow \text{CH}_3\text{COH}^* + *$	$k_f(23) y_{16} y_2 - k_r(23) y_{17} y_0$
R24	$\text{CHCO}^* + \text{H}^* \leftrightarrow \text{CHCHO}^* + *$	$k_f(24) y_{11} y_2 - k_r(24) y_{14} y_0$
R25	$\text{CH}_2\text{CO}^* + \text{H}^* \leftrightarrow \text{CH}_2\text{CHO}^* + *$	$k_f(25) y_{12} y_2 - k_r(25) y_{15} y_0$

Table B8 Continued

R.No.	Reaction	Rate Expression
R26	$\text{CHCHO}^* + \text{H}^* \leftrightarrow \text{CH}_2\text{CHO}^* + ^*$	$\text{kf}(26) \cdot \text{y}14 \cdot \text{y}2 - \text{kr}(26) \cdot \text{y}15 \cdot \text{y}0$
R27	$\text{CH}_2\text{CHO}^* + \text{H}^* \leftrightarrow \text{CH}_3\text{CHO}(\text{g}) + 2^*$	$\text{kf}(27)(\text{y}15 \cdot \text{y}2 - \text{Pch}3\text{cho} \cdot \text{y}0 \cdot \text{y}0 / \text{Kch}3\text{cho})$
R28	$\text{CH}_2\text{O}^* + \text{CH}_2^* \leftrightarrow \text{CH}_3\text{COH}^* + ^*$	$\text{kf}(28) \cdot \text{y}4 \cdot \text{y}7 - \text{kr}(28) \cdot \text{y}17 \cdot \text{y}0$
R29	$\text{O}^* + \text{H}^* \leftrightarrow \text{OH}^* + ^*$	$\text{kf}(29) \cdot \text{y}20 \cdot \text{y}2 - \text{kr}(29) \cdot \text{y}21 \cdot \text{y}0$
R30	$\text{OH}^* + \text{H}^* \leftrightarrow \text{H}_2\text{O}(\text{g}) + 2^*$	$\text{kf}(30) \cdot (\text{y}2 \cdot \text{y}21 - \text{Ph}2\text{o} \cdot \text{y}0 \cdot \text{y}0 / \text{Kh}2\text{o})$
R31	$\text{CH}_2\text{COH}^* + \text{H}^* \leftrightarrow \text{CH}_2\text{CHOH}^* + ^*$	$\text{kf}(31) \cdot \text{y}16 \cdot \text{y}2 - \text{kr}(31) \cdot \text{y}18 \cdot \text{y}0$
R32	$\text{CH}_2\text{CHOH}^* + \text{H}^* \leftrightarrow \text{CH}_3\text{CHOH}^* + ^*$	$\text{kf}(32) \cdot \text{y}18 \cdot \text{y}2 - \text{kr}(32) \cdot \text{y}19 \cdot \text{y}0$
R33	$\text{CH}_2\text{CHO}^* + \text{H}^* \leftrightarrow \text{CH}_2\text{CHOH}^* + ^*$	$\text{kf}(33) \cdot \text{y}15 \cdot \text{y}2 - \text{kr}(33) \cdot \text{y}18 \cdot \text{y}0$
R34	$\text{CH}_2\text{OH}^* + \text{H}^* \leftrightarrow \text{CH}_3\text{OH}(\text{g}) + 2^*$	$\text{kf}(34)(\text{y}10 \cdot \text{y}2 - \text{Pch}3\text{oh} \cdot \text{y}0 \cdot \text{y}0 / \text{Kch}3\text{oh})$
R35	$\text{HCO}^* + \text{H}^* \leftrightarrow \text{CHOH}^* + ^*$	$\text{kf}(35) \cdot \text{y}3 \cdot \text{y}2 - \text{kr}(35) \cdot \text{y}9 \cdot \text{y}0$
R36	$\text{CH}_3\text{O}^* + \text{H}^* \leftrightarrow \text{CH}_3\text{OH}(\text{g}) + 2^*$	$\text{kf}(36)(\text{y}2 \cdot \text{y}5 - \text{Pch}3\text{oh} \cdot \text{y}0 / \text{Kch}3\text{oh})$
R37	$\text{CHOH}^* + \text{H}^* \leftrightarrow \text{CH}_2\text{OH}^* + ^*$	$\text{kf}(37) \cdot \text{y}9 \cdot \text{y}2 - \text{kr}(37) \cdot \text{y}10 \cdot \text{y}0$
R38	$\text{CH}^* + \text{CH}_2^* \leftrightarrow \text{CHCH}_2^* + ^*$	$\text{kf}(38) \cdot \text{y}6 \cdot \text{y}7 - \text{kr}(38) \cdot \text{y}1 \cdot \text{y}0$
R39	$\text{CHCH}_2^* + \text{H}^* \leftrightarrow \text{CH}_2\text{CH}_2^* + ^*$	$\text{kf}(39) \cdot \text{y}1 \cdot \text{y}2 - \text{kr}(39) \cdot \text{y}23 \cdot \text{y}0$
R40	$\text{CHCH}_2^* + \text{H}^* \leftrightarrow \text{CH}_2\text{CH}_2(\text{g}) + 2^*$	$\text{kf}(40) \cdot (\text{y}2 \cdot \text{y}1 - \text{Pch}2\text{ch}2 \cdot \text{y}0 \cdot \text{y}0 / \text{Kch}2\text{ch}21)$
R41	$\text{CH}_3^* + \text{CH}_2^* \leftrightarrow \text{CH}_3\text{CH}_2^* + ^*$	$\text{kf}(41) \cdot \text{y}8 \cdot \text{y}7 - \text{kr}(41) \cdot \text{y}24 \cdot \text{y}0$
R42	$\text{CH}_3\text{CH}_2^* + \text{H}^* \leftrightarrow \text{CH}_3\text{CH}_3(\text{g}) + 2^*$	$\text{kf}(42) \cdot (\text{y}2 \cdot \text{y}24 - \text{Pch}3\text{ch}3 \cdot \text{y}0 \cdot \text{y}0 / \text{Kch}3\text{ch}3)$
R43	$\text{CH}_2\text{CH}_2^* + \text{H}^* \leftrightarrow \text{CH}_3\text{CH}_2^* + ^*$	$\text{kf}(43) \cdot \text{y}23 \cdot \text{y}2 - \text{kr}(43) \cdot \text{y}24 \cdot \text{y}0$
R44	$\text{CH}_2^* + \text{CH}_2^* \leftrightarrow \text{CH}_2\text{CH}_2^* + ^*$	$\text{kf}(44) \cdot \text{y}7 \cdot \text{y}7 - \text{kr}(44) \cdot \text{y}23 \cdot \text{y}0$
R45	$\text{CHCH}_2^* + ^* \leftrightarrow \text{CH}_2\text{CH}_2(\text{g}) + 2^*$	$\text{kf}(45) \cdot (\text{y}23 \cdot \text{y}0 - \text{Pch}2\text{ch}2 \cdot \text{y}0 \cdot \text{y}0 / \text{Kch}2\text{ch}22)$
R46	$\text{CH}_3\text{CH}_2^* + \text{OH}^* \leftrightarrow \text{CH}_3\text{CH}_2\text{OH}(\text{g}) + 2^*$	$\text{kf}(46) \cdot (\text{y}24 \cdot \text{y}21 - \text{Pch}3\text{ch}2\text{oh} \cdot \text{y}0 \cdot \text{y}0 / \text{Kch}3\text{ch}2\text{oh}2)$

8. Change in the fractional coverage of species with respect to time is written in terms of rate of reactions. These ODE are written for all 24 intermediate species and solved simultaneously to get the coverages on catalyst. For gasphase species change in number of moles is represented using batch reactor design equations.

Table B9. Differential equations

Symbol	INTERMEDIATES	DIFFERENTIAL EQUATIONS
Y0	EMPTY SITE	$1 - (y_1 + y_2 + y_3 + y_4 + y_5 + y_6 + y_7 + y_8 + y_9 + y_{10} + y_{11} + y_{12} + y_{13} + y_{14} + y_{15} + y_{16} + y_{17} + y_{18} + y_{19} + y_{20} + y_{21} + y_{22} + y_{23} + y_{24})$
Y1	CO	$dy_1/dt = r_1 - r_3 - r_{12} - r_{13} - r_{14}$
Y2	H	$dy_2/dt = r_2 - r_3 - r_4 - r_5 - r_9 - r_{10} - r_{11} - r_{15} - r_{16} - r_{17} - r_{18} - r_{19} - r_{20} - r_{21} - r_{22} - r_{23} - r_{24} - r_{25} - r_{26} - r_{27} - r_{29} - r_{30} - r_{31} - r_{32} - r_{33} - r_{34} - r_{35} - r_{36} - r_{37} - r_{39} - r_{40} - r_{42} - r_{43}$
Y3	HCO	$dy_3/dt = r_3 - r_4 - r_6 - r_{35}$
Y4	CH ₂ O	$dy_4/dt = r_4 - r_5 - r_7 - r_{21} - r_{28}$
Y5	CH ₃ O	$dy_5/dt = r_5 - r_8 - r_{36}$
Y6	CH	$dy_6/dt = r_6 - r_9 - r_{12} - r_{38}$
Y7	CH ₂	$dy_7/dt = r_7 + r_9 - r_{10} - r_{13} - r_{28} - r_{38} - r_{41} - r_{44}$
Y8	CH ₃	$dy_8/dt = r_8 + r_{10} - r_{11} - r_{14} - r_{41}$
Y9	CHOH	$dy_9/dt = r_{35} - r_{37}$
Y10	CH ₂ OH	$dy_{10}/dt = r_{21} - r_{34} + r_{37}$
Y11	CHCO	$dy_{11}/dt = r_{12} - r_{15} - r_{24}$
Y12	CH ₂ CO	$dy_{12}/dt = r_{13} + r_{15} - r_{16} - r_{22} - r_{25}$
Y13	CH ₃ CO	$dy_{13}/dt = r_{14} + r_{16} - r_{17} - r_{18}$
Y14	CHCHO	$dy_{14}/dt = r_{24} - r_{26}$
Y15	CH ₂ CHO	$dy_{15}/dt = r_{25} + r_{26} - r_{27} - r_{33}$
Y16	CH ₂ COH	$dy_{16}/dt = r_{22} - r_{23} - r_{31}$
Y17	CH ₃ COH	$dy_{17}/dt = r_{18} - r_{19} + r_{23} + r_{28}$
Y18	CH ₂ CHOH	$dy_{18}/dt = r_{31} - r_{32} + r_{33}$
Y19	CH ₃ CHOH	$dy_{19}/dt = r_{19} - r_{20} + r_{32}$

Table B9 Continued

Symbol	INTERMEDIATES	DIFFERENTIAL EQUATIONS
Y20	O	$dy_{20}dt = r_6 + r_7 + r_8 - r_{29}$
Y21	OH	$dy_{21}dt = r_{29} - r_{30} - r_{46}$
Y1	CHCH ₂	$dy_1dt = r_{38} - r_{39} - r_{40}$
Y23	CH ₂ CH ₂	$dy_{23}dt = r_{39} - r_{43} + r_{44} - r_{45}$
Y24	CH ₃ CH ₂	$dy_{24}dt = r_{41} - r_{42} + r_{43} - r_{46}$
Y25	CO (g)	$dy_{25}dt = (mcat * s / (Na * w)) * (-r_1)$
Y26	H ₂ (g)	$dy_{26}dt = (mcat * s / (Na * w)) * (-r_2 / 2)$
Y27	CH ₄ (g)	$dy_{27}dt = (mcat * s / (Na * w)) * (r_{11})$
Y28	CH ₃ OH (g)	$dy_{28}dt = (mcat * s / (Na * w)) * (r_{34} + r_{36})$
Y29	CH ₃ CH ₂ OH (g)	$dy_{29}dt = (mcat * s / (Na * w)) * (r_{20} + r_{46})$
Y30	CH ₃ CHO (g)	$dy_{30}dt = (mcat * s / (Na * w)) * (r_{17} + r_{27})$
Y31	H ₂ O (g)	$dy_{31}dt = (mcat * s / (Na * w)) * (r_{30})$
Y32	CH ₂ CH ₂ (g)	$dy_{32}dt = (mcat * s / (Na * w)) * (r_{40} + r_{45})$
Y33	CH ₃ CH ₃ (g)	$dy_{33}dt = (mcat * s / (Na * w)) * (r_{42})$

APPENDIX C

Micro kinetic modeling

Supporting documentation for combined model (Chapter 5)

1. Microkinetic model is built using Matlab R2016b, a batch reactor is modeled to obtain the time dependent concentrations of reactants and products. Table C1 has a list of constants and tunable parameters in the model.

Table C1. Constants used in this model

Boltzmann constant (k_b)	1.3806488 e-23	J/K
Universal gas constant (R)	8.3144621	J/mol K
Planks constant (h)	6.62606957e-34	J*s
Avogadro number (N_a)	6.02214129e23	molecules/mol
Temperature (T)	523	K
Surface area of catalyst /mass of it (s)	1e ⁶	m ² /kg
Surface area / active site (ω)	1.57 x 10 ⁻¹⁹	m ² /active site
Mass of catalyst (mcat)	9e-7	mg
Initial moles of CO (nCO)	7 x 10 ⁻⁵	moles
Initial moles of H ₂ (nH ₂)	14 x 10 ⁻⁵	moles
Volume of the reactor (vol)	1e-6	m ³
Mass of carbon monoxide (mco)	4.6512e-26	Kg
Mass of hydrogen (mh ₂)	3.3538e-27	Kg
Mass of methane (mch ₄)	2.6635e-26	Kg
Mass of methanol (mch ₃ oh)	5.3204e-26	Kg
Mass of acetaldehyde (mch ₃ cho)	7.314e-26	Kg

Table C1 continued

Mass of ethanol (mch3ch2oh)	7.6443e-26	Kg
Mass of water (mh2o)	2.9923e-26	Kg
Mass of ethane (mch3ch3)	4.9925e-26	Kg
Mass of ethylene (mch2ch2)	4.6579e-26	Kg

2. Sticking coefficients used to calculate collision theory dependent rate constants for gas phase species is represented in Tables C2 (Pd surface), C3 (Co surface), C4 (CoPd surface).

Table C2. Sticking Coefficients on palladium surface

Gas phase species	Symbol used	Sticking coefficient	Reference
Hydrogen	SCh2_Pd	1.5e-7	A
Methane	SCch4_Pd	1e-11	B
Methanol	SCch3cho_Pd	0.04	assumed similar to ethanol
Acetaldehyde	SCch3cho_Pd	0.1	approximate value
Ethanol	SCch3ch2oh_Pd	0.04	C
Ethylene	SCch2ch2_Pd	1e-11	assumed similar to methane
Ethane	SCch3ch3_Pd	1e-11	assumed similar to methane

- a. K.I.Lunstrom et al. Journal of Applied Physics **26**, (2008); 10.1063/1.88053 ¹
b. H.stotz et al. Top Catal (2017) 60.83–109 ²
c. M.Bowker et al. Surface Science 370 (1997) 113-124 ³

Coverage dependent sticking coefficient of carbon monoxide on palladium ⁴:

$$SC_{Co_Pd} = (a_1 + c_1 y_1^2 + e_1 y_1^4) / (1 + b_1 y_1^2 + d_1 y_1^4 + f_1 y_1^6) \quad \text{Reference (d)}$$

Where,

y₁ = concentration of CO on Pd surface

$$a_1 = 0.593999221$$

$$b_1 = -5.360127273$$

$$c_1 = -3.434120556$$

$$d_1 = 19.47053542$$

$$e_1 = 4.722521824$$

$$f_1 = 353.3218192$$

Table C3. Sticking Coefficients on cobalt surface

Gas phase species	Symbol used	Sticking coefficient	Reference
Hydrogen	SCh2_Co	0.045	e
Methane	SCch4_Co	5.18e-8	f
Methanol	SCch3cho_Co	0.4	assumed similar to ethanol
Acetaldehyde	SCch3cho_Co	0.1	approximate value
Ethanol	SCch3ch2oh_Co	0.04	approximate value
Ethylene	SCch2ch2_Co	5.18e-8	assumed similar to methane
Ethane	SCch3ch3_Co	5.18e-8	assumed similar to methane

e. W. Lisowski et al. Lisowski et al. Applied Surface Science 35 (1988-89) 399408⁵

f. H. Burghgraef et al. The Journal of Chemical Physics **101**, 11012 (1994)⁶

Coverage dependent sticking coefficient of carbon monoxide on cobalt⁷:

Equation relating sticking coefficient and coverage of carbon monoxide on cobalt surface^h

$$SC_{Co_Co} = (a_3 + c_3 y_{43}^2 + e_3 y_{43}^4 + g_3 y_{43}^6) / (1 + b_3 y_{43}^2 + d_3 y_{43}^4 + f_3 y_{43}^6)$$

Where,

y_{43} = concentration of CO on Co surface

$$a_3 = 0.647374526$$

$$b_3 = -14.42835968$$

$$c_3 = -9.938044222$$

$$d_3 = 67.4470774$$

$$e_3 = 49.78140341$$

$$f_3 = -65.08072897$$

$$g_3 = -71.83630315$$

Table C4. Sticking Coefficients on cobalt-palladium surface

Sticking Coefficients on CoPd surface are obtained by taking average of sticking coefficients on CO and Pd surfaces

Gas phase species	Symbol used	Sticking coefficient	Reference
Hydrogen	SCh2_CoPd	2.25e-2	average of values from Co and Pd surfaces
Methane	SCch4_CoPd	5e-12	
Ethanol	SCch3cho_CoPd	0.04	
Acetaldehyde	SCch3cho_CoPd	0.1	
Ethanol	SCch3ch2oh_CoPd	0.04	
Ethylene	SCch2ch2_CoPd	5e-12	
Ethane	SCch3ch3_CoPd	5e-12	

Coverage dependent sticking coefficient of carbon monoxide on cobalt: Equation

relating sticking coefficient and coverage of carbon monoxide on cobalt surface

$$SC_{Co} = (a_3 + c_3 y_2^2 + e_3 y_2^4 + g_3 y_2^6) / (1 + b_3 y_2^2 + d_3 y_2^4 + f_3 y_2^6)$$

Where,

y_2 = concentration of CO on CoPd surface

$a_3 = 0.647374526$

$b_3 = -14.42835968$

$c_3 = -9.938044222$

$d_3 = 67.4470774$

$e_3 = 49.78140341$

$f_3 = -65.08072897$

$g_3 = -71.83630315$

3. Activation energies of 44 reactions calculated from BEP and NEB combined.

Activation energies on cobalt surface are represented in C5, on CoPd surface are represented in C6 and activation energies on palladium surface are represented in table C7.

Table C5. Activation energies on cobalt surface

R.No.	Reaction	Activation energy on Cobalt	
		E _{af}	E _{ar}
R1	CO(g)+* \leftrightarrow CO*	0.00	0.00
R2	H ₂ (g)+2* \leftrightarrow 2H*+*	0.00	0.00
R3	CO*+H* \leftrightarrow HCO*+*	1.30	0.58
R4	HCO*+H* \leftrightarrow CH ₂ O*+*	0.64	0.75
R5	CH ₂ O*+H* \leftrightarrow CH ₃ O*+*	0.46	0.97
R6	HCO*+* \leftrightarrow CH*+O*	0.84	0.92
R7	CH ₂ O*+* \leftrightarrow CH ₂ *+O*	0.95	1.33
R8	CH ₃ O*+* \leftrightarrow CH ₃ *+O*	1.16	1.41
R9	CH*+H* \leftrightarrow CH ₂ *+*	0.31	0.71
R10	CH ₂ *+H* \leftrightarrow CH ₃ *+*	0.54	0.92
R11	CH ₃ *+H* \leftrightarrow CH ₄ (g)+2*	0.87	0.71
R12	CH*+CO* \leftrightarrow CHCO*+*	0.88	1.13
R13	CH ₂ *+CO* \leftrightarrow CH ₂ CO*+*	0.95	0.74
R14	CH ₃ *+CO* \leftrightarrow CH ₃ CO*+*	1.20	0.54
R15	CHCO*+H* \leftrightarrow CH ₂ CO*+*	0.71	0.66
R16	CH ₂ CO*+H* \leftrightarrow CH ₃ CO*+*	0.73	0.66
R17	CH ₃ CO*+H* \leftrightarrow CH ₃ CHO(g)+2*	1.25	0.64
R18	CH ₃ CO*+H* \leftrightarrow CH ₃ COH*+*	1.08	0.32
R19	CH ₃ COH*+H* \leftrightarrow CH ₃ CHOH*+*	1.06	0.69
R20	CH ₃ CHOH*+H* \leftrightarrow CH ₃ CH ₂ OH(g)+2*	0.30	0.66

Table C5 Continued

R.No.	Reaction	Activation energy on Cobalt	
		E _{af}	E _{ar}
R21	$\text{CH}_2\text{O}^* + \text{H}^* \leftrightarrow \text{CH}_2\text{OH}^* + ^*$	1.14	0.70
R22	$\text{CH}_2\text{CO}^* + \text{H}^* \leftrightarrow \text{CH}_2\text{COH}^* + ^*$	0.91	0.63
R23	$\text{CH}_2\text{COH}^* + \text{H}^* \leftrightarrow \text{CH}_3\text{COH}^* + ^*$	1.30	0.75
R24	$\text{CHCO}^* + \text{H}^* \leftrightarrow \text{CHCHO}^* + ^*$	0.62	0.87
R25	$\text{CH}_2\text{CO}^* + \text{H}^* \leftrightarrow \text{CH}_2\text{CHO}^* + ^*$	0.32	0.71
R26	$\text{CHCHO}^* + \text{H}^* \leftrightarrow \text{CH}_2\text{CHO}^* + ^*$	0.89	0.99
R27	$\text{CH}_2\text{CHO}^* + \text{H}^* \leftrightarrow \text{CH}_3\text{CHO}(\text{g}) + 2^*$	1.74	0.66
R28	$\text{CH}_2\text{O}^* + \text{CH}_2^* \leftrightarrow \text{CH}_3\text{COH}^* + ^*$	1.11	0.69
R29	$\text{O}^* + \text{H}^* \leftrightarrow \text{OH}^* + ^*$	0.98	1.16
R30	$\text{OH}^* + \text{H}^* \leftrightarrow \text{H}_2\text{O}(\text{g}) + ^*$	1.39	0.83
R31	$\text{CH}_2\text{COH}^* + \text{H}^* \leftrightarrow \text{CH}_2\text{CHOH}^* + ^*$	0.93	0.81
R32	$\text{CH}_2\text{CHOH}^* + \text{H}^* \leftrightarrow \text{CH}_3\text{CHOH}^* + ^*$	1.32	0.53
R33	$\text{CH}_2\text{CHO}^* + \text{H}^* \leftrightarrow \text{CH}_2\text{CHOH}^* + ^*$	1.50	0.69
R34	$\text{CH}_2\text{OH}^* + \text{H}^* \leftrightarrow \text{CH}_3\text{OH}(\text{g}) + 2^*$	1.05	0.67
R35	$\text{HCO}^* + \text{H}^* \leftrightarrow \text{CHOH}^* + ^*$	1.42	0.86
R36	$\text{CH}_3\text{O}^* + \text{H}^* \leftrightarrow \text{CH}_3\text{OH}(\text{g}) + 2^*$	1.48	0.13
R37	$\text{CHOH}^* + \text{H}^* \leftrightarrow \text{CH}_2\text{OH}^* + ^*$	0.58	0.81
R38	$\text{CH}^* + \text{CH}_2^* \leftrightarrow \text{CHCH}_2^* + ^*$	0.73	1.13
R39	$\text{CHCH}_2^* + \text{H}^* \leftrightarrow \text{CH}_2\text{CH}_2^* + ^*$	0.39	0.78
R40	$\text{CHCH}_2^* + \text{H}^* \leftrightarrow \text{CH}_2\text{CH}_2(\text{g}) + 2^*$	0.78	0.72
R41	$\text{CH}_2^* + \text{CH}_2^* \leftrightarrow \text{CH}_3\text{CH}_2^* + ^*$	1.04	0.79
R42	$\text{CH}_3\text{CH}_2^* + \text{H}^* \leftrightarrow \text{CH}_3\text{CH}_3(\text{g}) + 2^*$	0.37	0.69
R43	$\text{CH}_2\text{CH}_2^* + \text{H}^* \leftrightarrow \text{CH}_3\text{CH}_2^* + ^*$	0.82	0.56

Table C5 Continued

R44	$\text{CH}_2^* + \text{CH}_2^* \rightleftharpoons \text{CH}_2\text{CH}_2^* + ^*\text{}$	0.63	1.02
R45	$\text{CHCH}_2^* + ^* \rightleftharpoons \text{CH}_2\text{CH}_2(\text{g}) + 2^*\text{}$	0.75	0.30
R46	$\text{CH}_3\text{CH}_2^* + \text{OH}^* \rightleftharpoons \text{CH}_3\text{CH}_2\text{OH}(\text{g}) + 2^*\text{}$	1.76	0.64

Table C6. Activation energies on cobalt- palladium surface

R.No.	Reaction	Activation energy on CoPd	
		E _{af}	E _{ar}
R1	$\text{CO(g)} + * \leftrightarrow \text{CO}^*$	0.00	0.00
R2	$\text{H}_2(\text{g}) + 2* \leftrightarrow 2\text{H}^* + *$	0.00	0.00
R3	$\text{CO}^* + \text{H}^* \leftrightarrow \text{HCO}^* + *$	1.31	0.42
R4	$\text{HCO}^* + \text{H}^* \leftrightarrow \text{CH}_2\text{O}^* + *$	0.60	0.55
R5	$\text{CH}_2\text{O}^* + \text{H}^* \leftrightarrow \text{CH}_3\text{O}^* + *$	0.37	0.50
R6	$\text{HCO}^* + * \leftrightarrow \text{CH}^* + \text{O}^*$	1.74	1.07
R7	$\text{CH}_2\text{O}^* + * \leftrightarrow \text{CH}_2^* + \text{O}^*$	1.22	1.07
R8	$\text{CH}_3\text{O}^* + * \leftrightarrow \text{CH}_3^* + \text{O}^*$	1.22	0.98
R9	$\text{CH}^* + \text{H}^* \leftrightarrow \text{CH}_2^* + *$	0.33	0.78
R10	$\text{CH}_2^* + \text{H}^* \leftrightarrow \text{CH}_3^* + *$	0.52	0.68
R11	$\text{CH}_3^* + \text{H}^* \leftrightarrow \text{CH}_4(\text{g}) + 2*$	0.58	0.54
R12	$\text{CH}^* + \text{CO}^* \leftrightarrow \text{CHCO}^* + *$	0.73	0.64
R13	$\text{CH}_2^* + \text{CO}^* \leftrightarrow \text{CH}_2\text{CO}^* + *$	0.88	0.56
R14	$\text{CH}_3^* + \text{CO}^* \leftrightarrow \text{CH}_3\text{CO}^* + *$	0.86	0.46
R15	$\text{CHCO}^* + \text{H}^* \leftrightarrow \text{CH}_2\text{CO}^* + *$	0.27	0.50
R16	$\text{CH}_2\text{CO}^* + \text{H}^* \leftrightarrow \text{CH}_3\text{CO}^* + *$	0.55	0.50
R17	$\text{CH}_3\text{CO}^* + \text{H}^* \leftrightarrow \text{CH}_3\text{CHO}(\text{g}) + 2*$	1.11	0.49
R18	$\text{CH}_3\text{CO}^* + \text{H}^* \leftrightarrow \text{CH}_3\text{COH}^* + *$	1.23	0.47
R19	$\text{CH}_3\text{COH}^* + \text{H}^* \leftrightarrow \text{CH}_3\text{CHOH}^* + *$	0.60	0.56
R20	$\text{CH}_3\text{CHOH}^* + \text{H}^* \leftrightarrow \text{CH}_3\text{CH}_2\text{OH}(\text{g}) + 2*$	0.64	0.50
R21	$\text{CH}_2\text{O}^* + \text{H}^* \leftrightarrow \text{CH}_2\text{OH}^* + *$	0.75	0.45
R22	$\text{CH}_2\text{CO}^* + \text{H}^* \leftrightarrow \text{CH}_2\text{COH}^* + *$	0.89	0.46
R23	$\text{CH}_2\text{COH}^* + \text{H}^* \leftrightarrow \text{CH}_3\text{COH}^* + *$	0.93	0.56
R24	$\text{CHCO}^* + \text{H}^* \leftrightarrow \text{CHCHO}^* + *$	0.38	0.63
R25	$\text{CH}_2\text{CO}^* + \text{H}^* \leftrightarrow \text{CH}_2\text{CHO}^* + *$	0.38	0.53

Table C6Continued

R.No.	Reaction	Activation energy on CoPd	
		E _{af}	E _{ar}
R26	$\text{CHCHO}^* + \text{H}^* \leftrightarrow \text{CH}_2\text{CHO}^{*+*}$	0.60	0.74
R27	$\text{CH}_2\text{CHO}^* + \text{H}^* \leftrightarrow \text{CH}_3\text{CHO}(\text{g}) + 2^*$	1.32	0.50
R28	$\text{CH}_2\text{O}^* + \text{CH}_2^* \leftrightarrow \text{CH}_3\text{COH}^{*+*}$	0.70	0.52
R29	$\text{O}^* + \text{H}^* \leftrightarrow \text{OH}^{*+*}$	0.51	0.77
R30	$\text{OH}^* + \text{H}^* \leftrightarrow \text{H}_2\text{O}(\text{g}) + ^*$	0.87	0.63
R31	$\text{CH}_2\text{COH}^* + \text{H}^* \leftrightarrow \text{CH}_2\text{CHOH}^{*+*}$	0.66	0.60
R32	$\text{CH}_2\text{CHOH}^* + \text{H}^* \leftrightarrow \text{CH}_3\text{CHOH}^{*+*}$	0.80	0.44
R33	$\text{CH}_2\text{CHO}^* + \text{H}^* \leftrightarrow \text{CH}_2\text{CHOH}^{*+*}$	1.16	0.52
R34	$\text{CH}_2\text{OH}^* + \text{H}^* \leftrightarrow \text{CH}_3\text{OH}(\text{g}) + 2^*$	0.86	0.50
R35	$\text{HCO}^* + \text{H}^* \leftrightarrow \text{CHOH}^{*+*}$	1.02	0.48
R36	$\text{CH}_3\text{O}^* + \text{H}^* \leftrightarrow \text{CH}_3\text{OH}(\text{g}) + 2^*$	1.31	0.51
R37	$\text{CHOH}^* + \text{H}^* \leftrightarrow \text{CH}_2\text{OH}^{*+*}$	0.44	0.60
R38	$\text{CH}^* + \text{CH}_2^* \leftrightarrow \text{CHCH}_2^{*+*}$	0.31	0.85
R39	$\text{CHCH}_2^* + \text{H}^* \leftrightarrow \text{CH}_2\text{CH}_2^{*+*}$	0.14	0.63
R40	$\text{CHCH}_2^* + \text{H}^* \leftrightarrow \text{CH}_2\text{CH}_2(\text{g}) + 2^*$	0.67	0.55
R41	$\text{CH}_2^* + \text{CH}_2^* \leftrightarrow \text{CH}_3\text{CH}_2^{*+*}$	0.72	0.59
R42	$\text{CH}_3\text{CH}_2^* + \text{H}^* \leftrightarrow \text{CH}_3\text{CH}_3(\text{g}) + 2^*$	0.28	0.52
R43	$\text{CH}_2\text{CH}_2^* + \text{H}^* \leftrightarrow \text{CH}_3\text{CH}_2^{*+*}$	1.08	0.41
R44	$\text{CH}_2^* + \text{CH}_2^* \leftrightarrow \text{CH}_2\text{CH}_2^{*+*}$	0.24	0.81
R45	$\text{CHCH}_2^{*+*} \leftrightarrow \text{CH}_2\text{CH}_2(\text{g}) + 2^*$	0.83	0.23
R46	$\text{CH}_3\text{CH}_2^* + \text{OH}^* \leftrightarrow \text{CH}_3\text{CH}_2\text{OH}(\text{g}) + 2^*$	0.87	0.49

Table C7. Activation energies on palladium surface

R.No.	Reaction	Activation energy on Palladium	
		E _{af}	E _{ar}
R1	$\text{CO(g)} + * \leftrightarrow \text{CO}^*$	0.00	0.00
R2	$\text{H}_2(\text{g}) + 2* \leftrightarrow 2\text{H}^{*+*}$	0.00	0.00
R3	$\text{CO}^* + \text{H}^* \leftrightarrow \text{HCO}^{*+*}$	1.62	0.59
R4	$\text{HCO}^* + \text{H}^* \leftrightarrow \text{CH}_2\text{O}^{*+*}$	1.41	0.66
R5	$\text{CH}_2\text{O}^* + \text{H}^* \leftrightarrow \text{CH}_3\text{O}^{*+*}$	0.60	0.57
R6	$\text{HCO}^{*+*} \leftrightarrow \text{CH}^* + \text{O}^*$	2.79	1.44
R7	$\text{CH}_2\text{O}^{*+*} \leftrightarrow \text{CH}_2^* + \text{O}^*$	1.39	1.44
R8	$\text{CH}_3\text{O}^{*+*} \leftrightarrow \text{CH}_3^* + \text{O}^*$	1.03	1.31
R9	$\text{CH}^* + \text{H}^* \leftrightarrow \text{CH}_2^{*+*}$	0.37	1.01
R10	$\text{CH}_2^* + \text{H}^* \leftrightarrow \text{CH}_3^{*+*}$	0.69	0.90
R11	$\text{CH}_3^* + \text{H}^* \leftrightarrow \text{CH}_4(\text{g}) + 2*$	0.76	0.71
R12	$\text{CH}^* + \text{CO}^* \leftrightarrow \text{CHCO}^{*+*}$	2.80	3.27
R13	$\text{CH}_2^* + \text{CO}^* \leftrightarrow \text{CH}_2\text{CO}^{*+*}$	0.78	0.74
R14	$\text{CH}_3^* + \text{CO}^* \leftrightarrow \text{CH}_3\text{CO}^{*+*}$	1.42	0.50
R15	$\text{CHCO}^* + \text{H}^* \leftrightarrow \text{CH}_2\text{CO}^{*+*}$	2.80	2.70
R16	$\text{CH}_2\text{CO}^* + \text{H}^* \leftrightarrow \text{CH}_3\text{CO}^{*+*}$	1.06	0.62
R17	$\text{CH}_3\text{CO}^* + \text{H}^* \leftrightarrow \text{CH}_3\text{CHO}(\text{g}) + 2*$	1.11	0.64
R18	$\text{CH}_3\text{CO}^* + \text{H}^* \leftrightarrow \text{CH}_3\text{COH}^{*+*}$	1.30	0.62
R19	$\text{CH}_3\text{COH}^* + \text{H}^* \leftrightarrow \text{CH}_3\text{CHOH}^{*+*}$	0.38	0.78
R20	$\text{CH}_3\text{CHOH}^* + \text{H}^* \leftrightarrow \text{CH}_3\text{CH}_2\text{OH}(\text{g}) + 2*$	1.11	0.66
R21	$\text{CH}_2\text{O}^* + \text{H}^* \leftrightarrow \text{CH}_2\text{OH}^*$	0.54	0.58

Table C7Continued

R.No.	Reaction	Activation energy on Palladium	
		E _{af}	E _{ar}
R22	$\text{CH}_2\text{CO}^* + \text{H}^* \leftrightarrow \text{CH}_2\text{COH}^{*+*}$	1.25	0.59
R23	$\text{CH}_2\text{COH}^* + \text{H}^* \leftrightarrow \text{CH}_3\text{COH}^{*+*}$	1.18	0.74

R24	$\text{CHCO}^* + \text{H}^* \leftrightarrow \text{CHCHO}^* + ^*$	2.80	2.27
R25	$\text{CH}_2\text{CO}^* + \text{H}^* \leftrightarrow \text{CH}_2\text{CHO}^* + ^*$	0.87	0.65
R26	$\text{CHCHO}^* + \text{H}^* \leftrightarrow \text{CH}_2\text{CHO}^* + ^*$	2.80	3.00
R27	$\text{CH}_2\text{CHO}^* + \text{H}^* \leftrightarrow \text{CH}_3\text{CHO}(\text{g}) + 2^*$	1.34	0.66
R28	$\text{CH}_2\text{O}^* + \text{CH}_2^* \leftrightarrow \text{CH}_3\text{COH}^* + ^*$	0.29	0.69
R29	$\text{O}^* + \text{H}^* \leftrightarrow \text{OH}^* + ^*$	1.04	0.95
R30	$\text{OH}^* + \text{H}^* \leftrightarrow \text{H}_2\text{O}(\text{g}) + ^*$	0.71	0.82
R31	$\text{CH}_2\text{COH}^* + \text{H}^* \leftrightarrow \text{CH}_2\text{CHOH}^* + ^*$	0.66	0.82
R32	$\text{CH}_2\text{CHOH}^* + \text{H}^* \leftrightarrow \text{CH}_3\text{CHOH}^* + ^*$	0.97	0.62
R33	$\text{CH}_2\text{CHO}^* + \text{H}^* \leftrightarrow \text{CH}_2\text{CHOH}^* + ^*$	1.00	0.71
R34	$\text{CH}_2\text{OH}^* + \text{H}^* \leftrightarrow \text{CH}_3\text{OH}(\text{g}) + 2^*$	1.09	0.67
R35	$\text{HCO}^* + \text{H}^* \leftrightarrow \text{CHOH}^* + ^*$	1.69	0.62
R36	$\text{CH}_3\text{O}^* + \text{H}^* \leftrightarrow \text{CH}_3\text{OH}(\text{g}) + 2^*$	1.04	0.68
R37	$\text{CHOH}^* + \text{H}^* \leftrightarrow \text{CH}_2\text{OH}^* + ^*$	0.43	0.80
R38	$\text{CH}^* + \text{CH}_2^* \leftrightarrow \text{CHCH}_2^* + ^*$	0.27	1.09
R39	$\text{CHCH}_2^* + \text{H}^* \leftrightarrow \text{CH}_2\text{CH}_2^* + ^*$	0.18	0.79
R40	$\text{CHCH}_2^* + \text{H}^* \leftrightarrow \text{CH}_2\text{CH}_2(\text{g}) + 2^*$	0.61	0.72
R41	$\text{CH}_2^* + \text{CH}_2^* \leftrightarrow \text{CH}_3\text{CH}_2^* + ^*$	0.74	0.78
R42	$\text{CH}_3\text{CH}_2^* + \text{H}^* \leftrightarrow \text{CH}_3\text{CH}_3(\text{g}) + 2^*$	0.37	0.69
R43	$\text{CH}_2\text{CH}_2^* + \text{H}^* \leftrightarrow \text{CH}_3\text{CH}_2^* + ^*$	1.09	0.55
R44	$\text{CH}_2^* + \text{CH}_2^* \leftrightarrow \text{CH}_2\text{CH}_2^* + ^*$	0.24	1.51
R45	$\text{CHCH}_2^* + ^* \leftrightarrow \text{CH}_2\text{CH}_2(\text{g}) + 2^*$	0.78	0.30
R46	$\text{CH}_3\text{CH}_2^* + \text{OH}^* \leftrightarrow \text{CH}_3\text{CH}_2\text{OH}(\text{g}) + 2^*$	0.66	0.64

Notes for tables C5, C6 and C7:

- 1) In tables C5, C6 and C7 the values in bold are derived from extensive DFT calculations. Other values are derived from BEP relationships.
- 2) Activation energies obtained from DFT and BEP are scaled by a factor of 0.7 on Co and Pd surfaces, whereas scaling factor for CoPd surface is 0.53.

4. Entropy of reactions is calculated using DFT. Selecting Vibrational frequencies in the Properties tab requests calculations of frequencies, infrared (ir) intensities, and thermochemical properties: heat capacity, entropy, enthalpy, and Gibbs free energy.

Table C8. DFT derived entropy of reaction for reactions involving gas phase species on three surfaces.

Entropy of reactions in J/mol K				
S.No.	Reactions	Cobalt	CoPd	Palladium
1	$\text{CO(g)} + 2^* \leftrightarrow \text{CO}^* + ^*$	-134.51	-133.35	-102.53
2	$\text{H}_2(\text{g}) + 2^* \leftrightarrow \text{H}^* + \text{H}^*$	-135.26	-145.10	-114.96
3	$\text{CH}_3^* + \text{H}^* \leftrightarrow \text{CH}_4(\text{g}) + 2^*$	143.35	159.63	131.54
4	$\text{CH}_2\text{OH}^* + \text{H}^* \rightarrow \text{CH}_3\text{OH}(\text{g}) + 2^*$	232.02	222.98	208.00
5	$\text{CH}_3\text{CO}^* + \text{H}^* \rightarrow \text{CH}_3\text{CHO}(\text{g}) + 2^*$	143.12	179.68	167.71
6	$\text{CH}_3\text{CHOH}^* + \text{H}^* \rightarrow \text{CH}_3\text{CH}_2\text{OH}(\text{g}) + 2^*$	160.72	150.50	143.45

Entropy of reactions in J/mol K				
S.No.	Reactions	Cobalt	CoPd	Palladium
7	$\text{OH}^* + \text{H}^* \rightarrow \text{H}_2\text{O}(\text{g}) + 2^*$	166.04	163.00	152.36
8	$\text{CH}_2\text{CHO}^* + \text{H}^* \rightarrow \text{CH}_3\text{CHO}(\text{g}) + 2^*$	204.19	214.82	197.97
9	$\text{CH}_3\text{O}^* + \text{H}^* \rightarrow \text{CH}_3\text{OH}(\text{g}) + 2^*$	220.42	219.21	213.67
10	$\text{CHCH}_2^* + \text{H}^* \rightarrow \text{CH}_2\text{CH}_2(\text{g}) + 2^*$	154.15	169.57	144.00
11	$\text{CH}_3\text{CH}_2^* + \text{H}^* \rightarrow \text{CH}_3\text{CH}_3(\text{g}) + 2^*$	144.93	129.69	126.89
12	$\text{CH}_2\text{CH}_2^* + ^* \rightarrow \text{CH}_2\text{CH}_2(\text{g}) + 2^*$	134.70	142.59	144.16
13	$\text{CH}_3\text{CH}_2^* + \text{OH}^* \rightarrow \text{CH}_3\text{CH}_2\text{OH}(\text{g}) + 2^*$	145.63	117.50	134.20

5. Enthalpy of reactions is calculated using DFT derived adsorption energies. All adsorption energies used to calculate enthalpies are zero point energy corrected and obtained using B3LYP.

Table C9. DFT derived enthalpy of reaction for reactions involving gas phase species on three surfaces.

Enthalpy of reactions in eV				
S.No.	Reactions	Cobalt	CoPd	Palladium
1	$\text{CO(g)}+2^* \leftrightarrow \text{CO}^*+^*$	-1.494	-1.736	-1.82
2	$\text{H}_2\text{(g)}+2^* \leftrightarrow \text{H}^*+\text{H}^*$	-0.593	-0.621	-0.65
3	$\text{CH}_3^*+\text{H}^* \leftrightarrow \text{CH}_4\text{(g)}+2^*$	0.231	0.00129	0.12
4	$\text{CH}_2\text{OH}^*+\text{H}^* \rightarrow \text{CH}_3\text{OH(g)}+2^*$	2.455	1.786	0.601
5	$\text{CH}_3\text{CO}^*+\text{H}^* \rightarrow \text{CH}_3\text{CHO(g)}+2^*$	0.875	1.189	0.674
6	$\text{CH}_3\text{CHOH}^*+\text{H}^* \rightarrow \text{CH}_3\text{CH}_2\text{OH(g)}+2^*$	1.49	0.272	0.646
7	$\text{OH}^*+\text{H}^* \rightarrow \text{H}_2\text{O(g)}+2^*$	1.94	1.519	0.78
8	$\text{CH}_2\text{CHO}^*+\text{H}^* \rightarrow \text{CH}_3\text{CHO(g)}+2^*$	1.547	1.547	0.78
9	$\text{CH}_3\text{O}^*+\text{H}^* \rightarrow \text{CH}_3\text{OH(g)}+2^*$	1.92	1.51	0.506
10	$\text{CHCH}_2^*+\text{H}^* \rightarrow \text{CH}_2\text{CH}_2\text{(g)}+2^*$	0.078	0.222	-0.167
11	$\text{CH}_3\text{CH}_2^*+\text{H}^* \rightarrow \text{CH}_3\text{CH}_3\text{(g)}+2^*$	-0.45	-0.455	-0.449

Table C9 continued

S.No.	Reactions	Cobalt	CoPd	Palladium
12	$\text{CH}_2\text{CH}_2^* + ^* \rightarrow \text{CH}_2\text{CH}_2(\text{g}) + 2^*$	0.645	1.146	0.694
13	$\text{CH}_3\text{CH}_2^* + \text{OH}^* \rightarrow \text{CH}_3\text{CH}_2\text{OH}(\text{g}) + 2^*$	1.59	0.73	0.016

6. Terminology used in MKM model for writing rate expressions and developing ODE equations is represented in table below.

Table C10. Symbols used in rate expressions, diffusion expressions and differential equations

Intermediates	On Pd sites	On CoPd sites	On Co sites
Empty Sites	yo_Pd	yo_CoPd	yo_Co
θ_{CO}	y1	y22	y43
θ_{H}	y2	y23	y44
θ_{HCO}	y3	y24	y45
$\theta_{\text{CH}_2\text{O}}$	y4	y25	y46
$\theta_{\text{CH}_3\text{O}}$	y5	y26	y47
θ_{CH}	y6	y27	y48
θ_{CH_2}	y7	y28	y49
θ_{CH_3}	y8	y29	y50
θ_{CHOH}	y9	y30	y51
$\theta_{\text{CH}_2\text{OH}}$	y10	y31	y52
θ_{CHCO}	y11	y32	y53
$\theta_{\text{CH}_2\text{CO}}$	y12	y33	y54
$\theta_{\text{CH}_3\text{CO}}$	y13	y34	y55

Table C10 continued

Intermediates	On Pd sites	On CoPd sites	On Co sites
θ_{CHCHO}	y14	y35	y56
$\theta_{\text{CH}_2\text{CHO}}$	y15	y36	y57
$\theta_{\text{CH}_2\text{COH}}$	y16	y37	y58
$\theta_{\text{CH}_3\text{COH}}$	y17	y38	y59
$\theta_{\text{CH}_2\text{CHOH}}$	y18	y39	y60
$\theta_{\text{CH}_3\text{CHOH}}$	y19	y40	y61
θ_{O}	y20	y41	y62
θ_{OH}	y21	y42	y63
θ_{CHCH_2}	y71	y74	y77
$\theta_{\text{CH}_2\text{CH}_2}$	y72	y75	y78
$\theta_{\text{CH}_3\text{CH}_2}$	y73	y76	y79

$n_{\text{CO}} \text{ (g)}$ (number of moles of CO)	y64
$n_{\text{H}_2} \text{ (g)}$ (number of moles of H ₂)	y65
$n_{\text{CH}_4} \text{ (g)}$ (number of moles of CH ₄)	y66
$n_{\text{CH}_3\text{OH}} \text{ (g)}$ (number of moles of CH ₃ OH)	y67
$n_{\text{CH}_3\text{CH}_2\text{OH}} \text{ (g)}$ (number of moles of CH ₃ CH ₂ OH)	y68
$n_{\text{CH}_3\text{CHO}} \text{ (g)}$ (number of moles of CH ₃ CHO)	y69
$n_{\text{H}_2\text{O}} \text{ (g)}$ (number of moles of H ₂ O)	y80
$n_{\text{CH}_2\text{CH}_2} \text{ (g)}$ (number of moles of CH ₂ CH ₂)	Y81
$n_{\text{CH}_3\text{CH}_3} \text{ (g)}$ (number of moles of CH ₃ CH ₃)	Y33

7. Rate of the surface reactions is represented as a product of rate constants and concentration of reactants. For reactions involving gas phase species, rates are represented in terms of DFT derived equilibrium constants.

Table C11. Rate expressions for surface reactions on palladium surface, similar equations are written for Co and CoPd surface

R.No.	Reaction	Rate Expression
R1	$\text{CO(g)} + * \leftrightarrow \text{CO}^*$	$k_f(1)(P_{\text{CO}}^{y_0-y_1}/K_{\text{CO}})$
R2	$\text{H}_2(\text{g}) + 2* \leftrightarrow 2\text{H}^* + *$	$K_f(2)(P_{\text{H}_2}^{y_0-y_2} y_2^2 / K_{\text{H}_2})$
R3	$\text{CO}^* + \text{H}^* \leftrightarrow \text{HCO}^* + *$	$k_f(3) y_1 y_2 - k_r(3) y_3 y_0$
R4	$\text{HCO}^* + \text{H}^* \leftrightarrow \text{CH}_2\text{O}^* + *$	$k_f(4) y_2 y_3 - k_r(4) y_4 y_0$
R5	$\text{CH}_2\text{O}^* + \text{H}^* \leftrightarrow \text{CH}_3\text{O}^* + *$	$k_f(5) y_4 y_2 - k_r(5) y_5 y_0$
R6	$\text{HCO}^* + * \leftrightarrow \text{CH}^* + \text{O}^*$	$k_f(6) y_3 y_0 - k_r(6) y_6 y_0$
R7	$\text{CH}_2\text{O}^* + * \leftrightarrow \text{CH}_2^* + \text{O}^*$	$k_f(7) y_0 y_4 - k_r(7) y_7 y_0$
R8	$\text{CH}_3\text{O}^* + * \leftrightarrow \text{CH}_3^* + \text{O}^*$	$k_f(8) y_5 y_0 - k_r(8) y_8 y_0$
R9	$\text{CH}^* + \text{H}^* \leftrightarrow \text{CH}_2^* + *$	$k_f(9) y_6 y_2 - k_r(9) y_7 y_0$
R10	$\text{CH}_2^* + \text{H}^* \leftrightarrow \text{CH}_3^* + *$	$k_f(10) y_7 y_2 - k_r(10) y_8 y_0$
R11	$\text{CH}_3^* + \text{H}^* \leftrightarrow \text{CH}_4(\text{g}) + 2*$	$k_f(11) y_2 y_8 - k_f(11) P_{\text{H}_2}^{y_0} y_0 / K_{\text{H}_2}$
R12	$\text{CH}^* + \text{CO}^* \leftrightarrow \text{CHCO}^* + *$	$k_f(12) y_1 y_6 - k_r(12) y_{11} y_0$
R13	$\text{CH}_2^* + \text{CO}^* \leftrightarrow \text{CH}_2\text{CO}^* + *$	$k_f(13) y_1 y_7 - k_r(13) y_{12} y_0$
R14	$\text{CH}_3^* + \text{CO}^* \leftrightarrow \text{CH}_3\text{CO}^* + *$	$k_f(14) y_1 y_8 - k_r(14) y_{13} y_0$
R15	$\text{CHCO}^* + \text{H}^* \leftrightarrow \text{CH}_2\text{CO}^* + *$	$k_f(15) y_2 y_{11} - k_r(15) y_{12} y_0$
R16	$\text{CH}_2\text{CO}^* + \text{H}^* \leftrightarrow \text{CH}_3\text{CO}^* + *$	$k_f(16) y_{12} y_2 - k_r(16) y_{13} y_0$
R17	$\text{CH}_3\text{CO}^* + \text{H}^* \leftrightarrow \text{CH}_3\text{CHO}(\text{g}) + 2*$	$k_f(17)(y_{13} y_2 - P_{\text{CH}_3\text{CHO}}^{y_0} y_0 / K_{\text{H}_2})$
R18	$\text{CH}_3\text{CO}^* + \text{H}^* \leftrightarrow \text{CH}_3\text{COH}^* + *$	$k_f(18) y_{13} y_2 - k_r(18) y_{17} y_0$
R19	$\text{CH}_3\text{COH}^* + \text{H}^* \leftrightarrow \text{CH}_3\text{CHOH}^* + *$	$k_f(19) y_{17} y_2 - k_r(19) y_{19} y_0$
R20	$\text{CH}_3\text{CHOH}^* + \text{H}^* \leftrightarrow \text{CH}_3\text{CH}_2\text{OH}(\text{g}) + 2*$	$k_f(20) ((y_{19} y_2) - P_{\text{CH}_3\text{CH}_2\text{OH}}^{y_0} y_0 / K_{\text{CH}_3\text{CH}_2\text{OH}})$
R21	$\text{CH}_2\text{O}^* + \text{H}^* \leftrightarrow \text{CH}_2\text{OH}^* + *$	$k_f(21) y_2 y_4 - k_r(21) y_{10} y_0$
R22	$\text{CH}_2\text{CO}^* + \text{H}^* \leftrightarrow \text{CH}_2\text{COH}^* + *$	$k_f(22) y_2 y_{12} - k_r(22) y_{16} y_0$
R23	$\text{CH}_2\text{COH}^* + \text{H}^* \leftrightarrow \text{CH}_3\text{COH}^* + *$	$k_f(23) y_{16} y_2 - k_r(23) y_{17} y_0$
R24	$\text{CHCO}^* + \text{H}^* \leftrightarrow \text{CHCHO}^* + *$	$k_f(24) y_{11} y_2 - k_r(24) y_{14} y_0$

Table C11. Continued

R.No.	Reaction	Rate Expression
R25	$\text{CH}_2\text{CO}^* + \text{H}^* \leftrightarrow \text{CH}_2\text{CHO}^* + ^*\text{}$	$\text{kf}(25) \cdot y_{12} \cdot y_2 - \text{kr}(25) \cdot y_{15} \cdot y_0$
R26	$\text{CHCHO}^* + \text{H}^* \leftrightarrow \text{CH}_2\text{CHO}^* + ^*\text{}$	$\text{kf}(26) \cdot y_{14} \cdot y_2 - \text{kr}(26) \cdot y_{15} \cdot y_0$
R27	$\text{CH}_2\text{CHO}^* + \text{H}^* \leftrightarrow \text{CH}_3\text{CHO}(\text{g}) + 2^*\text{}$	$\text{kf}(27)(y_{15} \cdot y_2 - \text{Pch3cho} \cdot y_0 \cdot y_0 / \text{Kch3cho})$
R28	$\text{CH}_2\text{O}^* + \text{CH}_2^* \leftrightarrow \text{CH}_3\text{COH}^* + ^*\text{}$	$\text{kf}(28) \cdot y_4 \cdot y_7 - \text{kr}(28) \cdot y_{17} \cdot y_0$
R29	$\text{O}^* + \text{H}^* \leftrightarrow \text{OH}^* + ^*\text{}$	$\text{kf}(29) \cdot y_{20} \cdot y_2 - \text{kr}(29) \cdot y_{21} \cdot y_0$
R30	$\text{OH}^* + \text{H}^* \leftrightarrow \text{H}_2\text{O}(\text{g}) + 2^*\text{}$	$\text{kf}(30) \cdot (y_2 \cdot y_{21} - \text{Ph2o} \cdot y_0 \cdot y_0 / \text{Kh2o})$
R31	$\text{CH}_2\text{COH}^* + \text{H}^* \leftrightarrow \text{CH}_2\text{CHOH}^* + ^*\text{}$	$\text{kf}(31) \cdot y_{16} \cdot y_2 - \text{kr}(31) \cdot y_{18} \cdot y_0$
R32	$\text{CH}_2\text{CHOH}^* + \text{H}^* \leftrightarrow \text{CH}_3\text{CHOH}^* + ^*\text{}$	$\text{kf}(32) \cdot y_{18} \cdot y_2 - \text{kr}(32) \cdot y_{19} \cdot y_0$
R33	$\text{CH}_2\text{CHO}^* + \text{H}^* \leftrightarrow \text{CH}_2\text{CHOH}^* + ^*\text{}$	$\text{kf}(33) \cdot y_{15} \cdot y_2 - \text{kr}(33) \cdot y_{18} \cdot y_0$
R34	$\text{CH}_2\text{OH}^* + \text{H}^* \leftrightarrow \text{CH}_3\text{OH}(\text{g}) + 2^*\text{}$	$\text{kf}(34)(y_{10} \cdot y_2 - \text{Pch3oh} \cdot y_0 \cdot y_0 / \text{Kch3oh})$
R35	$\text{HCO}^* + \text{H}^* \leftrightarrow \text{CHOH}^* + ^*\text{}$	$\text{kf}(35) \cdot y_3 \cdot y_2 - \text{kr}(35) \cdot y_9 \cdot y_0$
R36	$\text{CH}_3\text{O}^* + \text{H}^* \leftrightarrow \text{CH}_3\text{OH}(\text{g}) + 2^*\text{}$	$\text{kf}(36)(y_2 \cdot y_5 - \text{Pch3oh} \cdot y_0 / \text{Kch3oh})$
R37	$\text{CHOH}^* + \text{H}^* \leftrightarrow \text{CH}_2\text{OH}^* + ^*\text{}$	$\text{kf}(37) \cdot y_9 \cdot y_2 - \text{kr}(37) \cdot y_{10} \cdot y_0$
R38	$\text{CH}^* + \text{CH}_2^* \leftrightarrow \text{CHCH}_2^* + ^*\text{}$	$\text{kf}(38) \cdot y_6 \cdot y_7 - \text{kr}(38) \cdot y_{71} \cdot y_0$
R39	$\text{CHCH}_2^* + \text{H}^* \leftrightarrow \text{CH}_2\text{CH}_2^* + ^*\text{}$	$\text{kf}(39) \cdot y_{71} \cdot y_2 - \text{kr}(39) \cdot y_{72} \cdot y_0;$
R40	$\text{CHCH}_2^* + \text{H}^* \leftrightarrow \text{CH}_2\text{CH}_2(\text{g}) + 2^*\text{}$	$\text{kf}(40) \cdot (y_2 \cdot y_{71} - \text{Pch2ch2} \cdot y_0 \cdot y_0 / \text{Kch2ch21})$
R41	$\text{CH}_3^* + \text{CH}_2^* \leftrightarrow \text{CH}_3\text{CH}_2^* + ^*\text{}$	$\text{kf}(41) \cdot y_8 \cdot y_7 - \text{kr}(41) \cdot y_{73} \cdot y_0$
R42	$\text{CH}_3\text{CH}_2^* + \text{H}^* \leftrightarrow \text{CH}_3\text{CH}_3(\text{g}) + 2^*\text{}$	$\text{kf}(42) \cdot (y_2 \cdot y_{73} - \text{Pch3ch3} \cdot y_0 \cdot y_0 / \text{Kch3ch3})$
R43	$\text{CH}_2\text{CH}_2^* + \text{H}^* \leftrightarrow \text{CH}_3\text{CH}_2^* + ^*\text{}$	$\text{kf}(43) \cdot y_{72} \cdot y_2 - \text{kr}(43) \cdot y_{73} \cdot y_0$
R44	$\text{CH}_2^* + \text{CH}_2^* \leftrightarrow \text{CH}_2\text{CH}_2^* + ^*\text{}$	$\text{kf}(44) \cdot y_7 \cdot y_7 - \text{kr}(44) \cdot y_{72} \cdot y_0$
R45	$\text{CHCH}_2^* + ^*\text{} \leftrightarrow \text{CH}_2\text{CH}_2(\text{g}) + 2^*\text{}$	$\text{kf}(45) \cdot (y_{72} \cdot y_0 - \text{Pch2ch2} \cdot y_0 \cdot y_0 / \text{Kch2ch22})$
R46	$\text{CH}_3\text{CH}_2^* + \text{OH}^* \leftrightarrow \text{CH}_3\text{CH}_2\text{OH}(\text{g}) + 2^*\text{}$	$\text{kf}(46) \cdot (y_{73} \cdot y_{21} - \text{Pch3ch2oh} \cdot y_0 \cdot y_0 / \text{Kch3ch2oh2})$

8. Diffusion reactions are modeled as elementary rate reactions in MKM. Table C12 represents the rate expressions for diffusion of species.

Table C12. Diffusion reactions and rate expressions

R.NO	Reaction	Rate expression
1.	$\text{HCO}^*_{\text{CoPd}+\text{Co}} \leftrightarrow \text{HCO}^*_{\text{Co}+\text{CoPd}}$	$\text{kfD}(1)*\text{y}24*\text{y}0_{\text{Co}} - \text{krD}(1)*\text{y}45*\text{y}0_{\text{CoPd}}$
2.	$\text{HCO}^*_{\text{CoPd}+\text{Pd}} \leftrightarrow \text{HCO}^*_{\text{Pd}+\text{CoPd}}$	$\text{kfD}(2)*\text{y}24*\text{y}0_{\text{Pd}} - \text{krD}(2)*\text{y}3*\text{y}0_{\text{CoPd}}$
3.	$\text{CH}_2\text{O}^*_{\text{CoPd}+\text{Co}} \leftrightarrow \text{CH}_2\text{O}^*_{\text{Co}+\text{CoPd}}$	$\text{kfD}(3)*\text{y}25*\text{y}0_{\text{Co}} - \text{krD}(3)*\text{y}46*\text{y}0_{\text{CoPd}}$
4.	$\text{CH}_2\text{O}^*_{\text{CoPd}+\text{Pd}} \leftrightarrow \text{CH}_2\text{O}^*_{\text{Pd}+\text{CoPd}}$	$\text{kfD}(4)*\text{y}25*\text{y}0_{\text{Pd}} - \text{krD}(4)*\text{y}4*\text{y}0_{\text{CoPd}}$
5.	$\text{CH}_3\text{O}^*_{\text{CoPd}+\text{Co}} \leftrightarrow \text{CH}_3\text{O}^*_{\text{Co}+\text{CoPd}}$	$\text{kfD}(5)*\text{y}26*\text{y}0_{\text{Co}} - \text{krD}(5)*\text{y}47*\text{y}0_{\text{CoPd}}$
6.	$\text{CH}_3\text{O}^*_{\text{CoPd}+\text{Pd}} \leftrightarrow \text{CH}_3\text{O}^*_{\text{Pd}+\text{CoPd}}$	$\text{kfD}(6)*\text{y}26*\text{y}0_{\text{Pd}} - \text{krD}(6)*\text{y}5*\text{y}0_{\text{CoPd}}$
7.	$\text{CH}_3\text{CO}^*_{\text{CoPd}+\text{Co}} \leftrightarrow \text{CH}_3\text{CO}^*_{\text{Co}+\text{CoPd}}$	$\text{kfD}(7)*\text{y}34*\text{y}0_{\text{Co}} - \text{krD}(7)*\text{y}55*\text{y}0_{\text{CoPd}}$
8.	$\text{CH}_3\text{CO}^*_{\text{CoPd}+\text{Pd}} \leftrightarrow \text{CH}_3\text{CO}^*_{\text{Pd}+\text{CoPd}}$	$\text{kfD}(8)*\text{y}34*\text{y}0_{\text{Pd}} - \text{krD}(8)*\text{y}13*\text{y}0_{\text{CoPd}}$
9.	$\text{CH}_3\text{COH}^*_{\text{CoPd}+\text{Co}} \leftrightarrow \text{CH}_3\text{COH}^*_{\text{Co}+\text{CoPd}}$	$\text{kfD}(9)*\text{y}38*\text{y}0_{\text{Co}} - \text{krD}(9)*\text{y}59*\text{y}0_{\text{CoPd}}$
10.	$\text{CH}_3\text{COH}^*_{\text{CoPd}+\text{Pd}} \leftrightarrow \text{CH}_3\text{COH}^*_{\text{Pd}+\text{CoPd}}$	$\text{kfD}(10)*\text{y}38*\text{y}0_{\text{Pd}} - \text{krD}(10)*\text{y}17*\text{y}0_{\text{CoPd}}$
11.	$\text{CH}_3\text{CHOH}^*_{\text{CoPd}+\text{Co}} \leftrightarrow \text{CH}_3\text{CHOH}^*_{\text{Co}+\text{CoPd}}$	$\text{kfD}(11)*\text{y}40*\text{y}0_{\text{Co}} - \text{krD}(11)*\text{y}61*\text{y}0_{\text{CoPd}}$
12.	$\text{CH}_3\text{CHOH}^*_{\text{CoPd}+\text{Pd}} \leftrightarrow \text{CH}_3\text{CHOH}^*_{\text{Pd}+\text{CoPd}}$	$\text{kfD}(12)*\text{y}40*\text{y}0_{\text{Pd}} - \text{krD}(12)*\text{y}19*\text{y}0_{\text{CoPd}}$
13.	$\text{OH}^*_{\text{CoPd}+\text{Co}} \leftrightarrow \text{OH}^*_{\text{Co}+\text{CoPd}}$	$\text{kfD}(13)*\text{y}42*\text{y}0_{\text{Co}} - \text{krD}(13)*\text{y}63*\text{y}0_{\text{CoPd}}$
14.	$\text{OH}^*_{\text{CoPd}+\text{Pd}} \leftrightarrow \text{OH}^*_{\text{Pd}+\text{CoPd}}$	$\text{kfD}(14)*\text{y}42*\text{y}0_{\text{Pd}} - \text{krD}(14)*\text{y}21*\text{y}0_{\text{CoPd}}$

Table C12. Continued

R.NO	Reaction	Rate expression
15.	$\text{CH}_2\text{CHO}^*_{\text{CoPd}} + ^*\text{Co} \leftrightarrow \text{CH}_2\text{CHO}^*_{\text{Co}} + ^*\text{CoPd}$	$\text{kfD}(15) * \text{y}36 * \text{y}0_{\text{Co}} - \text{krD}(15) * \text{y}57 * \text{y}0_{\text{CoPd}}$
16.	$\text{CH}_2\text{CHO}^*_{\text{CoPd}} + ^*\text{Pd} \leftrightarrow \text{CH}_2\text{CHO}^*_{\text{Pd}} + ^*\text{CoPd}$	$\text{kfD}(16) * \text{y}36 * \text{y}0_{\text{Pd}} - \text{krD}(16) * \text{y}15 * \text{y}0_{\text{CoPd}}$
17.	$\text{CH}_2^*_{\text{CoPd}} + ^*\text{Co} \leftrightarrow \text{CH}_2^*_{\text{Co}} + ^*\text{CoPd}$	$\text{kfD}(17) * \text{y}28 * \text{y}0_{\text{Co}} - \text{krD}(17) * \text{y}49 * \text{y}0_{\text{CoPd}}$
18.	$\text{CH}_2^*_{\text{CoPd}} + ^*\text{Pd} \leftrightarrow \text{CH}_2^*_{\text{Pd}} + ^*\text{CoPd}$	$\text{kfD}(18) * \text{y}28 * \text{y}0_{\text{Pd}} - \text{krD}(18) * \text{y}7 * \text{y}0_{\text{CoPd}}$
19.	$\text{CH}_3^*_{\text{CoPd}} + ^*\text{Co} \leftrightarrow \text{CH}_3^*_{\text{Co}} + ^*\text{CoPd}$	$\text{kfD}(19) * \text{y}29 * \text{y}0_{\text{Co}} - \text{krD}(19) * \text{y}50 * \text{y}0_{\text{CoPd}}$
20.	$\text{CH}_3^*_{\text{CoPd}} + ^*\text{Pd} \leftrightarrow \text{CH}_3^*_{\text{Pd}} + ^*\text{CoPd}$	$\text{kfD}(20) * \text{y}29 * \text{y}0_{\text{Pd}} - \text{krD}(20) * \text{y}8 * \text{y}0_{\text{CoPd}}$
21.	$\text{CH}_3\text{CH}_2^*(\text{CoPd}) + ^*(\text{Co}) \leftrightarrow \text{CH}_3\text{CH}_2^*(\text{Co}) + ^*(\text{CoPd})$	$\text{kfD}(19) * \text{y}76 * \text{y}0_{\text{Co}} - \text{krD}(19) * \text{y}79 * \text{y}0_{\text{CoPd}}$
22.	$\text{CH}_3\text{CH}_2^*(\text{CoPd}) + ^*(\text{Pd}) \leftrightarrow \text{CH}_3\text{CH}_2^*(\text{Pd}) + ^*(\text{CoPd})$	$\text{r}22_{\text{D}} = \text{kfD}(20) * \text{y}76 * \text{y}0_{\text{Pd}} - \text{krD}(20) * \text{y}73 * \text{y}0_{\text{CoPd}}$

9. Change in the fractional coverage of species with respect to time is written in terms of rate of reactions. These ODE are written for all 24 intermediate species and solved simultaneously to get the coverages on catalyst. For gasphase species change in number of moles is represented using batch reactor design equations.

Table C13. Differential equations

Symbol	INTERMEDIATES	DIFFERENTIAL EQUATIONS
Y0	EMPTY SITE	1- (y1+y2+y3+y4+y5+y6+y7+y8+y9+y10+y11+y12+y13+y14+y15+y16+y17+y18+y19+y20+y21+y22+y23+y24)
Y1	CO	dy1dt= r1-r3-r12-r13-r14
Y2	H	dy2dt= r2-r3-r4-r5-r9-r10-r11-r15-r16-r17-r18-r19-r20-r21-r22-r23-r24-r25-r26-r27-r29-r30-r31-r32-r33-r34-r35-r36-r37-r39-r40-r42-r43;
Y3	HCO	dy3dt= r3-r4-r6-r35+r2_D
Y4	CH ₂ O	dy4dt= r4-r5-r7-r21-r28+r4_D
Y5	CH ₃ O	dy5dt= r5-r8-r36+r6_D
Y6	CH	dy6dt= r6-r9-r12-r38
Y7	CH ₂	dy7dt= r7+r9-r10-r13-r28-r38-r41-r44+r18_D
Y8	CH ₃	dy8dt= r8+r10-r11-r14-r41+r20_D
Y9	CHOH	dy9dt= r35-r37
Y10	CH ₂ OH	dy10dt= r21-r34+r37
Y11	CHCO	dy11dt= r12-r15-r24
Y12	CH ₂ CO	dy12dt= r13+r15-r16-r22-r25
Y13	CH ₃ CO	dy13dt= r14+r16-r17-r18+r8_D
Y14	CHCHO	dy14dt= r24-r26
Y15	CH ₂ CHO	dy15dt= r25+r26-r27-r33+r16_D
Y16	CH ₂ COH	dy16dt= r22-r23-r31

Table C13. Continued

Y17	CH ₃ COH	dy17dt= r18-r19+r23+r28+r10_D
Y18	CH ₂ CHOH	dy18dt= r31-r32+r33
Y19	CH ₃ CHOH	dy19dt= r19-r20+r32+r12_D
Y20	O	dy20dt= r6+r7+r8-r29
Y21	OH	dy21dt= r29-r30-r46+r14_D
Y22	CHCH ₂	dy22dt=r38-r39-r40
Y23	CH ₂ CH ₂	dy23dt=r39-r43+r44-r45
Y24	CH ₃ CH ₂	dy24dt=r41-r42+r43-r46+r22_D
Y25	CO (g)	dy25dt =(mcat*s/(Na*w))*(-r1)
Y26	H ₂ (g)	dy26dt =(mcat*s/(Na*w))*(-r2/2)
Y27	CH ₄ (g)	dy27dt =(mcat*s/(Na*w))*(r11)
Y28	CH ₃ OH (g)	dy28dt =(mcat*s/(Na*w))*(r34+r36)
Y29	CH ₃ CH ₂ OH (g)	dy29dt=(mcat*s/(Na*w))*(r20+r46)
Y30	CH ₃ CHO (g)	dy30dt=(mcat*s/(Na*w))*(r17+r27)
Y31	H ₂ O (g)	dy31dt=(mcat*s/(Na*w))*(r30)
Y32	CH ₂ CH ₂ (g)	dy32dt=(mcat*s/(Na*w))*(r40+r45)
Y33	CH ₃ CH ₃ (g)	dy33dt=(mcat*s/(Na*w))*(r42)

References

1. - A hydrogen-sensitive pd-gate MOS transistor. - *Journal of Applied Physics*. (- 9):- 3876. doi: - 10.1063/1.322185.
2. - *Topics in Catalysis*. (- 1):- 83. doi: - 10.1007/s11244-016-0717-5.
3. - Molecular beam studies of ethanol oxidation on pd(110). - *Surface Science*. (- 2):- 113. doi: - [https://doi.org/10.1016/S0039-6028\(96\)00959-4](https://doi.org/10.1016/S0039-6028(96)00959-4).

4. - Adsorption of CO on pd(100). - *The Journal of Chemical Physics*. (- 6):- 2984. doi: - 10.1063/1.440430.

5. - Kinetics and thermodynamics of hydrogen interaction with thin cobalt films. - *Applied Surface Science*. (- 3):- 399. doi: - [https://doi.org/10.1016/0169-4332\(89\)90022-6](https://doi.org/10.1016/0169-4332(89)90022-6).

6. - Electronic structure calculations and dynamics of methane activation on nickel and cobalt. - *The Journal of Chemical Physics*. (- 12):- 11012. doi: - 10.1063/1.467852.

7. - Adsorption and structure dependent desorption of CO on co(0001). - *Surface Science*. (- 3):- 502. doi: - [https://doi.org/10.1016/S0039-6028\(98\)00711-0](https://doi.org/10.1016/S0039-6028(98)00711-0).


```
[t,y]=ode15s(@(t,y) cleanedup(t,y,nPd,nCoPd,nCo),timespan,initial,options);  
format short G;
```

```
% formatting output
```

```
a=[nPd,nCoPd,nCo,t(3),y(3,[64:70 80 81]));  
allonestring=sprintf('%0.3f,%0.3f, %0.3f, %d, %0.3e, %0.3e, %0.3e, %0.3e, %0.3e, %0.3e,  
%0.3e, %0.3e',a);  
allonestring  
end  
***** End *****
```

B) Command to compile main.m function

```
% Compiling Matlab code main.m to create an executable main
```

```
*****
```

```
mcc -R -nodisplay -R -singleCompThread -R -nojvm -m main.m
```

C) Microkinetic model code (Cleanedup.m)

Function Cleanedup.m is microkinetic code for batch reactor design

```
*****  
function [ f ] = Cleanedup( ~,y,nPd,nCoPd,nCo )  
%Declaring and assigning variables  
% Variables y1 to y21 represent concentration of intermediates species on Pd surface  
y1=y(1);    %CO  
y2=y(2);    %H  
y3=y(3);    %HCO  
y4=y(4);    %CH2O  
y5=y(5);    %CH3O  
y6=y(6);    %CH  
y7=y(7);    %CH2  
y8=y(8);    %CH3  
y9=y(9);    %CHOH  
y10=y(10);  %CH2OH  
y11=y(11);  %CHCO  
y12=y(12);  %CH2CO  
y13=y(13);  %CH3CO  
y14=y(14);  %CHCHO  
y15=y(15);  %CH2CHO  
y16=y(16);  %CH2COH  
y17=y(17);  %CH3COH  
y18=y(18);  %CH2CHOH  
y19=y(19);  %CH3CHOH  
y20=y(20);  %O  
y21=y(21);  %OH  
y71=y(71);  %CHCH2  
y72=y(72);  %CH2CH2  
y73=y(73);  %CH3CH2  
  
%% Variables y22 to y42 represent concentration of intermediates species on CoPd  
surface  
y22=y(22);  %CO  
y23=y(23);  %H  
y24=y(24);  %HCO  
y25=y(25);  %CH2O  
y26=y(26);  %CH3O  
y27=y(27);  %CH
```

y28=y(28); %CH2
 y29=y(29); %CH3
 y30=y(30); %CHOH
 y31=y(31); %CH2OH
 y32=y(32); %CHCO
 y33=y(33); %CH2CO
 y34=y(34); %CH3CO
 y35=y(35); %CHCHO
 y36=y(36); %CH2CHO
 y37=y(37); %CH2COH
 y38=y(38); %CH3COH
 y39=y(39); %CH2CHOH
 y40=y(40); %CH3CHOH
 y41=y(41); %O
 y42=y(42); %OH
 y74=y(74); %CHCH2
 y75=y(75); %CH2CH2
 y76=y(76); %CH3CH2

%% Variables y43 to y63 represent concentration of intermediates species on Co surface

y43=y(43); %CO
 y44=y(44); %H
 y45=y(45); %HCO
 y46=y(46); %CH2O
 y47=y(47); %CH3O
 y48=y(48); %CH
 y49=y(49); %CH2
 y50=y(50); %CH3
 y51=y(51); %CHOH
 y52=y(52); %CH2OH
 y53=y(53); %CHCO
 y54=y(54); %CH2CO
 y55=y(55); %CH3CO
 y56=y(56); %CHCHO
 y57=y(57); %CH2CHO
 y58=y(58); %CH2COH
 y59=y(59); %CH3COH
 y60=y(60); %CH2CHOH
 y61=y(61); %CH3CHOH
 y62=y(62); %O

```
y63=y(63); %OH
y77=y(77); %CHCH2
y78=y(78); %CH2CH2
y79=y(79); %CH3CH2
```

% Variables y64 to y70 represent number of moles of gas phase species

```
y64=y(64); %CO GAS PHASE
y65=y(65); %H2 GAS PHASE
y66=y(66); %CH4 GAS PHASE
y67=y(67); %CH3OH GAS PHASE
y68=y(68); %CH3CH2OH GAS PHASE
y69=y(69); %CH3CHO GAS PHASE
y70=y(70); %H2O GAS PHASE
y80=y(80); %CH2CH2 GAS PHASE
y81=y(81); %CH3CH3 GAS PHASE
```

%Constants used in the model

```
kb=1.38e-23; %Boltzmann Constant [J/K]
R=8.314; %Ideal gas constant [J/mol*K]
h=6.62606957e-34; %Planks constant [J*s]
unit=96153.8; %Conversion factor [1 eV/molec equals 96153.8 J/mol]
Na=6.02214129e23; %Avogadro's number [molecules/mol]
mco=4.6512e-26; % kg
mh2=3.3538e-27; % kg
mch4=2.6635e-26; % kg
mch3oh=5.3204e-26; % kg
mch3cho=7.314e-26; % kg
mch3ch2oh=7.6443e-26; % kg
mh2o=2.9923e-26; % kg
mch2ch2=4.6579e-26; % kg
mch3ch3=4.9925e-26; % kg
```

%Variables in the model

```
s=1E6; %surface area of catalyst per mass of it [m2/kg]
vol=1E-06; % reactor volume [m3]
scaling=0.70; % scaling factor for activation energies
scaling2=0.5;
w=1.57e-19; % Surface area per active site [m2 per active site]
mcat=9e-7; % mass of catalyst [kg]
Tadj=0; % Temperature [K]
T= 523+Tadj;% Temperature, [K]
```

%Activation energies on Pd Surface [ev]

EafPd=[0.00,0.00,2.31,2.01,0.86,3.98,1.99,1.47,0.53,0.99,1.08,0.62,1.11,2.03,4.00,1.51,1.59,1.85,0.54,1.58,0.78,1.79,1.69,4.00,1.24,4.00,1.92,0.42,1.48,1.02,0.94,1.38,1.43,1.55,2.41,1.48,0.62,0.39,0.26,0.87,1.05,0.53,1.55,0.35,1.12,0.94];

EarPd=[0.66,0.51,0.84,0.94,0.82,2.06,2.06,1.87,1.44,1.28,1.01,1.28,1.06,0.72,4.67,0.89,0.92,0.88,1.11,0.94,0.83,0.84,1.06,3.24,0.93,4.29,0.94,0.98,1.35,1.17,1.17,0.88,1.02,0.95,0.88,0.97,1.14,1.56,1.12,1.03,1.11,0.98,0.78,2.16,0.43,0.92];

%Activation energies on CoPd Surface [ev]

EafCoPd=[0.00,0.00,2.48,1.14,0.69,3.28,2.30,2.30,0.60,1.20,1.14,1.37,1.66,1.63,0.50,1.03,2.11,2.32,1.14,1.21,1.42,1.68,1.76,0.71,0.72,1.14,2.49,1.32,0.96,1.64,1.24,1.51,2.18,1.63,1.93,2.48,0.83,0.59,0.26,1.26,1.37,0.53,2.03,0.45,1.57,1.65];

EarCoPd=[0.65,0.51,0.80,1.03,0.94,2.02,2.02,1.85,1.48,1.28,1.01,1.20,1.05,0.86,0.94,0.95,0.92,0.89,1.06,0.94,0.84,0.86,1.06,1.18,1.00,1.39,0.94,0.98,1.45,1.19,1.14,0.83,0.99,0.95,0.91,0.97,1.14,1.61,1.18,1.03,1.11,0.98,0.78,1.53,0.43,0.92];

%Activation energies on Co Surface [ev]

EafCo =
[0.00,0.00,1.85,0.92,0.66,1.20,1.35,1.66,0.44,0.77,1.24,1.25,1.36,1.71,1.01,1.04,1.79,1.54,1.51,0.43,1.63,1.30,1.85,0.88,0.45,1.27,2.49,1.59,1.40,1.99,1.32,1.88,2.14,1.50,2.03,2.11,0.83,1.04,0.55,1.11,0.76,0.38,1.17,0.91,1.07,2.52];

EarCo =
[0.62,0.40,0.83,1.07,1.39,1.32,1.90,2.02,1.02,1.32,1.01,1.30,1.06,0.77,0.94,0.94,0.92,0.46,0.98,0.94,1.00,0.90,1.07,1.24,1.02,1.41,0.94,0.99,1.65,1.18,1.15,0.76,0.99,0.95,1.23,0.19,1.15,1.62,1.12,1.12,1.13,0.83,0.80,1.46,0.43,0.92];

% Activation energies for Diffusion steps [ev]

EafD=[1.19,1.25,0.76,0.28,0.38,0.63,1.24,1.53,1.84,2.41,1.37,0.78,0.36,1.49,1.49,0.81,0.50,1.47,0.42,4.00,0.42,4.00];

EarD=[0.58,2.18,0.32,1.00,0.80,1.76,1.36,1.36,0.87,2.53,1.06,0.53,0.98,1.64,1.86,1.57,0.55,0.65,0.42,4.00,0.42,4.00];

%Heat of reactions from DFT on Pd surface (J/mol)

Eadsco_Pd=-1.82*scaling*unit;

Eadsh2_Pd=-0.65*scaling*unit;

Eadsch4_Pd=0.12*scaling*unit;

Eadsch3cho1_Pd=0.674*scaling*unit;

Eadsch3cho2_Pd=0.981*scaling*unit;

Eadsch3ch2oh1_Pd= 0.646*scaling*unit;

Eadsh2o_Pd= 0.78*scaling*unit;

Eadsch3oh1_Pd= 0.601*scaling*unit;
Eadsch3oh2_Pd=0.506*scaling*unit;
Eadsch2ch21_Pd=-0.167*scaling*unit;
Eadsch2ch22_Pd=0.694*scaling*unit;
Eadsch3ch3_Pd=-0.449*scaling*unit;
Eadsch3ch2oh2_Pd= 0.016*scaling*unit;

%Heat of reactions from DFT on CoPd surface (J/mol)

Eadsco_CoPd =-1.736*scaling*unit;
Eadsh2_CoPd =-0.621*scaling*unit;
Eadsch4_CoPd = 0.00129*scaling*unit;
Eadsch3cho1_CoPd =1.189*scaling*unit;
Eadsch3cho2_CoPd =1.547*scaling*unit;
Eadsch3ch2oh1_CoPd = 0.272*scaling*unit;
Eadsh2o_CoPd = 1.519*scaling*unit;
Eadsch3oh1_CoPd = 1.786*scaling*unit;
Eadsch3oh2_CoPd =1.510*scaling*unit;
Eadsch2ch21_CoPd=0.222*scaling*unit;
Eadsch2ch22_CoPd=1.146*scaling*unit;
Eadsch3ch3_CoPd=-0.455*scaling*unit;
Eadsch3ch2oh2_CoPd = 0.730*scaling*unit;

%Heat of reactions from DFT on Co surface (J/mol)

Eadsco_Co =-1.494*scaling*unit;
Eadsh2_Co =-0.593*scaling*unit;
Eadsch4_Co = 0.231*scaling*unit;
Eadsch3cho1_Co =0.875*scaling*unit;
Eadsch3cho2_Co =1.547*scaling*unit;
Eadsch3ch2oh1_Co =1.49*scaling*unit;
Eadsh2o_Co =1.94*scaling*unit;
Eadsch3oh1_Co =2.455*scaling*unit;
Eadsch3oh2_Co =1.920*scaling*unit;
Eadsch2ch21_Co=0.078*scaling*unit;
Eadsch2ch22_Co=0.645*scaling*unit;
Eadsch3ch3_Co=-0.450*scaling*unit;
Eadsch3ch2oh2_Co =1.59*scaling*unit;

%Entropy of reactions on Palladium from DFT in J/molK

Sco_Pd=-102.53*scaling;
Sh2_Pd=-114.96*scaling;
Sch4_Pd=131.54*scaling;
Sch3oh1_Pd=208.00*scaling;

Sch3oh2_Pd=213.67*scaling;
Sh2o_Pd=152.36*scaling;
Sch3ch2oh1_Pd=143.45*scaling;
Sch3cho1_Pd=167.72*scaling;
Sch3cho2_Pd= 177.89*scaling;
Sch2ch21_Pd=144*scaling;
Sch2ch22_Pd=144.16*scaling;
Sch3ch3_Pd=126.89*scaling;
Sch3ch2oh2_Pd=134.20*scaling;

%Entropy of reactions on CoPd from DFT in J/molK

Sco_CoPd=-133.35*scaling;
Sh2_CoPd=-145.10*scaling;
Sch4_CoPd=159.63*scaling;
Sch3oh1_CoPd=222.98*scaling;
Sch3oh2_CoPd=219.21*scaling;
Sh2o_CoPd=163.00*scaling;
Sch3ch2oh1_CoPd=150.50*scaling;
Sch3cho1_CoPd=179.68*scaling;
Sch3cho2_CoPd=194.74*scaling;
Sch2ch21_CoPd=169.57*scaling;
Sch2ch22_CoPd=142.59*scaling;
Sch3ch3_CoPd=129.69*scaling;
Sch3ch2oh2_CoPd=117.50*scaling;

%Entropy of reactions on Co from DFT in J/molK

Sco_Co=-134.51*scaling;
Sh2_Co=-135.26*scaling;
Sch4_Co=143.35*scaling;
Sch3oh1_Co=232.02*scaling;
Sch3oh2_Co=220.42*scaling;
Sh2o_Co=166.04*scaling;
Sch3ch2oh1_Co=160.72*scaling;
Sch3cho1_Co=143.12*scaling;
Sch3cho2_Co=184.11*scaling;
Sch2ch21_Co=154.15*scaling;
Sch2ch22_Co=134.70*scaling;
Sch3ch3_Co=144.93*scaling;
Sch3ch2oh2_Co=117.50*scaling;

%Sticking Coefficients Pd surface

% Sticking of CO on Palladium is dependent on CO coverage on surface

%a to f are constants used in the equation relating sticking coefficient

%to coverage

%J. Chern. Phys., Vol. 73, No. , 15 September 1980

a1 = 0.593999221;

b1 = -5.360127273;

c1 = -3.434120556;

d1 = 19.47053542;

e1 = 4.722521824;

f1 = 353.3218192;

SCco_Pd =

$((a1+c1*(y1/nPd)^2+e1*(y1/nPd)^4)/(1+b1*(y1/nPd)^2+d1*(y1/nPd)^4+f1*(y1/nPd)^6)$
);

%SCco_Pd=0.96;

SCh2_Pd=1.5e-7;

SCch4_Pd=1e-11;

SCch3oh_Pd=0.04;% not from literature

SCch3cho_Pd=0.1;% not from literature

SCch3ch2oh_Pd=0.04;

SCh2o_Pd=1;

SCch2ch2_Pd=1e-11;

SCch3ch3_Pd=1e-11;

%Sticking Coefficients on CoPd surface (Average of CO and Pd surfaces)

a2 = 0.627374526;

b2 = -14.42835968;

c2 = -9.938044222;

d2 = 67.4470774;

e2 = 49.78140341;

f2 = -65.08072897;

g2 = -71.83630315;

SCco_CoPd= $((a2+c2*(y22/nCoPd)^2+e2*(y22/nCoPd)^4+g2*(y22/nCoPd)^6)/(1+b2*(y22/nCoPd)^2+d2*(y22/nCoPd)^4+f2*(y22/nCoPd)^6)$);

%SCco_CoPd= $((a2+c2*(y22*nCoPd)^2+e2*(y22*nCoPd)^4+g2*(y22*nCoPd)^6)/(1+b2*(y22*nCoPd)^2+d2*(y22*nCoPd)^4+f2*(y22*nCoPd)^6)$);

%SCco_CoPd=0.8;

SCh2_CoPd=2.25e-2;

SCch4_CoPd=5e-12;

SCch3oh_CoPd=0.04;

SCch3cho_CoPd=0.1;

```

SCch3ch2oh_CoPd=0.04;
SCh2o_CoPd=1;
SCch2ch2_CoPd=5e-12;
SCch3ch3_CoPd=5e-12;
%Sticking Coefficients on Co surface
% Sticking of CO on cobalt is dependent on CO coverage on surface
%a to g are constants used in the equation relating sticking coefficient to coverage
%Surface Science 418 (1998) 502\226510

a3 = 0.647374526;
b3 = -14.42835968;
c3 = -9.938044222;
d3 = 67.4470774;
e3 = 49.78140341;
f3 = -65.08072897;
g3 = -71.83630315;
SCco_Co=((a3+c3*(y43/nCo)^2+e3*(y43/nCo)^4+g3*(y43/nCo)^6)/(1+b3*(y43/nCo)^2+
d3*(y43/nCo)^4+f3*(y43/nCo)^6));
%SCco_Co=((a3+c3*(y43*nCo)^2+e3*(y43*nCo)^4+g3*(y43*nCo)^6)/(1+b3*(y43*nCo)^
2+d3*(y43*nCo)^4+f3*(y43*nCo)^6));

%SCco_Co=0.64;%SCco=1;
SCh2_Co=0.045;
%SCch4=1;
SCch4_Co=5.18e-8;
%SCch4=9.81e-15;
SCch3oh_Co=0.4;
SCch3cho_Co=0.1;
SCch3ch2oh_Co=0.04;
SCh2o_Co=1;
SCch2ch2_Co=5.18e-8;
SCch3ch3_Co=5.18e-8;
%Rate constants on Pd surface
for i=1:1:46
    kfPd(i)=(kb*T/h)*exp(-(scaling*EafPd(i)*unit)/(R*T));
    krPd(i)=(kb*T/h)*exp(-(scaling*EarPd(i)*unit)/(R*T));
end
%Rate constants on CoPd surface
for i=1:1:46
    kfCoPd(i)=(kb*T/h)*exp(-(scaling2*EafCoPd(i)*unit)/(R*T));
    krCoPd(i)=(kb*T/h)*exp(-(scaling2*EarCoPd(i)*unit)/(R*T));

```

```

end

for i=1:1:2
    kfCoPd(i)=(kb*T/h)*exp(-(scaling*EafCoPd(i)*unit)/(R*T));
    krCoPd(i)=(kb*T/h)*exp(-(scaling*EarCoPd(i)*unit)/(R*T));
end
for i=5:1:7
    kfCoPd(i)=(kb*T/h)*exp(-(scaling*EafCoPd(i)*unit)/(R*T));
    krCoPd(i)=(kb*T/h)*exp(-(scaling*EarCoPd(i)*unit)/(R*T));
end
for i=11:1:12
    kfCoPd(i)=(kb*T/h)*exp(-(scaling*EafCoPd(i)*unit)/(R*T));
    krCoPd(i)=(kb*T/h)*exp(-(scaling*EarCoPd(i)*unit)/(R*T));
end
for i=14:1:31
    kfCoPd(i)=(kb*T/h)*exp(-(scaling*EafCoPd(i)*unit)/(R*T));
    krCoPd(i)=(kb*T/h)*exp(-(scaling*EarCoPd(i)*unit)/(R*T));
end
for i=34:1:46
    kfCoPd(i)=(kb*T/h)*exp(-(scaling*EafCoPd(i)*unit)/(R*T));
    krCoPd(i)=(kb*T/h)*exp(-(scaling*EarCoPd(i)*unit)/(R*T));
end
end
%Rate constants on Co surface
% for i=1:1:44
%   kfCo(i)=(kb*T/h)*exp(-(scaling*EafCo(i)*unit)/(R*T));
%   krCo(i)=(kb*T/h)*exp(-(scaling*EarCo(i)*unit)/(R*T));
% end
for i=1:1:46
    kfCo(i)=(kb*T/h)*exp(-(scaling*EafCo(i)*unit)/(R*T));
    krCo(i)=(kb*T/h)*exp(-(scaling*EarCo(i)*unit)/(R*T));
end
% for i=37:1:44
%   kfCo(i)=(kb*T/h)*exp(-(scaling2*EafCo(i)*unit)/(R*T));
%   krCo(i)=(kb*T/h)*exp(-(scaling2*EarCo(i)*unit)/(R*T));
% end

% for i=32:1:32
%   kfCo(i)=(kb*T/h)*exp(-(scaling2*EafCo(i)*unit)/(R*T));
%   krCo(i)=(kb*T/h)*exp(-(scaling2*EarCo(i)*unit)/(R*T));
% end

```

%Rate constants for diffusion steps

for i=1:22

kfD(i)=(kb*T/h)*exp(-(scaling*EafD(i)*unit)/(R*T));

krD(i)=(kb*T/h)*exp(-(scaling*EarD(i)*unit)/(R*T));

end

%Adsorption rate constants (gas phase species) on Pd surface

kfPd(1)=w*SCco_Pd/sqrtm(2*3.14159*mco*kb*T); % 1/Pa.s, CO

kfPd(2)=w*SCh2_Pd/sqrtm(2*3.14159*mh2*kb*T); % 1/Pa.s, H2

krPd(11)=w*SCch4_Pd/sqrtm(2*3.14159*mch4*kb*T); % 1/Pa.s, CH4

krPd(17)=w*SCch3cho_Pd/sqrtm(2*3.14159*mch3cho*kb*T); % 1/Pa.s, CH3CHO

krPd(20)=w*SCch3ch2oh_Pd/sqrtm(2*3.14159*mch3ch2oh*kb*T); % 1/Pa.s,

CH3CH2OH

krPd(27)=w*SCch3cho_Pd/sqrtm(2*3.14159*mch3cho*kb*T); % 1/Pa.s, CH3CHO

krPd(30)=w*SCh2o_Pd/sqrtm(2*3.14159*mh2o*kb*T); % 1/Pa.s, H2O

krPd(34)=w*SCch3oh_Pd/sqrtm(2*3.14159*mch3oh*kb*T); % 1/Pa.s, CH3OH

krPd(36)=w*SCch3oh_Pd/sqrtm(2*3.14159*mch3oh*kb*T); % 1/Pa.s, CH3OH

krPd(40)=w*SCch2ch2_Pd/sqrtm(2*3.14159*mch2ch2*kb*T);

krPd(42)=w*SCch3ch3_Pd/sqrtm(2*3.14159*mch3ch3*kb*T);

krPd(45)=w*SCch2ch2_Co/sqrtm(2*3.14159*mch2ch2*kb*T);

krPd(46)=w*SCch3ch2oh_Co/sqrtm(2*3.14159*mch3ch2oh*kb*T);

%Adsorption rate constants (gas phase species) on CoPd surface

kfCoPd(1)=w*SCco_CoPd/sqrtm(2*3.14159*mco*kb*T); % 1/Pa.s, CO

kfCoPd(2)=w*SCh2_CoPd/sqrtm(2*3.14159*mh2*kb*T); % 1/Pa.s, H2

krCoPd(11)=w*SCch4_CoPd/sqrtm(2*3.14159*mch4*kb*T); % 1/Pa.s, CH4

krCoPd(17)=w*SCch3cho_CoPd/sqrtm(2*3.14159*mch3cho*kb*T); % 1/Pa.s, CH3CHO

krCoPd(20)=w*SCch3ch2oh_CoPd/sqrtm(2*3.14159*mch3ch2oh*kb*T); % 1/Pa.s, CH3CH

2OH

krCoPd(27)=w*SCch3cho_CoPd/sqrtm(2*3.14159*mch3cho*kb*T); % 1/Pa.s, CH3CHO

krCoPd(30)=w*SCh2o_CoPd/sqrtm(2*3.14159*mh2o*kb*T); % 1/Pa.s, H2O

krCoPd(34)=w*SCch3oh_CoPd/sqrtm(2*3.14159*mch3oh*kb*T); % 1/Pa.s, CH3OH

krCoPd(36)=w*SCch3oh_CoPd/sqrtm(2*3.14159*mch3oh*kb*T); % 1/Pa.s, CH3OH

krCoPd(40)=w*SCch2ch2_CoPd/sqrtm(2*3.14159*mch2ch2*kb*T);

krCoPd(42)=w*SCch3ch3_CoPd/sqrtm(2*3.14159*mch3ch3*kb*T);

krCoPd(45)=w*SCch2ch2_Co/sqrtm(2*3.14159*mch2ch2*kb*T);

krCoPd(46)=w*SCch3ch2oh_Co/sqrtm(2*3.14159*mch3ch2oh*kb*T);

%Adsorption rate constants (gas phase species) on Co surface

kfCo(1)=w*SCco_Co/sqrtm(2*3.14159*mco*kb*T); % 1/Pa.s, CO

kfCo(2)=w*SCh2_Co/sqrtm(2*3.14159*mh2*kb*T); % 1/Pa.s, H2

krCo(11)=w*SCch4_Co/sqrtm(2*3.14159*mch4*kb*T); % 1/Pa.s, CH4

krCo(17)=w*SCch3cho_Co/sqrtm(2*3.14159*mch3cho*kb*T); % 1/Pa.s, CH3CHO

```

krCo(20)=w*SCch3ch2oh_Co/sqrtm(2*3.14159*mch3ch2oh*kb*T); % 1/Pa.s,
CH3CH2OH
krCo(27)=w*SCch3cho_Co/sqrtm(2*3.14159*mch3cho*kb*T); % 1/Pa.s, CH3CHO
krCo(30)=w*SCh2o_Co/sqrtm(2*3.14159*mh2o*kb*T); % 1/Pa.s, H2O
krCo(34)=w*SCch3oh_Co/sqrtm(2*3.14159*mch3oh*kb*T); % 1/Pa.s, CH3OH
krCo(36)=w*SCch3oh_Co/sqrtm(2*3.14159*mch3oh*kb*T); % 1/Pa.s, CH3OH
krCo(40)=w*SCch2ch2_Co/sqrtm(2*3.14159*mch2ch2*kb*T);
krCo(45)=w*SCch2ch2_Co/sqrtm(2*3.14159*mch2ch2*kb*T);
krCo(42)=w*SCch3ch3_Co/sqrtm(2*3.14159*mch3ch3*kb*T);
krCo(46)=w*SCch3ch2oh_Co/sqrtm(2*3.14159*mch3ch2oh*kb*T);
%Equilibrium constants on Pd surface
Kco_Pd = exp(-(Eadsco_Pd-(T*Sco_Pd))/(R*T));
Kh2_Pd = exp(-(Eadsh2_Pd-(T*Sh2_Pd))/(R*T));
Kch4_Pd = exp(-(Eadsch4_Pd-(T*Sch4_Pd))/(R*T));
Kch3oh1_Pd = exp(-(Eadsch3oh1_Pd-(T*Sch3oh1_Pd))/(R*T));
Kch3oh2_Pd = exp(-(Eadsch3oh2_Pd-(T*Sch3oh2_Pd))/(R*T));
Kch3ch2oh1_Pd= exp(-(Eadsch3ch2oh1_Pd-(T*Sch3ch2oh1_Pd))/(R*T));
Kh2o_Pd= exp(-(Eadsh2o_Pd-(T*Sh2o_Pd))/(R*T));
Kch3cho1_Pd= exp(-(Eadsch3cho1_Pd-(T*Sch3cho1_Pd))/(R*T));
Kch3cho2_Pd= exp(-(Eadsch3cho2_Pd-(T*Sch3cho2_Pd))/(R*T));
Kch2ch21_Pd= exp(-(Eadsch2ch21_Pd-(T*Sch2ch21_Pd))/(R*T));
Kch2ch22_Pd= exp(-(Eadsch2ch22_Pd-(T*Sch2ch22_Pd))/(R*T));
Kch3ch3_Pd= exp(-(Eadsch3ch3_Pd-(T*Sch3ch3_Pd))/(R*T));
Kch3ch2oh2_Pd= exp(-(Eadsch3ch2oh2_Pd-(T*Sch3ch2oh2_Pd))/(R*T));
%Equilibrium constants on CoPd surface
Kco_CoPd = exp(-(Eadsco_CoPd-(T*Sco_CoPd))/(R*T));
Kh2_CoPd = exp(-(Eadsh2_CoPd-(T*Sh2_CoPd))/(R*T));
Kch4_CoPd = exp(-(Eadsch4_CoPd-(T*Sch4_CoPd))/(R*T));
Kch3oh1_CoPd = exp(-(Eadsch3oh1_CoPd-(T*Sch3oh1_CoPd))/(R*T));
Kch3oh2_CoPd = exp(-(Eadsch3oh2_CoPd-(T*Sch3oh2_CoPd))/(R*T));
Kch3ch2oh1_CoPd= exp(-(Eadsch3ch2oh1_CoPd-(T*Sch3ch2oh1_CoPd))/(R*T));
Kh2o_CoPd= exp(-(Eadsh2o_CoPd-(T*Sh2o_CoPd))/(R*T));
Kch3cho1_CoPd= exp(-(Eadsch3cho1_CoPd-(T*Sch3cho1_CoPd))/(R*T));
Kch3cho2_CoPd= exp(-(Eadsch3cho2_CoPd-(T*Sch3cho2_CoPd))/(R*T));
Kch2ch21_CoPd= exp(-(Eadsch2ch21_CoPd-(T*Sch2ch21_CoPd))/(R*T));
Kch2ch22_CoPd= exp(-(Eadsch2ch22_CoPd-(T*Sch2ch22_CoPd))/(R*T));
Kch3ch3_CoPd= exp(-(Eadsch3ch3_CoPd-(T*Sch3ch3_CoPd))/(R*T));
Kch3ch2oh2_CoPd= exp(-(Eadsch3ch2oh2_CoPd-(T*Sch3ch2oh2_CoPd))/(R*T));
%Equilibrium constants on Co surface
%Kco_Co = Kco_Pd;
Kco_Co = exp(-(Eadsco_Co-(T*Sco_Co))/(R*T));

```

```

Kh2_Co = exp(-(Eadsh2_Co-(T*Sh2_Co))/(R*T));
Kch4_Co = exp(-(Eadsch4_Co-(T*Sch4_Co))/(R*T));
Kch3oh1_Co = exp(-(Eadsch3oh1_Co-(T*Sch3oh1_Co))/(R*T));
Kch3oh2_Co = exp(-(Eadsch3oh2_Co-(T*Sch3oh2_Co))/(R*T));
Kch3ch2oh1_Co = exp(-(Eadsch3ch2oh1_Co-(T*Sch3ch2oh1_Co))/(R*T));
Kh2o_Co = exp(-(Eadsh2o_Co-(T*Sh2o_Co))/(R*T));
Kch3cho1_Co = exp(-(Eadsch3cho1_Co-(T*Sch3cho1_Co))/(R*T));
Kch3cho2_Co = exp(-(Eadsch3cho2_Co-(T*Sch3cho2_Co))/(R*T));
Kch2ch21_Co = (exp(-(Eadsch2ch21_Co-(T*Sch2ch21_Co))/(R*T)));
Kch2ch22_Co = exp(-(Eadsch2ch22_Co-(T*Sch2ch22_Co))/(R*T));
Kch3ch3_Co = exp(-(Eadsch3ch3_Co-(T*Sch3ch3_Co))/(R*T));
Kch3ch2oh2_Co = exp(-(Eadsch3ch2oh2_Co-(T*Sch3ch2oh2_Co))/(R*T));
%Desorption rate constants(gas phase species) on Pd surface
krPd(1)=kfPd(1)/Kco_Pd;          % 1/Pa.s, CO
krPd(2)=kfPd(2)/Kh2_Pd;        % 1/Pa.s, H2
kfPd(11)=krPd(11)*Kch4_Pd;
kfPd(17)=krPd(17)*Kch3cho1_Pd;
kfPd(20)=krPd(20)*Kch3ch2oh1_Pd;
kfPd(27)=krPd(27)*Kch3cho2_Pd;
kfPd(30)=krPd(30)*Kh2o_Pd;
kfPd(34)=krPd(34)*Kch3oh1_Pd;
kfPd(36)=krPd(36)*Kch3oh2_Pd;
kfPd(40)=krPd(40)*Kch2ch21_Pd;
kfPd(42)=krPd(42)*Kch3ch3_Pd;
kfPd(45)=krPd(45)*Kch2ch22_Pd;
kfPd(46)=krPd(46)*Kch3ch2oh2_Pd;
%Desorption rate constants on CoPd surface
krCoPd(1)=kfCoPd(1)/Kco_CoPd;
krCoPd(2)=kfCoPd(2)/Kh2_CoPd;
kfCoPd(11)=krCoPd(11)*Kch4_CoPd;
kfCoPd(17)=krCoPd(17)*Kch3cho1_CoPd;
kfCoPd(20)=krCoPd(20)*Kch3ch2oh1_CoPd;
kfCoPd(27)=krCoPd(27)*Kch3cho2_CoPd;
kfCoPd(30)=krCoPd(30)*Kh2o_CoPd;
kfCoPd(34)=krCoPd(34)*Kch3oh1_CoPd;
kfCoPd(36)=krCoPd(36)*Kch3oh2_CoPd;
kfCoPd(40)=krCoPd(40)*Kch2ch21_CoPd;
kfCoPd(42)=krCoPd(42)*Kch3ch3_CoPd;
kfCoPd(45)=krCoPd(45)*Kch2ch22_CoPd;
kfCoPd(46)=krCoPd(46)*Kch3ch2oh2_CoPd;
%Desorption rate constants on Co surface

```

```

krCo(1)=kfCo(1)/Kco_Co;
krCo(2)=kfCo(2)/Kh2_Co;
kfCo(11)=krCo(11)*Kch4_Co;
kfCo(17)=krCo(17)*Kch3cho1_Co;
kfCo(20)=krCo(20)*Kch3ch2oh1_Co;
kfCo(27)=krCo(27)*Kch3cho2_Co;
kfCo(30)=krCo(30)*Kh2o_Co;
kfCo(34)=krCo(34)*Kch3oh1_Co;
kfCo(36)=krCo(36)*Kch3oh2_Co;
kfCo(40)=krCo(40)*Kch2ch21_Co;
kfCo(42)=krCo(42)*Kch3ch3_Co;
kfCo(45)=krCo(45)*Kch2ch22_Co;
kfCo(46)=krCo(46)*Kch3ch2oh2_Co;

```

% Partial Pressure of gas phase species

% y64 to y70 are number of moles of gases

```

Pco=y64*R*T/vol;
Ph2=y65*R*T/vol;
Pch4=y66*R*T/vol;
Pch3oh=y67*R*T/vol;
Pch3ch2oh=y68*R*T/vol;
Pch3cho=y69*R*T/vol;
Ph2o=y70*R*T/vol;
Pch2ch2=y80*R*T/vol;
Pch3ch3=y81*R*T/vol;

```

% Concentration of empty sites on all three surfaces

```

y0_Pd=(nPd)-
(y1+y2+y3+y4+y5+y6+y7+y8+y9+y10+y11+y12+y13+y14+y15+y16+y17+y18+y19+y20+y2
1+y71+y72+y73);
y0_CoPd=(nCoPd)-
(y22+y23+y24+y25+y26+y27+y28+y29+y30+y31+y32+y33+y34+y35+y36+y37+y38+y39+
y40+y41+y42+y74+y75+y76);
y0_Co=(nCo)-
(y43+y44+y45+y46+y47+y48+y49+y50+y51+y52+y53+y54+y55+y56+y57+y58+y59+y60+
y61+y62+y63+y77+y78+y79);

```

%reactions and rate expressions on Pd surface

%R1 CO(g)+*<-->CO*

r1_Pd=kfPd(1)*(Pco*y0_Pd-y1/Kco_Pd);

%R2 H2(g)+2*<-->H*+H*

$r_{2_Pd} = k_{fPd}(2) \cdot (P_{H_2} \cdot y_{O_Pd} \cdot y_{O_Pd} - y_2^2 / K_{h2_Pd});$
 %R3 $CO^* + H^* \leftrightarrow HCO^* + ^*$
 $r_{3_Pd} = k_{fPd}(3) \cdot y_1 \cdot y_2 - k_{rPd}(3) \cdot y_3 \cdot y_{O_Pd};$
 %R4 $HCO^* + H^* \leftrightarrow CH_2O^* + ^*$
 $r_{4_Pd} = k_{fPd}(4) \cdot y_2 \cdot y_3 - k_{rPd}(4) \cdot y_4 \cdot y_{O_Pd};$
 %R5 $CH_2O^* + H^* \leftrightarrow CH_3O^* + ^*$
 $r_{5_Pd} = k_{fPd}(5) \cdot y_4 \cdot y_2 - k_{rPd}(5) \cdot y_5 \cdot y_{O_Pd};$
 %R6 $HCO^* + ^* \leftrightarrow CH^* + O^*$
 $r_{6_Pd} = k_{fPd}(6) \cdot y_3 \cdot y_{O_Pd} - k_{rPd}(6) \cdot y_6 \cdot y_{2O};$
 %R7 $CH_2O^* + ^* \leftrightarrow CH_2^* + O^*$
 $r_{7_Pd} = k_{fPd}(7) \cdot y_{O_Pd} \cdot y_4 - k_{rPd}(7) \cdot y_7 \cdot y_{2O};$
 %R8 $CH_3O^* + ^* \leftrightarrow CH_3^* + O^*$
 $r_{8_Pd} = k_{fPd}(8) \cdot y_5 \cdot y_{O_Pd} - k_{rPd}(8) \cdot y_8 \cdot y_{2O};$
 %R9 $CH^* + H^* \leftrightarrow CH_2^* + ^*$
 $r_{9_Pd} = k_{fPd}(9) \cdot y_6 \cdot y_2 - k_{rPd}(9) \cdot y_7 \cdot y_{O_Pd};$
 %R10 $CH_2^* + H^* \leftrightarrow CH_3^* + ^*$
 $r_{10_Pd} = k_{fPd}(10) \cdot y_7 \cdot y_2 - k_{rPd}(10) \cdot y_8 \cdot y_{O_Pd};$
 %R11 $CH_3^* + H^* \leftrightarrow CH_4(g) + 2^*$
 $r_{11_Pd} = k_{fPd}(11) \cdot (y_2 \cdot y_8 - P_{ch4} \cdot y_{O_Pd} \cdot y_{O_Pd} / K_{ch4_Pd});$
 %R12 $CH^* + CO^* \leftrightarrow CHCO^* + ^*$
 $r_{12_Pd} = k_{fPd}(12) \cdot y_1 \cdot y_6 - k_{rPd}(12) \cdot y_{11} \cdot y_{O_Pd};$
 %R13 $CH_2^* + CO^* \leftrightarrow CH_2CO^* + ^*$
 $r_{13_Pd} = k_{fPd}(13) \cdot y_1 \cdot y_7 - k_{rPd}(13) \cdot y_{12} \cdot y_{O_Pd};$
 %R14 $CH_3^* + CO^* \leftrightarrow CH_3CO^* + ^*$
 $r_{14_Pd} = k_{fPd}(14) \cdot y_1 \cdot y_8 - k_{rPd}(14) \cdot y_{13} \cdot y_{O_Pd};$
 %R15 $CHCO^* + H^* \leftrightarrow CH_2CO^* + ^*$
 $r_{15_Pd} = k_{fPd}(15) \cdot y_2 \cdot y_{11} - k_{rPd}(15) \cdot y_{12} \cdot y_{O_Pd};$
 %R16 $CH_2CO^* + H^* \leftrightarrow CH_3CO^* + ^*$
 $r_{16_Pd} = k_{fPd}(16) \cdot y_{12} \cdot y_2 - k_{rPd}(16) \cdot y_{13} \cdot y_{O_Pd};$
 %R17 $CH_3CO^* + H^* \leftrightarrow CH_3CHO(g) + 2^*$
 $r_{17_Pd} = k_{fPd}(17) \cdot ((y_{13} \cdot y_2) - P_{ch3cho} \cdot y_{O_Pd} \cdot y_{O_Pd} / K_{ch3cho1_Pd});$
 %R18 $CH_3CO^* + H^* \leftrightarrow CH_3COH^* + ^*$
 $r_{18_Pd} = k_{fPd}(18) \cdot y_{13} \cdot y_2 - k_{rPd}(18) \cdot y_{17} \cdot y_{O_Pd};$
 %R19 $CH_3COH^* + H^* \leftrightarrow CH_3CHOH^* + ^*$
 $r_{19_Pd} = k_{fPd}(19) \cdot y_{17} \cdot y_2 - k_{rPd}(19) \cdot y_{19} \cdot y_{O_Pd};$
 %R20 $CH_3CHOH^* + H^* \leftrightarrow CH_3CH_2OH(g) + 2^*$
 $r_{20_Pd} = k_{fPd}(20) \cdot ((y_{19} \cdot y_2) - P_{ch3ch2oh} \cdot y_{O_Pd} \cdot y_{O_Pd} / K_{ch3ch2oh1_Pd});$
 %R21 $CH_2O^* + H^* \leftrightarrow CH_2OH^* + ^*$
 $r_{21_Pd} = k_{fPd}(21) \cdot y_2 \cdot y_4 - k_{rPd}(21) \cdot y_{10} \cdot y_{O_Pd};$
 %R22 $CH_2CO^* + H^* \leftrightarrow CH_2COH^* + ^*$
 $r_{22_Pd} = k_{fPd}(22) \cdot y_2 \cdot y_{12} - k_{rPd}(22) \cdot y_{16} \cdot y_{O_Pd};$

%R23 CH₂COH*+H* \leftrightarrow CH₃COH*+*
 r23_Pd=kfPd(23)*y₁₆*y₂-krPd(23)*y₁₇*y₀_Pd;
 %R24 CHCO*+H* \leftrightarrow CHCHO*+*
 r24_Pd=kfPd(24)*y₁₁*y₂-krPd(24)*y₁₄*y₀_Pd;
 %R25 CH₂CO*+H* \leftrightarrow CH₂CHO*+*
 r25_Pd=kfPd(25)*y₁₂*y₂-krPd(25)*y₁₅*y₀_Pd;
 %R26 CHCHO*+H* \leftrightarrow CH₂CHO*+*
 r26_Pd=kfPd(26)*y₁₄*y₂-krPd(26)*y₁₅*y₀_Pd;
 %R27 CH₂CHO*+H* \leftrightarrow CH₃CHO(g)+2*
 r27_Pd=kfPd(27)*((y₁₅*y₂)-Pch3cho*y₀_Pd*y₀_Pd/Kch3cho2_Pd);
 %R28 CH₂O*+CH₂* \leftrightarrow CH₃COH*+*
 r28_Pd=kfPd(28)*y₄*y₇-krPd(28)*y₁₇*y₀_Pd;
 %R29 O*+H* \leftrightarrow OH*+*
 r29_Pd=kfPd(29)*y₂₀*y₂-krPd(29)*y₂₁*y₀_Pd;
 %R30 OH*+H* \leftrightarrow H₂O(g)+*
 r30_Pd=kfPd(30)*((y₂*y₂₁)-Ph₂o*y₀_Pd*y₀_Pd/Kh₂o_Pd);
 %R31 CH₂COH*+H* \leftrightarrow CH₂CHOH*+*
 r31_Pd=kfPd(31)*y₁₆*y₂-krPd(31)*y₁₈*y₀_Pd;
 %R32 CH₂CHOH*+H* \leftrightarrow CH₃CHOH*+*
 r32_Pd=kfPd(32)*y₁₈*y₂-krPd(32)*y₁₉*y₀_Pd;
 %R33 CH₂CHO*+H* \leftrightarrow CH₂CHOH*+*
 r33_Pd=kfPd(33)*y₁₅*y₂-krPd(33)*y₁₈*y₀_Pd;
 %R34 CH₂OH*+H* \leftrightarrow CH₃OH(g)+2*
 r34_Pd=kfPd(34)*((y₁₀*y₂)-Pch3oh*y₀_Pd*y₀_Pd/Kch3oh1_Pd);
 %R35 HCO*+H* \leftrightarrow CHOH*+*
 r35_Pd=kfPd(35)*y₃*y₂-krPd(35)*y₉*y₀_Pd;
 %R36 CH₃O*+H* \leftrightarrow CH₃OH(g)+2*
 r36_Pd=kfPd(36)*(y₂*y₅-Pch3oh*y₀_Pd*y₀_Pd/Kch3oh2_Pd);
 %R37 CHOH*+H* \leftrightarrow CH₂OH*+*
 r37_Pd=kfPd(37)*y₉*y₂-krPd(37)*y₁₀*y₀_Pd;
 %R38 CH*+CH₂* \leftrightarrow CHCH₂*+*
 r38_Pd=kfPd(38)*y₆*y₇-krPd(38)*y₇₁*y₀_Pd;
 %R39 CHCH₂*+H* \leftrightarrow CH₂CH₂*+*
 r39_Pd=kfPd(39)*y₇₁*y₂-krPd(39)*y₇₂*y₀_Pd;
 %r39_Pd=0;
 %R40 CHCH₂*+H* \leftrightarrow CH₂CH₂(g)+2*
 r40_Pd=kfPd(40)*(y₂*y₇₁-Pch2ch2*y₀_Pd*y₀_Pd/Kch2ch21_Pd);
 %R41 CH₃*+CH₂* \leftrightarrow CH₃CH₂*+*
 r41_Pd=kfPd(41)*y₈*y₇-krPd(41)*y₇₃*y₀_Pd;
 %R42 CH₃CH₂*+H* \leftrightarrow CH₃CH₃(g)+2*
 r42_Pd=kfPd(42)*(y₂*y₇₃-Pch3ch3*y₀_Pd*y₀_Pd/Kch3ch3_Pd);

```

%R43 CH2CH2*+H* $\leftrightarrow$ CH3CH2*+*
r43_Pd=kfPd(43)*y72*y2-krPd(43)*y73*y0_Pd;
%R44 CH2*+CH2* $\leftrightarrow$ CH2CH2*+*
r44_Pd=kfPd(44)*y7*y7-krPd(44)*y72*y0_Pd;
%r44_Pd=0;
%R45 CHCH2*+* $\leftrightarrow$ CH2CH2(g)+2*
r45_Pd=kfPd(45)*(y72*y0_Pd-Pch2ch2*y0_Pd*y0_Pd/Kch2ch22_Pd);
%R46 CH3CH2*+OH* $\leftrightarrow$ CH3CH2OH(g)+2*
r46_Pd=kfPd(46)*(y73*y21-Pch3ch2oh*y0_Pd*y0_Pd/Kch3ch2oh2_Pd);

```

%reactions and rate expressions on CoPd surface

```

%R1 CO(g)+* $\leftrightarrow$ CO*
r1_CoPd=kfCoPd(1)*(Pco*y0_CoPd-y22/Kco_CoPd);
%R2 H2(g)+2* $\leftrightarrow$ H*+H*
r2_CoPd=kfCoPd(2)*(Ph2*y0_CoPd*y0_CoPd-y23*y23/Kh2_CoPd);
%R3 CO*+H* $\leftrightarrow$ HCO*+*
r3_CoPd=kfCoPd(3)*y22*y23-krCoPd(3)*y24*y0_CoPd;
%R4 HCO*+H* $\leftrightarrow$ CH2O*+*
r4_CoPd=kfCoPd(4)*y23*y24-krCoPd(4)*y25*y0_CoPd;
%R5 CH2O*+H* $\leftrightarrow$ CH3O*+*
r5_CoPd=kfCoPd(5)*y25*y23-krCoPd(5)*y26*y0_CoPd;
%R6 HCO*+* $\leftrightarrow$ CH*+O*
r6_CoPd=kfCoPd(6)*y24*y0_CoPd-krCoPd(6)*y27*y41;
%R7 CH2O*+* $\leftrightarrow$ CH2*+O*
r7_CoPd=kfCoPd(7)*y0_CoPd*y25-krCoPd(7)*y28*y41;
%R8 CH3O*+* $\leftrightarrow$ CH3*+O*
r8_CoPd=kfCoPd(8)*y26*y0_CoPd-krCoPd(8)*y29*y41;
%R9 CH*+H* $\leftrightarrow$ CH2*+*
r9_CoPd=kfCoPd(9)*y27*y23-krCoPd(9)*y28*y0_CoPd;
%R10 CH2*+H* $\leftrightarrow$ CH3*+*
r10_CoPd=kfCoPd(10)*y28*y23-krCoPd(10)*y29*y0_CoPd;
%R11 CH3*+H* $\leftrightarrow$ CH4(g)+2*
r11_CoPd=kfCoPd(11)*(y23*y29-Pch4*y0_CoPd*y0_CoPd/Kch4_CoPd);
%R12 CH*+CO* $\leftrightarrow$ CHCO*+*
r12_CoPd=kfCoPd(12)*y22*y27-krCoPd(12)*y32*y0_CoPd;
%R13 CH2*+CO* $\leftrightarrow$ CH2CO*+*
r13_CoPd=kfCoPd(13)*y22*y28-krCoPd(13)*y33*y0_CoPd;
%R14 CH3*+CO* $\leftrightarrow$ CH3CO*+*
r14_CoPd=kfCoPd(14)*y22*y29-krCoPd(14)*y34*y0_CoPd;
%R15 CHCO*+H* $\leftrightarrow$ CH2CO*+*
r15_CoPd=kfCoPd(15)*y23*y32-krCoPd(15)*y33*y0_CoPd;

```

%R16 $\text{CH}_2\text{CO}^* + \text{H}^* \leftrightarrow \text{CH}_3\text{CO}^* + ^*$
 $r_{16_CoPd} = k_f CoPd(16) \cdot y_{33} \cdot y_{23} - k_r CoPd(16) \cdot y_{34} \cdot y_{0_CoPd}$;
 %R17 $\text{CH}_3\text{CO}^* + \text{H}^* \leftrightarrow \text{CH}_3\text{CHO}(g) + 2^*$
 $r_{17_CoPd} = k_f CoPd(17) \cdot ((y_{34} \cdot y_{23}) - Pch3cho \cdot y_{0_CoPd} \cdot y_{0_CoPd} / Kch3cho1_CoPd)$;
 %R18 $\text{CH}_3\text{CO}^* + \text{H}^* \leftrightarrow \text{CH}_3\text{COH}^* + ^*$
 $r_{18_CoPd} = k_f CoPd(18) \cdot y_{34} \cdot y_{23} - k_r CoPd(18) \cdot y_{38} \cdot y_{0_CoPd}$;
 %R19 $\text{CH}_3\text{COH}^* + \text{H}^* \leftrightarrow \text{CH}_3\text{CHOH}^* + ^*$
 $r_{19_CoPd} = k_f CoPd(19) \cdot y_{38} \cdot y_{23} - k_r CoPd(19) \cdot y_{40} \cdot y_{0_CoPd}$;
 %R20 $\text{CH}_3\text{CHOH}^* + \text{H}^* \leftrightarrow \text{CH}_3\text{CH}_2\text{OH}(g) + 2^*$
 $r_{20_CoPd} = k_f CoPd(20) \cdot ((y_{40} \cdot y_{23}) - Pch3ch2oh \cdot y_{0_CoPd} \cdot y_{0_CoPd} / Kch3ch2oh1_CoPd)$;
 %R21 $\text{CH}_2\text{O}^* + \text{H}^* \leftrightarrow \text{CH}_2\text{OH}^* + ^*$
 $r_{21_CoPd} = k_f CoPd(21) \cdot y_{23} \cdot y_{25} - k_r CoPd(21) \cdot y_{31} \cdot y_{0_CoPd}$;
 %R22 $\text{CH}_2\text{CO}^* + \text{H}^* \leftrightarrow \text{CH}_2\text{COH}^* + ^*$
 $r_{22_CoPd} = k_f CoPd(22) \cdot y_{23} \cdot y_{33} - k_r CoPd(22) \cdot y_{37} \cdot y_{0_CoPd}$;
 %R23 $\text{CH}_2\text{COH}^* + \text{H}^* \leftrightarrow \text{CH}_3\text{COH}^* + ^*$
 $r_{23_CoPd} = k_f CoPd(23) \cdot y_{37} \cdot y_{23} - k_r CoPd(23) \cdot y_{38} \cdot y_{0_CoPd}$;
 %R24 $\text{CHCO}^* + \text{H}^* \leftrightarrow \text{CHCHO}^* + ^*$
 $r_{24_CoPd} = k_f CoPd(24) \cdot y_{32} \cdot y_{23} - k_r CoPd(24) \cdot y_{35} \cdot y_{0_CoPd}$;
 %R25 $\text{CH}_2\text{CO}^* + \text{H}^* \leftrightarrow \text{CH}_2\text{CHO}^* + ^*$
 $r_{25_CoPd} = k_f CoPd(25) \cdot y_{33} \cdot y_{23} - k_r CoPd(25) \cdot y_{36} \cdot y_{0_CoPd}$;
 %R26 $\text{CHCHO}^* + \text{H}^* \leftrightarrow \text{CH}_2\text{CHO}^* + ^*$
 $r_{26_CoPd} = k_f CoPd(26) \cdot y_{35} \cdot y_{23} - k_r CoPd(26) \cdot y_{36} \cdot y_{0_CoPd}$;
 %R27 $\text{CH}_2\text{CHO}^* + \text{H}^* \leftrightarrow \text{CH}_3\text{CHO}(g) + 2^*$
 $r_{27_CoPd} = k_f CoPd(27) \cdot ((y_{36} \cdot y_{23}) - Pch3cho \cdot y_{0_CoPd} \cdot y_{0_CoPd} / Kch3cho2_CoPd)$;
 %R28 $\text{CH}_2\text{O}^* + \text{CH}_2^* \leftrightarrow \text{CH}_3\text{COH}^* + ^*$
 $r_{28_CoPd} = k_f CoPd(28) \cdot y_{25} \cdot y_{28} - k_r CoPd(28) \cdot y_{38} \cdot y_{0_CoPd}$;
 %r28_CoPd=0;
 %R29 $\text{O}^* + \text{H}^* \leftrightarrow \text{OH}^* + ^*$
 $r_{29_CoPd} = k_f CoPd(29) \cdot y_{41} \cdot y_{23} - k_r CoPd(29) \cdot y_{42} \cdot y_{0_CoPd}$;
 %R30 $\text{OH}^* + \text{H}^* \leftrightarrow \text{H}_2\text{O}(g) + ^*$
 $r_{30_CoPd} = k_f CoPd(30) \cdot ((y_{23} \cdot y_{42}) - Ph2o \cdot y_{0_CoPd} \cdot y_{0_CoPd} / Kh2o_CoPd)$;
 %R31 $\text{CH}_2\text{COH}^* + \text{H}^* \leftrightarrow \text{CH}_2\text{CHOH}^* + ^*$
 $r_{31_CoPd} = k_f CoPd(31) \cdot y_{37} \cdot y_{23} - k_r CoPd(31) \cdot y_{39} \cdot y_{0_CoPd}$;
 %R32 $\text{CH}_2\text{CHOH}^* + \text{H}^* \leftrightarrow \text{CH}_3\text{CHOH}^* + ^*$
 $r_{32_CoPd} = k_f CoPd(32) \cdot y_{39} \cdot y_{23} - k_r CoPd(32) \cdot y_{40} \cdot y_{0_CoPd}$;
 %R33 $\text{CH}_2\text{CHO}^* + \text{H}^* \leftrightarrow \text{CH}_2\text{CHOH}^* + ^*$
 $r_{33_CoPd} = k_f CoPd(33) \cdot y_{36} \cdot y_{23} - k_r CoPd(33) \cdot y_{39} \cdot y_{0_CoPd}$;
 %R34 $\text{CH}_2\text{OH}^* + \text{H}^* \leftrightarrow \text{CH}_3\text{OH}(g) + 2^*$
 $r_{34_CoPd} = k_f CoPd(34) \cdot ((y_{31} \cdot y_{23}) - Pch3oh \cdot y_{0_CoPd} \cdot y_{0_CoPd} / Kch3oh1_CoPd)$;
 %R35 $\text{HCO}^* + \text{H}^* \leftrightarrow \text{CHOH}^* + ^*$
 $r_{35_CoPd} = k_f CoPd(35) \cdot y_{24} \cdot y_{23} - k_r CoPd(35) \cdot y_{30} \cdot y_{0_CoPd}$

```

%R36 CH3O*+H* $\leftrightarrow$ CH3OH(g)+2*
r36_CoPd=kfCoPd(36)*(y23*y26-Pch3oh*y0_CoPd/Kch3oh2_CoPd);
%R37 CHOH*+H* $\leftrightarrow$ CH2OH*+*
r37_CoPd=kfCoPd(37)*y30*y23-krCoPd(37)*y31*y0_CoPd;
%R38 CH*+CH2* $\leftrightarrow$ CHCH2*+*
r38_CoPd=kfCoPd(38)*y27*y28-krCoPd(38)*y74*y0_CoPd;
%R39 CHCH2*+H* $\leftrightarrow$ CH2CH2*+*
r39_CoPd=kfCoPd(39)*y74*y23-krCoPd(39)*y75*y0_CoPd;
%r39_CoPd=0;
%R40 CHCH2*+H* $\leftrightarrow$ CH2CH2(g)+2*
r40_CoPd=kfCoPd(40)*(y23*y74-Pch2ch2*y0_CoPd*y0_CoPd/Kch2ch21_CoPd);
%R41 CH3*+CH2* $\leftrightarrow$ CH3CH2*+*
r41_CoPd=kfCoPd(41)*y29*y28-krCoPd(41)*y76*y0_CoPd;
%R42 CH3CH2*+H* $\leftrightarrow$ CH3CH3(g)+2*
r42_CoPd=kfCoPd(42)*(y23*y76-Pch3ch3*y0_CoPd*y0_CoPd/Kch3ch3_CoPd);
%R43 CH2CH2*+H* $\leftrightarrow$ CH3CH2*+*
r43_CoPd=kfCoPd(43)*y75*y23-krCoPd(43)*y76*y0_CoPd;
%R44 CH2*+CH2* $\leftrightarrow$ CH2CH2*+*
r44_CoPd=kfCoPd(44)*y28*y28-krCoPd(44)*y75*y0_CoPd;
%R45 CHCH2*+* $\leftrightarrow$ CH2CH2(g)+2*
r45_CoPd=kfCoPd(45)*(y75*y0_CoPd-Pch2ch2*y0_CoPd*y0_CoPd/Kch2ch22_CoPd);
%r45_CoPd=0;
%R46 CH3CH2*+OH* $\leftrightarrow$ CH3CH2OH(g)+2*
r46_CoPd=kfCoPd(46)*(y76*y42-Pch3ch2oh*y0_CoPd*y0_CoPd/Kch3ch2oh2_CoPd);
%reactions and rate expressions on Co surface
%R1 CO(g)+* $\leftrightarrow$ CO*
r1_Co=kfCo(1)*(Pco*y0_Co-y43/Kco_Co);
%R2 H2(g)+2* $\leftrightarrow$ H*+H*
r2_Co=kfCo(2)*(Ph2*y0_Co*y0_Co-y44*y44/Kh2_Co);
%R3 CO*+H* $\leftrightarrow$ HCO*+*
r3_Co=kfCo(3)*y43*y44-krCo(3)*y45*y0_Co;
%R4 HCO*+H* $\leftrightarrow$ CH2O*+*
r4_Co=kfCo(4)*y44*y45-krCo(4)*y46*y0_Co;
%R5 CH2O*+H* $\leftrightarrow$ CH3O*+*
r5_Co=kfCo(5)*y46*y44-krCo(5)*y47*y0_Co;
%R6 HCO*+* $\leftrightarrow$ CH*+O*
r6_Co=kfCo(6)*y45*y0_Co-krCo(6)*y48*y62;
%R7 CH2O*+* $\leftrightarrow$ CH2*+O*
r7_Co=kfCo(7)*y0_Co*y46-krCo(7)*y49*y62;
%R8 CH3O*+* $\leftrightarrow$ CH3*+O*
r8_Co=kfCo(8)*y47*y0_Co-krCo(8)*y50*y62;

```

```

%R9  CH*+H* $\leftrightarrow$ CH2*+*
r9_Co=kfCo(9)*y48*y44-krCo(9)*y49*y0_Co;
%R10 CH2*+H* $\leftrightarrow$ CH3*+*
r10_Co=kfCo(10)*y49*y44-krCo(10)*y50*y0_Co;
%R11 CH3*+H* $\leftrightarrow$ CH4(g)+2*
r11_Co=kfCo(11)*(y44*y50-Pch4*y0_Co*y0_Co/Kch4_Co);
%R12 CH*+CO* $\leftrightarrow$ CHCO*+*
r12_Co=kfCo(12)*y43*y48-krCo(12)*y53*y0_Co;
%R13 CH2*+CO* $\leftrightarrow$ CH2CO*+*
r13_Co=kfCo(13)*y43*y49-krCo(13)*y54*y0_Co;
%R14 CH3*+CO* $\leftrightarrow$ CH3CO*+*
r14_Co=kfCo(14)*y43*y50-krCo(14)*y55*y0_Co;
%R15 CHCO*+H* $\leftrightarrow$ CH2CO*+*
r15_Co=kfCo(15)*y44*y53-krCo(15)*y54*y0_Co;
%R16 CH2CO*+H* $\leftrightarrow$ CH3CO*+*
r16_Co=kfCo(16)*y54*y44-krCo(16)*y55*y0_Co;
%R17 CH3CO*+H* $\leftrightarrow$ CH3CHO(g)+2*
r17_Co=kfCo(17)*((y55*y44)-Pch3cho*y0_Co*y0_Co/Kch3cho1_Co);
%R18 CH3CO*+H* $\leftrightarrow$ CH3COH*+*
r18_Co=kfCo(18)*y55*y44-krCo(18)*y59*y0_Co;
%R19 CH3COH*+H* $\leftrightarrow$ CH3CHOH*+*
r19_Co=kfCo(19)*y59*y44-krCo(19)*y61*y0_Co;
%R20 CH3CHOH*+H* $\leftrightarrow$ CH3CH2OH(g)+2*
r20_Co=kfCo(20)*((y61*y44)-Pch3ch2oh*y0_Co*y0_Co/Kch3ch2oh1_Co);
%R21 CH2O*+H* $\leftrightarrow$ CH2OH+*
r21_Co=kfCo(21)*y44*y46-krCo(21)*y52*y0_Co;
%R22 CH2CO*+H* $\leftrightarrow$ CH2COH*+*
r22_Co=kfCo(22)*y44*y54-krCo(22)*y58*y0_Co;
%R23 CH2COH*+H* $\leftrightarrow$ CH3COH*+*
r23_Co=kfCo(23)*y58*y44-krCo(23)*y59*y0_Co;
%R24 CHCO*+H* $\leftrightarrow$ CHCHO*+*
r24_Co=kfCo(24)*y53*y44-krCo(24)*y56*y0_Co;
%R25 CH2CO*+H* $\leftrightarrow$ CH2CHO*+*
r25_Co=kfCo(25)*y54*y44-krCo(25)*y57*y0_Co;
%R26 CHCHO*+H* $\leftrightarrow$ CH2CHO*+*
r26_Co=kfCo(26)*y56*y44-krCo(26)*y57*y0_Co;
%R27 CH2CHO*+H* $\leftrightarrow$ CH3CHO(g)+2*
r27_Co=kfCo(27)*((y57*y44)-Pch3cho*y0_Co*y0_Co/Kch3cho2_Co);
%R28 CH2O*+CH2* $\leftrightarrow$ CH3COH*+*
r28_Co=kfCo(28)*y46*y49-krCo(28)*y59*y0_Co;
%r28_Co=0;

```

```

%R29 O*+H* $\leftrightarrow$ OH*+*
r29_Co=kfCo(29)*y62*y44-krCo(29)*y63*y0_Co;
%R30 OH*+H* $\leftrightarrow$ H2O(g)+*
r30_Co=kfCo(30)*((y44*y63)-Ph2o*y0_Co*y0_Co/Kh2o_Co);
%R31 CH2COH*+H* $\leftrightarrow$ CH2CHOH*+*
r31_Co=kfCo(31)*y58*y44-krCo(31)*y60*y0_Co;
%R32 CH2CHOH*+H* $\leftrightarrow$ CH3CHOH*+*
r32_Co=kfCo(32)*y60*y44-krCo(32)*y61*y0_Co;
%R33 CH2CHO*+H* $\leftrightarrow$ CH2CHOH*+*
r33_Co=kfCo(33)*y57*y44-krCo(33)*y60*y0_Co;
%R34 CH2OH*+H* $\leftrightarrow$ CH3OH(g)+2*
r34_Co=kfCo(34)*((y52*y44)-Pch3oh*y0_Co*y0_Co/Kch3oh1_Co);
%R35 HCO*+H* $\leftrightarrow$ CHOH*+*
r35_Co=kfCo(35)*y46*y44-krCo(35)*y51*y0_Co;
%R36 CH3O*+H* $\leftrightarrow$ CH3OH(g)+2*
r36_Co=kfCo(36)*(y44*y47-Pch3oh*y0_Co/Kch3oh2_Co);
%R37 CHOH*+H* $\leftrightarrow$ CH2OH*+*
r37_Co=kfCo(37)*y51*y44-krCo(37)*y52*y0_Co;
%R38 CH*+CH2* $\leftrightarrow$ CHCH2*+*
r38_Co=kfCo(38)*y48*y49-krCo(38)*y77*y0_CoPd;
%R39 CHCH2*+H* $\leftrightarrow$ CH2CH2*+*
r39_Co=kfCo(39)*y77*y44-krCo(39)*y78*y0_Co;
%r39_Co=0;
%R40 CHCH2*+H* $\leftrightarrow$ CH2CH2(g)+2*
r40_Co=kfCo(40)*(y44*y77-Pch2ch2*y0_Co*y0_Co/Kch2ch21_Co);
%R41 CH3*+CH2* $\leftrightarrow$ CH3CH2*+*
r41_Co=kfCo(41)*y49*y50-krCo(41)*y79*y0_Co;
%R42 CH3CH2*+H* $\leftrightarrow$ CH3CH3(g)+2*
r42_Co=kfCo(42)*(y44*y79-Pch3ch3*y0_Co*y0_Co/Kch3ch3_Co);
%R43 CH2CH2*+H* $\leftrightarrow$ CH3CH2*+*
r43_Co=kfCo(43)*y78*y44-krCo(43)*y79*y0_Co;
%R44 CH2*+CH2* $\leftrightarrow$ CH2CH2*+*
r44_Co=kfCo(44)*y49*y49-krCo(44)*y78*y0_Co;
%r44_Co=0;
%R45 CHCH2*+* $\leftrightarrow$ CH2CH2(g)+2*
r45_Co=kfCo(45)*(y78*y0_Co-Pch2ch2*y0_Co*y0_Co/Kch2ch22_Co);
%R46 CH3CH2*+OH* $\leftrightarrow$ CH3CH2OH(g)+2*
r46_Co=kfCo(46)*(y79*y63-Pch3ch2oh*y0_Co*y0_Co/Kch3ch2oh2_Co);

```

% Diffusion equations

```

% R1 HCO*(CoPd)+*(Co) $\leftrightarrow$  HCO*(Co)+*(CoPd)

```

$r1_D = kfD(1) \cdot y_{24} \cdot y_{0_Co} - krD(1) \cdot y_{45} \cdot y_{0_CoPd}$;
 $\% R2 \text{ HCO}^*(\text{CoPd}) + ^*(\text{Pd}) \leftrightarrow \text{HCO}^*(\text{Pd}) + ^*(\text{CoPd})$
 $r2_D = kfD(2) \cdot y_{24} \cdot y_{0_Pd} - krD(2) \cdot y_3 \cdot y_{0_CoPd}$;
 $\% R3 \text{ CH}_2\text{O}^*\text{CoPd} + ^*\text{Co} \leftrightarrow \text{CH}_2\text{O}^*\text{Co} + ^*\text{CoPd}$
 $r3_D = kfD(3) \cdot y_{25} \cdot y_{0_Co} - krD(3) \cdot y_{46} \cdot y_{0_CoPd}$;
 $\% R4 \text{ CH}_2\text{O}^*(\text{CoPd}) + ^*(\text{Pd}) \leftrightarrow \text{CH}_2\text{O}^*(\text{Pd}) + ^*(\text{CoPd})$
 $r4_D = kfD(4) \cdot y_{25} \cdot y_{0_Pd} - krD(4) \cdot y_4 \cdot y_{0_CoPd}$;
 $\% R5 \text{ CH}_3\text{O}^*(\text{CoPd}) + ^*(\text{Co}) \leftrightarrow \text{CH}_3\text{O}^*(\text{Co}) + ^*(\text{CoPd})$
 $r5_D = kfD(5) \cdot y_{26} \cdot y_{0_Co} - krD(5) \cdot y_{47} \cdot y_{0_CoPd}$;
 $\% R6 \text{ CH}_3\text{O}^*(\text{CoPd}) + ^*(\text{Pd}) \leftrightarrow \text{CH}_3\text{O}^*(\text{Pd}) + ^*(\text{CoPd})$
 $r6_D = kfD(6) \cdot y_{26} \cdot y_{0_Pd} - krD(6) \cdot y_5 \cdot y_{0_CoPd}$;
 $\% R7 \text{ CH}_3\text{CO}^*(\text{CoPd}) + ^*(\text{Co}) \leftrightarrow \text{CH}_3\text{CO}^*(\text{Co}) + ^*(\text{CoPd})$
 $r7_D = kfD(7) \cdot y_{34} \cdot y_{0_Co} - krD(7) \cdot y_{55} \cdot y_{0_CoPd}$;
 $\% R8 \text{ CH}_3\text{CO}^*(\text{CoPd}) + ^*(\text{Pd}) \leftrightarrow \text{CH}_3\text{CO}^*(\text{Pd}) + ^*(\text{CoPd})$
 $r8_D = kfD(8) \cdot y_{34} \cdot y_{0_Pd} - krD(8) \cdot y_{13} \cdot y_{0_CoPd}$;
 $\% R9 \text{ CH}_3\text{COH}^*(\text{CoPd}) + ^*(\text{Co}) \leftrightarrow \text{CH}_3\text{COH}^*(\text{Co}) + ^*(\text{CoPd})$
 $r9_D = kfD(9) \cdot y_{38} \cdot y_{0_Co} - krD(9) \cdot y_{59} \cdot y_{0_CoPd}$;
 $\% R10 \text{ CH}_3\text{COH}^*(\text{CoPd}) + ^*(\text{Pd}) \leftrightarrow \text{CH}_3\text{COH}^*(\text{Pd}) + ^*(\text{CoPd})$
 $r10_D = kfD(10) \cdot y_{38} \cdot y_{0_Pd} - krD(10) \cdot y_{17} \cdot y_{0_CoPd}$;
 $\% R11 \text{ CH}_3\text{CHOH}^*(\text{CoPd}) + ^*(\text{Co}) \leftrightarrow \text{CH}_3\text{CHOH}^*(\text{Co}) + ^*(\text{CoPd})$
 $r11_D = kfD(11) \cdot y_{40} \cdot y_{0_Co} - krD(11) \cdot y_{61} \cdot y_{0_CoPd}$;
 $\% R12 \text{ CH}_3\text{CHOH}^*(\text{CoPd}) + ^*(\text{Pd}) \leftrightarrow \text{CH}_3\text{CHOH}^*(\text{Pd}) + ^*(\text{CoPd})$
 $r12_D = kfD(12) \cdot y_{40} \cdot y_{0_Pd} - krD(12) \cdot y_{19} \cdot y_{0_CoPd}$;
 $\% R13 \text{ OH}^*(\text{CoPd}) + ^*(\text{Co}) \leftrightarrow \text{OH}^*(\text{Co}) + ^*(\text{CoPd})$
 $r13_D = kfD(13) \cdot y_{42} \cdot y_{0_Co} - krD(13) \cdot y_{63} \cdot y_{0_CoPd}$;
 $\% R14 \text{ OH}^*(\text{CoPd}) + ^*(\text{Pd}) \leftrightarrow \text{OH}^*(\text{Pd}) + ^*(\text{CoPd})$
 $r14_D = kfD(14) \cdot y_{42} \cdot y_{0_Pd} - krD(14) \cdot y_{21} \cdot y_{0_CoPd}$;
 $\% R15 \text{ CH}_2\text{CHO}^*(\text{CoPd}) + ^*(\text{Co}) \leftrightarrow \text{CH}_2\text{CHO}^*(\text{Co}) + ^*(\text{CoPd})$
 $r15_D = kfD(15) \cdot y_{36} \cdot y_{0_Co} - krD(15) \cdot y_{57} \cdot y_{0_CoPd}$;
 $\% R16 \text{ CH}_2\text{CHO}^*(\text{CoPd}) + ^*(\text{Pd}) \leftrightarrow \text{CH}_2\text{CHO}^*(\text{Pd}) + ^*(\text{CoPd})$
 $r16_D = kfD(16) \cdot y_{36} \cdot y_{0_Pd} - krD(16) \cdot y_{15} \cdot y_{0_CoPd}$;
 $\% R17 \text{ CH}_2^*(\text{CoPd}) + ^*(\text{Co}) \leftrightarrow \text{CH}_2^*(\text{Co}) + ^*(\text{CoPd})$
 $r17_D = kfD(17) \cdot y_{28} \cdot y_{0_Co} - krD(17) \cdot y_{49} \cdot y_{0_CoPd}$;
 $\% R18 \text{ CH}_2^*(\text{CoPd}) + ^*(\text{Pd}) \leftrightarrow \text{CH}_2^*(\text{Pd}) + ^*(\text{CoPd})$
 $r18_D = kfD(18) \cdot y_{28} \cdot y_{0_Pd} - krD(18) \cdot y_7 \cdot y_{0_CoPd}$;
 $\% R19 \text{ CH}_3^*(\text{CoPd}) + ^*(\text{Co}) \leftrightarrow \text{CH}_3^*(\text{Co}) + ^*(\text{CoPd})$
 $r19_D = kfD(19) \cdot y_{29} \cdot y_{0_Co} - krD(19) \cdot y_{50} \cdot y_{0_CoPd}$;
 $\% R20 \text{ CH}_3^*(\text{CoPd}) + ^*(\text{Pd}) \leftrightarrow \text{CH}_3^*(\text{Pd}) + ^*(\text{CoPd})$
 $r20_D = kfD(20) \cdot y_{29} \cdot y_{0_Pd} - krD(20) \cdot y_8 \cdot y_{0_CoPd}$;
 $\% R19 \text{ CH}_3\text{CH}_2^*(\text{CoPd}) + ^*(\text{Co}) \leftrightarrow \text{CH}_3\text{CH}_2^*(\text{Co}) + ^*(\text{CoPd})$
 $r21_D = kfD(19) \cdot y_{76} \cdot y_{0_Co} - krD(19) \cdot y_{79} \cdot y_{0_CoPd}$

```

% R20 CH3CH2*(CoPd)+*(Pd)<--> CH3CH2*(Pd)+*(CoPd)
r22_D =kfD(20)*y76*y0_Pd-krD(20)*y73*y0_CoPd;
%
r1_D=0; r2_D=0; r3_D=0; r4_D=0; r5_D=0; r6_D=0; r7_D=0; r8_D=0; r9_D=0; r10_D=0;
r11_D=0; r12_D=0; r13_D=0; r14_D=0; r15_D=0; r16_D=0; r17_D=0; r18_D=0; r19_D=0;
r20_D=0;r21_D=0; r22_D=0;
% %

% Change in concentration of intermediates with time on Pd surface
%dy1dt=r1_Pd;
dy1dt=r1_Pd-r3_Pd-r12_Pd-r13_Pd-r14_Pd;
% H*
%dy2dt=r2_Pd;
dy2dt=r2_Pd-r3_Pd-r4_Pd-r5_Pd-r9_Pd-r10_Pd-r11_Pd-r15_Pd-r16_Pd-r17_Pd-r18_Pd-
r19_Pd-r20_Pd-r21_Pd-r22_Pd-r23_Pd-r24_Pd-r25_Pd-r26_Pd-r27_Pd-r29_Pd-r30_Pd-
r31_Pd-r32_Pd-r33_Pd-r34_Pd-r35_Pd-r36_Pd-r37_Pd-r39_Pd-r40_Pd-r42_Pd-r43_Pd;
%HCO*
dy3dt=r3_Pd-r4_Pd-r6_Pd-r35_Pd+r2_D;
% CH2O*
dy4dt=r4_Pd-r5_Pd-r7_Pd-r21_Pd-r28_Pd+r4_D;
%CH3O*
dy5dt=r5_Pd-r8_Pd-r36_Pd+r6_D;
%CH*
dy6dt=r6_Pd-r9_Pd-r12_Pd-r38_Pd;
%CH2*
dy7dt=r7_Pd+r9_Pd-r10_Pd-r13_Pd-r28_Pd-r38_Pd-r41_Pd-r44_Pd+r18_D;
%CH3*
dy8dt=r8_Pd+r10_Pd-r11_Pd-r14_Pd-r41_Pd+r20_D;
%CHOH*
dy9dt=r35_Pd-r37_Pd;
%CH2OH*
dy10dt=r21_Pd-r34_Pd+r37_Pd;
%CHCO*
dy11dt=r12_Pd-r15_Pd-r24_Pd;
%CH2CO*
dy12dt=r13_Pd+r15_Pd-r16_Pd-r22_Pd-r25_Pd;
%CH3CO*
dy13dt=r14_Pd+r16_Pd-r17_Pd-r18_Pd+r8_D;
%CHCHO*
dy14dt=r24_Pd-r26_Pd;
%CH2CHO*

```


$dy_{15dt} = r_{25_Pd} + r_{26_Pd} - r_{27_Pd} - r_{33_Pd} + r_{16_D};$
 %CH2COH*
 $dy_{16dt} = r_{22_Pd} - r_{23_Pd} - r_{31_Pd};$
 %CH3COH*
 $dy_{17dt} = r_{18_Pd} - r_{19_Pd} + r_{23_Pd} + r_{28_Pd} + r_{10_D};$
 %CH2CHOH*
 $dy_{18dt} = r_{31_Pd} - r_{32_Pd} + r_{33_Pd};$
 %CH3CHOH*
 $dy_{19dt} = r_{19_Pd} - r_{20_Pd} + r_{32_Pd} + r_{12_D};$
 %O*
 $dy_{20dt} = r_{6_Pd} + r_{7_Pd} + r_{8_Pd} - r_{29_Pd};$
 %OH*
 $dy_{21dt} = r_{29_Pd} - r_{30_Pd} - r_{46_Pd} + r_{14_D};$
 %CHCH2*
 $dy_{71dt} = r_{38_Pd} - r_{39_Pd} - r_{40_Pd};$
 %CH2CH2*
 $dy_{72dt} = r_{39_Pd} - r_{43_Pd} + r_{44_Pd} - r_{45_Pd};$
 %CH3CH2*
 $dy_{73dt} = r_{41_Pd} - r_{42_Pd} + r_{43_Pd} - r_{46_Pd} + r_{22_D};$
 % Change in concentration of intermediates with time on CoPd surface
 %dy1dt=r1_CoPd;
 $dy_{22dt} = r_{1_CoPd} - r_{3_CoPd} - r_{12_CoPd} - r_{13_CoPd} - r_{14_CoPd};$
 % H*
 %dy2dt=r2_CoPd;
 $dy_{23dt} = r_{2_CoPd} - r_{3_CoPd} - r_{4_CoPd} - r_{5_CoPd} - r_{9_CoPd} - r_{10_CoPd} - r_{11_CoPd} - r_{15_CoPd} - r_{16_CoPd} - r_{17_CoPd} - r_{18_CoPd} - r_{19_CoPd} - r_{20_CoPd} - r_{21_CoPd} - r_{22_CoPd} - r_{23_CoPd} - r_{24_CoPd} - r_{25_CoPd} - r_{26_CoPd} - r_{27_CoPd} - r_{29_CoPd} - r_{30_CoPd} - r_{31_CoPd} - r_{32_CoPd} - r_{33_CoPd} - r_{34_CoPd} - r_{35_CoPd} - r_{36_CoPd} - r_{37_CoPd} - r_{39_CoPd} - r_{40_CoPd} - r_{42_CoPd} - r_{43_CoPd};$
 %HCO*
 $dy_{24dt} = r_{3_CoPd} - r_{4_CoPd} - r_{6_CoPd} - r_{35_CoPd} - r_{1_D} - r_{2_D};$
 % CH2O*
 $dy_{25dt} = r_{4_CoPd} - r_{5_CoPd} - r_{7_CoPd} - r_{21_CoPd} - r_{28_CoPd} - r_{3_D} - r_{4_D};$
 %CH3O*
 $dy_{26dt} = r_{5_CoPd} - r_{8_CoPd} - r_{36_CoPd} - r_{5_D} - r_{6_D};$
 %CH*
 $dy_{27dt} = r_{6_CoPd} - r_{9_CoPd} - r_{12_CoPd} - r_{38_CoPd};$
 %CH2*
 $dy_{28dt} = r_{7_CoPd} + r_{9_CoPd} - r_{10_CoPd} - r_{13_CoPd} - r_{28_CoPd} - r_{38_CoPd} - r_{41_CoPd} - r_{44_CoPd} - r_{17_D} - r_{18_D};$
 %CH3*

dy29dt=r8_CoPd+r10_CoPd-r11_CoPd-r14_CoPd-r41_CoPd-r19_D-r20_D;
 %CHOH*
 dy30dt=r35_CoPd-r37_CoPd;
 %CH2OH*
 dy31dt=r21_CoPd-r34_CoPd+r37_CoPd;
 %CHCO*
 dy32dt=r12_CoPd-r15_CoPd-r24_CoPd;
 %CH2CO*
 dy33dt=r13_CoPd+r15_CoPd-r16_CoPd-r22_CoPd-r25_CoPd;
 %CH3CO*
 dy34dt=r14_CoPd+r16_CoPd-r17_CoPd-r18_CoPd-r7_D-r8_D;
 %CHCHO*
 dy35dt=r24_CoPd-r26_CoPd;
 %CH2CHO*
 dy36dt=r25_CoPd+r26_CoPd-r27_CoPd-r33_CoPd-r15_D-r16_D;
 %CH2COH*
 dy37dt=r22_CoPd-r23_CoPd-r31_CoPd;
 %CH3COH*
 dy38dt=r18_CoPd-r19_CoPd+r23_CoPd+r28_CoPd-r9_D-r10_D;
 %CH2CHOH*
 dy39dt=r31_CoPd-r32_CoPd+r33_CoPd;
 %CH3CHOH*
 dy40dt=r19_CoPd-r20_CoPd+r32_CoPd-r11_D-r12_D;
 %O*
 dy41dt=r6_CoPd+r7_CoPd+r8_CoPd-r29_CoPd;
 %OH*
 dy42dt=r29_CoPd-r30_CoPd-r46_CoPd-r13_D-r14_D;
 %CHCH2*
 dy74dt=r38_CoPd-r39_CoPd-r40_CoPd;
 %dy74dt=0;
 %CH2CH2*
 dy75dt=r39_CoPd-r43_CoPd-r45_CoPd+r44_CoPd;
 %CH3CH2*
 dy76dt=r41_CoPd-r42_CoPd+r43_CoPd-r46_CoPd-r21_D-r22_D;

% Change in concentration of intermediates with time on Co surface
 %CO
 %dy43dt=1e-50;
 dy43dt=r1_Co-r3_Co-r12_Co-r13_Co-r14_Co;
 % H*
 %dy44dt=1e-150;

dy44dt=r2_Co-r3_Co-r4_Co-r5_Co-r9_Co-r10_Co-r11_Co-r15_Co-r16_Co-r17_Co-
 r18_Co-r19_Co-r20_Co-r21_Co-r22_Co-r23_Co-r24_Co-r25_Co-r26_Co-r27_Co-r29_Co-
 r30_Co-r31_Co-r32_Co-r33_Co-r34_Co-r35_Co-r36_Co-r37_Co-r39_Co-r40_Co-r42_Co-
 r43_Co;
 %HCO*
 dy45dt=r3_Co-r4_Co-r6_Co-r35_Co+r1_D;
 % CH2O*
 dy46dt=r4_Co-r5_Co-r7_Co-r21_Co-r28_Co+r3_D;
 %CH3O*
 dy47dt=r5_Co-r8_Co-r36_Co+r5_D;
 %CH*
 dy48dt=r6_Co-r9_Co-r12_Co-r38_Co;
 %CH2*
 dy49dt=r7_Co+r9_Co-r10_Co-r13_Co-r28_Co-r38_Co-r41_Co-r44_Co+r17_D;
 %CH3*
 dy50dt=r8_Co+r10_Co-r11_Co-r14_Co-r41_Co+r19_D;
 %CHOH*
 dy51dt=r35_Co-r37_Co;
 %CH2OH*
 dy52dt=r21_Co-r34_Co+r37_Co;
 %CHCO*
 dy53dt=r12_Co-r15_Co-r24_Co;
 %CH2CO*
 dy54dt=r13_Co+r15_Co-r16_Co-r22_Co-r25_Co;
 %CH3CO*
 dy55dt=r14_Co+r16_Co-r17_Co-r18_Co+r7_D;
 %CHCHO*
 dy56dt=r24_Co-r26_Co;
 %CH2CHO*
 dy57dt=r25_Co+r26_Co-r27_Co-r33_Co+r15_D;
 %CH2COH*
 dy58dt=r22_Co-r23_Co-r31_Co;
 %CH3COH*
 dy59dt=r18_Co-r19_Co+r23_Co+r28_Co+r9_D;
 %CH2CHOH*
 dy60dt=r31_Co-r32_Co+r33_Co;
 %CH3CHOH*
 dy61dt=r19_Co-r20_Co+r32_Co+r11_D;
 %O*
 dy62dt=r6_Co+r7_Co+r8_Co-r29_Co;
 %OH*

```

dy63dt=r29_Co-r30_Co+r13_D-r46_Co;
%CHCH2*
dy77dt=r38_Co-r39_Co-r40_Co;
%CH2CH2*
dy78dt=r39_Co-r43_Co+r44_Co-r45_Co;
%dy78dt=0;
%CH3CH2*
dy79dt=r41_Co-r42_Co+r43_Co-r46_Co+r21_D;

% Change in number of moles of Gas phase species with time
%CO(g)
dy64dt =(mcat*s/(Na*w))*(-r1_Pd-r1_CoPd-r1_Co);
%H2(g)
dy65dt =(mcat*s/(Na*w))*((-r2_Pd-r2_CoPd-r2_Co)/2);
%CH4(g)
dy66dt =(mcat*s/(Na*w))*(r11_Pd+r11_CoPd+r11_Co);
%CH3OH(g)
dy67dt =(mcat*s/(Na*w))*(r34_Pd+r34_CoPd+r34_Co+r36_Pd+r36_CoPd+r36_Co);
%CH3CH2OH(g)
dy68dt=(mcat*s/(Na*w))*(r20_Pd+r20_CoPd+r20_Co+r46_Pd+r46_CoPd+r46_Co);
%CH3CHO(g)
dy69dt=(mcat*s/(Na*w))*(r17_Pd+r17_CoPd+r17_Co+r27_Pd+r27_CoPd+r27_Co);
%H2O(g)
dy70dt=(mcat*s/(Na*w))*(r30_Pd+r30_CoPd+r30_Co);
%CH2CH2(g)
dy80dt=(mcat*s/(Na*w))*(r40_Pd+r40_CoPd+r40_Co+r45_Pd+r45_CoPd+r45_Co);
%CH3CH3(g)
dy81dt=(mcat*s/(Na*w))*(r42_Pd+r42_CoPd+r42_Co);

f=[dy1dt; dy2dt; dy3dt; dy4dt; dy5dt; dy6dt; dy7dt; dy8dt; dy9dt; dy10dt; dy11dt;
dy12dt; dy13dt; dy14dt; dy15dt; dy16dt; dy17dt; dy18dt; dy19dt; dy20dt; dy21dt;
dy22dt; dy23dt; dy24dt; dy25dt; dy26dt;dy27dt; dy28dt; dy29dt; dy30dt; dy31dt;
dy32dt; dy33dt; dy34dt; dy35dt; dy36dt;dy37dt; dy38dt; dy39dt; dy40dt; dy41dt;
dy42dt; dy43dt; dy44dt; dy45dt; dy46dt; dy47dt; dy48dt; dy49dt; dy50dt; dy51dt;
dy52dt; dy53dt; dy54dt; dy55dt; dy56dt; dy57dt; dy58dt; dy59dt; dy60dt; dy61dt;
dy62dt; dy63dt; dy64dt; dy65dt; dy66dt;dy67dt; dy68dt;dy69dt; dy70dt; dy71dt;
dy72dt; dy73dt; dy74dt; dy75dt; dy76dt;dy77dt; dy78dt;dy79dt; dy80dt; dy81dt];

end

*****

```

D) PBS script

```
#PBS -N commads2
#PBS -l select=1:ncpus=20:mem=120gb,walltime=48:00:00
```

```
module load matlab/2016a
module add gnu-parallel
```

```
cd $PBS_O_WORKDIR
```

```
cat trial.txt | parallel -j20
```

E) Sample file trial.txt

Trial.txt contains set of nPd, nCoPd, nCo values at which main is executed

```
./main 0.01 0.01 0.98 > 0.01_0.01_0.98.out
./main 0.01 0.02 0.97 > 0.01_0.02_0.97.out
./main 0.01 0.03 0.96 > 0.01_0.03_0.96.out
./main 0.01 0.04 0.95 > 0.01_0.04_0.95.out
./main 0.01 0.05 0.94 > 0.01_0.05_0.94.out
./main 0.01 0.06 0.93 > 0.01_0.06_0.93.out
./main 0.01 0.07 0.92 > 0.01_0.07_0.92.out
./main 0.01 0.08 0.91 > 0.01_0.08_0.91.out
./main 0.01 0.09 0.9 > 0.01_0.09_0.9.out
./main 0.01 0.1 0.89 > 0.01_0.1_0.89.out
./main 0.01 0.11 0.88 > 0.01_0.11_0.88.out
```

VITA

Anuradha (Anu) Gundamaraju (Eluripati) is born in Hyderabad, India which is the capital city of the new Telangana state located in the southern part of India. She is the youngest of four siblings. Her father is a primary care physician and her mother is a home maker.

After completing high school in Mahbubnagar town, Anu moved to the city of Hyderabad for her college/undergraduate education. She completed her Bachelors of Engineering and Technology (or B.Tech) in Chemical Engineering at Jawaharlal Nehru Technological University (JNTU). After undergraduate study, she continued her education with a Masters degree in Engineering and Technology (or M.Tech) also in Chemical Engineering at JNTU in the city of Anantapur. One of her academic achievements is scoring a 13th rank (out of 1000s of applicants) in the special entrance examination for graduate studies. During her graduate school, Anu did an internship program at Indian Institute of Chemical Technology (IICT) on a project called "Process Development for HFC-134A". The aim of program is to develop an indigenous technology for making HFC-134A in a conventional flow system in the presence of a catalyst.

After completing her Masters, Anu started teaching at Sri Indu College of Engineering and Technology in Hyderabad, India. She taught subjects such as Process Engineering Principles and Biochemical Reaction Engineering. She also conducted laboratories in Bioprocess Engineering and Downstream Processing.

Anu got married in 2009 and moved to the United States of America along with her husband to Greenville, South Carolina. With an interest to continue her career in teaching & research, Anu pursued a PhD program in Chemical Engineering at Clemson University and started her doctorate in 2011. At Clemson University, she continued her research work in the field of Catalysis. She also worked as a teaching assistant for a few semesters in the Chemical Engineering department.

Anu continues to live in Greenville, South Carolina with her husband (Ravi Eluripati) and her daughter (Laasya Eluripati).